Magnetostrictive excitation of Atomic Force Microscopy cantilevers when operating in liquid environments

Tesis para optar al grado de Doctor en Ciencias Físicas presentada por:

Marcos Penedo García

Dirigida por la Doctora Mónica Luna Estévez

y el Profesor Fernando Briones Fernández-Pola

Tutelada por el Profesor Rodolfo Miranda Soriano

Instituto de Microelectrónica de Madrid
(Centro Nacional de Microelectrónica)

Departamento de Física de la Materia Condensada

Facultad de Ciencias

Universidad Autónoma de Madrid

Diciembre 2013

Adicado a miña familia
e a Alba

Agradecimientos

La realización de esta tesis no habría sido posible sin la contribución de varias personas. En especial, me gustaría agradecer a mis directores Fernando Briones y Mónica Luna toda la ayuda y comprensión recibida a lo largo de estos años. Sin sus ideas, ayuda y colaboración no habría sido posible haber realizado esta tesis. Ellos me han enseñado el oficio y la exigencia que conlleva este trabajo.

Agradecer a miña familia todo o apoio que me deron. Sempre que o ánimo estaba baixo, estaban ahí dando folgos. Sen eles, tanto esta tese coma todo o que teño non tería sido posible. Todas a grazas que poidese dar non serían abondo.

Unha parte desta tese pertenze tamén a Alba. Sempre estiveches ahí, nos momentos malos en nos bos. Acougándome cando o necesitaba, e afastando os meus medos. Un gran anaco disto é teu. Grazas Albiña.

Me gustaría también agradecer el apoyo recibido por la empresa Nanotec Electrónica. En todo momento han estado ahí para mis problemas y dudas. Estoy especialmente agradecido a Adriana Gil, Pablo Ares, Eduardo Delgado y Jaime de Sousa.

I am also indebted to Prof. Arvind Raman (Purdue University, USA) for his wise and sagacious advices that led me to enquire about the efficciency of magnetostriction in exciting higher modes.

I would like to thank Prof. Hans Hug and Miguel Marioni for all the support and help received in recent months. I really appreciate it.

También agradecer a Jesús M. de la Fuente el trato recibido durante los tres meses en el INA. Y a toda la gente de Zaragoza, que me hicieron sentir como en casa: Sara Puertas, Pablo, Sara Rivera, Bea, Yulán, Íñigo, Valería, María, Ester, Yulán y Miguel (espero no olvidarme de nadie).

Hay algunas personas que me han ayudado durante el desarrollo de esta tesis a las que me gustaría dar las gracias de una manera especial. A Iván Fernández, que siempre ha estado ahí para cualquier cosa que haya necesitado, siendo un gran apoyo. A Iván Prieto, el máster de la sala blanca, siempre resolviendo dudas (grazas polos dous últimos findes). A los técnicos, verdaderos pilares del IMM. Agradecer especialmente a Patricia, Raquel y Merce. Estoy se vendría abajo sin vosotras. A Mariana, que siempre estaba ahí para todo, resolviendo mis interminables dudas. A Alfonso Taboada, que me daba las collejas necesarias "pa tirar palante". Te debo una muy grande. A esa gente que ha hecho esos pequeños esfuerzos por mi: Carmen, Sergio, Nacho, Tere y Amaia. A Mariano Cuenca y Tomás Vallés, por el diseño y montaje de los equipos electrónicos utilizados en esta tesis.

Ha sido también una agran ayuda toda la gente con la que he convivido estos años y me han ayudado a diario: Alberto, Diego, Irene, Eli, Clara, Alba, Manuel y Tiago.

No quiero olvidar a mis compañeros de despacho, con esas interminables discusiones: Elias (Mojo, con el chiste te sobra, no te hacen falta los 50 pavos), Elena (infinita, pero la antigua), ZP (el guapo e interesante), Carlos (ooooogame), Horacio (el oráculo de Cochabamba), Jorge (Joljito), Blaca (o Blanquiña), Valerio (mi comsolador) y a Mayra (ese ronsito). Grazas tamén a Xesús, que é máis que un amigo, sempre ahí pra escoitar e pra tomarlle unha en caso de necesidade. A Edu, o Lionel da noite, un grande de España, e un gran apoio nos momentos duros. Grazas meu. A Malvar e a Estela, esa parella que de algún modo rematará xunta e que sempre aledan o día. A Etor, ese mago de la pelota, entrañable y atento siempre. Gracias por los ánimos que siempre me has dado. La verdad que eres cojonudo. A Cristina Vicente, siempre para dar un abrazo cuando se necesita. A Chris, con esa sonrisa permanente. A Fuster, por descubrirnos lo peligrosa que puede ser una alpaca (quien lo habría imaginado). A bam bam Benito, un referente a seguir, tanto profesionalmente como en la vida. A Diana por esos momentos deportistas (como echo de menos esos partidillos de tenis). A Lau, Nebris, Julián y David, por esos momentos de relax y esas escapaditas. A Dani Ramos, siempre resolutivo en dudas de última hora. A Rui, ese galán al que Dios le dio un codo milagroso. A Javi Martínez, por esas buenas noches Madrileñas. A Llorens, por esos comentarios que siempre te alegran el día. A Margarita, por sus grandes historias de ciencia ficción. A Julio, Xue y Johannes por los últimos empujonciños. A Ripi, TamaTama, Miguel, Chemi, Paco, Kamal, Liav y Joselo por esas pachanguitas. A Jesús, por esas conversaciones que hacían mas llevaderas las estancias en el AFM. A Manuel, un recepcionista sobranceiro donde los haya. A Ricardo, o artista gráfico. Y a todo el personal del IMM, resolviendo esos pequeños problemas que siempre aparecen.

Y finalmente, a todas esas personas que durante estos años han estado ahí aportando su granito de arena: Jony, Prisci, Lucas, Marco, Lorena, Fran, Juan, Olga, Jaime, Diana, Ryu, Begoña, Marta, Carmen, Carmiña, Ana, Maki, Paco, Nuria, Maki, Pablo, Silvia, Martina, Andra, Alma, Dani, Jerónimo, Alan, Mario, Mercedes.

Contents

Motivation, objectives and methodology

Nanoscience studies matter at nanometer scale. New materials and devices based on nanoscience constitute what is called "nanotechnology". Considering the large relevance that nanotechnology is already experiencing, Richard Feynman's vision of miniaturization with "[...] plenty of room at the bottom" [1] may have already been materialized to a certain extent.

Nanoscale systems and products are already in the market (telecommunication, health, military, etc.), and prospects point out that the new nanotechnology applications development will have an even higher impact on our economy and society in the coming years [1]. In the field of biological and biomedical applications, nanotechnology holds the promise of a wide range of applications such as cheaper, faster and less invasive diagnose and disease detection methods. The importance ascribed to this research area by the scientific community becomes quantitatively evident by the large number of publications related to nanotechnology that have appeared in the last decades.

The development of new instrumentation is a fundamental requirement to continue the progress in nanotechnology. Among the current nanotechnological techniques, Scanning Probe Microscopy (SPM) stands out for its versatility and ability to provide images in real space at nanometer scale and for its capability to manipulate matter. SPM techniques are already established as invaluable characterization and manipulation nanotools.

One kind of scanning probe microscope, the Atomic Force Microscope (AFM), is proving to be particularly useful in the emerging field of nanobiotechnology, where biological processes are studied and controlled at nanometer scale and in an individual basis. AFM employs a cantilever furnished with a sharp tip as a probe. As it is scanned over the sample, the local interaction of the tip with it affects the cantilever in a measurable way. It can be used to obtain images of the surface topography down to atomic scales. In addition, it is used to measure many different physical properties: magnetic properties [2], surface work function [3], surface dielectric constant values [4], protein flexibility [5], etc. Furthermore, AFM has become a multifunctional nanotool. It can be also employed for tip-based nano manufacturing techniques such as dip-pen lithography [6] and local oxidation [7]. Its impact on bio-nano-medicine stems from its adaptability to water operation. If the tip is biofunctionalized, the AFM probe becomes a laboratory on a tip that can detect, while scanning, many different biophysical and chemical structures and interactions [8]. High resolution AFM topographic images of large biomolecules, membranes or tissues [9] convey an idea of the AFM imaging capabilities.

[1] Annual meeting of the American Physical Society at Caltech (1959).

Motivation

The fact that AFM can work in different media, like vacuum or liquids, and especially in water-based solutions where biological processes take place, makes it essential for nano-bio-medical studies.

Thus, for example, AFM is used for obtaining images of protein molecules or biological surfaces in their natural environment. AFM is also being used to measure surface viscoelastic properties and/or search for molecular recognition sites on living cells [9].

Several difficulties need to be overcome in order to achieve an efficient AFM inspection of biological matter. For instance, the minimization of vertical forces exerted on the surface [10] is essential to avoid biological sample damage during surface scanning. One way to achieve this goal is to operate the AFM in dynamic modes. Dynamic AFM requires the mechanical oscillation of the tip at or near its resonance frequency and/or higher resonance modes. Another demand is the study of the proteins or biological surfaces in their natural physiological environment, to avoid the morphological and functional changes that may occur when biological matter is measured in air. Even though achieving a good cantilever actuation, which is a must for a proper operation, is easy in vacuum or air, it is not so in liquid environments. The acoustic actuation used for air operation produces cantilever resonance spectra with spurious peaks. These peaks come from the excitation of different liquid cell resonances and the fluid borne excitation.

Recently, new measurement techniques based on the simultaneous excitation and/or detection of several harmonics and/or modes (flexural or torsional) of the AFM cantilever oscillation have been developed [11]. Multi-harmonic AFM can be used to obtain compositional contrast of biological materials in liquids [12]. It has been successfully used to map the nanomechanical properties of living cells [13] and also to measure the vitro local material properties of intact and disrupted virions at high resolution [14]. Bimodal techniques [15] have been used for molecular resolution imaging and quantitative mapping of material properties simultaneously [5], increasing compositional resolution and sensitivity [16]. In addition, multifrequency techniques have also contributed to high-speed imaging[17], as well as to topics such as energy storage [18] or nanomedicine [19]. On the other hand, resonant micromechanical sensors also benefit from the improvement of the quality factor Q and the mass sensing resolution obtained when operating with high eigenmodes.

Objectives

In general terms, this PhD thesis is centered in the development of novel instrumentation and experimental methods for the improvement of bio-AFM. In particular, the thesis work is focused on the development of an application of magnetostriction: its use for inducing the mechanical excitation of cantilevers. Along this thesis, it will be demonstrated that this original magnetostrictive actuation method overcomes many of the problems presented by the current excitation techniques when operating in liquid environments.

The particular objectives of this work are:

- Theoretical analysis, modeling and experimental study of the magnetostrictive cantilever actuation.
- Implementation of the new actuation method in a commercial AFM microscope for liquids.

- Selective higher order vibrational modes excitation enhancement by means of specific magnetostrictive film areas micro-mecanization or ions implantation by Focused Ion Beam technique (FIB, iLine equipment from Raith).

An important part of the objectives and specific work planning will be devoted to solve technical and engineering issues. The new implementation will require working on the actuation electronics. For example, an external lock-in amplifier will be needed in the detection of the different harmonics. Also, we will acquire specific amplifiers/generators adapted to the system characteristics.

Methodology

The basis of this new magnetostrictive excitation technique is the deposition and patterning of a magnetostrictive layer which is placed on the cantilever upper surface. Since magnetostrictive materials change dimensions under a variation of their magnetization state, the application of an external magnetic field will induce the cantilever bending. Accordingly, an AC magnetic field and adequate frequency will induce a clear resonance oscillation of the cantilever, even under liquid high damping conditions.

Therefore, main methodology landmarks of the work carried out in this thesis can be specified as follows:

1. Proof of concept experimental verification: magnetostrictive phenomenon applied to the generation of mechanical vibration of the cantilevers (Chapter 2).

2. Theoretical analysis, modeling and experimental study of the current actuation techniques (Chapter 4).

3. Implementation of the new method in a liquid operating AFM. Preparation and characterization of the coating film (Chapter 2). Development of a new liquid cell (Chapter 3). Implementation of new electronics and magnetostrictive technique in a commercial AFM when operating in liquids (Chapters 3 and 6).

4. Comparative study of the high modes excitation efficiency and oscillation amplitude of the different actuation methods (Chapter 4).

5. Higher order vibrational modes excitation enhancement research achieved by means of micro-mechanization or ion implantation of specific magnetostrictive film areas by Focused Ion Beam technique (Chapter 5).

Selection of the magnetostrictive material (Fe-B-N) for this AFM application is based in the previous research carried out by Dr. Iván Fernández in his PhD thesis [20], at our group in the Instituto de Microelectrónica de Madrid (IMM-CSIC). In this work, we followed his procedure as he demonstrated the excellent mechanical and magnetostrictive properties of Fe-B-N thin films deposited by sputtering.

As a first step in this thesis, the deposition process of amorphous magnetostrictive Fe-B-N thin films by sputtering needs to be optimized by controlling the magnetic anisotropy direction in the magnetostrictive film induced by the applied magnetic field during deposition. The methodology in this part will be based on the structural (X-ray) and magnetic (magneto optic

Kerr effect, MOKE) characterization of thin film deposited on glass or silicon, as it is difficult to use the MOKE technique directly on cantilevers due to its small size.

An important phase of the methodology was the development of a liquid cell specially designed for a Nanotec Electrónica AFM microscope. Finite elements model simulations have to be performed in order to optimize the electromagnet placement and geometry, minimizing the current through the coil. Furthermore, the final prototype must present low mechanical noise and must be able to produce clean cantilever resonance spectra in liquid environments.

Furthermore, due to the current interest in ultra flat metal surfaces as substrates for SPM, a novel template-stripping method was developed (Chapter 7). Some of these surfaces must be used in liquid environments, and they must be resistant without being degraded.

Motivación, objetivos y metodología

La nanociencia estudia la materia a escala nanométrica. Se conoce como nanotecnología a los nuevos materiales y dispositivos basados en la nanociencia. Considerando la gran relevancia que está experimentado la nanotecnología, la visión de Richard Feynman sobre la miniaturización con "[...] plenty of room at the bottom"[2] se ha llegado a materializar hasta cierto punto.

Ya podemos encontrar sistemas y productos a escala nanométrica en el mercado (telecomunicaciones, salud, militar, etc.), y se prevé que los desarrollos de las nuevas aplicaciones nanotecnológicas tendrán incluso un impacto mayor en los próximos años [1]. En el campo de las aplicaciones biológicas o biomédicas, la nanotecnología promete un amplio abanico de aplicaciones, como métodos de diagnostico y detección más baratos, rápidos y menos invasivos. El gran numero de trabajos científicos que han aparecido estas últimas décadas relacionados con la nanotecnología nos proporciona una idea cuantitativa de la importancia de esta área de investigación.

El desarrollo de nuevos instrumentos es un requisito fundamental para continuar progresando en la nanotecnología. Entre las técnicas nanotecnológicas actuales, la Microscopía de Sonda de Barrido (SPM por sus siglas en inglés, Scanning Probe Microscopy) sobresale por su habilidad para proporcionar imágenes reales a escala nanométrica y por la posibilidad de manipular la materia. Las técnicas basadas en SPM están actualmente consideradas como importantes nanoherramientas para la caracterización y manipulación.

Un tipo de SPM, el Microscopio de Fuerzas Atómicas (AFM por sus siglas en inglés, Atomic Force Microscope), se ha mostrado como una herramienta muy útil en el campo emergente de la nanobiotecnología, donde se estudian los procesos biológicos a escala nanométrica. El AFM emplea una micropalanca con una punta muy afilada como sonda. Cuando la punta escanea la muestra, la interacción local punta/muestra afecta a la micropalanca de una forma que podemos medir. El AFM se puede utilizar para obtener imágenes topográficas de superficies alcanzando resolución atómica, y su versatilidad ha llevado al desarrollo de diferentes técnicas muy específicas. Actualmente, el AFM se utiliza para medir diferentes propiedades físicas: propiedades magnéticas [2], función de trabajo de superficies [3], valores de la constante dieléctrica de superficies [4], flexibilidad en proteínas [5], etc. Además, el AFM se ha convertido en una nanoherramienta multifuncional. Puede ser empleado para técnicas de nanomanufacturación basado en puntas, como por ejemplo la litografía "dip-pen" [6] o la oxidación local [7]. Su impacto en la bio-nano-medicina descansa en su versatilidad. Si la punta de la micropalanca es biofuncionalizada, la sonda del AFM se convierte en un laboratorio en donde se pueden detectar, al mismo tiempo que se escanea la superficie, diferentes estructuras químicas y biofísicas [8]. Para hacerse una idea de las capacidades del AFM, basta con ver las imágenes topográficas de alta resolución de biomoléculas, membranas o tejidos que es capaz de realizar un AFM.

[2]Reunión anual de la American Physical Society en Caltech (1959).

Motivación

Lo que hace esencial al AFM en estudio nano-bio-médicos es su capacidad para trabajar en diferentes medios, desde sistemas en vacío hasta en ambientes líquidos y, en particular, en las soluciones acuosas en donde se producen los procesos biológicos.

Así, por ejemplo, el AFM se utiliza rutinariamente para realizar imágenes de proteínas o superficies biológicas en sus medios naturales. El AFM también se usa para medir las propiedades viscoelásticas de superficies y/o buscar lugares de reconocimiento molecular en células vivas [9].

Sin embargo, para lograr una inspección eficiente de las muestras biológicas con el AFM se necesitan superar algunas dificultades. Por ejemplo, para evitar dañar la muestra biológica durante el escaneo de su superficie es crucial minimizar las fuerzas verticales ejercidas en su superficie [10]. Una forma de lograr esto es operar el AFM en modo dinámico. En los métodos dinámicos la micropalanca se hace oscilar cerca o a su frecuencia de resonancia natural, o incluso en uno o varios modos altos de resonancia. Otro requerimiento es poder estudiar las proteínas o las superficies biológicas en sus medios fisiológicos naturales, para evitar cambios funcionales o morfológicos que pueden ocurrir cuando los materiales biológicos se miden en aire. Aunque es fácil de conseguir una buena actuación de las micropalancas en vacío o en aire, no ocurre lo mismo en medios líquidos. La actuación acústica típicamente usada para la operación en aire produce espectros de resonancia de las micropalancas con picos espurios. Estos picos provienen de la excitación de las diferentes resonancias de la celda líquida, y de la excitación transmitida por el fluido que rodea a la micropalanca.

Recientemente, se han desarrollado nuevas técnicas de medida en las que se excitan y/o detectan varios armónicos y/o modos de resonancia (flexurales o torsionales) de la oscilación de la micropalanca[11]. El AFM Multifrecuencia puede usarse para la obtención de contraste composicional en material biológico en líquidos [12]. Ha sido utilizado exitosamente para el mapeo de las propiedades nanomecánicas de células vivas [13] y también para medir 'in vitro' las propiedades locales de viriones a alta resolución [14]. Las técnica bimodales [15] has sido usadas para la adquisición simultánea de imágenes de alta resolución de moléculas y el mapeo cuantitativo de las propiedades del material [5], incrementando la resolución y la sensibilidad [16]. Además, los armónicos o los modos altos de resonancia de la micropalanca, tanto flexurales como torsionales, han ayudado a la aparición del AFM a alta velocidad [17]. La excitación y la detección de múltiples frecuencias ha estimulado también la utilización del AFM en nuevos campos, como el almacenamiento de energía [18] o la nanomedicina [19]. Así, para el uso de estas técnicas multifrecuencia es necesario un método de actuación de las micropalancas que sea eficiente y que genere la excitación necesaria para hacer oscilar los modos altos de vibración de las micropalancas.

Objetivos

En términos generales, esta tesis doctoral está centrada en el desarrollo de instrumentación y métodos experimentales novedosos para la mejora del AFM en aplicaciones "bio". En particular, está centrado en el desarrollo de una aplicación de la magnetostricción: su uso para inducir la excitación mecánica de las micropalancas. A lo largo de esta tesis se demostrará que esta

técnica de actuación supera los problemas que presentan los métodos actuales de excitación de micropalancas de AFM en medios líquidos.

Los objetivos de este trabajo son:

- El estudio teórico/experimental y el modelado de la actuación magnetostrictiva de micropalancas.
- Implementación de un nuevo método de actuación de micropalancas en líquidos en un AFM comercial.
- El aumento específico de un modo de resonancia de la micropalanca mediante micromecanización o implantación de iones en áreas específicas de la capa magnetostrictiva mediante litografía por Haz de Iones Focalizados (FIB en sus siglas en inglés, Focused Ion Beam, equipo iLine de Raith)

Una parte importante del plan de trabajo y de los objetivos se emplearán en solucionar problemas técnicos y de ingeniería. Esta nueva implementación requerirá de nuevos montajes electrónicos. Por ejemplo, el uso de un amplificador lock-in para la detección de los diferentes armónicos. También, la adquisición de amplificadores/generadores adaptados a las características del sistema.

Metodología

Esta nueva técnica de excitación magnetostrictiva se fundamenta en el recubrimiento de la superficie superior de la micropalanca con una capa magnetostrictiva. Como los materiales magnetostrictivos sufren un cambio en su forma y/o dimensiones cuando su imanación varía, la aplicación de un campo magnético externo producirá la deflexión de la micropalanca. Por lo tanto, un campo magnético AC a una frecuencia adecuada producirá la oscilación de la micropalanca, incluso bajo el alto amortiguamiento en líquidos.

Así, los puntos más relevantes del trabajo presentado pueden ser especificados como sigue:

1. Prueba de concepto: verificación experimental de la ideoneidad de la aplicación de la actuación magnetostrictiva para la generación de oscilación mecánica en micropalancas (Capítulo 2).
2. Estudio teórico, modelado y análisis experimental de las principales técnicas de actuación utilizadas actualmente (Capítulo 4).
3. Implementación del nuevo método en un AFM operando en líquidos. Preparación y caracterización de la capa magnetostrictiva que recubre las micropalancas (Capítulo 2). Desarrollo de una nueva celda líquida (Capítulo 3). Implementación de la electrónica necesaria para el uso de la actuación magnetostrictiva en un AFM comercial cuando opera en líquidos (Capítulos 3 y 6).
4. Estudio comparativo de la eficiencia en la excitación de los modos de altos de resonancia de las micropalancas entre los diferentes métodos de excitación (Capítulo 4).
5. Investigar cómo aumentar la oscilación y la eficiencia de los modos altos de resonancia de las micropalancas (Capítulo 5).

La selección del material magnetostrictivo (Fe-B-N) como recubrimiento para esta aplicación de la actuación de micropalancas de AFM está basada en un trabajo previo realizado por el Dr. Iván Fernández en su tesis [20], en el Instituto de Microelectrónica de Madrid (IMM-CSIC). En este trabajo hemos seguido los procedimientos descritos en esa tesis donde se han demostrado unas excelentes propiedades mecánicas y magnetostrictivas de las películas delgadas de Fe-B-N depositadas por pulverización catódica.

Como primer paso en esta tesis, se ha optimizado el proceso de depósito de películas magnetostrictivas delgadas de Fe-B-N amorfo, controlando la dirección de anisotropía magnética en la película magnetostrictiva inducida por la aplicación de un campo magnético durante la deposición. La metodología en esta parte se basará en la caracterización estructural (Rayos–X) y magnética (efecto magneto óptico Kerr, MOKE) de la capa depositada sobre vidrio o silicio, debido a la dificultad del uso del MOKE directamente en micropalancas por su pequeño tamaño.

Una etapa importante en la metodología fue el desarrollo de una celda líquida especialmente diseñada para el microscopio AFM de Nanotec Electrónica. Se realizarán simulaciones por elementos finitos para optimizar la posición y geometría del electroimán, minimizando la corriente a través de la bobina. El prototipo final deberá presentar bajo ruido mecánico y ser capaz de producir espectros de resonancia de micropalancas limpios en entornos líquidos.

Además, se desarrolló un nuevo metodo de fabricación de superficies ultraplanas debido a su interés como sustratos en SPM (Capítulo 7). Algunas de estas superficies son utilizadas en ambientes líquidos, por lo que deben presentar resistencia a la degradación en estas condiciones acuosas.

Chapter 1

Introduction to AFM operated in liquids and mechanical cantilever excitation methods

Atomic Force Microscopy (AFM) is already established as a powerful tool for nanometer scale characterization and matter nanomanipulation for a wide variety of samples. For example, high resolution images of proteins, DNA or organic molecules have already been obtained in air and liquid. A liquid environment is necessary when trying to avoid artifacts and structural and/or functional changes. The actuation technique plays a central role in order to obtain nanometer resolution in liquid media, as well as quantitative measurements. In this chapter, we will present different actuation methods for AFM operation in liquid environments. In next chapters, we will model and discuss these actuation methods, comparing the different excitation techniques with the one developed in this thesis, the magnetostrictive actuation.

1.1 History of AFM

Since the creation of the first microscope in the 16^{th} century by two Dutch lens grinders, Hans and Zacharias Jansse, by means of placing two lenses on a tube, scientists have faced the challenge to observe smaller objects every time. Nowadays, there are different branches of microscopy, based on different physical principles. Among them, optical, electron and scanning probe microscopy could be highlighted.

Optical microscopy involves passing visible light transmitted through or reflected from the sample through a single or multiple lenses system. These configurations should provide a magnified view of the sample. The main drawback of this technique is its resolution, because of the 0.2 μm light diffraction limit.

Electronic microscope obtains a measurement of the sample through an incident beam of electrons. The diffraction limit of this microscopy is below the nanometer. However, they need a high vacuum environment to operate. Therefore, the measurement of biological material in their physiological media is not possible.

The microscopes known as local probe microscopes detect the changes in the properties of the tip-sample system. They can operate in air, liquid or vacuum. One of these microscopes is the Atomic Force Microscope (AFM) (Figure 1.1).

Atomic Force Microscope is a powerful image tool developed by Binnig, Quate and Gerber in 1986 (Figure 1.1) [21]. AFM belongs to the family of Scanning Probe Microscopy (SPM). In AFM, a small and sharp probe scans the surface of a sample while measuring force interactions,

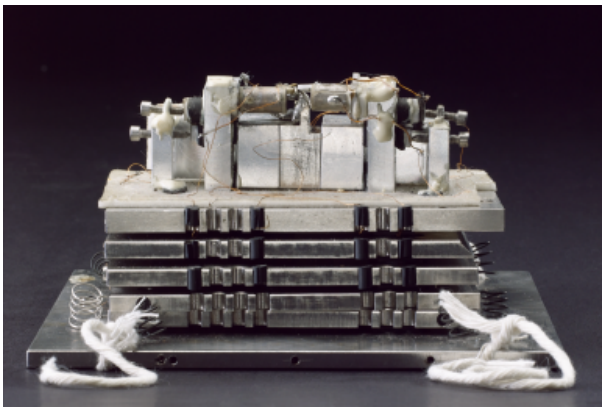

Figure 1.1: First Atomic Force Microscope, developed by Binnig, Quate and Gerber in 1986.

and uses those interactions to form an image. The first SPM invention was the Scanning Tunnelling Microscope (STM) developed by Gerber, Binnig and Rohrer in the early 1980s at IBM Research in Zurich [22]. It is based on the detection of the tunnel current between a conductive tip and a conductive surface separated a few angstroms. This current decreases exponentially with the tip-sample distance increase. An external feedback keeps constant the distance between the tip and the sample by measuring the tunnel current and keeping it constant. This microscope can achieve atomic resolution. The limitation of this technique is that the sample has to be conductive, making this method not suitable for biological measurements because most samples are resistant to electric current. Furthermore, most measurements have to be carried out in high vacuum, making difficult the inspection of biological samples. The AFM overcomes some of its limitations.

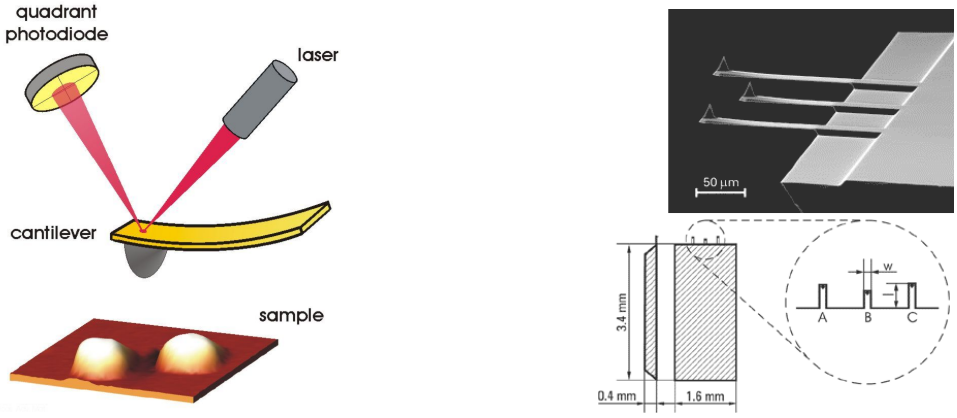

Figure 1.2: Scheme of the AFM (left) and example of microcantilevers from Mikromasch (right) [23]. Adapted from [24].

Most AFMs consist of a microcantilever ended in a sharp tip which scans a surface (Figure 1.2). Usually, the microcantilever has micrometer dimensions and the tip has a radius of curvature on the nanometer scale. It is usually made of silicon or silicon nitride (Figure 1.2). When the tip gets close to a sample surface, it starts to be sensitive to different types of interaction forces that arise between the tip and the surface at a nanometer scale: van der Waals, chemical, electrostatic, magnetic, mechanical, capillary, etc. All these forces may produce a deflection on

the microcantilever, which is usually detected by means of a laser reflected on the top surface at the end of the microcantilever, and measured in a photodiode. Depending on the experiment set-up, it is possible to measure different forces, and even more than one at the same time [11].

The most extended detection system is Optical Beam Deflection (OBD) [25], where a laser beam is reflected on the top surface of the microcantilever (which is normally coated with a metal for reflection enhancement) and then collected by a photodetector which is a few centimeters apart. Changes in the slope of the microcantilever will be detected on the photodetector, which converts the reflected beam into an electrical signal which is further processed in the microscope electronics. The electronic noise of the detection system introduced in the AFM electronics is a quantity to minimize. In the OBD case, it depends mainly on the distance between the microcantilever and the photodetector, the laser beam diameter and the shot and the Johnson-Nyquist noise of the photodetector [26].

1.2 Imaging modes in AFM

The main AFM working methods can be classified in two different groups:

1. **Static methods.** In these methods, the cantilever does not oscillate. Static contact method was the first AFM imaging mode that was used in AFM, in which the deflection was measured by an STM [21]. The forces that play a role in this case are predominately the main forces in contact: Pauli and ionic repulsion forces. These contact forces are the ones that produce the main bending on the cantilever: the higher the force, the greater the deflection. During the scanning, this deflection is kept constant at a fixed deflection value. When the system scans an area with variable topography, this deflection may be kept constant by moving the sample upwards or downwards the tip via a piezoelectric ceramic. Commonly, this piezoceramic element is placed below the sample, and it is used to move the sample in the X, Y and Z directions by means of an applied electric field. The electric feedback signal controls the piezoelectric ceramic in order to raise or lower the sample, keeping constant the cantilever deflection. The topographic information is obtained from the piezoelectric ceramic feedback signal by means of a previous calibration. This calibration relates the voltage applied to the piezoelectric ceramic to maintain a constant cantilever deflection to the piezoelectric vertical elongation.

   In the static methods, as well in dynamic methods, it is also possible to obtain different types of information besides topography. For example, the friction properties of the surface. While scanning the surface, the friction between the tip and the sample will cause the lateral deflection of the cantilever, recording an horizontal change in the position of the laser beam in the photodiode. This friction depends on several properties of the sample surface such as molecular adhesion, viscoelasticity, contact area, asperities geometry and size, etc., which cause the lateral tilting of the cantilever. This lateral bending will provide information about nano tribological properties of the surface.

   The contact method has its drawbacks. For example, on soft surfaces, the normal and/or lateral force exerted on the surface by the tip can destroy or modify the surface under measurement, e.g., in biological samples (proteins, cell membranes, etc.). For this reason, this type of surfaces are often measured in dynamic modes.

2. **Dynamic methods.** In the dynamic operation modes, the cantilever is deliberately vibrated. As will be discussed in detail in section 4.2.1, the microcantilever can be modeled

as a point mass (a sphere with mass, Figure 1.3) on a spring with displacement $z_0(t)$ (tip deflection) that is driven by an external force in the presence of the tip-surface forces. This is a very simple model, where non-linearities are not taken into account. Nevertheless, this approximation is valid to understand how the cantilever and tip-sample interactions work in a wide range of situations, giving rise to the following second order differential equation of a forced damped harmonic oscillator:

$$m_{eff}\ddot{z}_0(t) + \alpha\dot{z}_0(t) + kz_0(t) = F_{ext}cos(\omega t) + F_{ts}(z, \dot{z}) \tag{1.1}$$

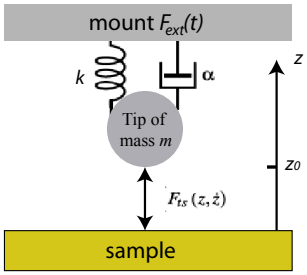

Figure 1.3: Sketch of the point mass model.

where m_{eff} is the effective mass of the cantilever, ω is the angular frequency ($\omega = 2\pi f$), k is the force constant of the cantilever, F_{ts} is the tip-sample interaction, F_{ext} is the external force exerted on the cantilever and α is the dissipative term (damping). If the tip-sample interaction is not considered, the solution of the differential equation 1.1 leads to the amplitude expression of the resonance spectrum $A(\omega)$

$$A(\omega) = \frac{F_{ext}/m_{eff}}{[(\omega_0^2 - \omega^2)^2 + (\frac{\omega\omega_0}{Q})^2]^{1/2}} \tag{1.2}$$

and its phase shift ϕ relative to the excitation

$$\tan(\phi) = \frac{\omega\omega_0/Q}{\omega_0^2 - \omega^2} \tag{1.3}$$

An example of an amplitude-phase versus frequency curve is shown in Figure 1.4, where the phase shift is 90^o at the resonance frequency.

When the tip is far from the sample surface and has a negligible interaction with it, the amplitude and the phase shift relative to the excitation signal depend on the frequency. At the free natural cantilever resonance f_0, the cantilever oscillation reaches the maximum amplitude A_0 and a 90^o phase shift (ϕ) (Figure 1.4) between the applied driven excitation and the cantilever displacement. To start the dynamic operation, first, the tip is approached to the surface and the tip-sample interactions start to be felt by the microcantilever. The resonance of the tip-sample system now deviates from the free resonance at which we keep oscillating the cantilever [27]. The first forces to be felt are attractive forces (van der Waals forces). When the tip gets even closer, repulsive forces (forces arising from Pauli and ionic repulsion) start having also a role [28, 29]. Thus, when the interaction is mainly repulsive the resonance frequency increases. On the contrary, when it is mainly attractive, the resonance frequency decreases [27].

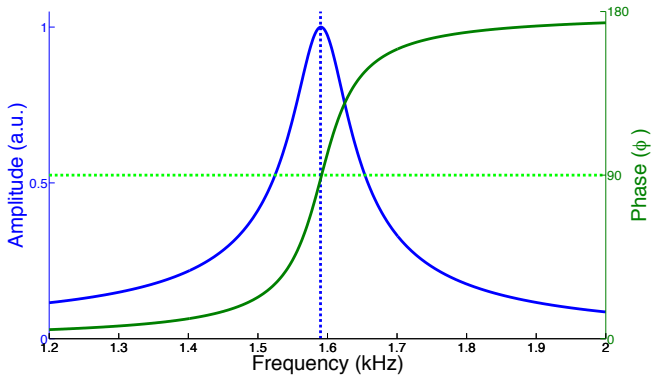

Figure 1.4: Resonance spectrum, where amplitude is in blue and phase is in green.

Among the dynamic methods, two operating modes that are quite commonly used are: Amplitude Modulation Atomic Force Microscopy (AM-AFM) and Frequency Modulation Atomic Force Microscopy (FM-AFM). In both methods, the cantilever has to be mechanically excited at or near its resonance frequency f_0.

- **Amplitude Modulation Atomic Force Microscopy (AM-AFM)**. In this mode, the oscillation amplitude is used as a feedback parameter, which means that the scanner z (piezoelectric ceramic) moves the sample vertically (upwards or downwards) so that the oscillation amplitude is kept at A_{sp}. The image obtained from the voltage signal that goes to the z piezo scanner can be generally interpreted as a topographic image. Another image with the phase shift information is also simultaneously obtained from the auxiliary signal ϕ. Commonly, this phase image can be interpreted in terms of energy dissipation [30].

  In AM-AFM the feedback is possible by using lock-in amplifiers, comparing in real time a reference signal with the signal of interest (cantilever deflection), resulting in DC signals (very low frequency) proportional to their amplitude and phase. This DC signal proportional to the cantilever oscillation amplitude is used for the feedback that keeps the A_{sp} constant.

  Within the AM-AFM technique, the operation parameters can be set so that different working conditions can be selected:

  - Non contact Amplitude Modulation AFM (NC-AM-AFM). The oscillation amplitude is typically a few nanometres (< 10 nm). The working amplitude (A_{sp}) is chosen to be small in reduction as compared with the free oscillation amplitude, since the objective is to operate in the range where attractive forces are predominant. Also, the tip radius should be small (< 10 nm). When these conditions are met and the sample properties are close to average, usually the tip of the cantilever does not (or very infrequently) contact the sample surface [31]. This technique is preferable to contact AFM or intermittent contact AFM for measuring soft samples in air, such as biological samples and organic thin films. Thus, soft samples will be less likely to be destroyed by the tip during scanning, due to indentation forces.
  - Intermittent contact AFM (also known as tapping AFM). The working oscillation amplitude is usually larger than in the previous mode or the tip oscillates closer to the surface and thus, the tip generally contacts intermittently the sam-

ple surface. This is the reason why this mode is also named tapping mode AFM[1]. The advantage of this technique is clear when working in ambient conditions, where hydrophilic samples develop a liquid layer, forming a liquid meniscus when the tip is close to the surface. This may make measurements unstable. By using large oscillation amplitudes, we can overcome this problem, since this large oscillations are able to disrupt the liquid meniscus.

In AM-AFM it is also important to know the time response of the microcantilever (τ) to a change in the interaction force. This quantity is not instantaneous, it will have a transient response [27]:

$$\tau = 2\frac{Q}{\omega_0} \tag{1.4}$$

where $\omega_0 = 2\pi f_0$ is the angular resonance frequency and Q is the quality factor of the oscillator (cantilever). In Ultra High Vacuum (UHV), the transient is too long (very high Q). For example, a typical quality factor value in UHV around $Q = 10000$ and a resonance frequency $f_0 = 50000$ Hz lead to a transient response around 60 ms, too long to perform a proper feedback[2]. This is the reason why this technique is restricted to air and liquids.

- **Frequency Modulation Atomic Force Microscopy (FM-AFM)**. In FM-AFM the excitation frequency is varied in order to keep the microcantilever at resonance [32]. The principle of FM-AFM relies on detecting small changes in the cantilever resonant frequency, which occur in response to the tip-sample interaction. These frequency shifts can then be used as a feedback signal for imaging or measuring force interactions between the tip and sample. A PLL (Phase Lock Loop) adjusts the frequency at resonance so that the phase shift between the cantilever oscillation and the excitation signal remains constant at 90^o.

  FM-AFM can be carried out either by using the constant excitation mode [33] or the constant amplitude mode [34]. In the former case, the controller simply adjusts the drive frequency proportionally, letting the response amplitude vary when dissipation is present, while in the latter case the circuit controls the gain of the variable-gain amplifier to maintain the vibration amplitude of the cantilever constant.

  The transient time τ in this case is [27]:

$$\tau = \frac{1}{\omega_0} \tag{1.5}$$

  that does not depend on the quality factor Q (transient times below the microsecond when $f_0 = 50000$ Hz and $Q = 10000$). Therefore, FM-AFM technology has historically been used for measurements in UHV where Q dependence of the transient made impossible to use AM-AFM. FM-AFM can be also successfully used in liquid media [35, 36].

[1] Tapping mode is a registered trademark of Veeco Instruments

[2] If a scanning line composed by 512 pixels is measured in 1 second, each pixel is recorded in 1.95 milliseconds. In air, considering a typical value $Q = 100$ and a resonance frequency $f_0 = 50000$ Hz, the transient response is 0.6 ms, enough for a proper feedback.

Therefore, the selection of a suitable working method is crucial in order to achieve good resolution. The choice depends on the sample characteristics and the environment. As many biological samples only preserve their structure and functionality in its physiological media, we will look for an AFM actuation method that can operate properly in liquids. In this environment, the cantilever excitation method must be efficient and with clean resonance spectra. Hence, in the next section, the different actuation methods for AFM in liquid media will be presented.

1.3 AFM operated in liquid environments

In recent years, the use of AFM has grown exponentially in many different scientific areas, because of its versatility. One of the fields that has taken advantage of this technique is biology, due to the AFM compatibility with the natural environment of the biological material: physiological media. In liquids, nanometer resolution can be achieved with small oscillation amplitudes [37–40]. AFM has been demonstrated as a successful tool for imaging from living cells and bacteria to single proteins, or lipid and carbohydrate layers.

Thus, if we desire to study the real properties and structure, we need to perform the measurements in their natural environment: physiological media. Unlike electron microscopy, the AFM allows us to carry out such kind of measurements in aqueous solutions.

The use of AFM in liquids is not restricted only to the biology field, but also to medicine monitoring drug action in tissues or cells, in biochemistry studying conformational changes in proteins or polymerization kinetics, or in physics studying degradations of surfaces by the action of different liquids. Furthermore, AFM allows to make real-time measurements, acquiring images in milliseconds [41]. An example of the versatility of the AFM in liquids is presented in Figure 1.5, with measurements on substantially different systems such as: atomic structures like mica (Figure 1.5a), proteins as aquaporin (Figure 1.5b), cells as E. Coli (Figure 1.5c) or even bacteriophage as Phi29 (Figure 1.5d).

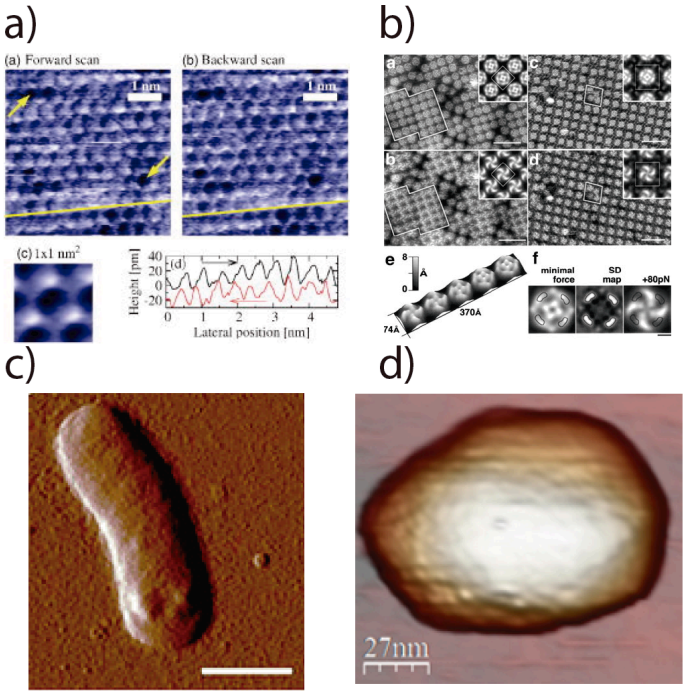

Figure 1.5: AFM measurements in liquids: a) atomic structure of mica, b) aquaporin structure, c) E. Coli cell, d) Phi29 bacteriophage, [37–40].

Contact AFM in liquids is highly successful with organic samples organized in periodic structures [38], but on individual molecules, the probe may exert lateral forces on the sample, displacing or deforming the sample. Therefore, in these cases is necessary to use dynamic methods where impact forces are predominately vertical.

Commonly in air, in order to excite the cantilever, the entire cantilever holder is shaken by a piezoelectric transducer. Due to the low damping in air, clean resonance spectra can be reached, ideal to perform the AFM measurements. Nevertheless, in liquid environment the damping is much higher. As the piezoelectric ceramic excites the entire cell and these vibrations are transmitted through the liquid to the microcantilever, its resonance spectrum includes many resonance peaks from the liquid cell. Thus, the resonance spectrum will be a convolution of the movement of the liquid cell and the movement of the cantilever, making difficult to perform measurements. This means that the cantilever is excited not only by the movement of its base, but also by the unsteady fluid motion around the cantilever, resulting in additional resonance peaks in the frequency response. It is difficult to place the piezoelectric transducer just below the cantilever to avoid the shaking of the entire cell, since the liquid may produce an electric shortcut between the two electrodes of the piezoelectric, inhibiting the vibration of the crystal. To overcome this problem, new excitation methods have been developed.

1.3.1 Why do we need a clear cantilever oscillation resonance spectrum?

Cantilever oscillation resonance spectra need to be free of spurious peaks to operate in Dynamic AFM because the selection of the proper resonance excitation peak enhances the sensitivity of the measurement and also allows to obtain quantitative measurements of the nanomechanical properties. For example, if we excite the cantilever acoustically, the fluid-born spurious resonances of the cell must be included in the equations of motion. Although great efforts have been done to include the effect of the unsteady motion of the surrounding fluid (fluid-borne excitation) in the equations [42], laborious calibrations are needed and still erroneous quantitative measurements can be performed.

It is, therefore, more recommendable to change the actuation method, making easier the modeling of the cantilever dynamics. As mentioned before, cleanness of the resonance peak is also critical for the image acquisition improvement in liquids. Even when a scanning image can be performed in the conditions provided by such spurious peaks, the measurement will be less sensitive and stable. Also instabilities in the phase can appear. It will be less sensitive because the decrease in amplitude is not bound solely to changes in the strength of tip-sample interaction, but also to changes in the hydrodynamic behaviour of the fluid surrounding the microcantilever. Moreover, the peak would be directly related to resonances of the cell or the fluid inside the liquid cell. This is very important when taking images of biomolecules, where a small change in force can destroy them.

1.3.2 Actuation methods for cantilever mechanical excitation

Acoustic actuation

In this actuation method, an electric signal is applied to a piezoelectric ceramic that vibrates, inducing the movement of the cantilever. This is the more widely used method when operating in air. As already detailed in the previous section, its main drawback when used in liquids is that the piezoelectric ceramic excites the entire liquid cell and these vibrations are transmitted through the liquid to the microcantilever.

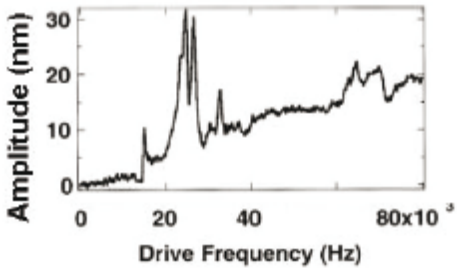

Figure 1.6: Resonance spectrum of acoustic actuation in liquids. Adapted from [43].

Hence, the resonance spectrum of the microcantilever includes many resonance peaks from the liquid cell. The resonance spectrum will be a convolution of the liquid cell movement and the cantilever vibration, resulting in the classic "forest of peaks" shown in Figure 1.6. This makes the measurement less sensitive and stable, as it is out of the cantilever resonance conditions. This is a problem as well to perform quantitative measurements, where you need clean and defined resonance spectra.

Magnetic actuation

The first magnetic excitation method was based on the positioning of a magnetic particle at the end of the microcantilever [44–46]. A magnetic force was applied to a particle attached to the microcantilever through a magnetic field generated by a solenoid. Later, Wenhai Han et al. [47] deposited a thin layer of a ferromagnetic material (Co, Ni...) on the cantilever. The magnetization direction was enclosed on the cantilever plane. Applying an oscillating magnetic field perpendicular to the cantilever, a magnetic torque force was exerted on it.

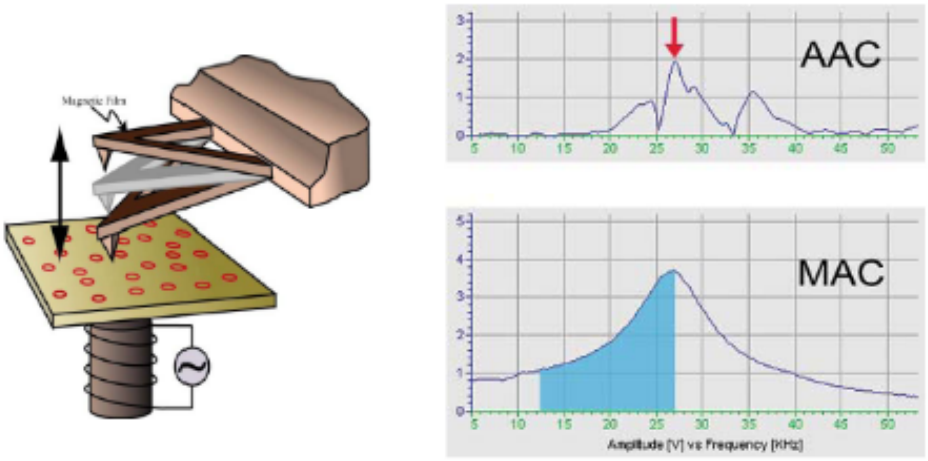

Figure 1.7: AFM liquid set-up from Agilent (left) and resonance spectra with acoustic mode (top right) and magnetic mode (bottom right). Adapted from [48].

This approach was applied for its commercialization. One important company that develops AFMs, Agilent Technologies, uses the MAC Mode^{TM} (Figure 1.7), where cantilevers are coated with a magnetic material and a magnetic field is applied through a solenoid located below the sample. Here, the microcantilever is the only element that moves, not the entire liquid cell, and

therefore all the spurious peaks due to resonances of the cell disappear. Thus, resonance spectra show only the peaks due to the resonances of the microcantilever. The main problem is that these magnetic materials are corroded in liquid environments, and can contaminate samples with heavy metals. Furthermore, placing the solenoid below the sample, leaves no space for an inverted microscope (optical), a configuration having a great use lately by researchers who are dedicated to biology. Moreover, as we will show in chapter 4, the magnetic torque force produced to excite the cantilever is not the most efficient strategy to excite high resonance modes.

Lorentz force actuation

In the Lorentz force actuation (iDrive^{TM} [49]), the excitation is produced by passing a current through a triangular microcantilever, creating a Lorentz force due to the current and the magnetic field [50–52]. This is the method used by Asylum, another important international company that develops and commercializes AFMs.

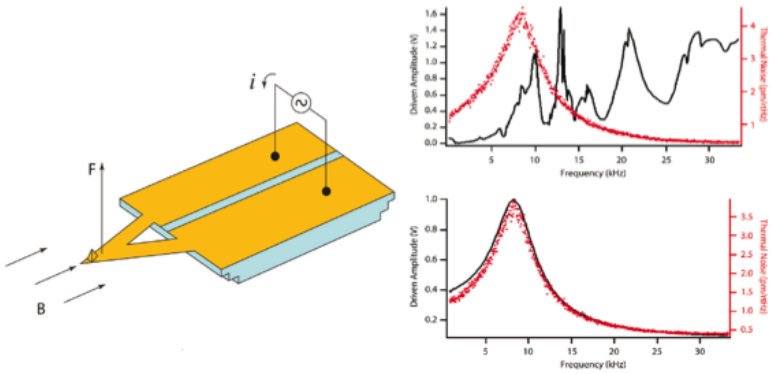

Figure 1.8: Lorentz actuation scheme for liquid environments (left) and liquid resonance spectrum (right). Adapted from [49].

An scheme is shown in Figure 1.8. A layer of gold is deposited on the tip side. Then, applying a oscillating current between the two contacts, a Lorentz force is produced, which bends the cantilever. It has the disadvantage of increasing the tip radius of curvature and it can only be used with triangular microcantilevers. The microfabrication process of these cantilevers implies the use sophisticated lithography methods for evaporation without shorting between the conductive paths, making it more complex and expensive.

Photothermal actuation

Photothermal excitation is based on the use of an intensity-modulated laser beam to induce mechanical vibration [53]. Figure 1.9 shows a scheme of this configuration. The main advantages of this actuation method are: it can be used in air and liquid; provides a wide frequency bandwidth excitation, needed for exciting small and high frequency cantilevers used in high speed scanning [54]; and supplies clean microcantilever resonance peaks in liquids, free of spurious resonances and phase distortions.

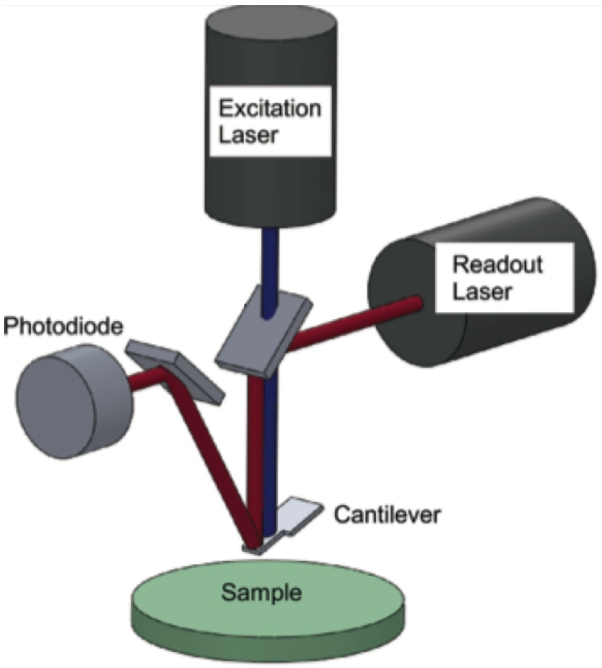

Figure 1.9: Schematic of a experimental photothermal actuation set-up. Adapted from [55].

The main disadvantage of the photothermal actuation method is its low oscillation amplitude efficiency [55]. It is possible to enhance the cantilever oscillation amplitude by increasing the laser applied power, but this could result in a problem: a high input power produces local heating of the microcantilever and sample, which may cause problems in extremely temperature sensitive experiments.

Although photothermal actuation has been successfully used by several groups in liquid environments [56–59], there is not any commercial AFM that employs this actuation technique. For this reason, the use of this technique is still limited.

Magnetostrictive actuation

One of the main goals of this work is the study and implementation of a new actuation method for AFM liquid operation: the magnetostrictive actuation.

Magnetostriction is a characteristic behaviour of magnetic materials, which produces a change in their shape or dimensions due to a modification in their magnetization state under the action of an external magnetic field. The magnetostrictive coefficient is defined as $\lambda = \frac{\Delta l}{l}$, where l is the length of the film and Δl is the increment in length (Figure 1.10).

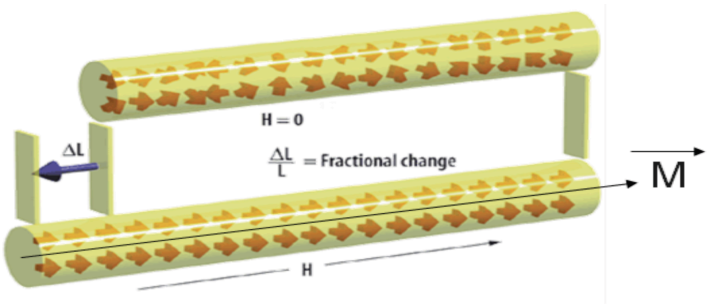

Figure 1.10: Schematics of magnetostriction: dimensional change of a material when magnetized. Adapted from [20].

The shape change is independent on the sign of the magnetization vector: magnetic fields with equal magnitude but opposite sign have the same effect on the magnetostrictive material. In addiction to a large magnetostriction coefficient, for AFM application it is important that the material reaches saturation at small applied magnetic fields (Figure 1.11) in order to avoid the use of large fields which require high currents in solenoids.

Material	λ (10^{-6})
$Fe_{80}B_{20}$(amorph.)	+35
Fe_{100}	+21
Fe_{111}	-21
$Fe_{policristalino}$	-8
Ni_{111}	-24
Ni_{100}	-46
$Ni_{policristalino}$	-5
Fe83Ga17	+207
FeTbDy	+1.600
NiMnGa	+50.000

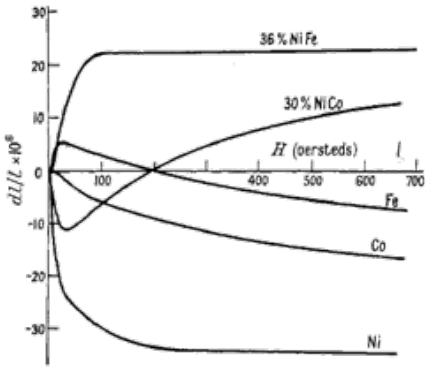

Figure 1.11: Magnetostrictive coefficients at saturation (left) and magnetostrictive strain versus magnetic field (right) of different materials. Adapted from [20].

We have chosen a $Fe_{80}B_{20}$ based amorphous alloy as magnetostrictive material (specifically, nitrided FeB, Fe-B-N), due to its high magnetostrictive coefficient and low saturation field, as shown in Figure 1.12 [60]. Fe-B-N is very stable in liquids, while the magnetostrictive coefficient and the saturation field can be tuned by changing the nitrogen composition percentage in the material (Figure 1.12 right graph) [61].

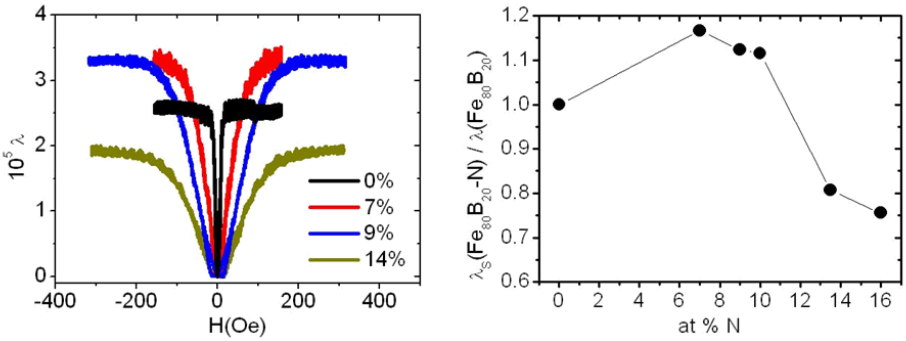

Figure 1.12: Magnetostrictive coefficient versus magnetic field (left) and normalized coefficient of Fe-B-N at different nitrogen concentrations (right). Adapted from [20].

When a cantilever coated with a Fe-B-N thick film is introduced in a variable magnetic field, the magnetostrictive layer expands forcing the microcantilever to bend. This film expansion originates a bending moment along the cantilever, as will be shown later in chapter 4. An alternating magnetic field will produce, therefore, cyclic expansions of the magnetostrictive layer inducing the oscillatory movement of the microcantilever [62]. This excitation technique leads to clean resonance spectra, as will be shown in the next chapter.

1.4 Multifrequency AFM

Multifrequency Force Microscopy is based on the simultaneous detection of several harmonics and/or modes (flexural or torsional, in Figure 1.13) of the cantilever oscillation amplitude [11]. Sometimes, two or more modes of the microcantilever are externally excited [16], while in other cases higher modes or harmonics are excited by the tip surface interaction [12]. These new channels at these different frequencies are used to extract information from the vibration of the microcantilever. Frequently, the topography information is extracted from the first resonance mode and higher resonance modes are used to extract information about other properties such as structural flexibility [5] or dielectric properties [63]. Usually, this technique increments the lateral resolution and sensitivity from the new channels of information [16] (harmonics of the fundamental resonance mode or higher resonance modes).

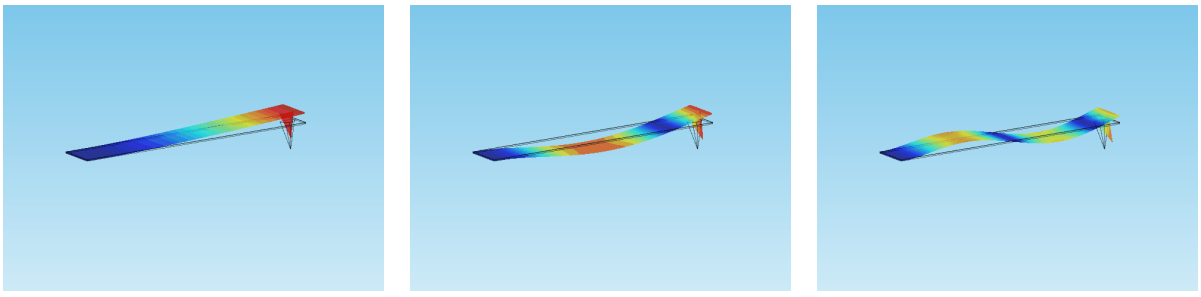

Figure 1.13: Three first flexural resonance mode shapes of a rectangular cantilever.

Force microscopy based on higher harmonics of the excitation frequency finds its optimal operating range in the repulsive regime, both in air and in liquid media, since in this regime the amplitude of the higher harmonics is enhanced. The main interest of these higher harmonics lies in their ability for the reconstruction of the interaction force and/or the local elasticity contrast mapping [12].

An example on the simultaneous detection of several harmonics can be seen in Figure 1.14, where purple membrane on mica in buffer solution is shown. In this case, integer multiples of the first resonance frequency are measured. The non linear tip-sample interaction in dynamic AFM induces cantilever vibrations at higher harmonics of the driven frequency [12]. In Figure 1.14, there is a very low contrast between purple membrane and mica in the 1^{st} harmonic. The contrast is clearly improved using higher harmonics compared with the lower ones. In fact, in lower harmonics contrast barely appears. In addition, we have the best contrast between harmonics 8^{th} and 12^{th}, which is the area where the second resonant frequency lies, enhancing the harmonics response.

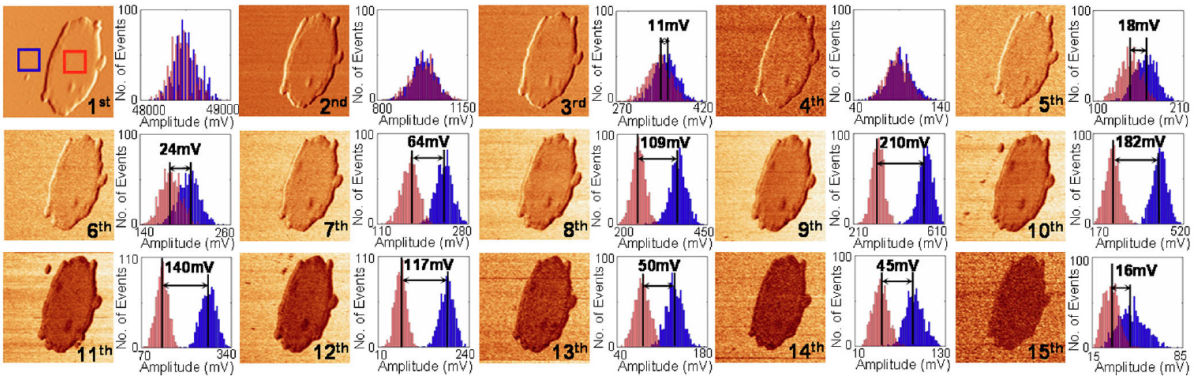

Figure 1.14: Higher harmonic images of purple membrane on mica in buffer solution, [12].

Multifrequency force microscopy also encompasses methods where several resonance modes are excited simultaneously. For example, it is possible to excite the first and the second flexural resonances of the microcantilever, where the first resonance is used to scan the topography and the second flexural mode is excited at very small amplitude. We can see a more detailed structure of IgM antibody acquiring information from the second resonance mode, as shown in the images d, c and f (phase) in Figure 1.15, rather than just acquiring the information from the first resonance mode, as we can see in the image b [16].

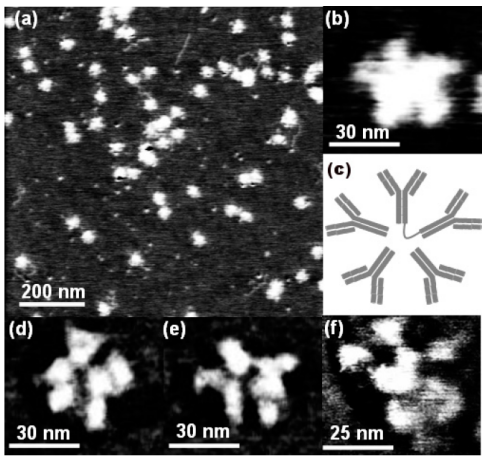

Figure 1.15: IgM antibody on mica, [16].

Furthermore, the use of higher harmonics and/or flexural modes have allowed the emergence of high-speed imaging, enabling the simultaneous imaging of the surface topography, energy dissipation and elasticity of materials [17]. Also, by exciting torsional cantilever resonance

modes, it is possible to measure some mechanical properties such as Young modulus [64], or the quantification of DNA molecules [19]. Moreover, the employment of torsional resonance modes have revealed significant differences in the fractal dimensionality of cancerous cells with respect to normal cells [65]. These examples demonstrate the potential of Multifrequency AFM in nanomedicine.

Additionally, Multifrequency AFM is used in different topics, such as energy storage. A Multifrequency AFM technique, band excitation [66] (application of AC signals at different frequencies simultaneously), was employed to map the ion diffusion [18]. In lithium-ion batteries, the movement of lithium ions into and out of electrodes is fundamental to a proper and efficient operation of those batteries.

As it will be demonstrated in next chapters, magnetostrictive actuation is the most efficient method in the excitation of higher resonance modes, making this actuation technique the most suitable for liquid environment operation and/or for Multifrequency AFM.

Chapter 2

Magnetostrictive film preparation, characterization and actuation

In the first part of this chapter, the magnetostrictive effect and its application for the cantilevers used in AFM will be presented.

The deposition conditions of the magnetostrictive thin film (Fe-B-N) on the cantilevers are discussed in section 2.2. This provides the necessary context to understand the magnetic characteristics of the films. These were studied by means of the magneto optic Kerr effect (MOKE). This technique is based on changes of the light reflected from a magnetized surface, in both polarization and reflected intensity. It is described in section 2.3. The magnetic characteristics of our Fe-N-B films obtained are discussed in section 2.4.

Finally, in section 2.5, the magnetostrictive actuation principles and the performance of its associated resonance spectra in magnetostrictive coated cantilevers will be discussed.

2.1 Introduction to magnetostriction

Magnetostriction is a phenomenon discovered in the 19th century by Joule. It is an abbreviation for magneto-elastic interaction. When a ferromagnet is magnetized, it shrinks or expands in the direction of the magnetization, depending on the sign of the magnetostrictive coefficient: a change in the magnetization orientation leads to a change on the material dimensions [67].

Magnetic domains can be modified by an applied field, and their evolution is strongly influenced by the magnetic anisotropy in the material. The rotation and movement of magnetic domains causes a physical length change in the material. Since the deformation is isochoric, there is an opposite dimensional change in the orthogonal directions: together with the deformation parallel to the applied magnetic field $\lambda_{\parallel} = \lambda_s$, there is a deformation in the other two perpendicular directions $\lambda_{\perp}$, as shown in Figure 2.1. The value of the perpendicular deformations is $-\lambda_s/2$.

The magnetostrictive coefficient $\lambda_s = \frac{\Delta l}{l}$ can range from nearly zero ($\lambda_s < 10^{-7}$) to 10^{-4} in $3d$ metals and alloys and to over 10^{-3} in some $4f$ metals, intermetallic compounds and alloys [68]. For example, cobalt is the pure material with higher magnetostrictive coefficient at room temperature ($\lambda_s = -60 \cdot 10^{-6}$). In the case of $Fe_{80}B_{20}$ amorphous alloy, the value is $\lambda_s = 30 \cdot 10^{-6}$ [20]). Furthermore, as $Fe_{80}B_{20}$ amorphous alloy is a soft magnetic material, the maximum deformation is obtained with small values of the applied magnetic field.

The inverse effect is also important. When a magnetic material is stressed or strained, a change in its magnetization is produced (Villari effect). Thus, the magnetization $\mathbf{M}$ and the stress/strain vectors in the material are coupled.

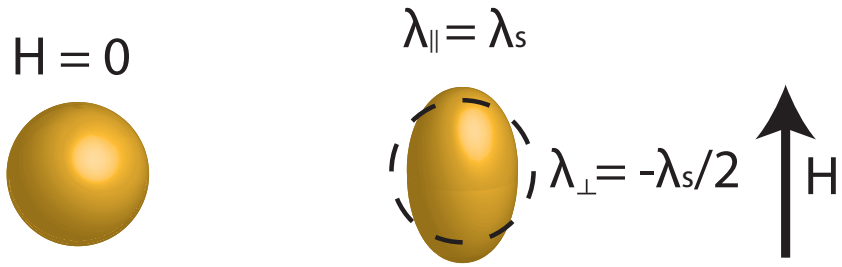

Figure 2.1: Parallel ($\lambda_{\parallel}$) and perpendicular/transversal ($\lambda_{\perp}$) deformation of a spherical sample for an applied magnetic field.

The magnetic characterization of the magnetostrictive thin films was carried out by MOKE techniques. From the MOKE measurements it is possible to extract the M−H hysteresis curve of the magnetic film, and from these curves we can infer its magnetization dynamics related to the magnetostrictive behaviour.

When a magnetic field is applied to a ferromagnetic material, the domain structure changes so that the average magnetization parallel to the field increases. This can be achieved either by a magnetization rotation (Figure 2.2, up) or by a domain wall movement (Figure 2.2, down), as observed in Figure 2.2. In our amorphous ferromagnetic materials, these two effects happen for lower fields than in their crystalline relatives. With respect to the magnetostriction, the change in dimensions is always associated to magnetization rotation [69]. Accordingly, we are interested in magnetization rotation instead of domain wall movement in our magnetostrictive films. Thus, while the magnetization is an odd function of the applied magnetic field, the magnetostriction is an even function of the applied magnetic field in the ferromagnet, as shown in Figure 2.2.

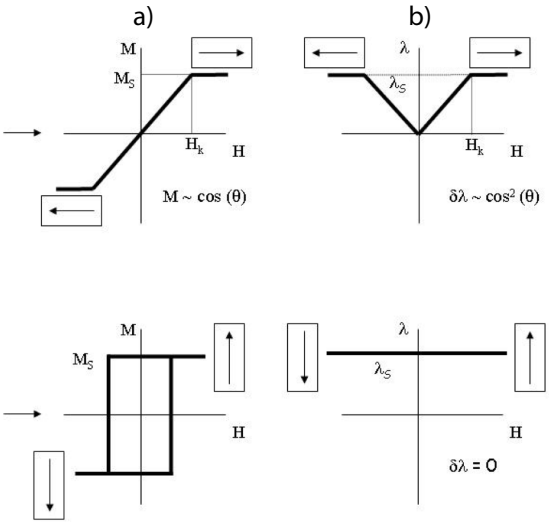

Figure 2.2: a) Magnetization as a function of the applied magnetic field H, by magnetization rotation (up) or by a domain wall movement (down). b) Corresponding magnetostriction as a function of the applied magnetic field H. Adapted from [20].

If the magnetostrictive film is deposited on flexible substrate, e.g. a cantilever, then its field-induced expansion/contraction could lead to a concurrent bending of the substrate (Figure 2.3). Any magnetostrictive strain will be matched by the substrate at the interface, and could

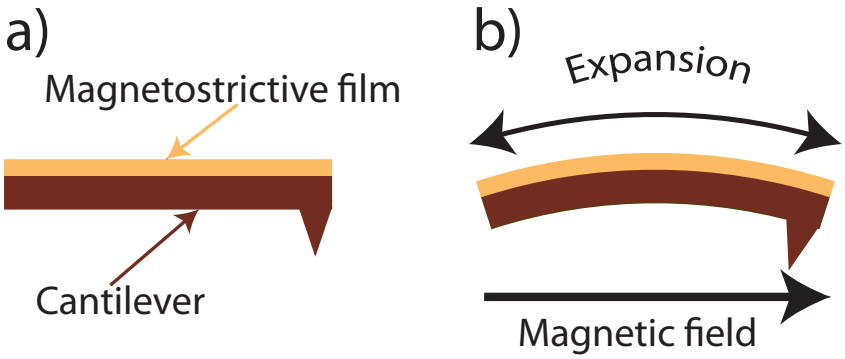

Figure 2.3: a) Sketch of a cantilever coated with a magnetostrictive film. b) The cantilever is bent when an external magnetic field is applied.

thus lead to a field-induced bending of the combined structure (Figure 2.3). For instance, a magnetostrictive film deposited along one side of a flexible cantilever could elongate/shrink (depending on the magnetostrictive coefficient sign) with a suitable applied field, thus causing the cantilever to bend until its elastic restoring force matches the magnetostrictive bending force. Similarly, a variable applied magnetic field could cause cantilever oscillation, and therefore, magnetostriction could be used to actuate cantilevers in AFM.

For applications in AFM it would be inconvenient to deposit a magnetostrictive film on the side of the cantilever holding the tip that probes the samples, because this is likely to blunt the tip, and cause a diminished spatial resolution. In order to maintain the tip radius, we have deposited the magnetostrictive film by sputtering in stress-free conditions (section 2.2) on the side opposite to the tip.

We have used amorphous Fe-B-N as the magnetostrictive material. It meets a combination of favourable properties: a comparatively large magnetostrictive effect ($\lambda_s = 30{\cdot}10^{-6}$ [20]), produced even at low applied magnetic fields (< 50 G), together with excellent mechanical and non-corrosive properties, which grant the cantilevers with a long time stability.

Commercial cantilevers were also tested, which are coated with polycrystalline Co-Sn films as magnetostrictive material. They are more accessible to be used in the actuation of micro-resonators or cantilevers for AFM than the ones coated with Fe-B-N. However, our experience demonstrates that they are less resistant to corrosion in liquid environment than the Fe-B-N coated cantilevers.

2.2 Sputter deposition

In order to deposit a Fe-B-N layer onto the cantilever surface, the sputtering deposition technique was used. This technique is widely used for thin film deposition. Its popularity stems from the comparative simplicity (and hence low cost) of the physical equipment involved, the accurate control of deposition rate, excellent film adhesion and high degree of reproducibility of the deposited films. It also allows depositing high melting point metals, insulators, and different compounds by co-deposition or by reactive sputtering with nitrogen, oxygen, etc.

Sputtering is a physical process whereby neutral atoms are ejected from a solid target by momentum transfer due to the bombardment of highly energetic gas ions. These ejected atoms travel through the vacuum sputtering chamber and are deposited onto the exposed surface of a substrate.

In particular, a triode sputtering system was used in this thesis for thin film deposition of

the magnetostrictive cantilever coatings [20]. The triode sputtering machine is schematically shown in Figures 2.4 and 2.5. For this sputtering configuration, specially adapted for high magnetization magnetic materials deposition where standard magnetron type sputtering sources are not suited, the ionization of the plasma supplying the ions for the sputtering is maintained independently from the target potential by electrons. Electrons are emitted from an auxiliary hot filament, which are accelerated by an anode with a positive potential, as shown in Figure 2.5. With this system it is possible to operate at Ar pressures around 10^{-4} - 10^{-3} mbar. The energy of the atoms when they reach the surface of the substrate depends not only on the target accelerating potential, but also on the sputtering chamber pressure, which scatters the sputtered atoms. It allows working with sputtered atoms of high kinetic energy, and reduces the number of collisions these atoms undergo while they travel towards the substrate. A magnetic field provided by two Helmholtz coils can be used to confine the plasma and increase its density, thereby enhancing the sputtering rate given the increased rate of ions hitting the target.

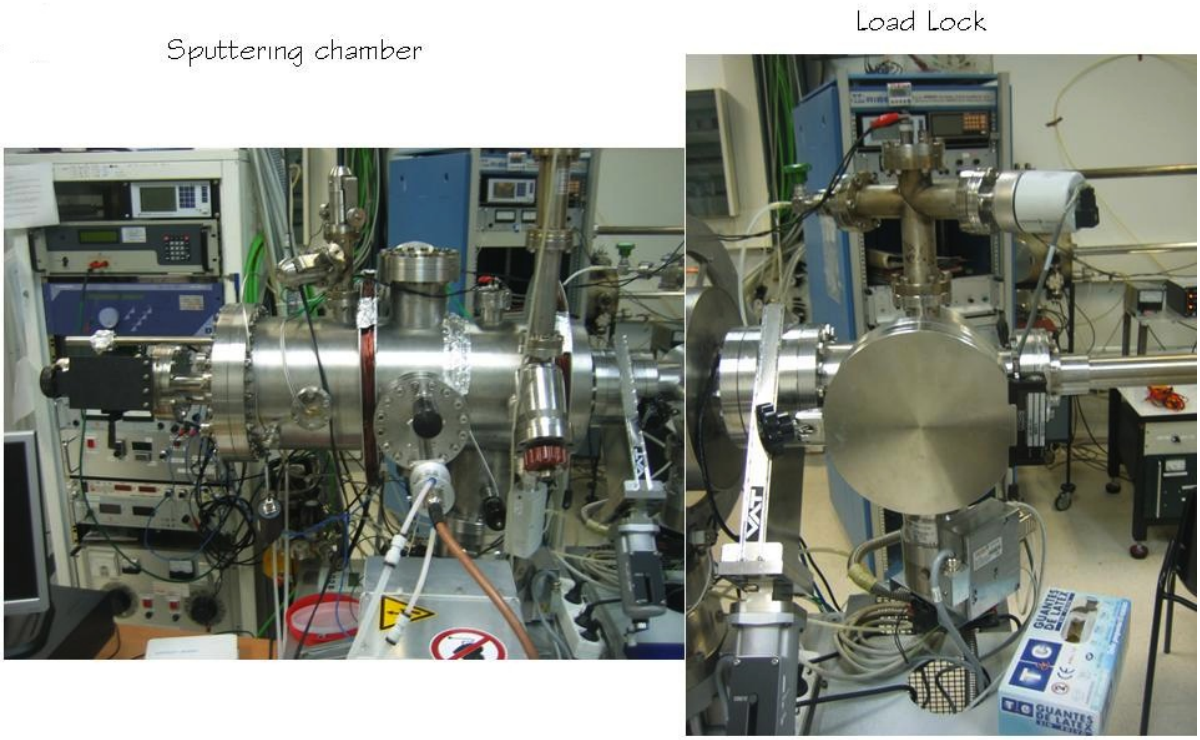

Figure 2.4: Sputtering chambers. Reproduced from [20].

Several sputtering parameters influence structural, and consequently the magnetic, mechanical, electrical, etc. properties of the deposited film. It is generally found that one set of sputtering parameters on a given sputtering system cannot be transferred to another system to deposit films with the same magnetic and structural properties. This illustrates how sensitive the film properties are to the sputtering parameters.

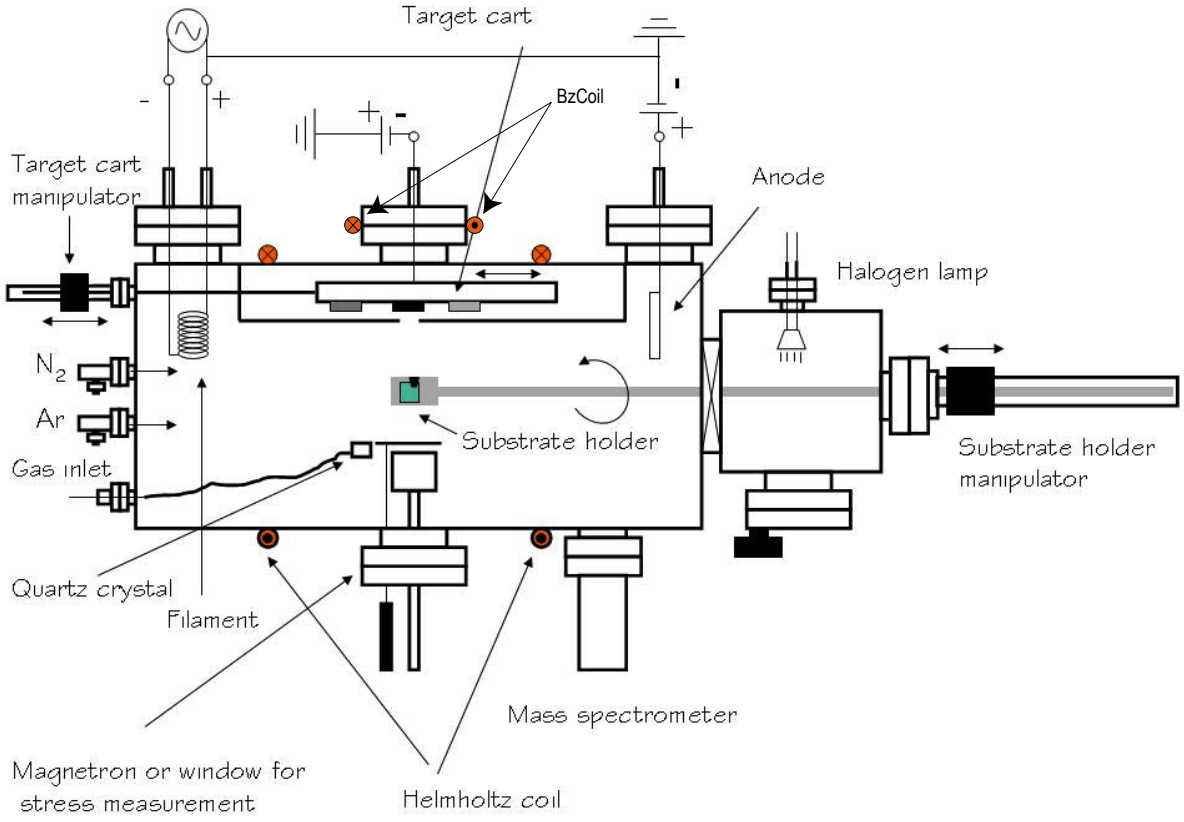

Figure 2.5: Schematic view of the triode sputtering machine. Adapted from [20].

The sputter deposition system we used is shown in Figure 2.5. It consists in a cylindrical chamber made of 304 grade stainless-steel, that is evacuated by a turbo-pump supported by a mechanical rotary pump, reaching a base pressure in the 10^{-9} mbar regime (Figure 2.4). The chamber pressure was monitored by a Pirani gauge, in the range 10^{2} - 10^{-2} mbar, and a Penning gauge in the range 10^{-2} - 10^{-10} mbar. The sputtering chamber is connected to a load lock chamber through a gate valve. Pumping in the load-lock chamber is also performed by a turbo-pump and a mechanical rotary pump, reaching a base pressure of 5×10^{-7} mbar in approximately 10 minutes. The substrate holder is transferred from the load-lock to the sputtering chamber by a linear magnetic manipulator that also allows the substrate holder to rotate. An halogen lamp in the load-lock chamber is used to degas the substrates at 200 °C. There are two gas inlet ports in the sputtering chamber to admit argon and nitrogen into the vacuum chamber. The respective gas flows were controlled by needle valves. High purity (99.999 %) Ar and N_2 gases were used. The sputtering chamber is connected to a mass spectrometers that allows leakage detection.

As shown in Figure 2.6, the system includes a thermo-emitter cathode, an anode placed opposite to the filament and a target holder. A positive voltage is applied to the anode to accelerate the electrons emitted by the cathode. These accelerated electrons strike and ionize the gas atoms producing the plasma. The thermo-emitter cathode consists in a heating filament coil made of 0.2 mm diameter tungsten wire in a spiral shape of 2 mm diameter and 20 mm long. The anode is made of a rectangular tantalum foil, 0.2 mm thick and 4×8 cm^2 area.

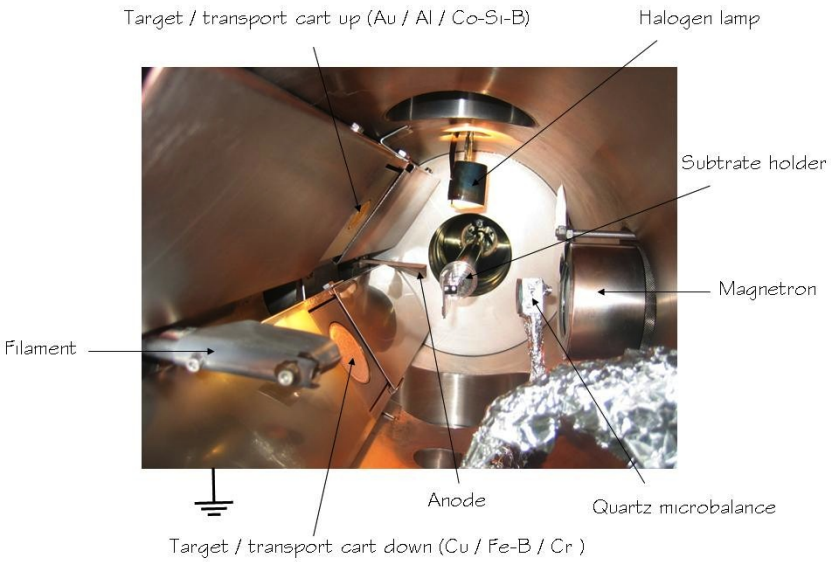

Figure 2.6: Picture of the inside of the sputtering chamber. Reproduced from [20].

The targets (50 mm diameter) were positioned perpendicular to the anode-cathode axis. An homogeneous magnetic field provided by an external Helmholtz coils is applied parallel to the anode-filament direction. This field confines the emitted electrons from the hot filament and the plasma.

For the cantilevers studied in this thesis, Fe-B-N amorphous thin films were deposited from a nominally $Fe_{80}B_{20}$ commercial target. By in situ stress measurements [61], the optimal deposition conditions to achieve films with nearly zero accumulated stress were previously determined. A target potential of -0.75 kV, an Ar+N_2 pressure of $8{\cdot}10^{-3}$ mbar, and a Fe-B-N thin film nitrogen concentration of 7%, as measured by non-Rutherford backscattering spectroscopy experiments (non-RBS) [60]. Under these deposition conditions, cantilevers were coated on the tip opposite side with thicknesses up to 50 nm at 0.05 nm/s. The stress related curvature of the deposited cantilevers is less than 1 % [61].

An important aspect of the sputtering process for amorphous thin films is the requirement to maintain a low temperature of the substrate during deposition to avoid crystallization. Most previous work [70, 71] on these materials has been carried out using relatively thick glass or silicon substrates cooled by direct contact to a substrate holder maintained at room temperature. However, during deposition on thin micro cantilevers with a very small thermal mass and heat dissipation limited in vacuum to pure radiation cooling, the heat in-flow caused by thermalization on the growing film surface by the impinging energetic neutral atoms and by bombardment with the secondary electrons emitted by the target has to be drastically limited. The electrons bombardment is avoided by their lateral deflection by the axial magnetic field in the system, but the energetic neutrals will still arrive to the substrate. They cannot be effectively thermalized at low pressures ($<10^{-3}$ mbar) by multiple collisions with the Ar or N_2 gas in the chamber. Therefore, the only way to avoid crystallization of the amorphous Fe-B-N film is to grow it a very slow rate (<0.1 nm/s) and to stop periodically the deposition to allow for cooling. X-ray characterization confirmed the amorphous (lowest coercitivity) structure of the films.

Another important aspect is the control of film composition, particularly the N concentration in $FeB_{1-x}N_x$ by controlling the relative abundance of N_2 and Ar gas in the chamber during

reactive sputtering of a $Fe_{80}B_{20}$ target. Increasing the N_2 partial pressure in the chamber effectively increases the x of the film but causes a significative reduction of the deposition rate. Therefore, a careful calibration procedure has to be carried out to reproduce the aimed composition. B element is a well known promoter of the amorphous structure, while N effectively nitridates Fe increasing magnetostriction coefficient and corrosion resistance.

2.3 TMOKE principles and set-up

The magnetic characterization of the sputtered Fe-B-N thin films was carried out using Magneto-Optical Kerr Effect (MOKE) techniques. It is based on the effect first observed by John Kerr in 1876 [72], where the change of the polarization of light upon reflection on the surface of a magnetic material depending on the material's magnetization intensity and direction.

The Magneto Optic (MO) effects can be classified in three different types according to the relative orientation of the magnetization of the sample **M** with respect to the sample surface and the light's incidence plane (Figure 2.7).

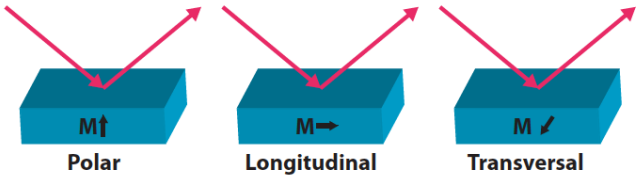

Figure 2.7: Different MOKE configurations depending on the magnetization vector direction of the material with respect to the reflecting surface and the light incidence plane.

To perform the M−H hysteresis loops measurements we have used the transversal configuration (TMOKE) in reflection (Figure 2.8), where the magnetization of the magnetic film is perpendicular to the plane of incidence and parallel to the surface.

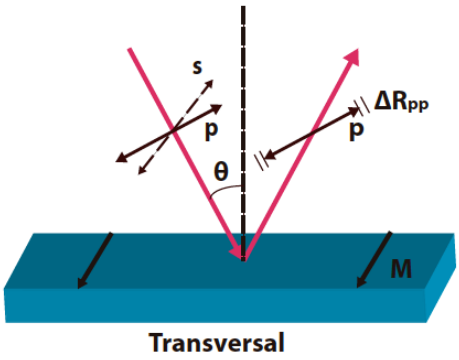

Figure 2.8: Schematic of the transversal Kerr effect configuration.

The property measured in the TMOKE technique is the intensity modulation of the reflected light as the magnetization of the sample is varied. From this modulation, we can measure the M−H hysteresis loops of magnetic samples with in-plane magnetization. These M−H hysteresis loops are related to the magnetization direction average of the magnetic domains on the surface. The relative reflectivity variation can be expressed as:

$$\frac{\triangle R_{pp}}{R_{pp}} = \frac{R_{pp}(M_S) - R_{pp}(0)}{R_{pp}(0)} \tag{2.1}$$

where $R_{pp}(M_S)$ is the p-reflectivity at saturation and $R_{pp}(0)$ is the p-reflectivity at zero field.

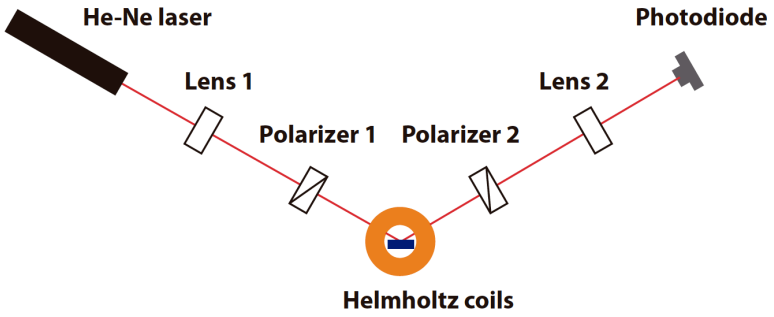

Figure 2.9: TMOKE set-up.

In our setup (Figure 2.9), we have used an He-Ne laser as a light source, that emits linearly polarized light at $\lambda \approx 630$ nm. The laser power excitation is 1.5 mW. We focus the emitted light by means of a lens. The laser beam was reflected off the magnetic surface of the sample which is placed at the center of a Helmholtz coil. The external magnetic field generated by the coil sets the magnetization state of the sample. The reflected light is polarized and focused by a second lens and finally, the intensity is measured by a photodiode. Both polarizers must be in p position (Figure 2.8) in order to maximize the Kerr/DC signal ratio in the photodiode. An internal amplifier in the photodiode is used to control the optimal DC output signal of the photodiode. Eventual excessive intensity of the reflected laser beam was corrected by coupling an attenuator to avoid undesired saturations of the collecting photodiode. The Helmholtz coil creates a homogeneous uni axial **H** field on the sample, perpendicular to the plane of incidence. The coils are driven by an amplifier with a sinusoidal wave at 5.1 Hz from a function generator. Thus, we can reach 70 G per ampere circulating through the Helmholtz coils. So as to filter the noise from laser instabilities or mechanical vibrations, we average the photodiode signal with an oscilloscope. Thereby, we can easily acquire the desired hysteresis curves.

After acquiring the experimental M−H data curves, we take data from the oscilloscope and process it with a Labview software. We plot M/M_s, which is the relationship of the magnetization of the magnetic film with respect of the saturation magnetization. We subtract the DC component of the laser beam signal and normalize the hysteresis loop to plot M/M_s, with appropriate data-processing in MATLAB mathematical software. The same tool was used to calculate the coercivity and the remanent magnetization.

2.4 Magnetic properties of the Fe-B-N thin films: induced magnetic uniaxial anisotropies

As explained in section 2.1, in order to obtain a maximum magnetostrictive strain, a coherent rotation of the magnetic moments is required. In the case of a material with a well defined in-plane uniaxial anisotropy, this maximum strain is achieved by applying a magnetic field along

the magnetic hard axis direction. For that reason, it is essential that the magnetic anisotropy is well defined.

This section is concerned with the magnetic anisotropy of the magnetostrictive Fe-B-N thin films deposited on AFM cantilevers. Due to the amorphous character of the Fe-B-N magnetostrictive films, no magnetocrystalline anisotropy appears, i.e. no preference of the magnetization to lie along a given crystallographic direction. A balance between two contributions to the magnetic anisotropy was found: field induced anisotropy, due to the presence of magnetic fields during magnetostrictive film growth, which induces a uniaxial magnetic anisotropy in the direction parallel to the applied magnetic field, and shape anisotropy, which is affected by the cantilever geometry. As films deposited at normal incidence and at nearly-zero stress conditions, neither oblique or stress induced anisotropy have contribution to the film final magnetic behaviour.

As shown in Figure 2.5, two coils are placed in the sputtering chamber for both increasing the plasma confinement and deposition rate: a Helmholtz coil which generates a magnetic field B_x perpendicular to the trajectory of the sputter material, along x in Figure 2.11, and a coil which generates a magnetic field B_z in the direction parallel to the trajectory of the sputter material. Thus, two magnetic fields within the plane defined by the substrate surface and with perpendicular direction are applied during sputtering deposition. The resulting film magnetic anisotropy was found to be a balance between two contributions: field induced anisotropies of the B_z (BzCoil) and B_x (Helmholtz coil) applied fields and shape anisotropy due to the rectangular shape of the cantilevers.

Due to the difficulty to perform the MOKE measurements directly on the cantilevers, we have studied the effect of the microcantilever shape and Fe-B-N deposition conditions on the magnetization properties of rectangular micro-patterned Fe-B-N arrays of structures on silicon substrates with sizes and shapes similar to the cantilever ones (see Figure 2.10). In particular, the structures' thickness was chosen at 50 nm, the length ranged from 100 to 350 μm and the width from 20 to 40 μm (typical sizes of commercial cantilevers). Practical considerations related to the AFM liquid cell that will be discussed in the next chapter call for applying the magnetic excitation field along the cantilever width. For that reason, the magnetic properties along that direction were studied.

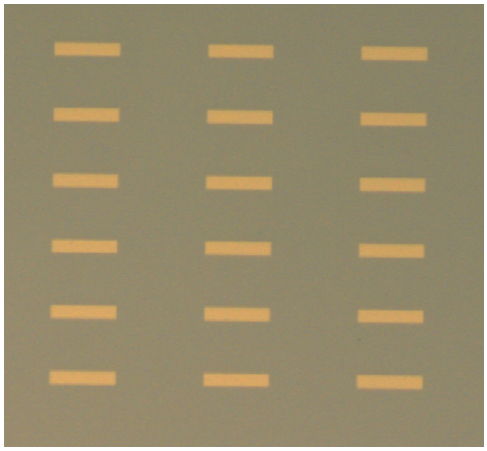

Figure 2.10: Example of Fe-B-N rectangular structures (150 $\times$ 30 μm) deposited on silicon substrate.

As sketched in Figure 2.11, four different configurations for the cantilever placement during sputtering deposition were chosen:

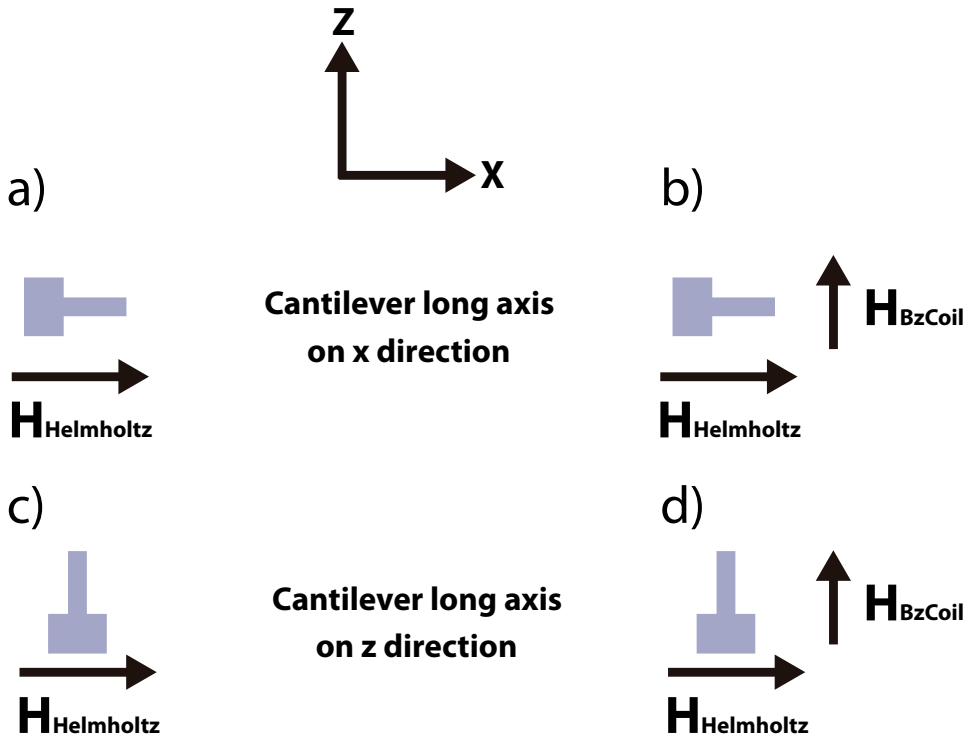

Figure 2.11: Different configuration for Fe-B-N films growth.

a) The long side of the rectangular structure[1] is parallel to x direction and B_z is kept at 0 Oe (Figure 2.11a).

b) The long side of the rectangular structure is parallel to x direction and $B_z \approx 5$ Oe (Figure 2.11b).

c) The long side of the rectangular structure is parallel to z direction and $B_z = 0$ Oe (Figure 2.11c).

d) The long side of the rectangular structure is parallel to z direction and $B_z \approx 5$ Oe (Figure 2.11d).

In all cases, the field generated by the Helmholtz coil was kept constant. The magnetization properties for films prepared according to the configurations described in Figure 2.11 were studied. Specifically, the coercivity and saturation fields obtained from hysteresis loops using the TMOKE techniques (see Figure 2.12) were considered. We are also interested in the effect of the cantilever dimension on the magnetization properties, as well as the effect of the B_zCoil (the magnetic field in the z direction). Also, the degree to which the magnetization process involves magnetization rotation and domain wall movement can be estimated.

[1]The long and short axis of the rectangular structure correspond to cantilever long and short axis in Figure 2.11.

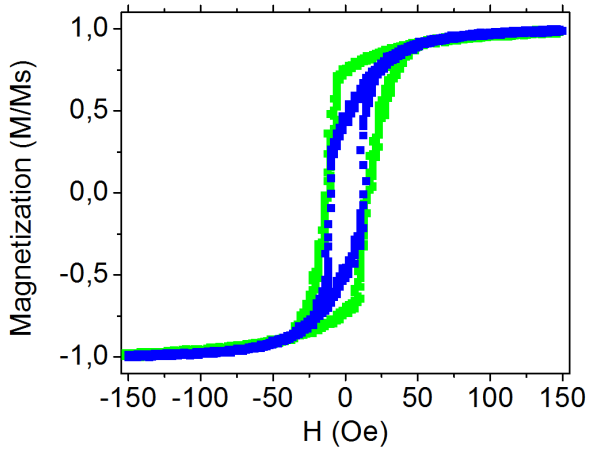

Figure 2.12: Magnetization curves of Fe-B-N (50 nm) on silicon. In blue, when the magnetization axis is perpendicular to the field of the Helmholtz coil. In green, when the magnetization axis is parallel.

As discussed in section 2.2 above, the desired magnetostrictive actuation calls for field-induced changes in the magnetization orientation. In this section, it is studied which characteristics of our Fe-N-B magnetostrictive films are conducive to this behaviour. As it is shown in Figure 2.12, 50 nm amorphous Fe-B-N on Si presents soft magnetic properties: in both directions, the coercivity is around 12 Oe and fields of about 50 Oe are sufficient to saturate the magnetization.

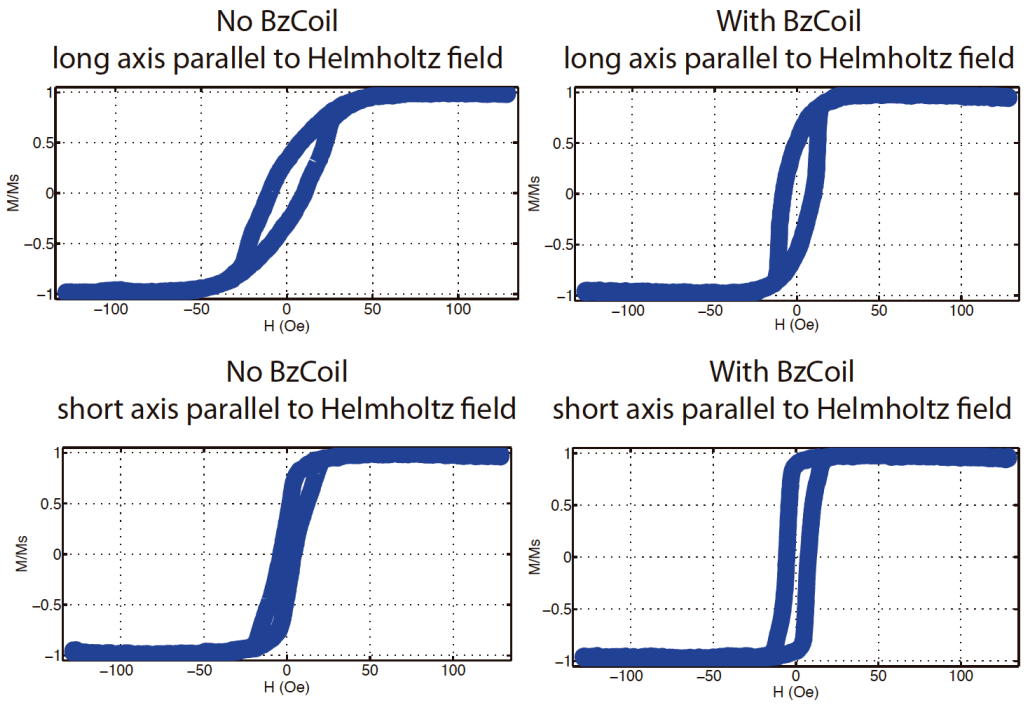

Figure 2.13: TMOKE magnetization curves along the short axis of Fe-B-N rectangular structures with size 250 $\times$ 30 μm deposited onto silicon.

An example of magnetization TMOKE curves measured in the short axis of Fe-B-N rectangular structures (size 250 × 30 μm) on silicon for different growth configurations are presented in Figure 2.13. When the rectangular structure's short axis direction is parallel to the Helmholtz coil during sputtering deposition (**c** and **d** configurations), the hysteresis loops have good squareness. However, if the short axis is perpendicular to the Helmholtz field axis direction (configurations **a** and **b**), hysteresis loops are more rounded, as would be expected for a harder direction, and the actuation is more effective, being able to produce magnetization rotation (Figure 2.2, up) instead of domain wall movement (Figure 2.2, down). As mentioned before, configuration **b** has lower saturation fields than configuration **a**. Thus, configuration **b** combines low saturation field and produces domain wall movement. Based on these considerations, we conclude that the best sputtering conditions are when the long axis of the microcantilever is parallel to the field created by the Helmholtz coil, and B_zCoil $\approx$ 5 Oe is applied (configuration **b**, Figure 2.14b).

Figure 2.14 presents the results for different sets of 50 nm thick Fe-N-B structures (following Figure 2.10) with different sizes for each configuration set-up of Figure 2.11.

These results show that the axial coercivity generally increases with structure length, as expected from the correspondingly decreasing demagnetization factors. Moreover, there is not huge deviations in the magnetic parameters when the structure size is changed.

Configuration **a**, corresponding to Figure 2.14a, needs higher external magnetic field to reach saturation than configuration **b**. The same occurs for configurations **c** and **d**, where configuration **c** has higher saturation field. Thus, the B_zCoil decreases the saturation field. The coercivity maintains similar for the different configurations, showing a decrease in configuration **b** respect to **a**.

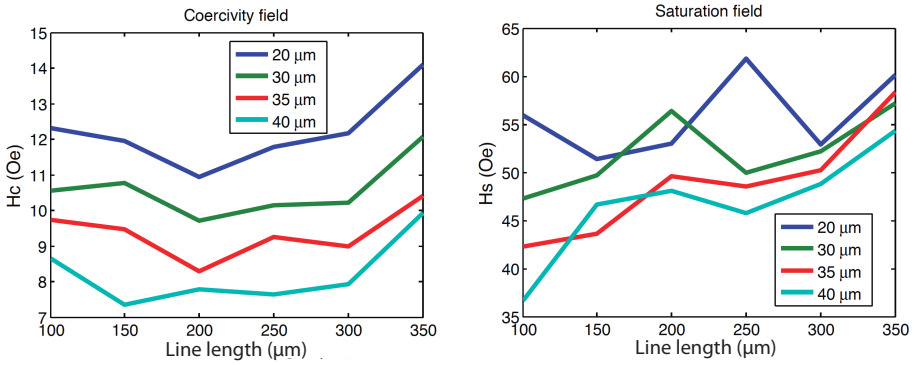

(a) The long axis parallel to x and with $B_z = 0$ Oe (Configuration **a** in Figure 2.11)

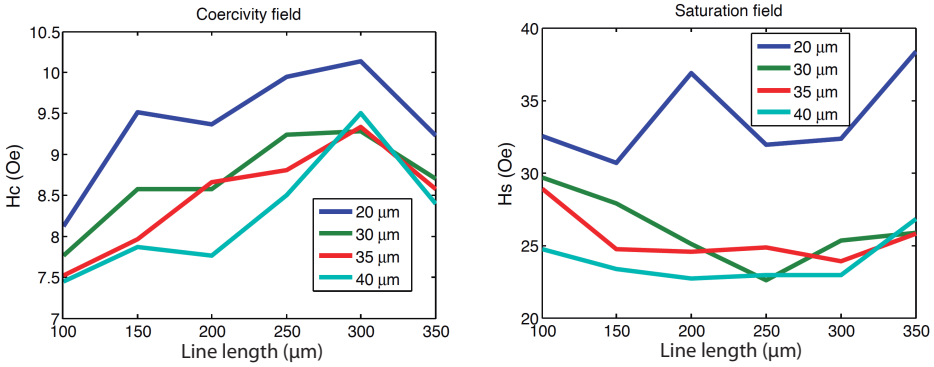

(b) The long axis parallel to x and with $B_z \approx 5$ Oe (Configuration **b** in Figure 2.11)

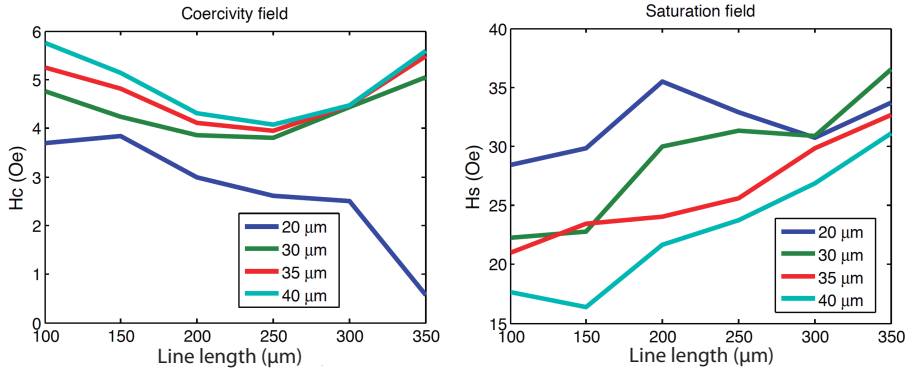

(c) The long axis perpendicular to x and with $B_z = 0$ Oe (Configuration **c** in Figure 2.11)

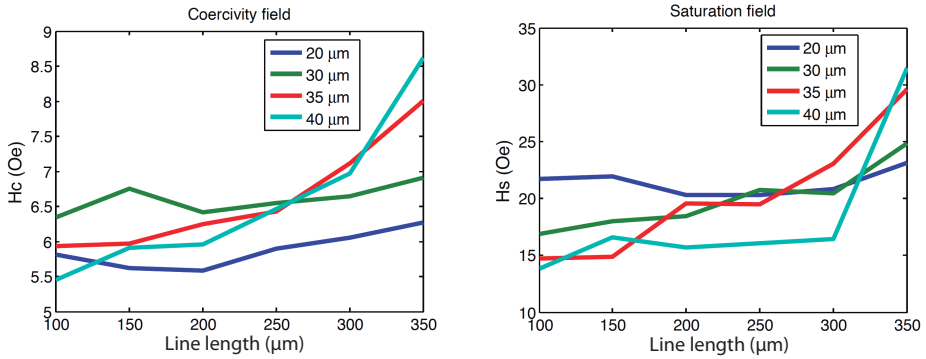

(d) The long axis perpendicular to x and with $B_z \approx 5$ Oe (Configuration **d** in Figure 2.11)

Figure 2.14: Coercivity and saturation field of Fe-B-N rectangular structures from magnetization curves along the short axis of the structures. The different line colours correspond to different rectangle widths.

2.5 Magnetostrictive actuation

Our study of magnetostrictive actuation comprised various stages. Initially, a simple set-up for a preliminary assessment of the actuation capability of our magnetostrictive layers at low frequencies out of resonance was built. In a later design, high frequencies were achieved when operating in liquids by means of magnetostriction. These developments were carried out in collaboration with Nanotec Electrónica [73] company. The different steps were carried out under the very demanding technical constraints imposed by the need to minimize the heat generated by the coils and hysteretic losses in the magnets at frequencies up to 1 MHz, and the space constraints imposed by the liquid cell design geometry.

In a first step, our standard AFM cell was modified by attaching a small ferrite electromagnet surrounding the sample area and the microcantilever holder. A sketch of the simple set-up is shown in Figure 2.15. The magnetic field is applied perpendicular to the microcantilever's long axis by means of a soft ferrite toroid (blue element in the center picture in Figure 2.15), coiled with a 500 microns diameter copper wire, which was coated with a layer of enamel. The chip of the microcantilever coated with the Fe-B-N magnetostrictive layer is placed in the gap of the toroid, where the field is most uniform in its plane and perpendicular to the microcantilever long axis.

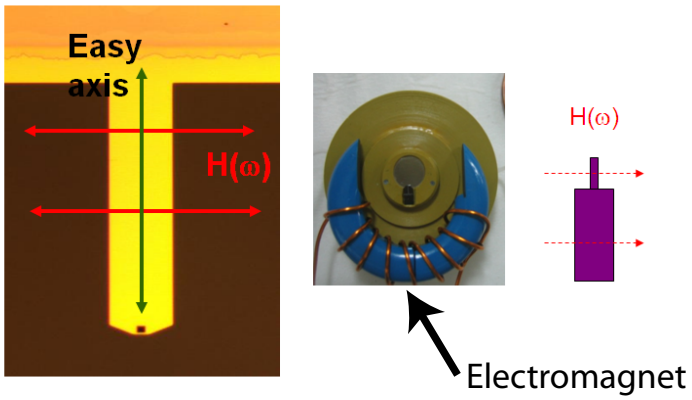

Figure 2.15: Schematics and picture of the first liquid cell set up. The cantilever is placed in the ferrite toroid gap. The magnetic field $\mathbf{H}(\omega)$ is applied perpendicular to the microcantilever long axis.

A first test was performed to check the oscillation of the coated microcantilevers. A silicon nitride cantilever from Olympus ($100 \times 40 \times 0.8$ μm, force constant k = 0.76 N/m) coated with 50 nm of Fe-B-N was used. The small electromagnet carried a sinusoidal current of 5.1 Hz and up to 40 mA_p, resulting in a peak applied field of 25 Oe. Figure 2.16 represents the deflection of the microcantilever versus the current applied to the coil. As shown, the application of an oscillating magnetic field leads to a periodic deflection of the microcantilever. The frequency of the sinusoidal field applied to the cantilever is intentionally low and far from any resonance frequency of both the cantilever and of any other mechanical resonance of the cell or electromagnet to avoid parasitic effect. As a consequence of being out of resonance, the amplitude of the cantilever bending is very small but it can be easily detected by the reflected laser beam deflection at the standard split photodiode of the AFM microscope cell. Figure 2.16 clearly shows that magnetostriction is an even as a function of the field, since both positive and negative peaks of the current (corresponding to positive or negative peaks in the magnetic field) produce the same deflection. This is important, because it indicates that a field oscillating

around zero with frequency ω will drive a magnetostrictive response at 2ω, for each complete cycle of the driving signal, the microcantilever will oscillate at twice the frequency of this driving signal.

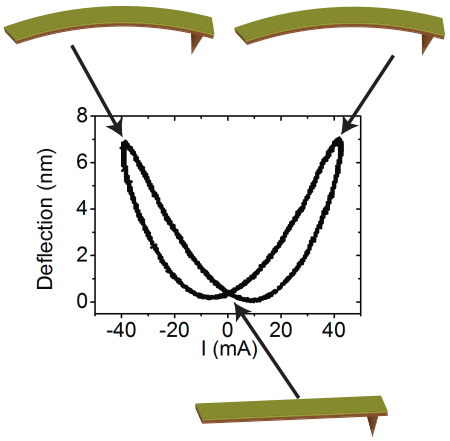

Figure 2.16: Microcantilever deflection under a sinusoidal magnetic field of 5.1 Hz. The even effect of magnetostriction is observed, as the deflection of the microcantilever occurs at twice the frequency of the excitation current through the coil.

Magnetic materials often exhibit a remanent magnetization, i.e. the magnetization vector $\mathbf{M}$ is different from zero if no magnetic field is applied ($\mathbf{M}_0 \neq 0$ when $\mathbf{H} = 0$). This phenomenon is sketched in Figure 2.17. Figure 2.17a shows the entire magnetostrictive cycle, while Figure 2.17b shows the small cantilever deflection due to low applied magnetic fields [2]. As the magnetic film on the microcantilever presents a remanent magnetization, the application of a low magnetic field moves the film magnetization around one of the curve lobes (blue shaded area on Figure 2.17a and black curve on Figure 2.17b), without reversal magnetization. This causes a microcantilever oscillation amplitude (red signal on Figure 2.17c) at the same frequency as the excitation current through the toroid (black signal on Figure 2.17c).

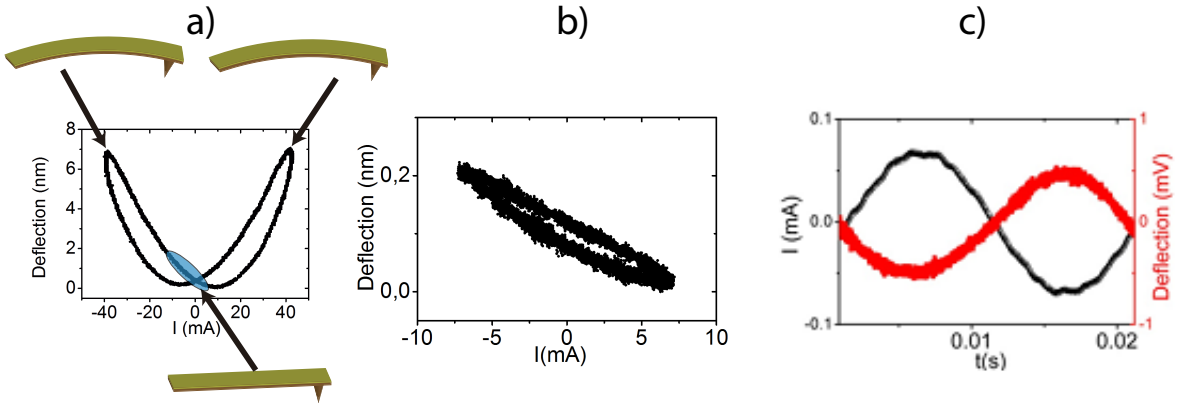

Figure 2.17: a) Microcantilever deflection loop when very high magnetic field amplitude is applied. b) Minor microcantilever deflection loop obtained when low magnetic field amplitude is applied, in particular this loop is the one that corresponds to the blue area in figure a). c) Intensity through the coil (black line) and cantilever deflection (red line).

[2] In this context, low, intermediate or high magnetic fields are related to the magnetic field required to saturate the magnetization.

This apparently disagrees with the expected microcantilever oscillation at twice the magnetic excitation frequency. However, for a low amplitude of the applied field (Figure 2.17b) magnetization follows a minor loop with practically no hysteresis and does not cover the two magnetization lobes (Figure 2.16).

Then, if the applied magnetic field is not enough to cause the magnetization reversion, the signal at twice the excitation frequency will not appear. This is shown in Figure 2.18, where the applied magnetic field is increased, and the cantilever starts to oscillate at twice the driving frequency.

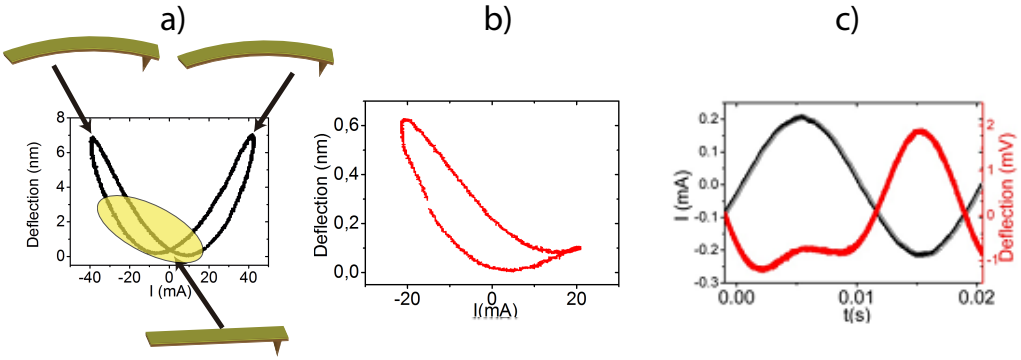

Figure 2.18: a) Microcantilever deflection loop when very high magnetic field amplitude is applied. b) Minor microcantilever deflection loop obtained when intermediate magnetic field amplitude is applied, in particular this loop is the one that corresponds to the yellow area in figure a). c) Intensity through the coil (black line) and cantilever deflection (red line).

Further increments on the sinusoidal magnetic field amplitude applied to the microcantilever clarify that the microcantilever vibrates at twice the current excitation frequency through the toroid (Figure 2.19c). In this case (Figure 2.19b), the magnetization range clearly crosses the center. It can be observed that the oscillation signal of the microcantilever is not symmetrical, having one of its maxima higher than the other. A symmetrical signal can be obtained if a magnetic field high enough to saturate the magnetostrictive film is applied or if the film starts with a zero magnetization, centered at the origin of the curve in Figure 2.16.

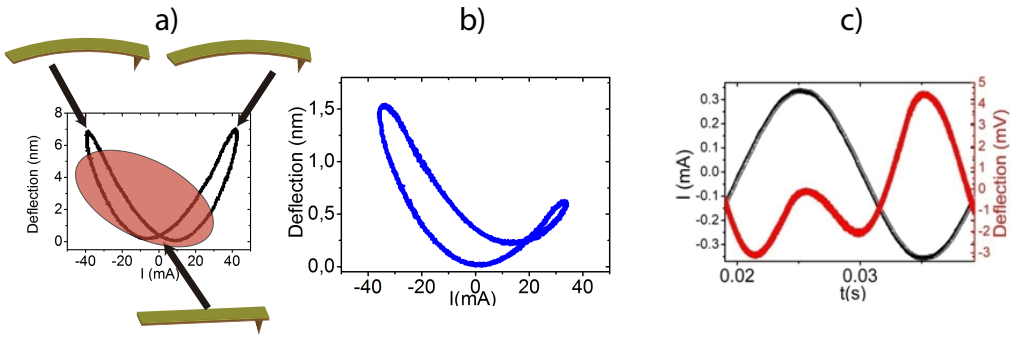

Figure 2.19: a) Microcantilever deflection loop when very high magnetic field amplitude is applied. b) Minor microcantilever deflection loop obtained when high magnetic field amplitude is applied, in particular this loop is the one that corresponds to the orange area in figure a). c) Intensity through the coil (black line) and cantilever deflection (red line).

In Figure 2.20, frequency sweeps with different amplitude driving currents are shown in order to obtain the spectrum of the microcantilever. The same silicon nitride cantilevers from Olympus ($100 \times 40 \times 0.8$ μm, force constant k = 0.76 N/m) have been used .

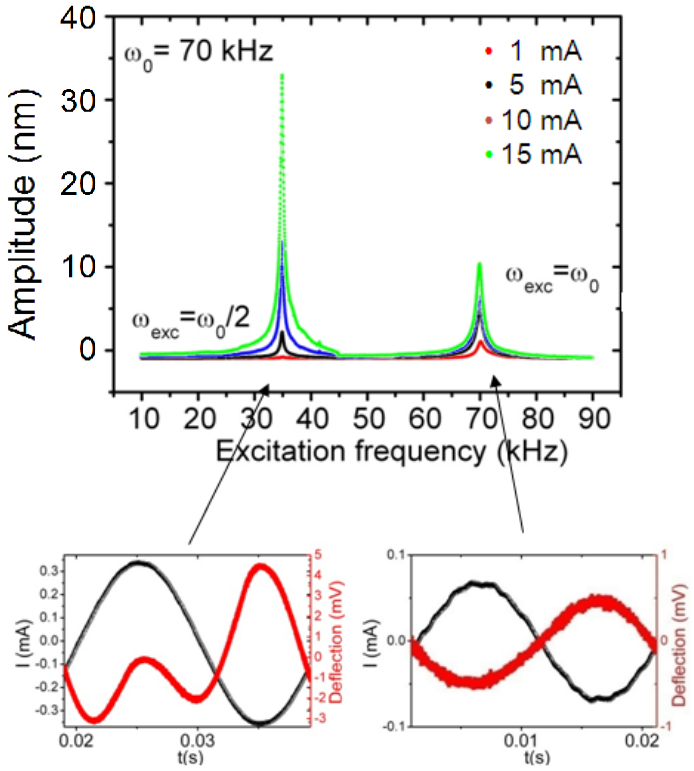

Figure 2.20: Resonance spectra of the microcantilever. The excitation frequency refers to the frequency of the electric current through the coils.

Figure 2.20 illustrates the oscillation amplitude of the microcantilever at different excitation frequencies (of the current flowing through the toroid). The Fe-B-N thin film has an initial magnetization, and therefore, at very small currents (1.5 mA), the oscillation of the lever has the same frequency as the excitation. When the magnetic field is increased (increasing the driving current, 10-15 mA), the signal at twice of the driving frequency appears and the hysteresis curve crosses the zero magnetization point. It is also important to highlight that, in this case, the oscillation amplitude is higher when the frequency of the current applied to the coil is half the resonant frequency of the microcantilever. This is because magnetostrictive effect is an even effect (Figure 2.16), and only at this driving frequency the whole magnetostrictive curve is used. These resonances have a quality factor Q of about 130.

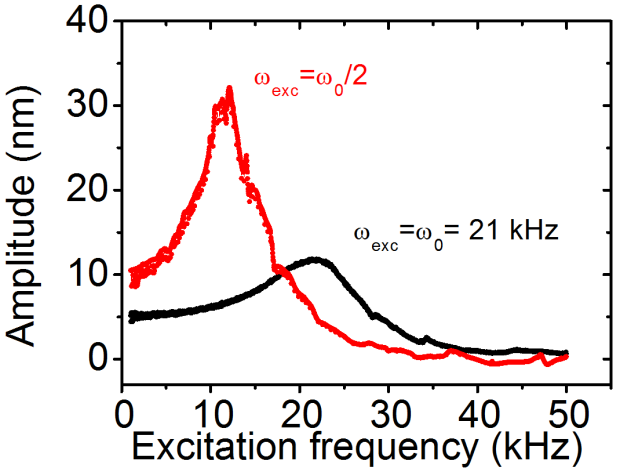

Figure 2.21: Resonance spectra in liquid.

The study performed in air was completed with an analysis of the same cantilevers oscillation in liquids. Resonance spectra [3] show again two peaks (Figure 2.21). The one with the highest intensity lies in an excitation frequency equal to $\omega_0/2$. The quality factor is approximately $Q = 3$.

2.6 Conclusions

The suitability of the Fe-B-N alloy for the magnetostrictive actuation has been demonstrated. It meets a combination of favourable properties: a good magnetostrictive effect produced at low applied magnetic fields, as well as excellent mechanical and non-corrosive properties.

By means of Fe-B-N coated cantilevers, the cantilever bending generated by sinusoidal external magnetic fields has been studied. Furthermore, the existence of two regimes has been explained: when the cantilever oscillates at the same frequency (low applied magnetic field amplitude) or when it oscillates at twice the frequency of the current excitation through the coil.

Moreover, it has been shown that magnetostrictive actuation produces clean resonance spectra in both air and liquids. This makes this actuation method adequate for AFM measurements in liquid environments.

Finally, it was studied the optimal deposition conditions in order to decrease the magnetic field needed to reach saturation and also to produce magnetization rotation instead of domain wall movement, necessary for a good magnetostrictive actuation. Low saturation field is important due to the magnetostriction direct relation with magnetization. A soft magnetic material is needed to avoid high current in the coils that will be embedded in the liquid cell. At high frequencies, it is difficult to achieve these high currents due to the high impedance of the coils. Thus, low currents permit to work at high frequencies, and the liquid cell will be not heated by the Joule effect.

[3] The red curve was measured with an external lock in amplifier connected to an external input of the Nanotec Electrónica electronics. The black one was directly measured with the Nanotec Electrónica electronics.

Chapter 3

AFM liquid cell development for magnetostrictive actuation

In this chapter, the suitability of magnetostrictive actuation for AFM measurements is demonstrated. This objective requires the development of a liquid cell that supports magnetostrictive cantilever excitation[1].

Different liquid cell configurations were tested during the quest towards an efficient implementation of the magnetostrictive actuation in an AFM set-up. In the first part of this chapter, the evolution towards the final liquid cell will be presented. The intermediate precursor designs are detailed and the aims that motivated the selection of the final prototype are explained. At the end of the chapter, examples of the high imaging resolution achieved with magnetostrictive actuation will be presented.

3.1 First prototype

The first prototype of the liquid cell was made of Torlon (Polyamide-imide), a thermoplastic amorphous polymer that has exceptional mechanical, thermal and chemical resistant properties (Young's modulus 4.5 GPa, linear thermal expansion coefficient 31 ppm/^{o}C, resistivity $2 \cdot 10^{17}$ ohm-cm, water absorption after 24 hours 0.33 %). Furthermore, Torlon is a biocompatible material and resistant to corrosion in water. It can be used in liquid bio-enviroments, with very low contamination risk. For these reasons, we have used this material in all the different prototypes built.

As shown in Figure 3.1, a sapphire window was installed in the cell to facilitate the laser optical path towards the cantilever. Two liquid inlet/outlet ports were added in order to inject the liquid solution close to the cantilever position (Figure 3.1, left). On the opposite side (on the right of Figure 3.1), there are three small metallic spheres acting as electric contacts between the liquid cell and the AFM head. One of these electric contacts can be used to connect either a piezoelectric element for acoustic actuation or a coil for magnetostrictive actuation. Once the cantilever is mounted and the liquid cell is placed on the AFM head, an O-ring is used to seal and confine the liquid on the gap between the cell and the sample [2].

[1] This work was performed in collaboration with the company Nanotec Electrónica [73], under a transference to industry project (TRA2009_0206).

[2] This O-ring can be implemented as well in the next prototypes presented below.

Figure 3.1: First prototype of the liquid cell.

The first tests were performed with a coil containing a ferrite core (magnetic susceptibility $\mu = 400$, Figure 3.2). The magnetic field is applied perpendicular to the cantilever short axis and then, the film magnetization is modified along the cantilever short axis. As previously mentioned in section 2.1, the magnetostrictive deformation is isochoric: when the film is elongated in one direction, it is shrunk in the orthogonal ones. Thus, it does not matter whether the magnetostrictive film magnetization is modified along the cantilever long or short axis. When the magnetostrictive film elongates along the cantilever long axis, it shrinks along the cantilever short axis, and vice-versa. Therefore, the applied magnetic field direction can be chosen at convenience: along the cantilever long or short axis.

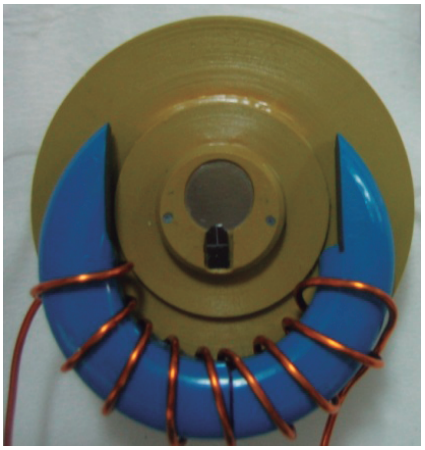

Figure 3.2: Configuration of the liquid cell with a coil used to perform resonance spectra in liquids.

In order to maximize the magnetic field intensity, the ferrite coil was positioned close to the cantilever. A silicon cantilever from MikroMasch [23] (CSC38/Al BS, force constant of $k = 0.08$ N/m) and a silicon nitride cantilever from Olympus [74] (ORC8-PS, force constant of $k = 0.1$ N/m) were coated.

The Fe-B-N cantilevers were excited by a 50 mA_{pp} alternating current through the coil, generating the corresponding alternating magnetic field of 25 Oe_p, as measured by a Gaussmeter in the low frequency regime.

As expected from a magnetostrictive strain, the coated cantilever oscillates at twice the frequency of the applied magnetic field ($\omega_{oscillation} = 2\omega_{field}$). The frequency spectrum of the cantilever oscillation is shown in Figure 3.3 both in air and in liquid environment. The cantilever oscillation amplitude is represented as a function of the cantilever mechanical oscillation

frequency $\omega_{oscillation}$, where $\omega_{oscillation} = 2\omega_{field}$.

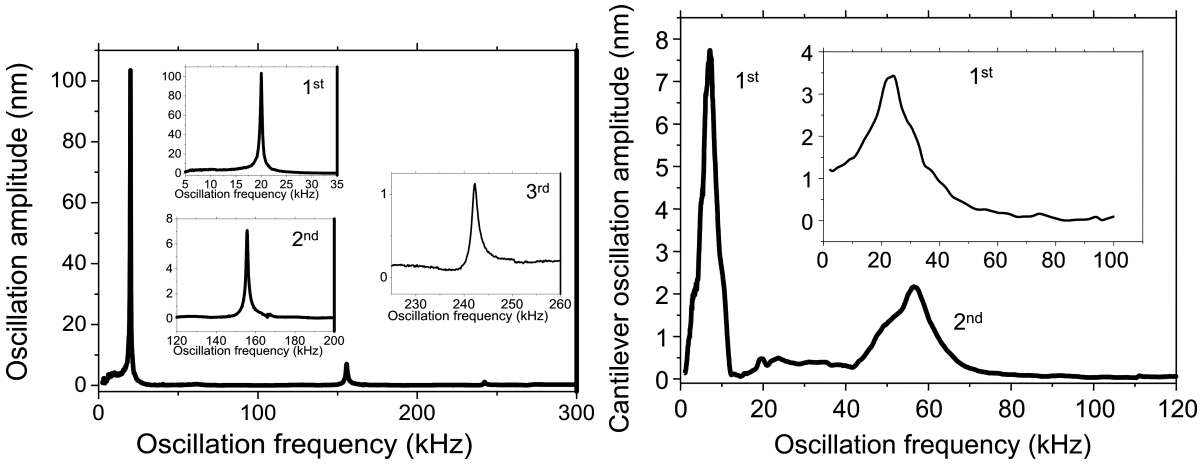

Figure 3.3: Oscillation amplitude spectra taken in air (left) and water (right) of a silicon cantilever from MikroMasch [23] (CSC38/Al BS, force constant of $k = 0.08$ N/m) driven by the magnetostrictive actuation technique with the liquid cell in Figure 3.2. The inset in the right graph shows a silicon nitride cantilever oscillation amplitude spectra in water (Olympus [74] ORC8-PS, force constant of $k = 0.1$ N/m).

In Figure 3.3, the first three resonance modes of the Fe-B-N coated silicon cantilever [23] (the first two flexural modes, 1^{st} and 2^{nd} in the figure, and the first torsional mode, 3^{rd} in the figure), are clearly observed. As expected, the oscillation amplitude at resonance is damped when the cantilever is immersed in liquid (the quality factor of the first mode is reduced from 130 to 4), while the resonance frequencies shift to lower values. The inset of Figure 3.3 shows the oscillation amplitude spectra of a the Fe-B-N coated silicon nitride cantilever [74] immersed in water. The curves on Figure 3.3 demonstrate that the spectra obtained from magnetostrictive actuation method are free from the spurious liquid cell resonances that appear often in the acoustic driven method. Also, cantilever resonant peaks are clearly observed despite the decrease in Q when operating in liquid environment[3].

In order to work in the magnetization linear region (Figure 3.4) and avoid the magnetization reversion, a bias DC current to the AC current signal is added. Thus, the cantilever will oscillate at the same frequency than the applied magnetic field and the ratio of magnetostrictive coefficient and magnetic field will be maximum.

An specific voltage to current amplifier was developed by a company specialized in electronics[4] with the aim of amplifying the voltage signal from the electronics of the AFM and convert it to a current signal with a flat frequency response. This amplifier has 4 BNC inputs that allow the input of 4 different input voltage signals, adding and amplifying them. This capability is useful for Multifrequency AFM, where different eigenmodes are excited and several excitation signals are needed. It is possible as well to add a DC component to the output current signal.

[3]It is important to notice that the predicted ratio between the oscillation amplitude of the first and the second mode is not fulfilled (these ratios will be explained in detail during the next chapter). The ferrite core of the coil increases the impedance at high frequencies, decreasing the applied current at the second resonance with respect to the first resonance and therefore, hampering the amplitude of the second resonance mode with respect to the first one.

[4]Vallés-Vila S.L.

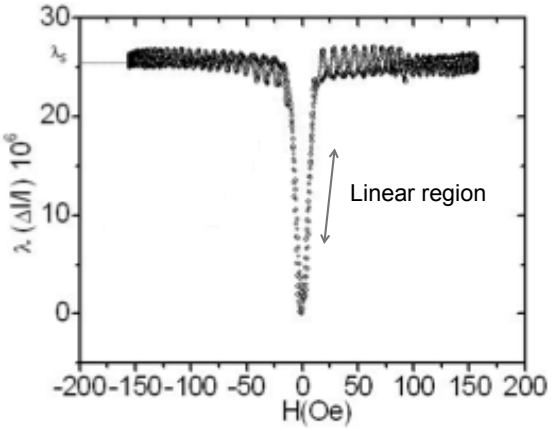

Figure 3.4: Evolution of the magnetostriction as a function of the applied magnetic field parallel to the x axis. Adapted from [20].

The amplifier has a range of $0 - 10$ V_p for input signals, a maximum output current of 1 A_p and a cut-off frequency of 1 MHz.

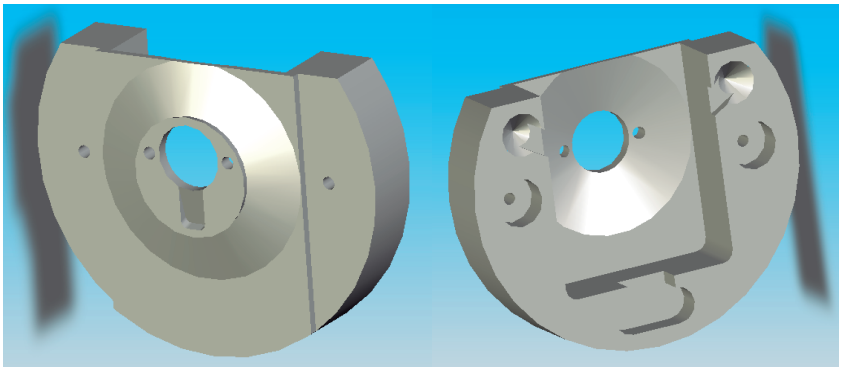

Figure 3.5: Modified design of the basic liquid cell (Figure 3.1).

The final design of the magnetostrictive liquid cell framework is presented in Figure 3.5. Also, the central part was emptied to make the coil mounting easier. The next steps are focused on the implementation of the coil in the liquid cell, being able to perform measurements in a Nanotec Electrónica microscope.

3.2 Liquid cell with a toroidal ferrite inside

The toroidal ferrite is placed inside the liquid cell in the second cell prototype, as shown in Figure 3.6. The toroidal coil with a ferrite core (with a relative permeability $\mu_r = 10000$) is rolled up with 100 turns of an enamelled copper wire (diameter of 150 μm). The coil creates a magnetic field of 10-15 Oe, measured by a Gaussmeter in a low frequency regime, when applying currents of about 500 mA through the coil.

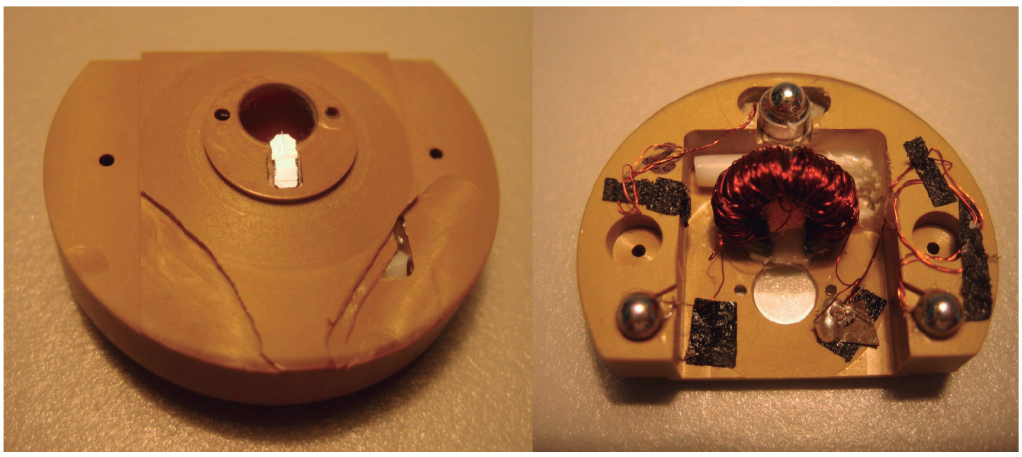

Figure 3.6: Picture of the liquid cell with a ferrite coil inside.

By means of the described voltage to current amplifier, the voltage signal from the AFM electronics is transformed into a current signal. Silicon cantilevers from Nanonsensors, with constant force $k = 2.8$ N/m were coated with 50 nm of Fe-B-N. The coil was fed with 200 mA_{pp} in air and with 600 mA_{pp} in liquid. In both cases, a bias DC component of 100 mA was added to the feeding current to increase the oscillation amplitude and avoid the twice frequency region.

The resonance spectra in air and liquid are shown in Figure 3.7. In the case of air, a small peak can be distinguish at half of the resonance frequency (Figure 3.7, left). This peak corresponds to the 2ω range. As detailed in the previous chapter, in this range the cantilever reaches the first resonance when applying a current frequency at half the value of the first mode. Although the oscillation frequency of the cantilever is at twice the driving current frequency, and the DC output signal of the lock in amplifier should be zero, the AFM internal lock-in amplifier yields a small DC output signal. Even when we add a DC current component, the reverse magnetization is reached. High DC components need to be avoided to prevent an eventual thermal damage of the copper wire.

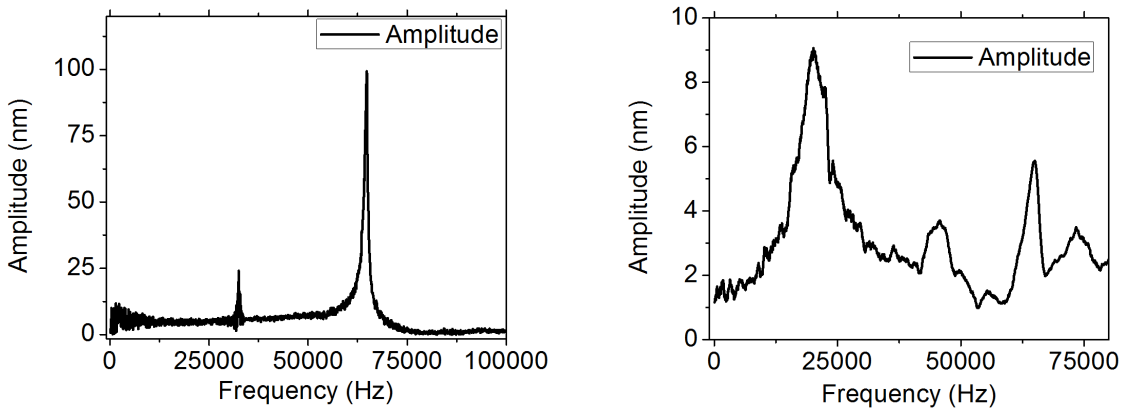

Figure 3.7: Resonance spectra of a Fe-B-N coated silicon cantilever [75] in air (left) and in water (right).

However, although the resonance spectra in air is fairly clean, in liquids it starts to be mixed

with spurious resonances. Several peaks that do not belong to the cantilever resonance modes are present when exciting in liquids (Figure 3.7, right), indicating the presence of mechanical noise.

For example, when we introduce in the liquid cell an uncoated cantilever (same silicon cantilever from Nanonsensors), the mechanical noise from the coil is able to induce the cantilever movement. Left graph of Figure 3.8 presents the resonance spectra of this non-coated silicon cantilever in air. The fact that the spectrum shows a resonance peak proves that the coil is inducing mechanical vibration in the cell. This is because the magnetic poles are placed at both sides of the toroid gap. They attract each other and produce a mechanical vibration, similar to a tuning fork.

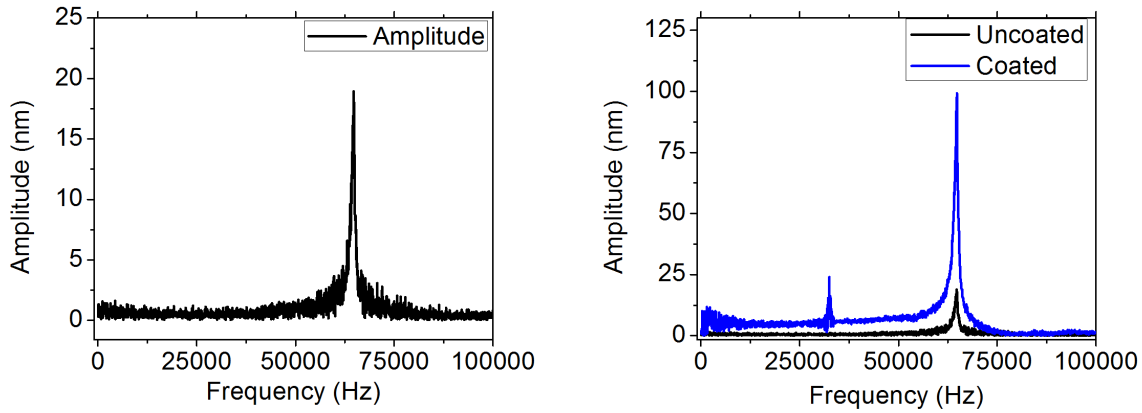

Figure 3.8: In the left graph, Resonance spectrum of an uncoated silicon cantilever [75] in air. In the right graph, comparative of the resonance spectrum of an uncoated and a Fe-B-N coated silicon cantilever [75] in air.

The resonance spectra for a coated and an uncoated cantilever are compared in the right graph of Figure 3.8. Both cantilevers were exited with the same driving current, 200 mA_{pp} and a DC component of 100 mA. Although the oscillation amplitude of the uncoated cantilever is 5 times lower, it is high enough to introduce spurious peaks in the resonance spectra in liquids, as shown in the right graph of Figure 3.7. In addition, we have used a relatively hard cantilever of 2.8 N/m and, despite its hardness, it is excited by the mechanical residual vibrations introduced by the coil in the cell. Moreover, we need to apply a high current to oscillate the cantilever in liquids, heating up the liquid cell. This introduces temperature drifts and heats up the sample, leading to structural changes in some biological samples. A change in the liquid cell configuration is needed to reduce the mechanical noise induced by the coil and the intensity of the current applied.

3.3 Liquid cell with a cantilever placed inside a coil in the outer part of the liquid cell

Several drawbacks arising from the design presented in the former section need to be overcome. The next evolution of the liquid cell design introduces changes in the coil configuration and position.

The cantilever is placed inside the coil in order to maximize the applied magnetic field, as depicted in Figure 3.9. The coil has two layers of 20 turns of an enamelled copper wire (diameter of 100 μm), with dimensions of $2.5 \times 2.5 \times 0.5$ mm. Furthermore, two small permanent magnets were introduced, which produce a magnetic field parallel to the long axis of the cantilever. This allows the application of a DC magnetic component without the need of a DC current.

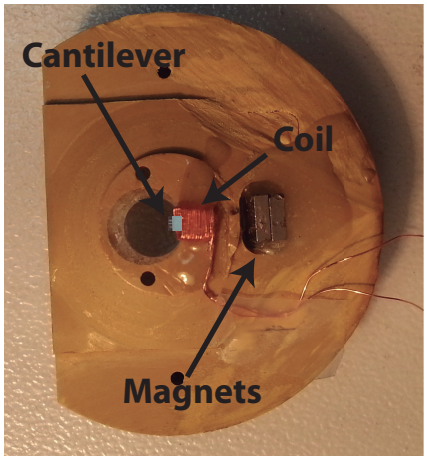

Figure 3.9: Picture of the liquid cell with a coil outside, where the cantilever is mounted.

In order to estimate the magnetic field distribution in the new cell design, a theoretical study by a finite elements method (FEM) software (COMSOL Multiphysics [76]) was performed.

In the simulation, a current of 200 mA was applied through the coil, attaining a magnetic field intensity around 14 Oe in the cantilever position. The magnetic field produced by the small magnets glued to the liquid cell, which introduce a DC magnetic component in the long cantilever axis, was not taken into account.

Using this cantilever-liquid cell configuration, resonance spectra in air and liquid were measured. The curves are displayed in the Figure 3.10. On these experiments, a silicon cantilever from Nanonsensors (force constant $k = 1.5$ N/m) coated with 50 nm of Fe-B-N was used. The coil was fed with 200 mA_{pp}. The air spectrum is very clean but in liquid environment some spurious resonances peaks appear. These peaks may come from the coil vibration, due to the spacial proximity of the glued permanent magnets. The existence of a magnetic torque force in the coil produced by the permanent magnets becomes evident in liquid media. This force causes the vibration of the entire cell, introducing the previously mentioned spurious peaks in the resonance spectra.

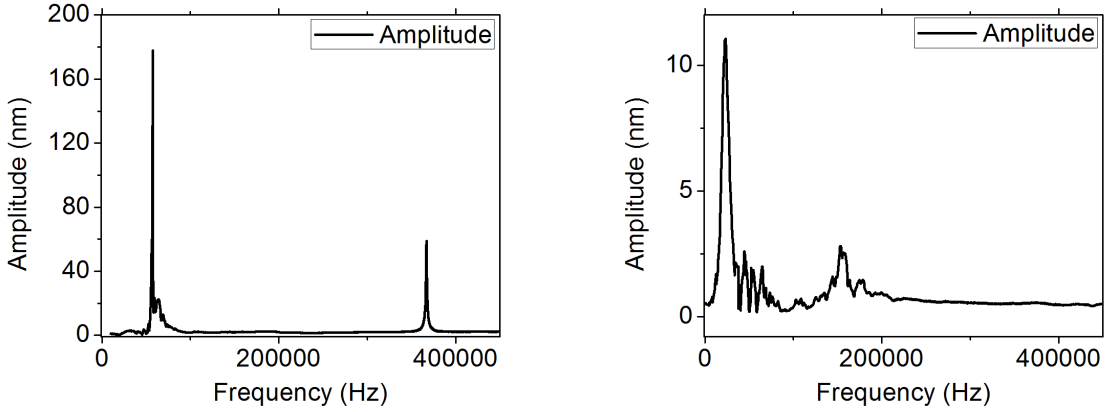

Figure 3.10: Resonance spectrum of a silicon cantilever from Nanonsensors (force constant $k = 1.5$ N/m) in air and in water.

In addition, the coil is in contact with liquid environment and it could warm it up. Another drawback of this design is that every single cantilever has to fit inside the coil and therefore, a different liquid cell needs to be manufactured for each new type of cantilever. Furthermore, despite its efficient operation with low currents, the Joule heating in the coil produces the movement of the cantilever position and then, a shift in the laser spot on the photodiode. Finally, the predicted ratio between the fist and second mode oscillation amplitudes is not fulfilled (section 4.2.3 in the next chapter). This may be explained by the misalignment of the cantilever long axis with the magnetic field created by the permanent magnet. This will produce a magnetic torque which will be added to the magnetostrictive component, leading to the reduction of the oscillation amplitude ratio between resonance peaks. Therefore, with this cell design, a pure magnetostrictive actuation is not exerted. Another liquid cell design is then mandatory because without the permanent magnets a DC current, which would produce thermal drifts, should be applied to the coil.

Summarizing, a more stable cantilever base is needed to be implemented, combined with a configuration that generates a good actuation at low applied currents.

3.4 Liquid cell with a ferrite inside a rectangular coil

In the final configuration, the ferrite can be placed as a base plate for the cantilever (Figures 3.11a and 3.12a) or inside of the liquid cell (Figures 3.11b and 3.12b), in order to avoid the contact with the cantilever and the liquid environment, even though the applied magnetic field in the cantilever position is lower.

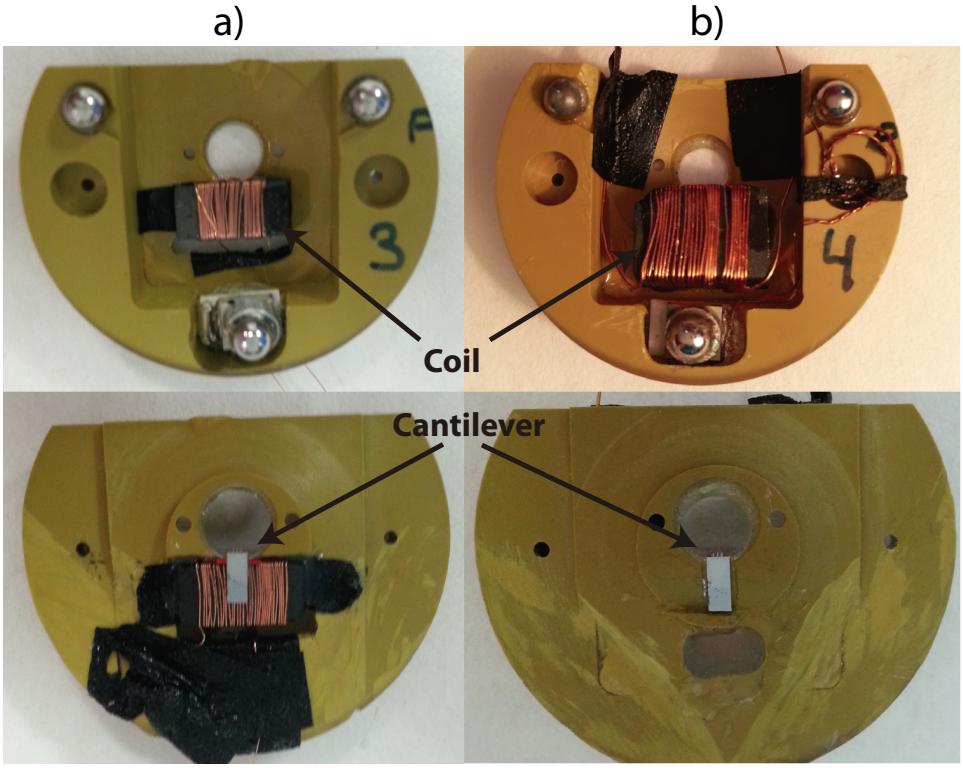

Figure 3.11: Design with a rectangular coil with a ferrite core inside the liquid cell, in contact with the cantilever (a) and separated from it (b).

A rectangular coil of a 25 turns enamelled copper wire (diameter of 100 μm) with a ferrite core (relative permeability $\mu_r = 400$ was used, whose dimensions are $8 \times 4 \times 4$ mm for the liquid cell in Figure 3.11a and $10 \times 8 \times 4$ mm for the one in Figure 3.11b).

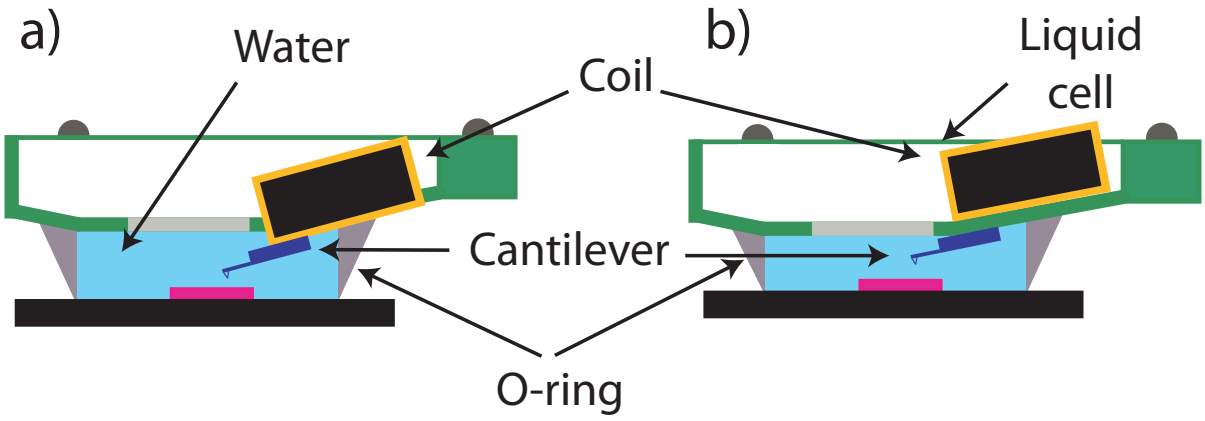

Figure 3.12: Sketch of the two liquid cell configurations: coil in contact with the cantilever (a) and separated from it (b).

A simulation of this ferrite-coil geometry was performed in COMSOL, with an applied current of 200 mA. From the simulations, an 8 Oe magnetic field can be estimated in the cantilever position for the liquid cell shown in the Figure 3.11b.

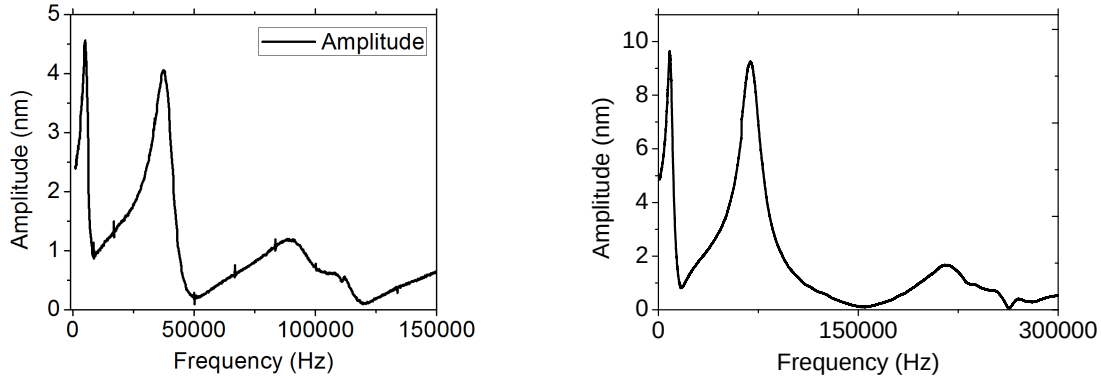

Figure 3.13: Experimental resonance spectra of a Fe-B-N coated silicon nitride cantilever from Olympus ($k = 0.1$ N/m) in the liquid cell of the Figure 3.11a (left) and a MAC Lever Type VII ($k = 0.14$ N/m) in the liquid cell of the Figure 3.11b (right) in water.

Figure 3.13 shows the resonance spectra of a silicon nitride cantilever from Olympus (force constant of $k = 0.1$ N/m) coated with 50 nm of Fe-B-N in liquid environment, using the liquid cell shown in the Figure 3.11a. A resonance spectra of a MAC Lever Type VII ($k = 0.14$ N/m) in water employing the liquid cell shown in the Figure 3.11b is also displayed. A current of 200 mA_p, with a DC component of 100 mA, was introduced in both cases. The results show clean resonance spectra. In the resonance spectra shown in Figure 3.13, the predicted ratio between the cantilever oscillation amplitude of the first and second resonance mode is fulfilled (this oscillation amplitude ratio will be presented in the next chapter, section 4.2.3), demonstrating that pure magnetostriction actuation is exerted.

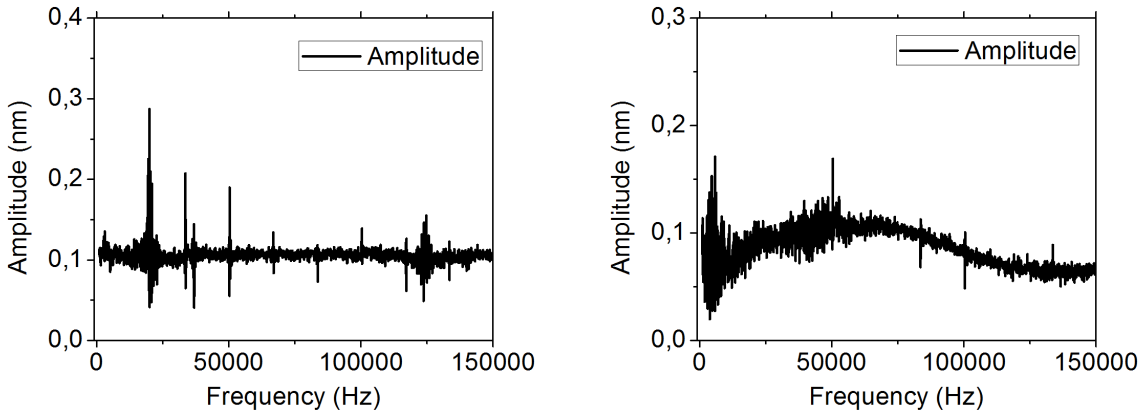

Figure 3.14: Resonance spectrum of a uncoated silicon nitride cantilever from Olympus (force constant of $k = 0.1$ N/m) in air (left) and water (right). Both spectra were measured using the liquid cell shown in the Figure 3.11b.

Control experiments carried out with uncoated cantilevers in the liquid cell show very low unwanted mechanical excitation both in air and in liquids (Figure 3.14), evidencing that the

liquid cell set-up introduces a very low mechanical noise.

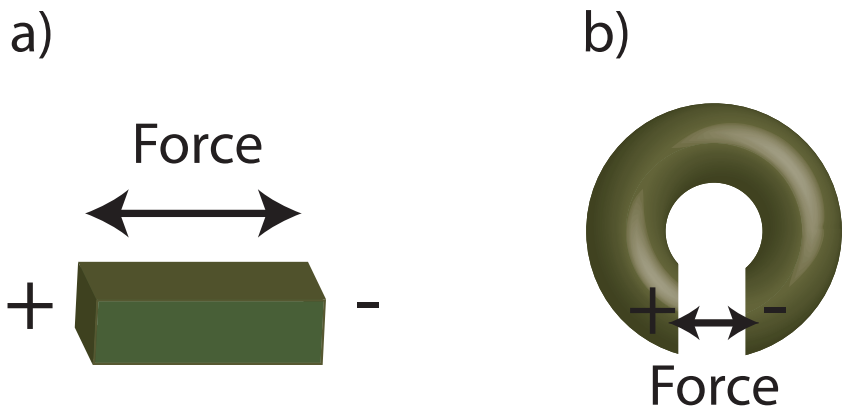

Figure 3.15: a) Rectangular core, where the magnetic poles are at the further edge of the ferrite slab, as in the configuration shown in Figure 3.11. b) Toroidal core, where the poles are at both sides of the gap, as in the configuration in Figure 3.6.

In this electromagnet core configuration, the magnetic poles are in the opposite extreme of the ferrite slab, as shown in Figure 3.15 a. Thus, the force between them will press/stretch the ferrite core, but this force will not introduce a significant mechanical noise as in the toroidal core configuration (Figure 3.15 b), where the magnetic poles at both sides of the gap and are able to induce unwanted mechanical noise.

Finally, not additional heating is noticed either in the coil or the liquid cell, avoiding the laser spot shift on the photodiode. Hence, applied currents around 300 mA_p can be used. This set-up also facilitates the cantilever exchange, as it can be simply attached with a special grease (for example, Silicone Vacuum Grease, from Beckman Coulter) that does not contaminate the liquid environment, with no need of clips to support the cantilever.

3.5 Operation in liquid environments

In this section, three topographic images are shown as a proof of concept of the magnetostrictive driven method in liquid environment. In order to perform the measurements, 50 nm of Fe-B-N was deposited on commercial cantilevers with the conditions described in the section 2.4.

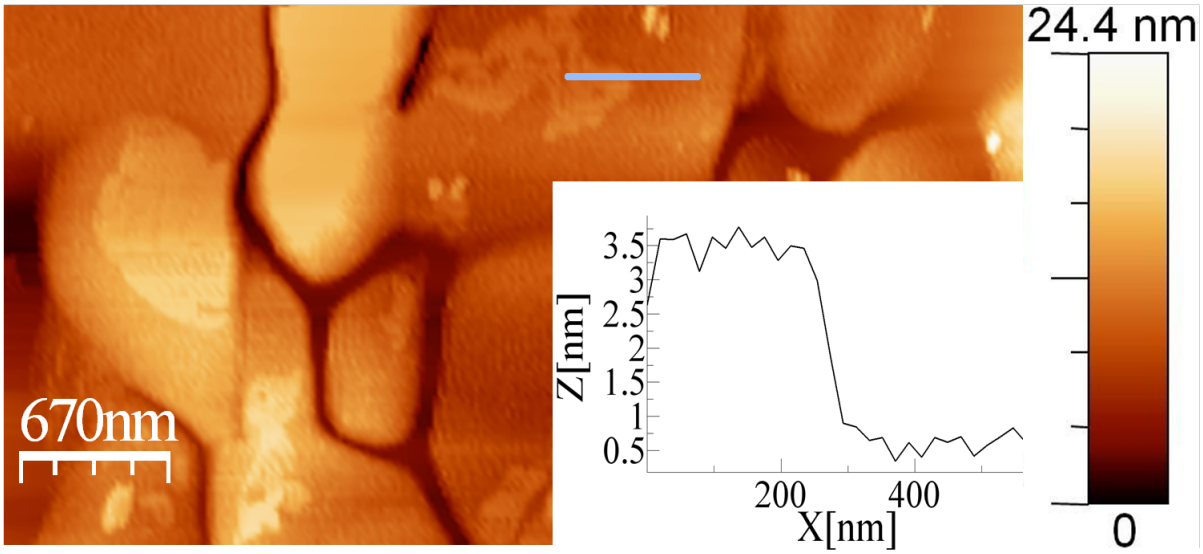

Figure 3.16: Dynamic atomic force microscopy topographic image of thiol islands C_{22} adsorbed on ultra flat gold (111) grains.

Figure 3.16 shows thiol islands ($C_{22}-SH$) self-assembled on flat terraces of gold (111) grains obtained with magnetostrictive drive with the sample immersed in water[5]. The islands height is approximately 3 nm, as shown in the profile of the Figure 3.16, a value which is close to the length of the thiols in solution [77] (e.g., 2.8 nm).

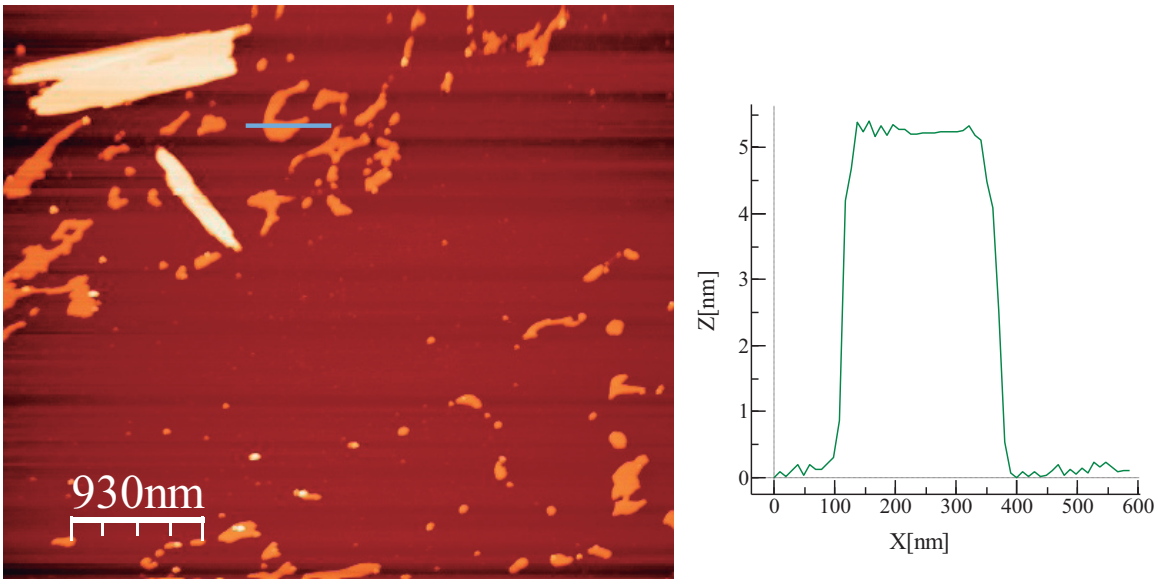

Figure 3.17: Dynamic atomic force microscopy topographic image 12-Hydroxy-stearic acid on mica.

Another example is shown in Figure 3.17, where a topography image of 12-Hydroxy-stearic acid on mica is presented[6]. A profile of a monolayer of 12-Hydroxy-stearic is also plotted, which

[5]I gratefully acknowledge Prof. C. Ocal and Prof. C. Munuera for the preparation of the thiol islands sample.
[6]I gratefully acknowledge Dr. J. A. Heredia-Guerrero, Dr. J. J. Benítez and Prof. A. Heredia for the acid on mica sample.

is around 5 nm in heigh. It is also possible to distinguish two monolayers in the brightest parts of the image.

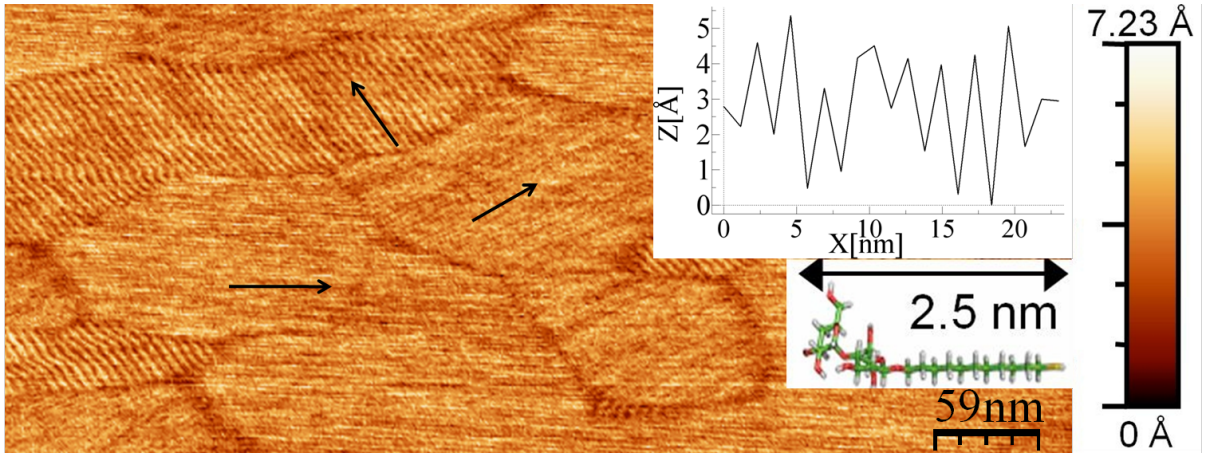

Figure 3.18: Dynamic atomic force microscopy topographic image of self-assembled maltoside neoglicoconjugate islands adsorbed on HOPG.

Finally, a dynamic AFM topographic image of self-assembled maltoside neoglicoconjugate [malto $C_{11} - S]_2$ islands adsorbed on Highly Ordered Pyrolytic Graphite (HOPG) is presented in Figure 3.18, obtained[7] by means of magnetostrictive drive with the sample immersed in water. The organic molecules adsorb flat on graphite following the preferential crystallographic directions of the HOPG hexagonal symmetry. The black arrows guide the eye in the identification of the different domain arrangements. The profile in the inset corresponds to the white line drawn in the image. A periodic pattern of 2.5 nm is observed (17.23 nm between the two points shown/seven peaks), which corresponds to the length of the molecule [78]. The excellent lateral resolution achieved in this image indicates that the tip sharpness is maintained during the cantilever deposition process.

3.6 Conclusions

In summary, it was demonstrated that cantilevers coated with sputtered thin Fe-B-N films can be used in magnetostrictive actuation when operating AFM in liquids. Fe-B-N coatings exhibit excellent magnetostrictive properties, good corrosion resistance when immersed in liquids and nearly zero accumulated stress under the optimized sputtering conditions.

A liquid cell prototype compatible with the commercial Cervantes AFM head [73] was designed and fabricated. We have optimized the design in order to reduce the mechanical noise induced by the coil and minimize the operation excitation current to avoid thermal effects. The performance of the liquid cell prototype was demonstrated by measuring different samples on liquid environment.

[7] I gratefully acknowledge the group of Prof. S. Penadés for the synthesis of the maltoside neoglycoconjugate molecules.

Chapter 4

Enhanced efficiency in the excitation of high modes by means of magnetostrictive actuation

4.1 Introduction

The need of higher compositional resolution, more information channels and sensitivity has led to explore imaging with higher harmonics and/or flexural or torsional cantilever modes. Traditionally, the method used to induce mechanical vibration in these dynamic modes is the piezoelectric excitation. However, in liquids, this actuation technique introduces spurious peaks in the resonance spectra. These peaks come from the excitation of different liquid cell resonances and the fluid borne excitation. Thus, the search of alternative actuation methods that overcome these problems have attracted the interest of several research groups around the world.

New measurement techniques have been developed based on the simultaneous excitation of two or more eigenmodes [16], obtaining compositional information, improvements on imaging contrast and reduction on imaging forces from the different eigenmodes [79]. It is possible as well to drive the microcantilever externally into a resonance of a specific eigenmode and read the different harmonics that may emerge, gaining information about compositional contrast [79, 80].

The use of high eigenmodes is also crucial in the limit detection of micromechanical resonator sensors. In these systems, the cantilever structure serves as a mechanically sensitive tool; the selectivity of the sensor to the detecting target is determined by a specific sensing material that is loaded on the cantilever surface. Theoretical and experimental studies have both indicated that the employment of higher-order resonance modes can effectively improve the Q factor and the mass sensing resolution in resonant cantilever bio/chemical sensors [81–83]. The mass sensitivity δm of a particular mode is proportional to [83]

$$\delta m \propto \mathcal{R}^{-1}\sqrt{\frac{1}{\omega_n Q_n}} \tag{4.1}$$

where $\mathcal{R} = 2\pi\frac{\Delta f}{\Delta m}$ is the mass responsivity, and Q_n and ω_n are the quality factor and the resonance frequency of the mode, respectively. When a cantilever is excited in air or in liquid environment, the use of higher eigenmodes leads to higher ω_n and Q_n [84, 85]. Therefore, it is crucial to operate at high frequencies and high eigenmodes to reach maximum sensibility in mechanical sensors, i.e., lower δm ($\uparrow Q_n \uparrow \omega_n \Rightarrow \downarrow \delta m$).

The operation of these advantageous techniques relies in the use of a low noise and efficient excitation method that promotes the activation of high eigenmodes in liquids. In this chapter, a theoretical model for different actuation modes will be presented: ideal acoustic, magnetic gradient force, Brownian motion, magnetic torque and magnetostrictive [62]. By comparing the efficiency in the excitation and the strength of fundamental and higher modes, it will be shown that the magnetostrictive actuation is the most appropriate method for AFM in liquid environments and for Multifrequency AFM.

4.2 Theoretical models for cantilever actuation

In this section, the microcantilever dynamics will be discussed, as well as the transfer function of the different excitation methods. Hence, from these theoretical studies, we can infer the advantages or disadvantages of the different actuation techniques, besides the suitability for multifrequency configurations. The section starts with the point mass model, modelling magnetic and acoustic actuation. Then, due to the unsuitability of the point mass model to be used for the magnetostrictive actuation, the continuous model will be employed to study the different excitation methods.

4.2.1 The point mass model

This is the simplest model, where non-linearities are neglected. A microcantilever can be modelled as a point mass (a sphere with mass) on a spring with displacement $z_0(t)$ (tip deflection) that is driven by an external force in the presence of the tip surface forces (Figure 4.1). Thus, the system can be described by a second order differential equation of a forced damped harmonic oscillator:

$$m_{eff}\ddot{z}_0(t) + \alpha\dot{z}_0(t) + kz_0(t) = F_{ext}cos(\omega t) + F_{ts}(z, \dot{z}) \tag{4.2}$$

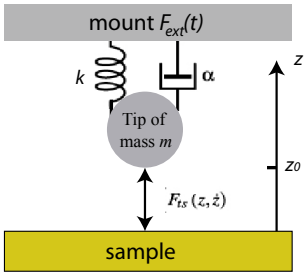

Figure 4.1: Sketch of the point mass model.

where m_{eff} and k are respectively the effective mass and the force constant of the cantilever, F_{ts} is the tip-sample interaction, F_{ext} is the external force exerted on the cantilever and α is the dissipative term (damping). This term can be defined as $\alpha = m_{eff}\omega_0/Q$, where ω_0 is the natural resonance frequency and Q is the quality factor (after a time $\frac{2Q}{\omega_0}$, the transient term of the solution of the equation 4.2 is reduced by a factor $1/e$), that describes the energy dissipated in the medium. If the tip is far from the sample, we can neglect the $F_{ts}(z, \dot{z})$ term.

The solution of a driven harmonic oscillator with damping has three different regimes depending on the damping term:

- Overdamped ($\frac{1}{2Q} > 1$). The system returns to steady state without oscillating in response to a step input external force.

- Critically damped ($\frac{1}{2Q} = 1$). It is the minimum amount of damping needed to return to steady state without oscillating in response to a step input external force.
- Underdamped ($\frac{1}{2Q} < 1$). The system oscillates with the amplitude exponentially decreasing to zero in response to a step input external force.

The relevant regime for most dynamic AFM experiments is the underdamped regime, where $Q > 0.5$. The solution in the underdamped regime has a transient (it goes to zero after a short period of time) and a steady motion term

$$z_0 = Be^{-\frac{\omega_0 t}{2Q}} \cos(\omega_r t - \delta) + A\cos(\omega t - \phi) \tag{4.3}$$

The steady motion is a sinusoidal function (harmonic) in the solution that oscillates at the excitation frequency ω and has a phase lag ϕ with respect to the excitation force. Solving the differential equation 4.2, we arrive to the expression of the resonance spectra amplitude $A(\omega)$ (blue curve in Figure 4.2)

$$A(\omega) = \frac{F_{ext}/m_{eff}}{[(\omega_0^2 - \omega^2)^2 + (\frac{\omega\omega_0}{Q})^2]^{1/2}} \tag{4.4}$$

and its phase lag ϕ (green curve in Figure 4.2)

$$\tan(\phi) = \frac{\omega\omega_0/Q}{\omega_0^2 - \omega^2} \tag{4.5}$$

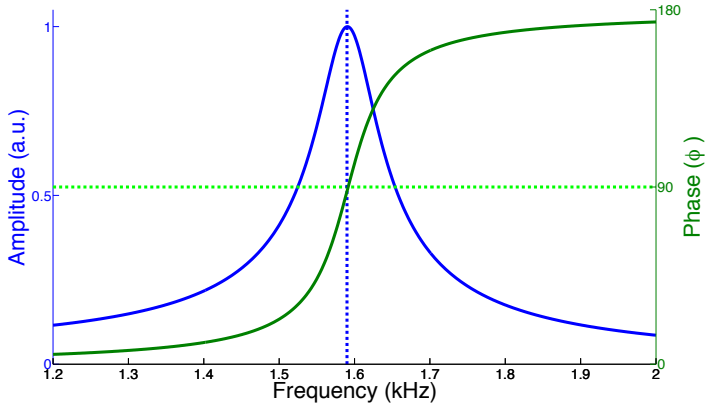

Figure 4.2: Resonance spectrum, where amplitude is in blue and phase is in green.

In a underdamped system, the oscillation amplitude of the point mass object is reduced due to a force synchronous with the velocity but opposite in direction to it. In these systems, the excitation frequency ω_m at which the system reaches the amplitude maximum do not match with the natural resonance frequency of the system (ω_0). Then, the maximum in amplitude happens at

$$\omega_m = \omega_0(1 - \frac{1}{2Q^2})^{1/2} \tag{4.6}$$

And the oscillation amplitude will be

$$A_m = \frac{QF_{exc}}{k} \frac{1}{(1 - 1/4Q^2)^{1/2}} \tag{4.7}$$

As we can see at this equation, this maximum depend on Q, k and F_{exc}. Furthermore, the oscillation amplitude of a damped harmonic system is $Q\frac{1}{(1-1/4Q^2)^{1/2}}$ times the deflection in the static system $\frac{F_{exc}}{k}$.

Using the point mass model, it is possible to study different cantilever actuation techniques. As we are interested in the cantilever actuation, the tip-sample interaction term $F_{ts}(z,\dot{z})$ is neglected.

A first case is the magnetic excitation, modelled as a periodic magnetic force exerted on the cantilever tip. The resulting differential equation is [86]

$$m_{eff}\ddot{z}_0(t) + \alpha\dot{z}_0(t) + kz_0(t) = F_{mag}cos(\omega t) \tag{4.8}$$

and the oscillation amplitude and phase are

$$A(\omega) = \frac{F_{mag}/m_{eff}}{[(\omega_0^2-\omega^2)^2 + (\frac{\omega\omega_0}{Q})^2]^{1/2}} \tag{4.9}$$

$$\tan(\phi) = \frac{\omega\omega_0/Q}{\omega_0^2-\omega^2} \tag{4.10}$$

A second case is the acoustic actuation. An scheme is shown in Figure 4.3. The movement of the base is the actuation force. No direct force is applied to the system.

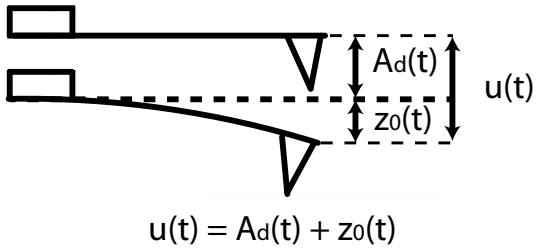

Figure 4.3: Schematic of the acoustic excitation. Adapted from [86].

Being $u(t)$ the total displacement of the tip, the governing equation when the base is oscillated with an amplitude A_d [86] is

$$m_{eff}\ddot{u}(t) + \alpha\dot{u}(t) + ku(t) = 0 \tag{4.11}$$

where $z_0(t) = u(t) - A_d\cos(\omega t)$ and A_d is the base displacement amplitude. The oscillation amplitude and phase are

$$A(\omega) = \frac{A_d\sqrt{\omega^4 + (\frac{\omega\omega_0}{Q})^2}}{[(\omega_0^2-\omega^2)^2 + (\frac{\omega\omega_0}{Q})^2]^{1/2}} \tag{4.12}$$

$$\tan(\phi) = \frac{\omega\omega_0/Q}{\omega_0^2-\omega^2} \tag{4.13}$$

The disadvantage of the point mass model becomes evident when we model the magnetostrictive actuation. It is not possible to introduce the strain produced by the magnetostrictive layer on the cantilever surface in the model, since it is a point mass model. Moreover, it does not stablish any difference between a homogeneously distributed force over the cantilever surface

(the same constant force in magnitude and direction at any point of the cantilever surface) and an inhomogeneous one (for example, a point force at the free end), or between an applied force or an induced bending moment. Furthermore, it does not take into account the different cantilever dimensions and shapes. Therefore, in order to model the different excitation methods, the continuous model will be used, which overcomes these limitations.

4.2.2 The continuous model

This model uses the Euler-Bernoulli equation to find the cantilever movement equations, with the following approximations:

- The material of the cantilever is isotropic, homogeneous and perfectly elastic.
- The thickness is much lower than the width, and both lower than the length (Figure 4.4).
- We neglect all torsional effects in the beam and only consider flexural modes of vibration.
- We consider amplitude deflections smaller than the thickness of the cantilever.
- The thickness and width are constant over the length of the cantilever.

The governing equation for the dynamic and small amplitude deflection of a thin and isotropic beam of constant cross section (Figure 4.4) is [87]

$$EI\frac{\partial^4 w(x,t)}{\partial x^4} + \beta EI\frac{\partial^4}{\partial x^4}\frac{\partial w(x,t)}{\partial t} + \mu\frac{\partial^2 w(x,t)}{\partial t^2} = f(x,t) \tag{4.14}$$

where $w(x,t)$ is the deflection of the neutral axis of the beam, E is Young's modulus along the longitudinal axis of the beam, I is the moment of inertia with respect to the x axis, β is the coefficient for the internal damping in the beam, μ is the mass per unit length of the beam, $f(x,t)$ is the force per unit length, x is the spatial coordinate along the beam and t is the time. The boundary conditions for equation 4.14 are the usual clamped and free conditions

$$w(x,t)\mid_{x=0} = \frac{\partial w(x,t)}{\partial x}\mid_{x=0} = \frac{\partial^2 w(x,t)}{\partial x^2}\mid_{x=L} = \frac{\partial^3 w(x,t)}{\partial x^3}\mid_{x=L} = 0 \tag{4.15}$$

where L is the length of the cantilever. The second and third order partial derivatives of the equation 4.15 are proportional to the bending moment and shear force (at the free end), respectively.

Scaling the spatial variable x with the length of the beam L ($\zeta = \frac{x}{L}$) and taking the Fourier transform of equation 4.14

$$\frac{EI(1-i\omega\beta)}{L^4}\frac{d^4 W(\zeta,\omega)}{d\zeta^4} - \mu\omega^2 W(\zeta,\omega) = F(\zeta,\omega) \tag{4.16}$$

where

$$Y(x,\omega) = \int_{-\infty}^{\infty} y(x,t)e^{-i\omega t}dt \tag{4.17}$$

for any function of time $y(x,t)$. The boundary conditions for $W(\zeta,\omega)$ are identical to those for $w(x,t)$, with all partial derivatives replaced by full derivatives and with the spatial variable replaced by its scaled quantity.

The total force $F(\zeta,\omega)$ applied to the cantilever beam can be separated into external exciting drive force $F_{drive}(\zeta,\omega)$ and the hydrodynamic loading component due to the motion of the fluid around the beam $F_h(\zeta,\omega)$

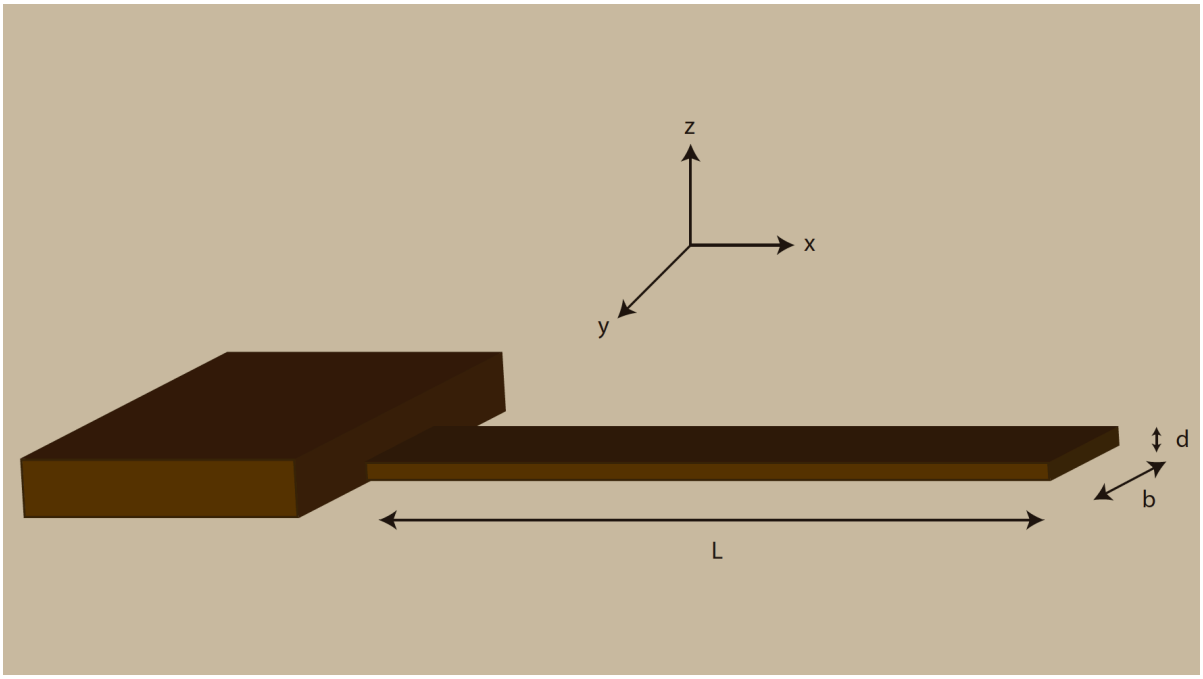

Figure 4.4: Sketch of a rectangular bar cantilever with the length L, width b and thickness d.

$$F(\zeta,\omega) = F_{drive}(\zeta,\omega) + F_h(\zeta,\omega) \tag{4.18}$$

The hydrodynamic force can be calculated from the motion fluid equations. For a rigid beam undergoing oscillatory motion it has the general form [88]

$$F_h(\zeta,\omega) = \frac{\pi}{4}\rho_f\omega^2 b^2\Gamma(\omega)W(\zeta,\omega) \tag{4.19}$$

where ρ_f is the fluid density and b is the width of the beam. $\Gamma(\omega)$ is the hydrodynamic function, and it is dimensionless (see Appendix A.1). Substituting equation 4.19 into equation 4.16, neglecting internal losses ($\beta = 0$) as they are much lower than viscous losses and rearranging

$$\frac{d^4W(\zeta,\omega)}{d\zeta^4} - \frac{\mu\omega^2L^4}{EI}\left(1 + \frac{\pi\rho_f b^2}{4\mu}\Gamma(\omega)\right)W(\zeta,\omega) = s(\zeta,\omega) \tag{4.20}$$

where

$$s(\zeta,\omega) = \frac{F_{drive}(\zeta,\omega)L^4}{EI} \tag{4.21}$$

Noting that the fundamental resonant frequency of the beam in vacuum is given by

$$\omega_{vac,1} = \frac{\lambda_1^2}{L^2}\sqrt{\frac{EI}{\mu}} \tag{4.22}$$

being $\lambda_1 = 1.875$ the smallest positive root of

$$1 + cos\lambda_i \cosh\lambda_i = 0, \qquad i = 1, 2, 3... \tag{4.23}$$

Substituting equation 4.22 into equation 4.20 gives

$$\frac{d^4W(\zeta,\omega)}{d\zeta^4} - B^4(\omega)W(\zeta,\omega) = s(\zeta,\omega) \tag{4.24}$$

where

$$B(\omega) = \lambda_1\sqrt{\frac{\omega}{\omega_{vac,1}}}\left(1 + \frac{\pi\rho_f b^2}{4\mu}\Gamma(\omega)\right)^{1/4} \tag{4.25}$$

The general solution to equation 4.24 in terms of the appropriate Green's function $G(\zeta,\zeta',\omega)$ is [88]

$$W(\zeta,\omega) = \int_0^1 G(\zeta,\zeta',\omega)s(\zeta',\omega)d\zeta' \tag{4.26}$$

with $G(\zeta,\zeta',\omega)$ being constructed as described in Appendix A.2 (Appendix A of [88]).

Finally, we have to find the normalized external driving force $s(\zeta,\omega)$ for each excitation method.

The solutions of the equation 4.26 for each excitation method can be found in Appendix B. In order to simplify the mathematical problem, we can assume that the cantilever is driven near its ith mode resonance frequency. Thus, we can approximate the cantilever [89] deflection $w(x,t)$ as

$$w(x,t) = \sum_i c_i(t)\psi_i(x) \tag{4.27}$$

where $c_i(t)$ is the complex magnitude of the ith mode and $\psi_i(x)$ is the normalized eigenfunction of the ith bending mode of a uniformly thin rectangular beam [90]. $\psi_i(x)$ is related to the cantilever oscillation amplitude at the position x for each resonance mode, providing the cantilever profile of the ith bending mode. For this reason, it is generally called the cantilever shape function.

Calculating the homogeneous solution of equation 4.14 with $\beta = 0$ and using equation 4.27 for the free and undamped cantilever

$$EIc_i(t)\frac{\partial^4\psi_i(x)}{\partial x^4} + \mu\psi_i(x)\frac{\partial^2 c_i(t)}{\partial t^2} = 0 \tag{4.28}$$

Dividing by $EIc_i(t)\psi_i(x)$ and operating

$$\frac{\frac{\partial^4\psi_i(x)}{\partial x^4}}{\psi_i(x)} = -\frac{\mu\frac{\partial^2 c_i(t)}{\partial t^2}}{EIc_i(t)} \tag{4.29}$$

As the time dependent function $c_i(t)$ and x dependent function $\psi_i(x)$ are independent each other, to satisfied the equation 4.29 both sides have to be equal to a constant k^4

$$\frac{\frac{\partial^4\psi_i(x)}{\partial x^4}}{\psi_i(x)} = k^4 \qquad \frac{\mu\frac{\partial^2 c_i(t)}{\partial t^2}}{EIc_i(t)} = -k^4 \tag{4.30}$$

Thus, equation 4.29 can be separated into two independent differential equations

$$\frac{\partial^4\psi_i(x)}{\partial x^4} - \psi_i(x)k^4 = 0 \tag{4.31}$$

$$\mu\frac{\partial^2 c_i(t)}{\partial t^2} + k^4 EIc_i(t) = 0 \tag{4.32}$$

Considering the boundary conditions of equations 4.15, we can solve the local part of the equation 4.31, for the free cantilever

$$\psi_i(x) = A_i \left(\sin(k_i x) - \sinh(k_i x) + \frac{(\sin(k_i L) + \sinh(k_i L))(\cosh(k_i x) - \cos(k_i x))}{cos(k_i L) + cosh(k_i L)} \right) \tag{4.33}$$

where A_i is the normalizing amplitude and $\psi_i(x)$ are normal eigenfunctions, i.e.

$$\int_0^L \psi_i(x)\psi_j(x)dx = \delta_{i,j} \tag{4.34}$$

where $\delta_{i,j} \neq 0$ only when $i = j$. Another important property of the shape function is

$$\frac{\partial^2 \psi_i(x)}{\partial x^2} = -k_i^2 \psi_i(x) \tag{4.35}$$

The expression $k_i L = \lambda_i$ can be calculated solving equation 4.23. All $\psi_i(x)$ are identical to each other for the forced and dumped cantilever [89], which is our case. If we normalize each eigenfunction so that $\psi_i(L) = 1$, then $c_i(t)$ is exactly the measured tip motion of the i mode. In the steady state, equation 4.14 (with $\beta = 0$) can be rewritten in the frequency domain using equation 4.27 as

$$EI\, C_i(\omega) \frac{\partial^4 \psi_i(x)}{\partial x^4} - \omega^2 \rho_c A\, C_i(\omega)\psi_i(x) = F_h(\omega) + F_{ext}(x, \omega) \tag{4.36}$$

where ρ_c is the mass density of the cantilever, $A = b \times d$ is the area of the cross section and $\rho_c A = \mu$. Hereafter, for bilayered cantilevers, we will use the effective values of ρ, μ and E, calculated in Appendix A.3. For a rectangular vibrating cantilever driven with frequency ω, the hydrodynamic resistance F_h is given by

$$F_h(\omega) = \frac{\pi}{4} \rho_f b^2 \omega^2 \Gamma_{rect}(\omega) W(x, \omega) = \frac{\pi}{4} \rho_f b^2 \omega^2 \Gamma_{rect}(\omega) C_i(\omega) \psi_i(x) \tag{4.37}$$

where ρ_f is the mass density of the surrounding fluid and Γ_{rect} is the hydrodynamic function for a beam with a rectangular cross section.

From equation 4.36, it is possible to calculate the transfer function for each method, which is the relationship between the input excitation (excitation force) and the output response (cantilever oscillation amplitude). The cantilever can be considered as an isolated input($\mathbf{X}$)/output($\mathbf{Y}$) system, linear and time invariant, that can be described by a transfer function ($\mathbf{H}$) [91]. The input/output parameters would be the actuation force and the vertical deflection, respectively. The ratio between the input and the output is the transfer function.

$$\mathbf{Y}(\omega) = \mathbf{X}(\omega)\mathbf{H}(\omega) \tag{4.38}$$

The transfer function describes how the cantilever resonance spectra is, and we can then extract the different actuation methods efficiency when exciting the different i bending eigenmodes, i.e., the ratio between the oscillation amplitude of the first and higher resonance modes (A_i/A_1). Finally, from equation 4.36, the transfer function of the cantilever can be calculated as follows:

$$\mathbf{H}(\omega) = \sum_i \frac{C_i(\omega)}{F_{exc,method}} \tag{4.39}$$

4.2.3 Theoretical study of the different actuation methods

In the literature, theoretical works are focused in the calculation of the different cantilever spectra parameters such as the resonance frequency of the different eigenmodes (f_n) and their respective quality factors (Q_n) [84, 85]; or the effect of an adding mass on the cantilever resonance frequency [81–83]. However, to the best of our knowledge, there is still no any study about the efficiency of the different actuation methods in exciting high resonance modes, which is important, for example, for Multifrequency AFM. Also, we have not found any theoretical work describing the cantilever magnetostrictive actuation. Therefore, in the next sections, a theoretical study of the different actuation methods (including magnetostriction) will be presented. Their respective transfer functions will be calculated, as well as a discussion about their capability to excite high resonance modes and their suitability for Multifrequency AFM.

In the first place, the acoustic excitation will be discussed. This actuation method is based on the periodic movement of the cantilever base (Figure 4.5). The mechanical noise induced by the liquid cell vibration and the unsteady motion of the surrounding fluid around the cantilever will be not included. For this reason, this is an idealistic case.

After the acoustic excitation, the different magnetic methods will be studied. The interaction forces between a magnetic film (the cantilever's coating) and a magnetic field may arise from different phenomena: magnetic gradient, magnetic torque or magnetostriction. All these different forces can be used to mechanically excitate the cantilever. These methods overcome the acoustic actuation problem: the cantilever spectra spurious peaks. These three different magnetic actuation methods have in common the use of an external magnetic field generated by an electromagnet. Also, in these methods, the cantilevers are coated with a magnetic/magnetostrictive thin film. An external magnetic field is applied perpendicular to the cantilever surface in both magnetic gradient and torque actuation. However, while in the first one the cantilever coated film magnetization is parallel to the magnetic field (Figure 4.6), in the second one the film magnetization is perpendicular to the magnetic field (Figure 4.7). On the contrary, in the magnetostrictive actuation, the external magnetic field is applied parallel to the cantilever surface and therefore, to the magnetic/magnetostrictive coating film plane (Figure 4.8). Thus, these variations in the magnetization/magnetic-field configurations will yield differences in the actuation mechanisms.

Furthermore, the Brownian driven motion will be discussed. The cantilever is excited by collisions from the Brownian motion of the molecules around it. Despite the low oscillation amplitude generated by Brownian driven motion, it is widely used in micromechanical resonator sensors. Moreover, there are examples of the Brownian driven excitation in dynamic AFM in air [92]. Hence, it is worth introducing this excitation method in the study of the different actuation methods. It is included in a common section with the magnetic gradient actuation method because, as will be shown later, the excitation driven force mechanism is similar.

It should be noted that the cantilever tip will not be considered in the models. This additional mass will just shift down the frequency of the resonance modes. We are, above all, interested in the shape of the resonance spectra and the relationship among the oscillation amplitude of the different resonance modes.

Furthermore, for the sake of reducing the computational burden and simplicity, the magnetic coating films are considered homogeneously magnetized in all the magnetic actuation methods. In the simulations, the magnetization will be constant in magnitude and direction in the entire volume of the magnetic film, considering the entire magnetic film as a single domain with a well defined magnetization. The presence of magnetic domains with different magnetization directions in the magnetic film will not be taken into account. These magnetic domains may have influence in the position of the forces and moments on the cantilever surface, complicating

the theoretical studies. However, these simplistic models gives us an general idea of the actuation mechanism and, from them, interesting characteristics such as the efficiency in the excitation or the strength of the actuation can be inferred, as will be presented in the next sections.

Ideal acoustic actuation

The cantilever response under ideal acoustic excitation conditions (not taking into account the fluid-borne excitation or the liquid cell resonances) is due to the periodic movement of cantilever base (up and down), as shown in Figure 4.5.

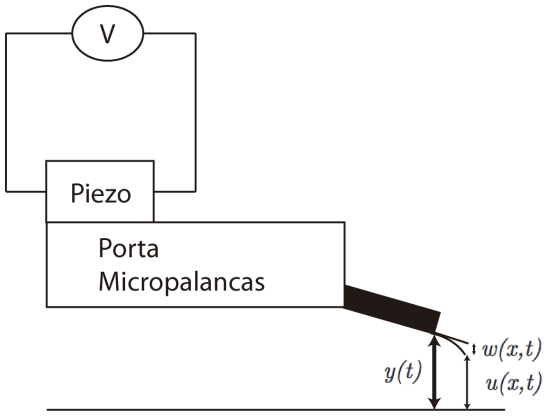

Figure 4.5: Cantilever movement in acoustic excitation. $u(x,t)$ is the absolute end motion and $w(x,t)$ is the relative end motion to the base motion $y(t)$.

The governing equation for the deflection of the cantilever can be written in the following form [93]

$$EI\frac{\partial^4 u(x,t)}{\partial x^4} + \rho A\frac{\partial^2 u(x,t)}{\partial t^2} = f_h(x,t) \tag{4.40}$$

where $u(x,t)$ is the absolute cantilever motion, ρ is the cantilever density and $f_h(x,t)$ is the hydrodynamic force per unit length. Since $w(x,t) = u(x,t) - y(t)$

$$EI\frac{\partial^4 w(x,t)}{\partial x^4} + \rho A\frac{\partial^2 w(x,t)}{\partial t^2} + \rho A\frac{\partial^2 y(t)}{\partial t^2} = f_h(x,t) \tag{4.41}$$

where $y(t)$ is the movement of the base. In frequency domain

$$EI\, C_i(\omega)\frac{\partial^4 \psi_i(x)}{\partial x^4} - \omega^2 \rho A\, C_i(\omega)\psi_i(x) - \omega^2 \rho A\, Y(\omega) = F_h(\omega) \tag{4.42}$$

Inserting equation 4.37 into equation 4.42, multiplying by $\psi_i(x)$ and integrating over the length of the cantilever leads to the transfer function of the ith mode

$$\frac{C_i(\omega)}{Y(\omega)} = \frac{\beta_i L\left(\rho A + \frac{\pi}{4}\rho_f b^2 \Gamma_{rect}\right)\omega^2}{EI\left(\frac{\lambda_i}{L}\right)^4 \alpha_i L - \omega^2\left(\rho A + \frac{\pi}{4}\rho_f b^2 \Gamma_{rect}\right)\alpha_i L} \tag{4.43}$$

where $\alpha_i L = \int_0^L \psi_i^2(x)dx$, $\beta_i L = \int_0^L \psi_i(x)dx$ and λ_i is the ith modal wavelength (equation 4.23). We have used the property

$$\frac{\partial^2 \psi_i(x)}{\partial x^2} = -k_i^2 \psi_i(x) \Rightarrow \frac{\partial^4 \psi_i(x)}{\partial x^4} = k_i^4 \psi_i(x)$$

Magnetic gradient and Brownian actuation

As previously introduced, in the magnetic gradient actuation method the cantilever is coated with a magnetic thin film. The total catilever thickness is d, being $d = d_1 + d_2$, where d_1 and d_2 are the cantilever and the magnetic film thicknesses, respectively. In order to induce the cantilever oscillation, a periodic external magnetic field is generated by an electromagnet. The magnetic film magnetization will tend to be aligned along the same direction as the applied magnetic field. This alignment will yield a magnetic force proportional to the magnetic field gradient (an homogeneously magnetic field does not produce a magnetic force) and the angle between the magnetic field and the magnetization on the film. In the most common situation, the magnetic film coating surface is perpendicular to the applied magnetic field, and the film magnetization, in the presence of the magnetic field, will change its magnetization direction and set it along the magnetic film direction.

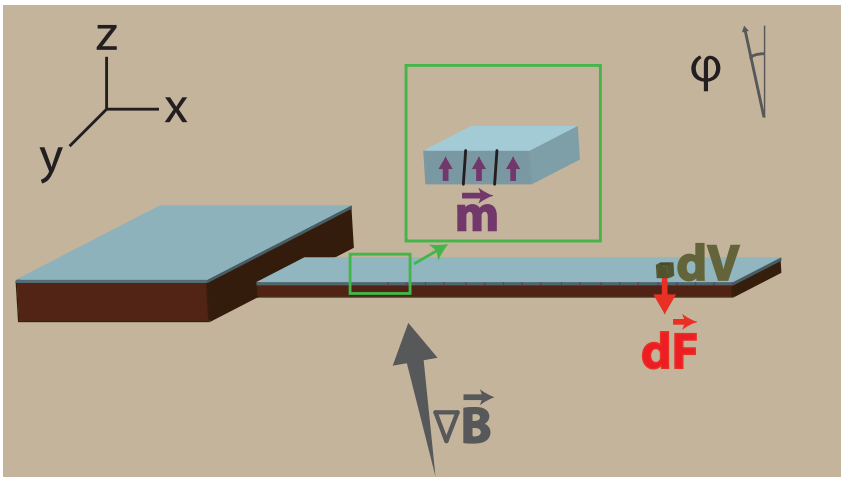

Figure 4.6: Schematic of a rectangular cantilever coated with a magnetic film. φ is the angle between the magnetic field $\mathbf{B}$ and the magnetic moments $\mathbf{m}$ of the magnetic film. Finally, $\mathbf{F}$ is the net force actuating on the cantilever, which is homogeneously distributed on the cantilever surface.

In this configuration, a magnetic film is directly evaporated onto the cantilever, as we can see in Figure 4.6. The cantilever bends under the influence of a magnetic force acting on the magnetic film. The cantilever movement is a consequence of a magnetic gradient force between a non homogeneous magnetic field and the magnetized film deposited on the cantilever. A magnetic field on z direction tends to magnetize the magnetic film on the cantilever in the same z direction, creating a magnetic moment component m_z, normal to the cantilever surface (the other perpendicular directions of the magnetization, m_x and m_y, do not produce a magnetic gradient force on the magnetic film). The magnetic force acting on a differential magnetic moment $d\mathbf{m}$ can be written as the derivative of the magnetic energy [94]

$$d\mathbf{F}_{grd} = \nabla(d\mathbf{m} \cdot \mathbf{B}) = \nabla(\mathbf{M}_{film} dV \cdot \mathbf{B}) \tag{4.44}$$

where $\mathbf{M}_{film}$ is the film magnetization, $\mathbf{B}$ is the magnetic flux density, $d\mathbf{m}$ is the differential of magnetic moment on the film and dV is the differential of volume. Ideally, for a pure magnetic gradient, we should consider the film uniformly magnetized only on the z direction, parallel to the magnetic field and x independent (neglecting torque effects). Also, due to the small size of the cantilever and for small oscillations, the magnetic field gradient $\nabla\mathbf{B}$ can be considered

constant over the magnetic film surface during the entire oscillation cycle. Thus, B_z gradient is taken as a constant (spatially) in the model. Therefore, considering the film magnetization constant over the entire magnetic film volume, the net force per unit length in the z direction on the cantilever surface is

$$F_{grd} = \int_0^b \int_0^{d_2} (\mathbf{M}_{film} \cdot \nabla)\, \mathbf{B}\, dzdydx = M_{film,z}\, b\, d_2 \cos(\varphi) \frac{\partial B_z}{\partial z} \tag{4.45}$$

Then, inserting this expression in equation 4.36 and operating as before, multiplying by $\psi_i(x)$ and integrating over the cantilever length, the transfer function in magnetic gradient excitation is

$$\frac{C_i(\omega)}{F_{grd}} = \frac{\beta_i L}{EI \left(\frac{\lambda_i}{L}\right)^4 \alpha_i L - \omega^2 \left(\rho A + \frac{\pi}{4}\rho_f b^2 \Gamma_{rect}\right) \alpha_i L} \tag{4.46}$$

As the magnetic field gradient is constant over the magnetic film surface and the film magnetization is considered homogeneous in the entire volume, this force can be considered as a homogeneously distributed force over the cantilever surface (a same constant force in magnitude and direction at any point of the magnetic film). Moreover, as the cantilever is coated (bilayered cantilever), the effective values of ρ, μ and E, calculated in Appendix A.3 have to be used.

Another example of a homogeneously distributed force is the Brownian excitation, also known as Brownian driven motion. In this case, the collisions of the fluid molecules with the cantilever are the driving force. The spectral density of the Brownian force is not white, i.e., the Brownian driven force is frequency dependent. It can be determined by the fluctuation-dissipation theorem [95]. This cantilevers fluctuations can be measured on the cantilever without any external excitation. The Brownian driven force can be approximated as [93]

$$F_B = 4K_B T \left(\frac{\pi}{4}\rho_f b^2\right) \omega\, img\{\Gamma_{rect}(j\omega)\} \tag{4.47}$$

where K_B is the Boltzmann's constant, T is the temperature and $img\{\Gamma_{rect}(j\omega)\}$ is the imaginary part of the hydrodynamic function $\Gamma_{rect}(j\omega)$. As observed in the last equation, the force is constant over the entire cantilever surface, independent of the position (x, y, z). For this reason, both Brownian motion and magnetic gradient actuation were include in the same section, since they are both examples of a homogeneously distributed force.

Inserting equation 4.47 in equation 4.36 and operating as before, the transfer function due to the Brownian motion is

$$\frac{C_i(\omega)}{F_{brw}} = \frac{\omega\, img\{\Gamma_{rect}\}\beta_i L}{EI \left(\frac{\lambda_i}{L}\right)^4 \alpha_i L - \omega^2 \left(\rho A + \frac{\pi}{4}\rho_f b^2 \Gamma_{rect}\right) \alpha_i L} \tag{4.48}$$

where $F_{brw} = 4K_B T \left(\frac{\pi}{4}\rho_f b^2\right)$ and C_i is the induced tip motion of the ith mode at a given absolute temperature T.

Magnetic torque actuation

Magnetic torque excitation method presents similarities with the formerly described homogeneously distributed magnetic force excitation: the cantilever is coated with a magnetic film, the oscillatory magnetic field $\mathbf{B}$ is applied on z direction perpendicular to the cantilever surface and the actuation force is produced by the interaction between an external magnetic field generated by an electromagnet and the magnetic film. However, the film magnetization on the x direction is coincident with the cantilever long axis instead of the z direction in the magnetic gradient

case, as depicted in Figure 4.7. Also, the magnetization is considered fixed and independent of the magnetic field direction. Furthermore, the magnetic field is uniformly distributed on z direction, in contrast to the magnetic gradient actuation, where the magnetic field must be inhomogeneous. Thus, when the film magnetization and the magnetic field have not the same direction, a magnetic torque is exerted on the microcantilever. This excitation method is known as MAC Mode^{TM}.

An oscillatory magnetic field creates a periodic magnetic torque dT in a magnetized differential element dx

$$d\mathbf{T} = d\mathbf{m} \times \mathbf{B} = dm_x B_z \sin(\varphi)\hat{\mathbf{y}} = M_x B_z \sin(\varphi) d_2 b \, dx \hat{\mathbf{y}} \tag{4.49}$$

where m_x and M_x are the x component of the magnetic moment and the magnetization on the film and B_z is the z component of the magnetic field.

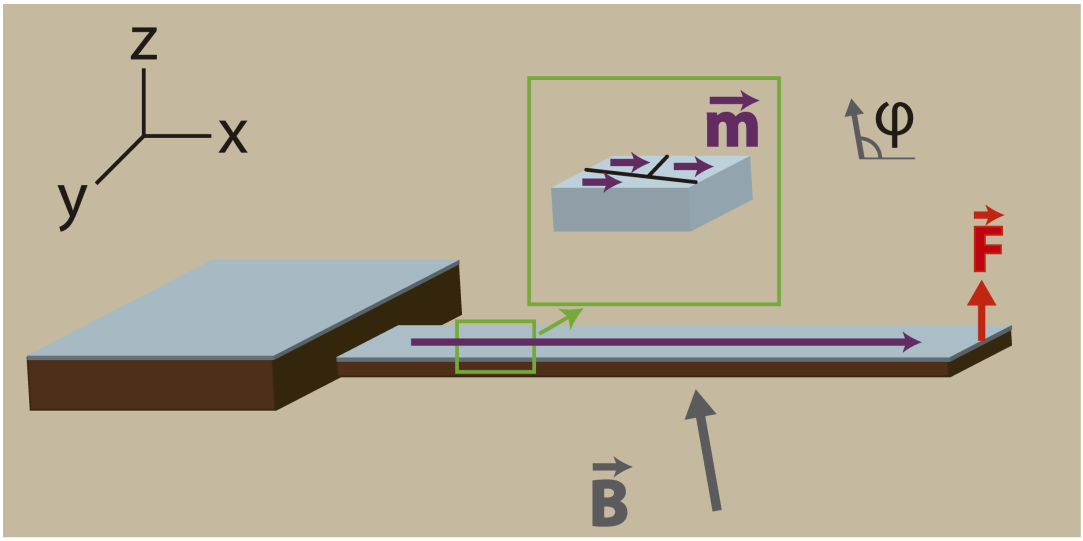

Figure 4.7: Schematic of a rectangular cantilever coated with a magnetic film. The angle φ between the magnetic field $\mathbf{B}$ and the film magnetization creates a torque in each differential volume element of the magnetic film. The addition of all these differential torques is equivalent to a total torque produced by a point force $\mathbf{F}$ at the free end of the cantilever.

Thus, the internal bending moment is

$$\mathbf{IM}(x) = \int_x^L d\mathbf{T} = M_x B_z \sin(\varphi) d_2 b \, L(1 - \frac{x}{L})\hat{\mathbf{y}} \tag{4.50}$$

This results in a force per unit length [1]

$$F_T(x) = -\frac{\partial^2 \mathbf{IM}(x)}{\partial x^2} = M_x B_z \sin(\varphi) d_2 b(\delta(x - L) - \delta(x)) = F_{trq}(\delta(x) - \delta(x - L)) \tag{4.51}$$

where δ is the Dirac delta function. Therefore, the magnetic torque excitation can be seen as a distributed applied moment along the cantilever long axis, where a differential torque is exerted to each differential volume element. The addition of all these differential torques is equivalent to a total torque produced by a point load at the free end of the cantilever, since $\delta(x)$ has not effect

[1] An internal bending moment $M(x)$ produces a force per unit length $F(x) = \frac{\partial^2 \mathbf{M}(x)}{\partial x^2}$ [96].

because it is applied at the clamping. Inserting this equation in equation 4.36, and considering the properties of the Dirac's delta, the transfer function in magnetic torque excitation is

$$\frac{C_i(\omega)}{F_{trq}} = \frac{\psi_i(0) - \psi_i(L)}{EI\left(\frac{\lambda_i}{L}\right)^4 \alpha_i L - \omega^2\left(\rho A + \frac{\pi}{4}\rho_f b^2 \Gamma_{rect}\right)\alpha_i L} \tag{4.52}$$

As this method needs coated cantilevers, the effective values of ρ, μ and E, calculated in Appendix A.3 have to be used.

In real AFM set-ups, there is always a combination of magnetic gradient and torque excitation, since the magnitude of magnetic field is not spatially homogeneous. However, in the common case of a strong in-plane anisotropy ($M_{film,z} \backsimeq 0$) due to the thinness of the magnetic film on the cantilever, the magnetic gradient contribution is negligible [43]. Thus, torque effect is what prevails over magnetic gradient actuation mode.

Lorentz actuation could be included as a magnetic actuation. This method is used by the AFM company Asylum to excite triangular cantilevers. In this case, a static magnetic field is applied in a perpendicular direction to the cantilever surface. However, the cantilever is not coated with a magnetic film, but it is gold coated. This method is based on the Lorentz force acting on an alternating current flowing through a V-shaped cantilever through the gold coating, which is placed into a static magnetic field, at appropriate orientation and strength. From the results obtained from our theoretical study and modelling (Appendix C), the total resulting force applied in the cantilever for movement generation can be approximated as a point force around the vertex.

Magnetostrictive actuation

As in the previously presented magnetic methods, in the magnetostrictive actuation a electromagnet is used in order to applied an external magnetic field. Also, the cantilever surface opposite to the tip has to be coated with a magnetostrictive thin film (amorphous Fe-B-N in our coated cantilevers), as shown in Figure 4.8. However, in this case, the magnetic field is applied along the same plane as the magnetostrictive film. This magnetic field will change the magnetostrictive film magnetization. As a magnetostrictive material experiences a dimensional change when its magnetization state is changed, an expansion of the magnetostrictive film on the cantilever surface is produced. This strain will lead to the cantilever bending. Consequently, an alternating magnetic field will produce cyclic expansions of the magnetostrictive layer inducing the oscillatory movement of the cantilever [62].

This actuation method is equivalent to photothermal [97] or piezoelectric (based on a piezoelectric thick-film coating the cantilever) [98] actuation, which are based on a thin film on the cantilever surface that suffers a periodic expansion. However, the first one may locally warm the sample due to the power supplied by the laser in order to excite the cantilever, and the second one is difficult to use in physiological environments.

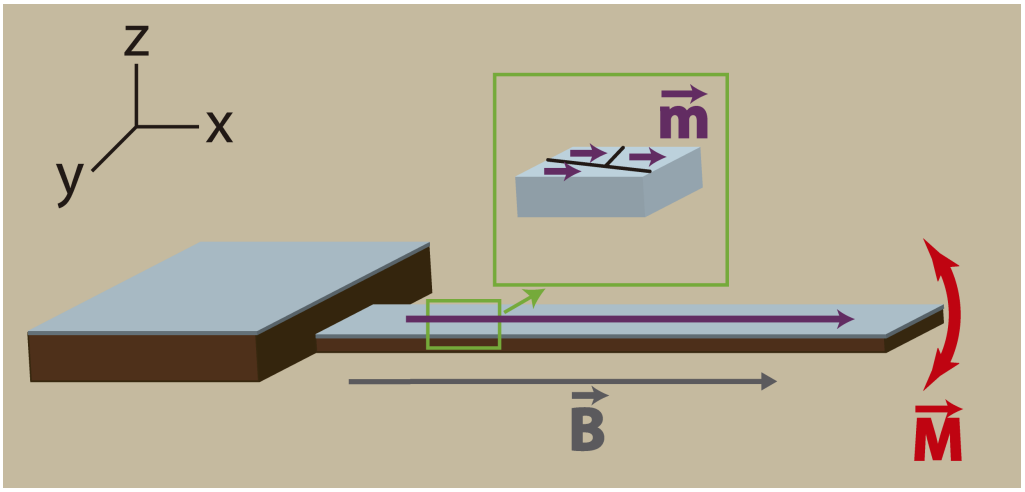

Figure 4.8: Figure of a rectangular cantilever coated with a magnetostrictive film. Magnetization changes on the magnetic film produce a uniform bending moment on the cantilever.

The magnetostrictive actuation transfer function calculation is based on the previous work of Guerrero and Wetherhold [99], related to the cantilever bending due to a strained magnetostrictive coating layer. According to that work, a strain on the x and y axis produced in magnetostrictive film yields to an expansion/contraction of the magnetic film parallel to the surface. This results in an internal bending moment along x axis equals to [100]

$$M_{int}(x) = -EI\frac{d^2w}{dx^2} = -EI(-\frac{1}{R_x}) = \frac{EI}{R_x} = K_{mgt} \tag{4.53}$$

where R_x is calculated in Appendix B.4 in equation B.4. The force per unit length is

$$F_{MT}(x) = -\frac{\partial^2 M_{int}(x)}{\partial x^2} = F_{mgt}(\delta^{'}(x-L) - \delta^{'}(x)) \tag{4.54}$$

This expression is equivalent to a uniform applied moment on the cantilever. $\delta^{'}(x)$ has not effect since it is applied in the clamping. Following the previous procedure, the transfer function for the ith mode is

$$\frac{C_i(\omega)}{F_{mgt}} = \frac{\psi_i^{'}(L) - \psi_i^{'}(0)}{EI\left(\frac{\lambda_i}{L}\right)^4 \alpha_i L - \omega^2\left(\rho A + \frac{\pi}{4}\rho_f b^2 \Gamma_{rect}\right)\alpha_i L} \tag{4.55}$$

As the cantilevers are coated with a magnetostrictive thin film, the effective values of ρ, μ and E, calculated in Appendix A.3 have to be used.

4.3 What do we measure in a laser beam deflection system?

Before showing the theoretical and experimental results, a brief summary about what is measured in a standard beam deflection set-up is presented.

Figure 4.9 shows us two cases:

- a) The vertical shift h_1 of the reflected spot due to a change in the slope of a cantilever when it is curved.
- b) The vertical shift h_2 of the reflected spot due to a vertical displacement of the cantilever.

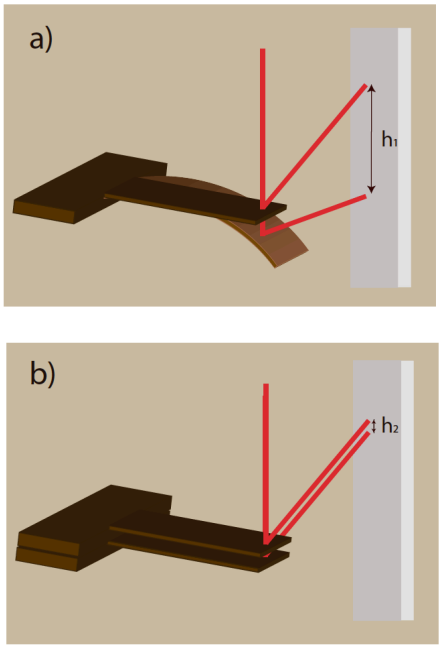

Figure 4.9: Shift of the spot by beam deflection due to a curvature of the cantilever in a) and due to a vertical displacement of the cantilever in b).

Beam deflection set-ups measure the slope of the cantilever [101, 102]. The quantity h_1 is always much higher than h_2, commonly more than two orders of magnitude in typical AFM set-ups [103]. Hence, if we perform a resonance spectrum, we must take into account that oscillation amplitude of higher eigenmodes will be overestimated in the photodiode, since the slope at the end of the cantilevers is higher for higher eigenmodes

$$\psi_i'(L) > \psi_j'(L) \quad , \quad i > j \tag{4.56}$$

Figure 4.10 depicts the shape functions of the three first flexural modes, and their derivatives.

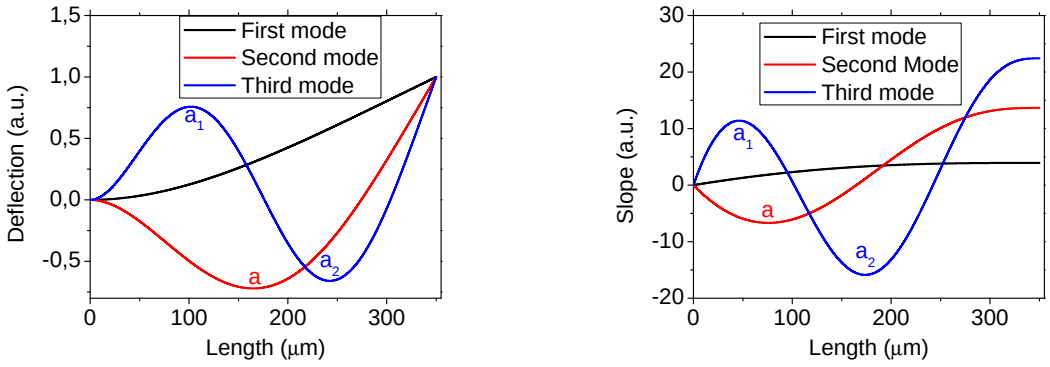

Figure 4.10: Examples of the shape function $\psi_i(x)$ (left) and the derivative shape function $\psi_i'(x)$ (right) of the first three cantilever modes.

Thus, the following ratio between the slopes at the free end of the cantilever respect to the

first mode are obtained

$$\begin{aligned}\frac{\psi_2^{'}(L)}{\psi_1^{'}(L)} &= 3.47\\ \frac{\psi_3^{'}(L)}{\psi_1^{'}(L)} &= 5.70\\ \frac{\psi_4^{'}(L)}{\psi_1^{'}(L)} &= 7.99\end{aligned} \tag{4.57}$$

Consequently, the amplitude of the second resonance mode will be overestimated in the photodiode 3.473 times, and the amplitude of the third resonance mode will be overestimated 5.706 times. For that reason, if we calculate the relationship between the oscillation amplitude of different resonance modes, we have to divide the oscillation voltage amplitudes of higher resonance modes measured in the photodiode by the values calculated in equation 4.57.

4.4 Theoretical results

In this section, the theoretical results for the frequency response of a typical cantilever beam for AFM from Olympus [74] are shown: $L = 200$ μm, $b = 40$ μm, $d_1 = 0.8$ μm. The material of the cantilever is silicon nitride, with a density of $\rho_1 = 3290$ kg/m^3, a Young's modulus $E_1 = 310$ GPa and Poisson's ratio $\nu_1 = 0.27$. The magnetostrictive/magnetic film has a width of $d_2 = 0.05$ μm, and a Young's modulus and Poisson's ratio $E_2 = 193$ GPa and $\nu_2 = 0.3$ respectively (Fe-B-N alloy) [20]. The density is $\rho = 7350$ kg/m^3, and the coefficient of magnetostriction of the Fe-B-N will be $\lambda = 30 \times 10^{-6}$. The medium used is water, whose density and viscosity is $\rho_{water} = 1000$ kg/m^3 and $\eta_{water} = 0.001$ Pa·s. MATLAB software was used in order to perform the calculations of the analytical results. To find the total transfer function for each excitation mode, the transfer function of each mode is added as follows

$$\mathbf{H}(\omega) = \sum_i \frac{C_i(\omega)}{F_{method}} \tag{4.58}$$

In Figure 4.11 the transfer function of the different excitation methods in water is plotted. As the oscillation amplitude resulting from the equations is in arbitrary units and we are interested in the ratio between the oscillation amplitude of the first and higher resonance modes (A_i/A_1), each curve is normalized to the amplitude of the first resonance mode. As displayed in Figure 4.11, the acoustic method is the most efficient in exciting high vibration modes: the higher the mode, the higher the oscillation amplitude. This is due to the fact that acoustic excitation is proportional to ω^2, as shown in equation 4.43. However, this analysis was performed for the ideal case, in which the vibrations of the liquid cell and the movement of the liquid around the cantilever are not considered. In a real case, a "forest of peaks" appears (Figure 3.7), worsening the operation conditions [93].

When comparing the rest of the actuation techniques (magnetic torque [47], magnetic gradient [104], Brownian motion and magnetostriction), it can be clearly observed that magnetostriction is more efficient when exciting high modes. The three magnetic field based methods need to implement a coil to create the magnetic field from a current through the coil. Consequently, in order to excite high eigenmodes, an efficient method is needed, since the higher the frequency, the higher impedance in the coil. This high impedance reduces the applied current through the coil, and therefore, the applied magnetic field.

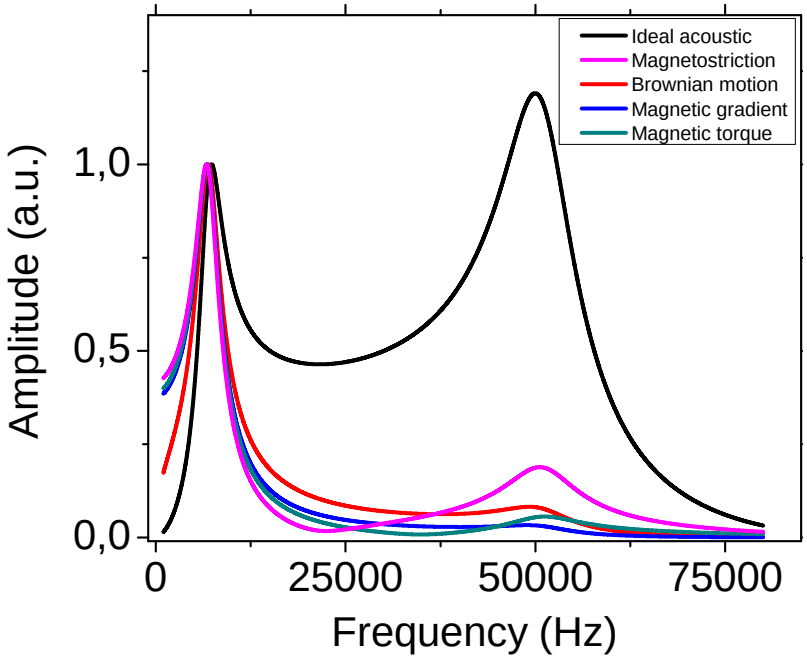

Figure 4.11: Plot of the transfer function module of the different excitation methods in water, normalized to the first resonance mode amplitude for each method.

In the magnetic gradient case, despite the comparatively low efficiency in the excitation of higher modes, another issue is present: it is very difficult to magnetize a magnetic thin film in the z direction unless very high fields are applied [43]. Thus, for the same magnetic film thickness, magnetic torque excitation and magnetostrictive actuation produce higher vibrations than magnetic gradient excitation. Brownian motion produces very small oscillation amplitudes in water, making difficult its use for AFM measurements.

Among magnetic methods, the most efficient for high vibration modes is magnetostriction. With this method, it is possible to reach higher efficiencies than with the magnetic gradient or the torque method. The ratio between the oscillation amplitude of the first and second resonance (A_2/A_1) for acoustic, magnetostriction, Brownian motion, magnetic torque and magnetic gradient excitation in water are respectively 1.19, 0.19, 0.08, 0.06 and 0.04.

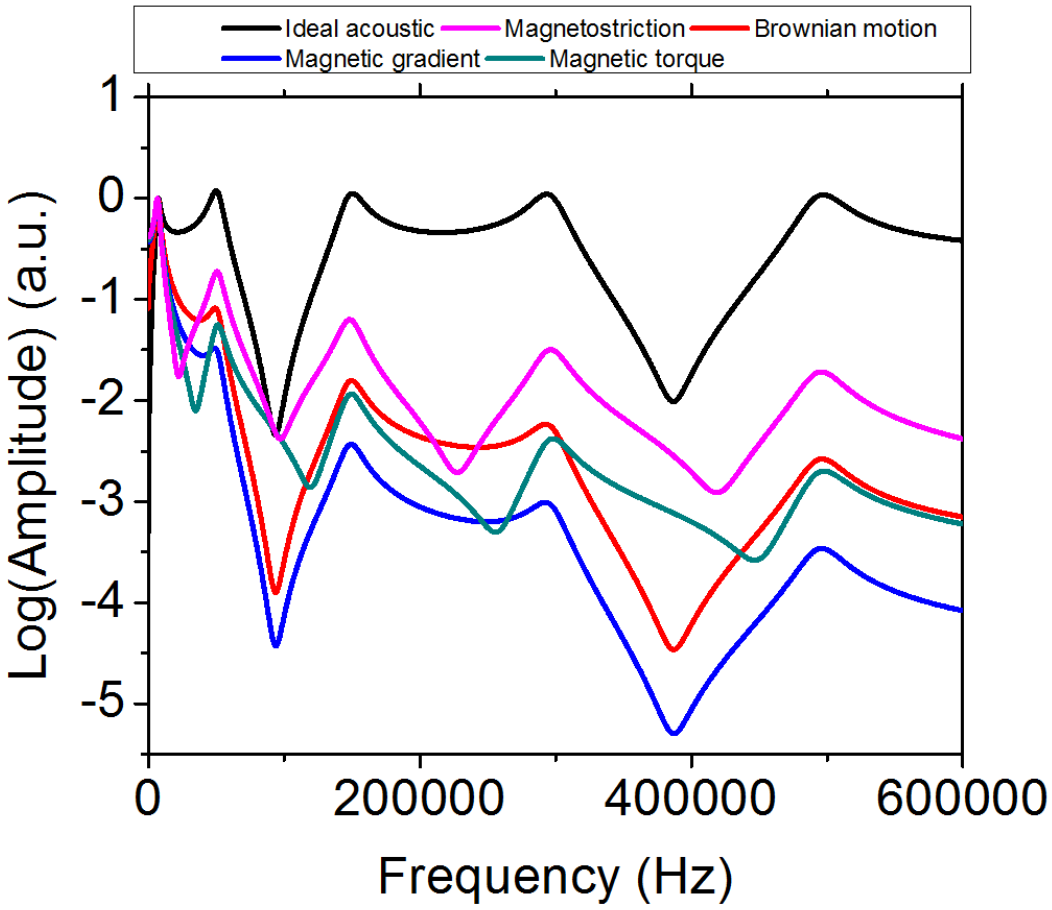

Figure 4.12: Plot in logarithmic scale of the transfer function module of the different excitation methods in water (the first five flexural resonances), normalized to the maximum of each spectra.

When frequency increases, the decreasing rate of the oscillation amplitude for each eigenmode is smaller for magnetostriction than for the other two magnetic methods. In Figure 4.12, the cantilever resonance spectra for the first five resonance modes are shown, where a faster efficiency decrease for magnetic torque and gradient can be noticed.

In addition to the analytical solutions of the equation of motion presented above, we also modeled the movement of the cantilevers for the different actuation cases by means of the finite elements method (FEM) software COMSOL Multiphysics, with the same parameters mentioned above. The results are plotted in Figure 4.13. Proceeding in the same way as in the former case, if we calculate the ratio between the oscillation amplitude of the first and second resonance mode (A_2/A_1) for magnetostriction, Brownian motion and magnetic torque from the data in Figure 4.13 the results are 0.201, 0.082 and 0.052 respectively, in good agreement with the results from analytical analysis shown before. The theoretical and modelling results are summarized in Table 4.1.

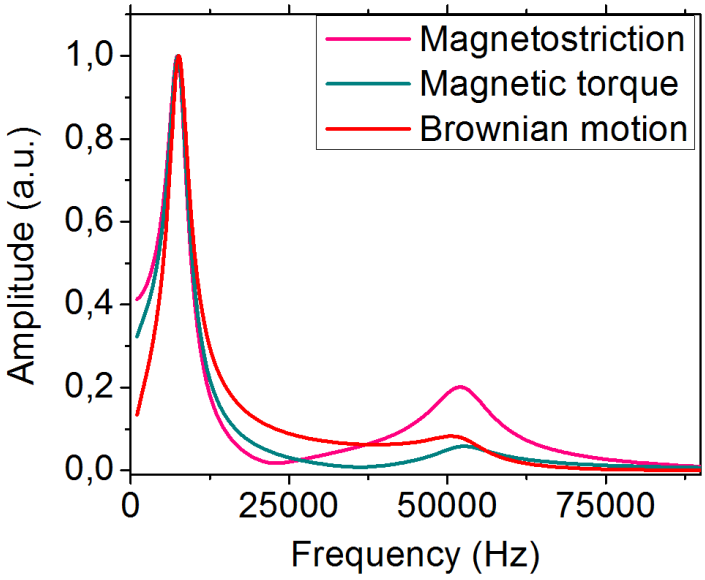

Figure 4.13: Image of the transfer function module of the different excitation methods in water, normalized to the first resonance mode amplitude for each method, obtained by the finite element analysis.

Efficiency ratios	Ideal acoustic	Magne-tostriction	Brownian motion	Magnetic torque	Magnetic gradient
Analytical	1.19	0.19	0.08	0.06	0.04
FEM	-	0.20	0.08	0.05	-

Table 4.1: Analytical and modelling efficiency ratios (A_2/A_1) for the different actuation methods in liquids.

The the efficiency ratio relationship between magnetic torque excitation and magnetostriction as a function of the cantilever dimensions was also studied. As we can see in equations 4.52 and 4.55, the efficiency ratio between the two techniques depends only on the numerators, since the denominators are the same. Furthermore, these numerators depend only on the cantilever length. The efficiency ratio for the i resonance mode can be defined as follows

$$Efficiency\ ratio_i = \frac{A_{i,magnetostriction}/A_{1,magnetostriction}}{A_{i,torque}/A_{1,torque}} = \frac{(\psi_i'(L)-\psi_i'(0))(\psi_1(0)-\psi_1(L))}{(\psi_1'(L)-\psi_1'(0))(\psi_i(0)-\psi_i(L))} \tag{4.59}$$

where $A_{i,magnetostriction}/A_{1,magnetostriction}$ is the amplitude ratio between mode 1 and mode i for magnetostriction, and $A_{i,torque}/A_{1,torque}$ is the same for magnetic torque. An $Efficiency\ ratio_i$ with a value R_i means that the magnetostrictive efficiency for the resonance mode i is R_i times higher than the magnetic torque efficiency for that resonance mode. Due to the fact that the function ψ_i is normalized and from equations 4.15, the last expression can be simplified to

$$Efficiency\ ratio_i = \frac{\psi_i'(L)}{\psi_1'(L)} = R_i \tag{4.60}$$

where $\psi_i'(L)$ is constant regardless of the L value. Thus, the efficiency is length independent and then, independent on the cantilever dimensions. Therefore, the higher efficiency of magnetostriction over magnetic torque is inherent to the actuation method, and independent of the cantilever dimensions: the higher the mode is, the greater will be the difference between the efficiencies of magnetostriction and magnetic torque, as shown in the Table 4.2. Hence, magnetostrictive actuation always leads to higher efficiencies at high resonance modes than magnetic torque actuation.

Mode	1	2	3	4	5
Efficiency ratio	1	3.47	5.70	7.99	10.27

Table 4.2: Efficiency ratios between magnetostriction and magnetic torque.

It is important to highlight that, in addition to high efficiency, the strength of the actuation method is essential to work in liquids. Therefore, it is necessary to study the oscillation amplitudes of both methods. In order to understand this, a FEM modeling was performed to observe the cantilever deflection in response to a static force/strain exerted on the cantilever. Then, as displayed in equation 4.7, the resonance oscillation amplitude will be approximated by $Q\frac{1}{(1-1/4Q^2)^{1/2}}$ times higher than the static deflection. Thus, it is possible to estimate the oscillation amplitude of magnetostrictive and magnetic torque excitation by calculating their static deflection.

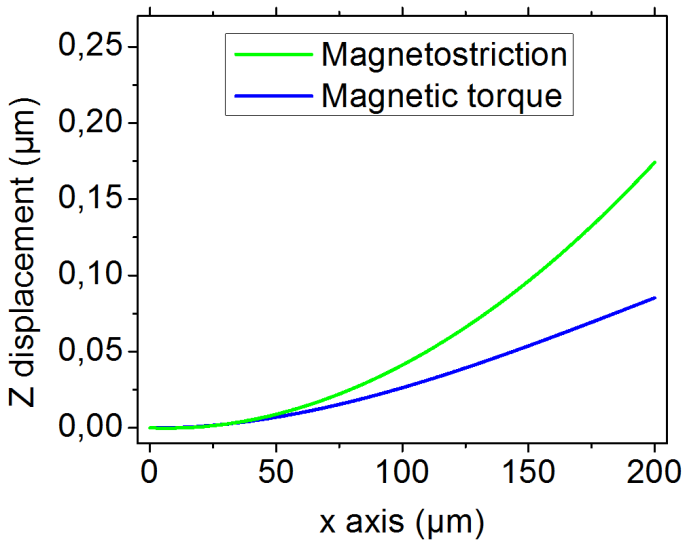

Figure 4.14: Comparison between the profile of a cantilever experiencing a static magnetic torque (blue) and a bending due to a static strain from a magnetostrictive film (green), in a FEM modelling (COMSOL Multiphysics).

In Figure 4.14 it is shown a FEM (COMSOL) analysis of a bent cantilever profile due to a static magnetic force (blue) and due to a static strain from a magnetostrictive film (green). For the magnetic torque approach, the material is considered to be magnetized at its saturation value $M_s = 1.05$ kG (Fe-B-N alloy). Moreover, a magnetic field $B_z = 100$ G perpendicular to the magnetization is applied. For the magnetostrictive actuation, the material magnetization reaches its saturation value and the strain is the magnetostrictive coefficient of Fe-B-N, $\lambda_x =$

30×10^{-6}. These values have been chosen for both actuations as they are the extreme conditions generally used in experimental set-ups. As shown in the figure, magnetostriction reaches higher static deflection than magnetic torque. Therefore, the strength is higher using magnetostrictive actuation, achieving higher oscillation amplitudes.

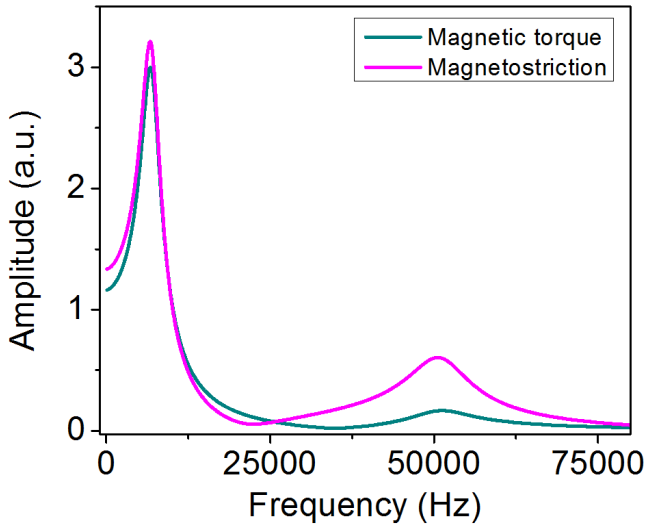

Figure 4.15: Not normalized resonance spectrum of magnetic torque and magnetostriction excitation methods, from the equations presented in section 4.2.3.

This can be also demonstrated by comparing the transfer function of the excitation methods in water as plotted in Figure 4.11 (equations presented in section 4.2.3.), but without normalizing them, and considering the magnetic/magnetostrictive film magnetization saturated ($M_s = 1.05$ kG). Also, a magnetic field $B_z = 100$ G perpendicular to the magnetization is applied for the magnetic torque case. Although the amplitude units are arbitrary, it is possible to compare the amplitude of the curves, since they are plotted in equivalent arbitrary units. In Figure 4.15 it is shown the not normalized magnetic torque and magnetostrictive methods resonance spectrum, showing that the strength of excitation is higher for magnetostrictive actuation than for magnetic torque.

4.5 Discussion

If we look more closely equations 4.46, 4.52 and 4.55 for the three different magnetic excitation techniques, it is possible to understand the underlying physics behind the equations. In the case of the magnetic gradient excitation (as well as Brownian excitation), the oscillation amplitude $C_i(\omega)$ results from the application of a homogeneously distributed force on the cantilever surface. Looking at carefully equation 4.46, the oscillation amplitude $C_i(\omega)$ is proportional to the following expression

$$C_i(\omega) \propto F_{grd}\beta_i = \int_0^L F_{grd}\psi_i(x)dx \tag{4.61}$$

As shown in the equation above, the oscillation amplitude $C_i(\omega)$ is proportional to the integral of the force along the cantilever shape function. The integral of the cantilever shape

function decreases its value at higher eigenmodes, since $\psi_i(x)$ presents positive and negative values, reducing the value of the integral (the first resonance mode is the only one where $\psi_i(x)$ presents only positive values). For that reason, the oscillation amplitude decreases rapidly at higher eigenmodes, showing a low efficiency in the excitation of higher eigenmodes.

Concerning magnetic torque actuation, from equation 4.52 it is possible to infer that the oscillation amplitude $C_i(\omega)$ is proportional to the shape function value at the free end of the cantilever ($\psi_i(0) = 0$ when the cantilever is totally covered by the magnetic layer)

$$C_i(\omega) \propto F_{trq}\psi_i(L) \tag{4.62}$$

This is equivalent to a point force at the free end of the cantilever. As $\psi_i(x)$ functions are normalized, this value will maintain constant for all the eigenmodes, and then, the oscillation amplitude for higher eigenmodes will reduce slower than in the former case (magnetic gradient and Brownian excitation).

In the last case, from equation 4.55 for the magnetostrictive actuation, the oscillation amplitude $C_i(\omega)$ is proportional to the shape function derivative value at the free end of the cantilever ($\psi_i^{'}(0) = 0$ when the cantilever is totally covered by the magnetic layer)

$$C_i(\omega) \propto F_{mgt}\psi_i^{'}(L) \tag{4.63}$$

This excitation technique is equivalent to a point moment at the free end of the cantilever. In contrast to the previous case, the value $\psi_i^{'}(L)$ increases at higher eigenmodes. Therefore, the oscillation amplitude for higher eigenmodes will reduce slower than magnetic torque excitation case. That is the reason why the magnetostrictive actuation is the most efficient method in exciting high vibration modes.

4.6 Experimental results

In order to validate the theoretical and modelling results, measurements of Brownian motion, magnetic torque and magnetostrictive excitation were performed in water for the same cantilever. We discarded magnetic gradient excitation due to the difficulty to magnetize the deposited film in the cantilever in the z direction. Also, it is worth saying that we did not perform the acoustic experiment since it produces a "forest of peaks" that makes resonance recognition difficult.

Figure 4.16 shows an example of an experimental resonance spectra of a cantilever coated with a magnetostrictive film. Each curve is normalized to the amplitude of the first resonance mode. The deposition conditions can be found in section 2.2. A cantilever with a length of 200 μm, width of 40 μm and thickness of 0.8 μm, from Olympus [74], was used. The thickness of the magnetostrictive film is 50 nm. We used a Nanotec Electrónica [73] microscope to perform the magnetostrictive and magnetic torque measurements, with a set-up including a electromagnet to produce the external applied magnetic field. The magnetic field **B** direction with respect to the cantilever surface plane was changed in order to excite torque (perpendicular) or magnetostriction (parallel), fixing the cantilever magnetostrictive film magnetization along the cantilever long axis with a permanent magnet in the case of the magnetic torque actuation. To perform the Brownian measurements, a Multimode microscope from the Bruker company has been used, a Nanoscope V. In Figure 4.16, we can see that among the plotted methods, magnetostrictive actuation is the most efficient in exciting the second resonance. The ratios between amplitude of the first and second resonance (A_2/A_1) are 0.905, 0.277 and 0.208 for magnetostrictive, magnetic torque and Brownian excitation, respectively.

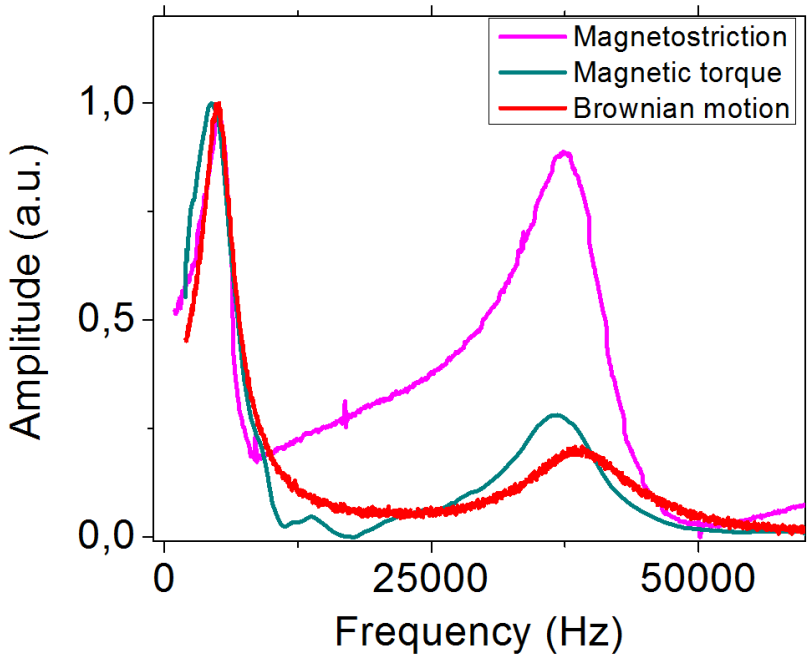

Figure 4.16: Experimental cantilever resonance spectra for cantilevers excited by means of magnetostriction (pink), Brownian force (red) and magnetic torque (gren). The spectra are normalized to the maximum of the first resonance mode.

Efficiency ratios	Ideal acoustic	Magne-tostriction	Brownian motion	Magnetic torque	Magnetic gradient
Analytical	1.19	0.19	0.08	0.06	0.04
FEM	-	0.20	0.08	0.05	-
Experimental	-	0.25	0.06	0.08	-

Table 4.3: Theoretical and experimental efficiency ratios (A_2/A_1) for the different actuation methods in liquids.

As mentioned in section 4.3, we have to take into account that the photodiode signal corresponds to the cantilever slope at its free end. This slope is higher in the second resonance, overestimating 3.47 times the amplitude of the second resonance. Thus, dividing by 3.47 the ratio factors, the corrected ratios for magnetostriction, magnetic torque and Brownian excitation are 0.25, 0.08 and 0.06, in good agreement with the theoretical predictions. However, as shown in next chapter, these ratio factors can be even higher when the magnetostrictive coating is modified. The results from the analytical solution, the FEM modeling and the experiments are summarized in Table 4.3.

In order to check the performance of commercial magnetic cantilevers, we repeated the experiments for magnetostrictive and magnetic torque actuation with a MAC Lever Type VII from Agilent ($125 \times 35 \times 0.8$ μm, silicon with a constant force of k = 0.14 N/m). The resonance spectra for three cantilevers were acquired in air and in water, comparing the resulting efficiencies when the cantilever is excited magnetostrictively or by means of magnetic torque actuation.

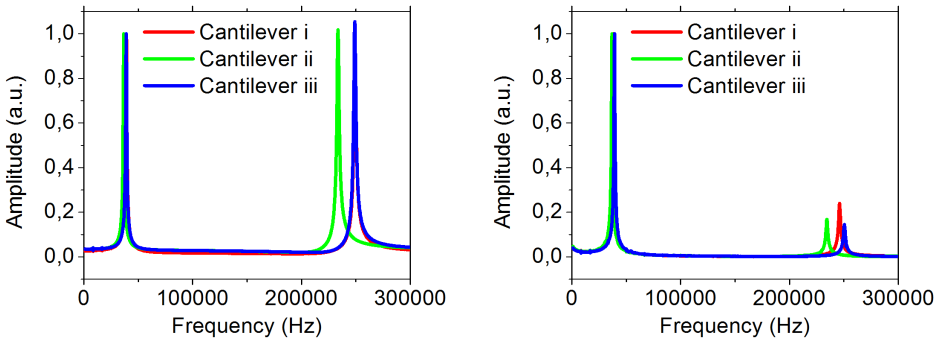

Figure 4.17: Experimental cantilever resonance spectra obtained by means of magnetostrictive (a) and magnetic torque (b) actuation ir air (MAC Lever Type VII) normalized to the first resonance mode amplitude for each method.

In Figure 4.17, the cantilever resonance spectra in air are represented. Although these magnetic commercial cantilevers are prepared to be used in magnetic torque actuation, the results show that these cantilevers exhibit also a good magnetostrictive performance. The graph displays that magnetostrictive actuation presents higher efficiency in the excitation of the second resonance mode, confirming our theoretical calculations. The different spectra efficiency results are summarized in Table 4.4, as well as the theoretical efficiency values calculated by means of the analytical models previously discussed. The correcting factor 3.47 due to the beam deflection measurement set up was applied to the calculated efficiency ratios.

	Magnetostriction			Torque		
Cantilever	i	ii	iii	i	ii	iii
Experimental efficiency	0.263	0.293	0.303	0.069	0.048	0.042
Theoretical efficiency	0.243			0.070		

Table 4.4: Theoretical and experimental efficiency ratios (A_2/A_1) for the magnetostrictive and magnetic torque actuation in air (MAC Lever Type VII).

The same experimental study was repeated in water environment. The resulting experimental resonance spectra are represented in Figure 4.18.

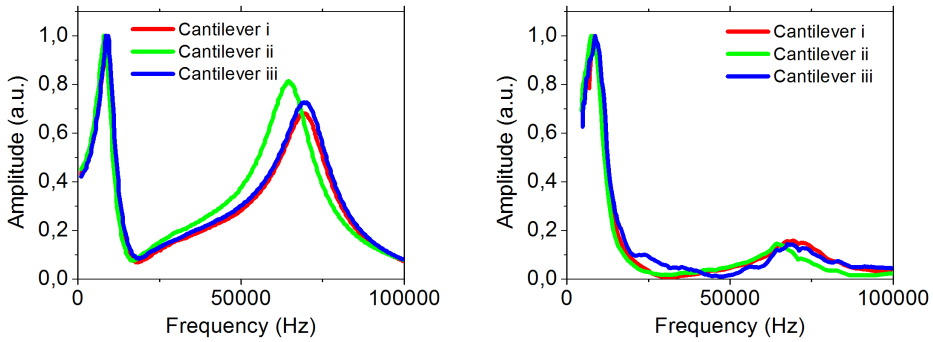

(a) (b)

Figure 4.18: Experimental cantilever resonance spectra obtained by means of magnetostrictive (a) and magnetic torque (b) actuation in water (MAC Lever Type VII) normalized to the first resonance mode amplitude for each method.

As expected, the efficiency is much higher for magnetostrictive actuation than for magnetic torque actuation. The efficiency values are displayed in Table 4.5

	Magnetostriction			Torque		
Cantilever	i	ii	iii	i	ii	iii
Experimental efficiency	0.195	0.233	0.210	0.045	0.042	0.041
Theoretical efficiency	0.195			0.057		

Table 4.5: Theoretical and experimental efficiency ratios (A_2/A_1) for the magnetostrictive and magnetic torque actuation in water (MAC Lever Type VII).

Those results validate the theoretical and modeling results, proving the suitability of magnetostrictive cantilever actuation for exciting higher modes. These results are also confirmed when commercial cantilevers are used, even though their coating has not been specifically selected for its magnetostrictive properties. Both, Fe-B-N coated cantilevers and commercial MAC Levers excite high resonance modes more efficiently when they are actuated magnetostrictively.

4.7 Conclusions

Summarizing, a theoretical study for the different actuation methods was performed: acoustic, magnetic gradient, Brownian, magnetic torque and magnetostrictive. Acoustic excitation is the most efficient, but in a real case, resonance frequencies are hidden behind a ”forest of peaks” that may complicate its operation in liquid environments.

When comparing the rest of the actuation techniques, it is clearly shown that magnetostriction is more efficient when exciting higher modes. In all these magnetic field based methods, a coil needs to be implemented in the set-up in order to create the magnetic field from an applied current, leading to high impedance in the coil at high frequencies. For this reason, the actuation efficiency at high frequencies is extremely important. Thus, it is recommended to use magnetostrictive actuation in order to ensure the efficiency, as it can reach higher oscillation amplitudes at higher frequencies. Furthermore, high eigenmodes improve the Q factor and the mass sensing resolution in resonant micromechanical sensors. Hence, magnetostrictive actuation is also suitable for them.

The high efficiency in the excitation of the cantilever high resonance modes is independent on the cantilever dimensions. In addition to being more efficient in the excitation of higher resonance modes, this method achieves oscillation amplitudes larger than magnetic torque. And as we shall see in the next chapter, by tailoring the magnetic coating area of the cantilever, a particular resonance mode can be enhanced.

Chapter 5

Selective enhancement of individual cantilever resonance modes

Due to its outstanding performance in liquids, magnetic excitation methods have became widely used in AFM. However, several issues such as the high coil impedances in the high frequency regime (where the high modes lie) still need to be overcome. It is, therefore, essential to find an efficient method to excite these high resonances. Both, in AFM and micromechanical sensors, it is also crucial to minimize the intensity of the applied currents to avoid undesired thermal effects and drifts in the AFM sample area. As shown in the previous chapter, among all magnetic methods, magnetostrictive actuation is the most efficient at exciting high resonance modes. When a magnetic field is applied parallel to the film plane, the cantilever excitation will have mainly a magnetostrictive component. In an opposite way, when a magnetic film is applied in a perpendicular direction to the cantilever surface, the magnetic torque excitation is produced.

In this chapter, an original method to selectively enhance the oscillation amplitude of individual eigenmodes will be shown. It consists in the patterning of specific areas of the magnetostrictive coating. Theoretical and experimental studies of the high resonance modes enhancement by selective etching of the magnetostrictive coating layer will be discussed. The magnetostrictive coating could be patterned, in principle, by adequate lithographic methods: using resist masks, chemical etching or deposition through shadow masks but, in our case, in order to use the already coated cantilevers, we employed the Focused Ion Beam tool (FIB, iLine equipment from Raith). Obviously, this is an expensive and slow patterning method to be used in an industrial production process, but it is the most convenient for us to carry out this exploratory study. We have focused in commercial MAC levers for two reasons. Firstly, to demonstrate that they can be magnetostrictively actuated in our AFM liquid cell. And secondly, because they are more reachable than the ones coated with Fe-B-N, since they are commercially available.

Another original way to perform such eigenmode amplitude enhancement is based on the effect of locally modifying the magnetic properties of the film such as magnetic anisotropy, coercivity and its magnetostriction coefficient by in depth ions implantation at selected areas of the magnetostrictive coating. This method consists in modifying the layer magnetic properties without the need of etching it away and the idea has been successfully demostrated by a previous worked performed in our research Institute with other ions implantation (N^+, P^+, As^+). The objective in that case was to nanopattern magnetic recording media [105]. Available Ga^+ ions and implantation energy (30 keV) in our iLine FIB equipment are probably not optimum for the cantilever magnetostrictive thin films, but according to the following preliminary modeling and experimental study, they are good enough to explore the validity of the method. In particular,

using low dose implantation instead of high dose ion etching will not modify the mechanical characteristics of the cantilevers, allowing for a more precise analysis of the high mode resonances and comparison with standard non patterned AFM cantilevers. After presenting the model calculations results in the following section, some experimental examples of high modes oscillation amplitude enhancement will be shown for different patterned and implanted AFM cantilever types, when operating both air and liquid.

5.1 Theoretical study

The most efficient magnetic excitation methods for AFM operation in liquid environments, previously introduced in last chapter, are based in magnetostriction and magnetic torque actuation. The transfer functions for magnetostriction and magnetic torque actuation deduced were, respectively

$$\frac{C_i(\omega)}{F_{mgt}} = \frac{\psi_i^{'}(x_2) - \psi^{'}(x_1)}{EI\left(\frac{\lambda_i}{L}\right)^4 \alpha_i L - \omega^2\left(\rho A + \frac{\pi}{4}\rho_f b^2 \Gamma_{rect}\right)\alpha_i L} \tag{5.1}$$

$$\frac{C_i(\omega)}{F_{trq}} = \frac{(\psi_i(x_1) - \psi_i(x_2))}{EI\left(\frac{\lambda_i}{L}\right)^4 \alpha_i L - \omega^2\left(\rho A + \frac{\pi}{4}\rho_f b^2 \Gamma_{rect}\right)\alpha_i L} \tag{5.2}$$

where x_1 and x_2 ($x_2 > x_1$) are the positions on the magnetic layer edges. When the cantilever is completely covered by the magnetic layer (Figure 5.1), $x_1 = 0$ and $x_2 = L$. If the cantilever is not completely covered, the contributions of the different coated areas must be added. In the next sections, a study for different kinds of cantilevers will be presented. The mass loss due to the etching of the layer will not be considered in the model. This mass removal will just slightly shift the frequency of the resonance modes, with negligible effect in the oscillation amplitude relationships between the different resonance modes.

From equations 5.1 and 5.2, the transfer function spectra for magnetostriction and magnetic torque can be theoretically calculated. The theoretical oscillation amplitude ratio between the first mode over higher modes for magnetostriction and magnetic torque actuation in air and liquid are summarized in Table 5.1. These data corresponds to a CSC38/Al BS lever from Mikromasch [23] ($350 \times 35 \times 1$ μm, silicon with a constant force of k = 0.03 N/m) completely covered with 50 nm of Fe-B-N. As expected, the most efficient method is magnetostriction.

	Air		Liquid	
Mode	Magnetostriction	Torque	Magnetostriction	Torque
1^{st}	1.000	1.000	1.000	1.000
2^{nd}	0.267	0.076	0.167	0.052
3^{rd}	0.098	0.017	0.054	0.010

Table 5.1: Oscillation amplitude ratios between the first mode over higher modes for magnetostriction and magnetic torque for a CSC38/Al BS cantilever.

As can be inferred from equations 5.1 and 5.2, the coating area effect in the magnetic torque and magnetostrictive actuation depends on the evaluation of the shape function ($\psi_i(x)$) and its derivative ($\psi_i^{'}(x)$) at the edges of the film, respectively.

In the common configuration where the cantilever is completely covered by the film (Figure 5.1), the magnetic layer edges are the clamping ($x_1 = 0$) and the free end ($x_2 = L$). From now on, this will be labelled as *Configuration 1.*

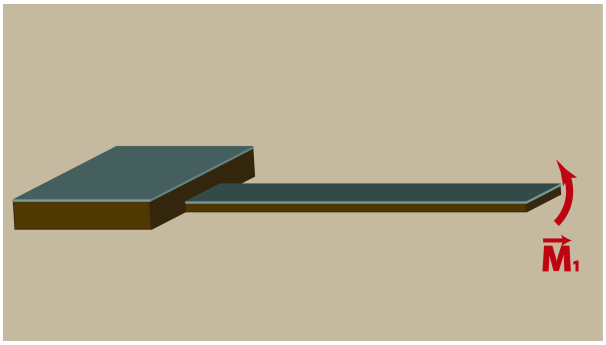

Figure 5.1: Standard configuration of the magnetic film (green layer on the cantilever) on a cantilever for AFM, where $x_1 = 0$ and $x_2 = L$ (*Configuration 1*).

In order to enhance a particular i resonance mode oscillation amplitude for cantilevers excited by magnetostrictive actuation, the expression $\psi_i'(x_2) - \psi_i'(x_1)$ must be maximized. Therefore, we have to choose x_2 where $\psi_i'(x_2)$ reaches the maximum value and x_1 where $\psi_i'(x_1)$ reaches the minimum value or vice-versa, since the amplitude is related to the module of the transfer function. In the right graph of Figure 5.2, the first mode oscillation amplitude maximization corresponds to $x_1 = 0$ and $x_2 = L$ (values that maximize the numerator of equation 5.1), i.e., when the cantilever is totally covered (Figure 5.1, named *Configuration 1*).

On the second mode, the maximum value is achieved when choosing $x_1 = a$ and $x_2 = L$ (Figure 5.3a, from now on labelled *Configuration 2*), since $x = a$ and $x = L$ are the minimum and the maximum value of $\psi'(x)$, respectively.

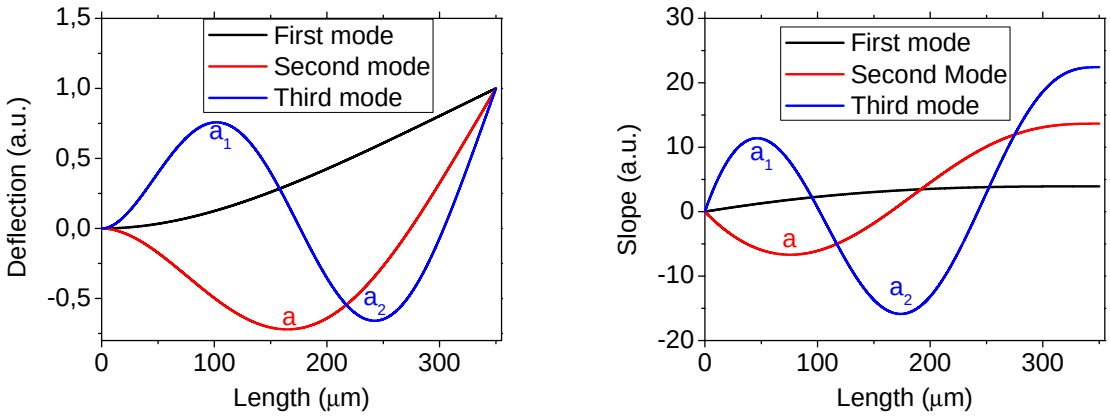

Figure 5.2: Shape function $\psi_i(x)$ (left) and derivative shape function $\psi_i'(x)$ (right) of the three first shape modes of a cantilever (CSC38/Al BS).

Finally, on the third mode, we have to divide the coated region in two areas: the first one from the clamping $x_{1,1} = 0$ to $x_{1,2} = a_1$ and from $x_{2,1} = a_2$ to the free end $x_{2,2} = L$ (Figure 5.3b, from now on named *Configuration 3*). It will be possible to choose just one area from $x = a_1$ to $x = a_2$, but the total $\psi_i'(x_2) - \psi_i'(x_1)$ value will be lower:

$$(\psi'(a_1) - \psi'(0)) + (\psi'(L) - \psi'(a_2)) > \psi'(a_2) - \psi'(a_1) \tag{5.3}$$

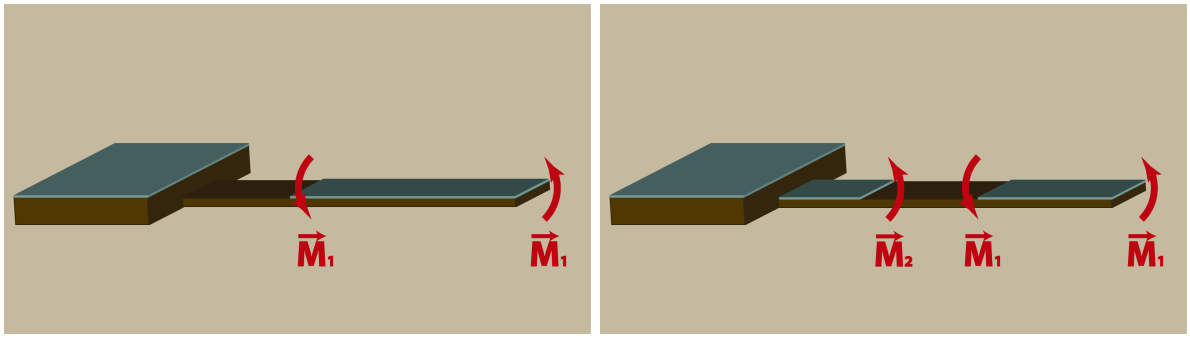

(a) *Configuration 2* (b) *Configuration 3*

Figure 5.3: Configuration to enhance the second (a) and the third (b) modes. The magnetostrictive film is coloured in green on the figures.

We will compare these three different configurations for magnetostriction and evaluate how these coating changes may affect the high modes resonance excitation efficiency and oscillation amplitude:

- *Configuration 1*: magnetostrictive film over the entire surface of the cantilever (Figure 5.1).
- *Configuration 2*: magnetostrictive film over an area next to the tip of the cantilever (Figure 5.3a) to enhance the second resonance mode.
- *Configuration 3*: magnetostrictive film divided in two areas of the cantilever surface (Figure 5.3b), to enhance the third resonance mode.

The results from the calculation performed on a CSC38/Al BS cantilever, with a=75.79 μm in *Configuration 2*, and a_1 =46.30 μm and a_2 =173.75 μm in *Configuration 3* are displayed in Figure 5.4.

In Figure 5.4 the calculated transfer functions for each configuration are compared. The spectra are normalized to the amplitude of the *Configuration 1* first mode. Thus, it is possible to compare the oscillation amplitude increment or decrement of the different resonance modes respect to the amplitude of the first resonance mode. *Configuration 2* and *Configuration 3* enhance the second and the third resonance modes respectively as compared to the *Configuration 1*. Although the amplitude of the first resonance mode is decreased with respect to *Configuration 2* and *Configuration 3*, the amplitude increment of the second and third modes is more important. These modes are at higher frequencies and then, they are more difficult to excite due to the higher coil impedance. Hence, in *Configuration 2* and *Configuration 3* the second and third mode are more efficiently excited. Thus, higher oscillation amplitudes are attained applying the same current through the coil.

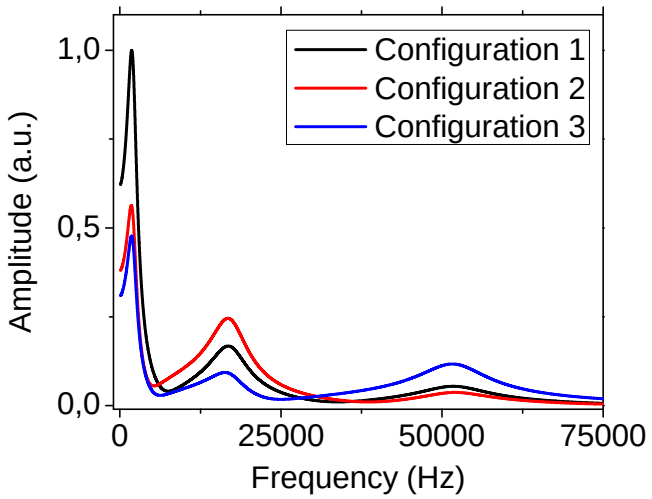

Figure 5.4: Resonance spectra for different configurations of the magnetostrictive film in water (commercial cantilever CSC38/Al BS). *Configuration 1* is plotted in black, *Configuration 2* in red and *Configuration 3* in blue, normalized to the amplitude of the first mode of the *Configuration 1*.

In Table 5.2, we can see the oscillation amplitude ratio among the different configurations for each resonance mode, normalized to the amplitude of the *Configuration 1* first mode.

Mode	Configuration 1	Configuration 2	Configuration 3
1^{st}	1.000	0.563	0.477
2^{nd}	0.167	0.245	0.093
3^{rd}	0.054	0.037	0.117

Table 5.2: Oscillation amplitude ratios among the different configurations for each resonance mode, normalized to the amplitude of the first mode of the *Configuration 1* for magnetostriction in water (commercial cantilever CSC38/Al BS).

It is shown in Table 5.2 that the second and third resonance mode oscillation amplitude can be increased using this etching method. To excite modes higher than the third, we should proceed in a similar way, studying the shape function derivative of these modes and etching the magnetostrictive film in the specific areas which maximize the transfer function.

An equivalent study was performed for the magnetic torque actuation. However, in this case the $\psi(x)$ function was evaluated instead of $\psi^{'}(x)$ function (equations 5.1 and 5.2). Here, the maximized parameters used are a =164.78 μm in *Configuration 2*, and a_1=101.92 μm and a_2 =242.32 μm in *Configuration 3*.

In Figure 5.5 the resonance spectra for the three configurations are shown. The oscillation amplitude ratios among the different configurations for each resonance mode are summarized in Table 5.3, normalized to the amplitude of the first mode of the *Configuration 1*.

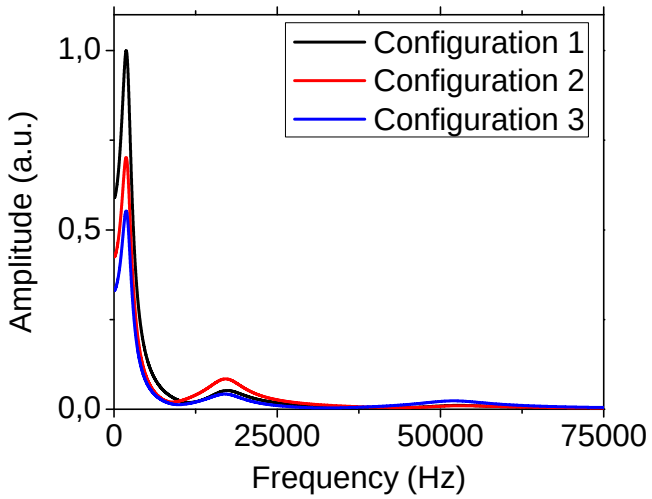

Figure 5.5: Resonance spectra for magnetic torque in water for the different configurations of the magnetic film (commercial cantilever CSC38/Al BS). *Configuration 1* is plotted in black, *Configuration 2* in red and *Configuration 3* in blue.

Mode	Configuration 1	Configuration 2	Configuration 3
1^{st}	1.000	0.702	0.552
2^{nd}	0.052	0.084	0.042
3^{rd}	0.010	0.009	0.023

Table 5.3: Oscillation amplitude ratios among the different configurations for each resonance mode, normalized to the amplitude of the first mode of the *Configuration 1* for torque in water.

Similarly to magnetostrictive actuation, it is possible to enhance a particular mode for magnetic torque. However, the efficiency of the magnetic torque is much lower than the magnetostrictive actuation.

We have repeated the same theoretical study for magnetostriction in a MAC Lever Type VII from Agilent [106] ($125 \times 35 \times 0.8$ μm, silicon with a constant force of k = 0.14 N/m) for the magnetostrictive actuation, since experimental results when using MAC Levers showed a good performance for magnetostrictive actuation. The magnetic layer deposited in these cantilevers presents good magnetostrictive properties. From the shape function derivative $\psi_i'(x)$ of the three first shape modes, we obtained the optimized parameters a =27.06 μm in *Configuration 2*, and $a_1 = 16.53$ μm and $a_2 = 62.05$ μm in *Configuration 3*. In the left image of Figure 5.6, the resonance spectra are displayed for the three configurations, showing a similar enhancement of higher eigenmodes amplitude for *Configuration 2* and *3* than the former case.[1].

[1]As we do not know the MAC Lever coating properties, we have used as an input for the calculations the Fe-B-N parameters. The magnetostrictive properties only affect the actuation strength, not the ratio among the resonance amplitudes. Furthermore, the points a, a_1 and a_2 are independent form the magnetostrictive properties.

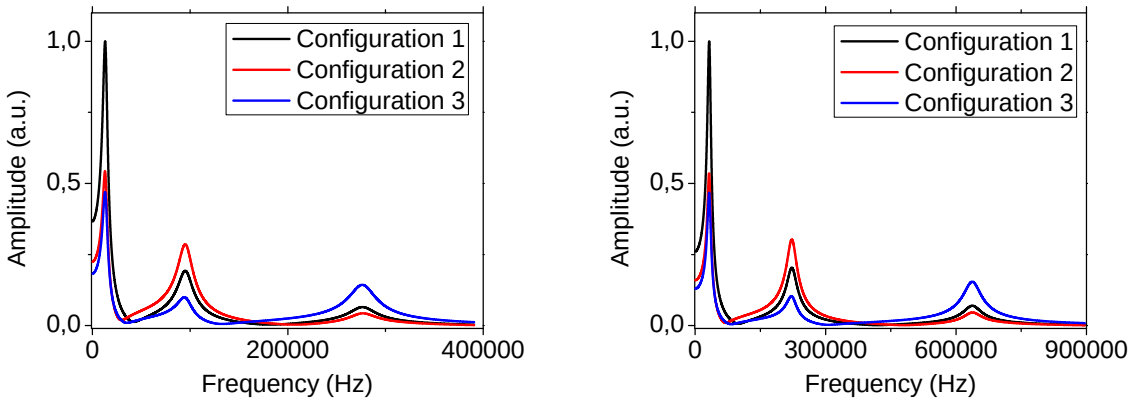

Figure 5.6: Resonance spectra for different configurations of the magnetostrictive film in water for MAC Lever Type VII (left) and Type II (right). *Configuration 1* is plotted in black, *Configuration 2* in red and *Configuration 3* in blue, normalized to the oscillation amplitude of the first mode of the *Configuration 1*.

Finally, the same study for a MAC Lever Type II from Agilent [106] (225 × 30 × 3 μm, silicon with a constant force of k = 2.8 N/m) was performed, for magnetostrictive actuation. The optimized parameters in this case are a =48.71 μm in *Configuration 2*, and a_1=29.7 μm and a_2=111.69 μm in *Configuration 3*. The resonance spectra for the three configurations are shown in the right image of Figure 5.6. The second and third mode oscillation amplitude are enhanced as well.

5.2 Magnetostrictive film etching for high resonance modes efficiency enhancement

In this section, a new method for the efficiency enhancement of a cantilever specific mode is experimentally shown. For this purpose, the magnetostrictive film on the cantilever is etched by means of the FIB technique. Instead of the focused electron beam that SEM uses for imaging a sample, FIB uses a focused ion beam. Moreover, FIB can be operated at low beam currents for imaging or high beam currents for site specific sputtering or etching. Also, FIB can be used to implant ions inside a specific material. In our case, FIB operates with gallium ions (Ga^+) at an accelerating voltage of 30 keV. Thus, by means of the FIB etching technique, the theoretical results that were presented in the previous section will be experimentally confirmed: the high resonance mode excitation efficiency and oscillation amplitude increase by selective patterning of the magnetostrictive layer.

All the resonance spectra in this chapter were performed in a Nanotec Electrónica AFM [73]. The cantilever resonance spectra before and after the etching will be compared. The efficiency of each mode is calculated as usual, the oscillation amplitude ratio between the mode of interest and the first one (A_i/A_1).

5.2.1 FIB calibration

Figure 5.7 shows the etching calibration results for Fe-B-N and the commercial MAC Mode Levers coating. The Fe-B-N film nominal thickness on the used cantilevers was 50 nm. The

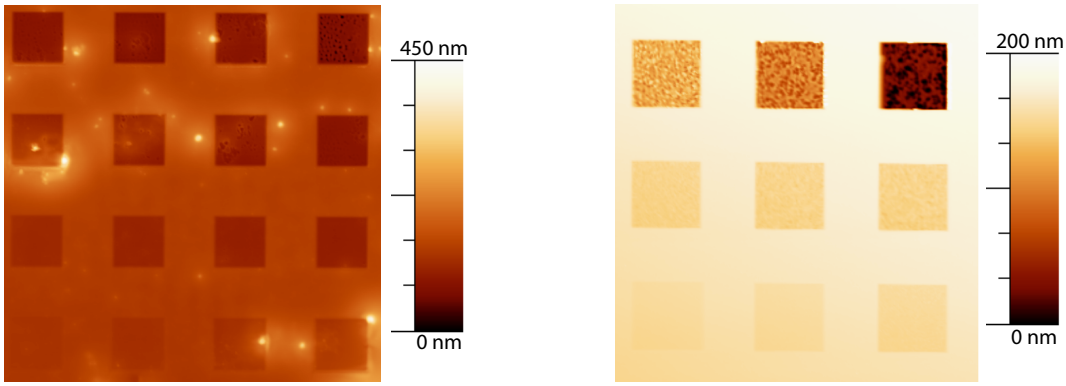

Figure 5.7: AFM images of an array of 5×5 μm square patterns for different FIB etching conditions on Fe-B-N (left) and MAC Lever Type VII (right) on the chip.

commercial MAC Mode Levers coating composition and thickness were originally unknown. A film thickness of $90-100$ nm was measured from SEM cantilever cross sections. The calibration was carried out in the cantilever chip. To find the optimal parameters that remove totally the magnetostrictive film from the cantilever surface, different etching conditions in an array of 5×5 μm squares were tested, as displayed in Figure 5.7.

The optimal conditions for the complete Fe-B-N and MAC lever magnetic film etching are the following: a total dose $D = 20000$ μC/cm^2 (5 loops of $D_{loop} = 4000$ μC/cm^2 to avoid material re-deposition) and a current of $I = 39$ pA with a beam aperture of $A = 40$ μm. These etching parameters were used in CSC38/Al BS cantilevers coated with Fe-B-N and MAC Levers Type II and VII.

Examples of partial etching for different configurations in a MAC Lever Type VII are shown in Figure 5.8. The etching area is different, depending on the mode to enhance, as calculated in the previous section.

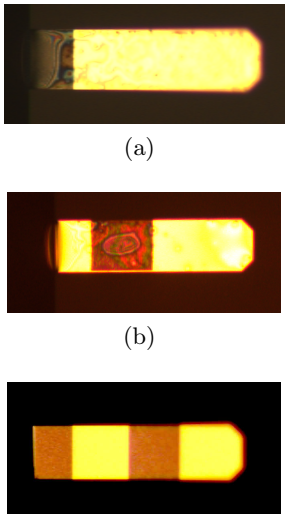

(a)

(b)

(c)

Figure 5.8: MAC Lever Type VII cantilever after FIB etching in order to enhance the oscillation amplitude of the second (a), third (b) or fourth (c) resonance mode.

5.2.2 Experimental results

In this section, the experimental enhancement of the cantilever specific mode efficiency by selective removal of the cantilever coating is presented. The etched area for each cantilever type and resonance mode was shown in section 5.1. Here, we will compare the cantilever resonance spectra after and before the FIB selective etching. The cantilever was placed in the same position in the liquid cell (Figure 3.11a) before and after the etching, and the same driving current was applied to the coils in all the experiments, 100 mA_{pp}, except in the case of the MAC Type II cantilevers in water, where the driving current was 350 mA_{pp}. By means of a permanent magnet, a constant magnetic field was applied to each cantilever before performing a resonance spectra (along the long axis) in order to carry out the experiments at the same initial film magnetization. Hence, it is possible to compare the cantilever oscillation amplitude after and before the film etching since the same initial conditions are maintained.

Low force constant cantilevers (commercially coated)

In Figure 5.9, experimental cantilever resonance spectra before and after the FIB etching for a MAC Lever Type VII (k = 0.14 N/m) in air are displayed. In the resonance spectra, the left axis corresponds to the oscillation amplitude of the first resonance mode (first peak in the image), while the right axis is the oscillation amplitude of the second mode (second peak in the figure), with the overestimation correction due to the beam deflection detection technique (divided by 3.47, section 4.3). Henceforth, the oscillation amplitude for the different resonance modes will be presented in this way: on the left axis will be displayed the oscillation amplitude of the first resonance mode (first peak), while the right axis displays the oscillation amplitude of the second, third or fourth resonance mode (second, third or fourth peak), depending on which resonance mode is desired to increase.

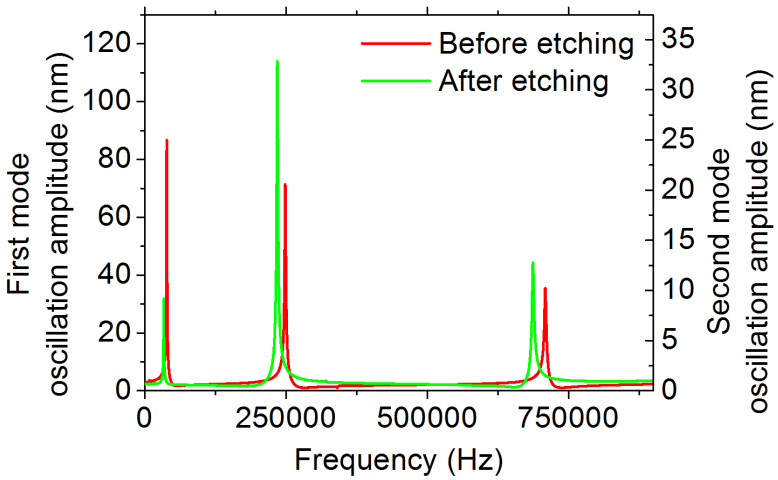

Figure 5.9: Experimental cantilever resonance spectra in air before and after etching the area to enhance the second mode oscillation amplitude (MAC Lever Type VII, k = 0.14 N/m).

As it is shown in Figure 5.9, the second mode oscillation amplitude rises from 20 nm before the etching to 32 nm after the etching (an increment of 59 %). Also, as expected, the oscillation amplitude of the first resonance mode is decreased. It can be noticed that the resonance frequencies are shifted down. This is because the mass removal, located near the clamping, implies a decrease of the effective cantilever stiffness [107, 108].

In Table 5.4, examples for other two MAC Type VII cantilevers (cantilever **a** corresponds

to the example shown in Figure 5.9) in air are shown. All of them exhibit an increase of the second mode oscillation amplitude.

	Efficiency A_2/A_1		Oscillation amplitude (nm)		
Cantilever	Before	After	Before	After	Oscillation increment (%)
a	0.24	1.03	20.57	32.82	59
b	0.38	0.77	24.11	29.70	23
c	0.26	0.88	13.95	41.85	200

Table 5.4: Second mode oscillation amplitudes (MAC Levers Type VII) in air before and after the etching.

An example of the third mode oscillation amplitude enhancement for the MAC Type VII lever in air is displayed in Figure 5.10. The third mode oscillation amplitude rises from 8 nm before the etching to 15 nm after the etching, almost duplicating the oscillation amplitude. Again, the first mode oscillation amplitude is decreased.

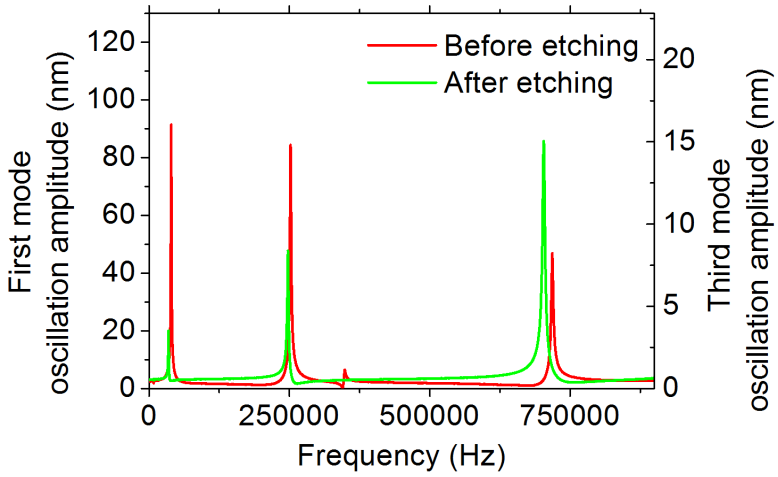

Figure 5.10: Experimental cantilever resonance spectra in air before and after etching the area to enhance the third mode oscillation amplitude (MAC Lever Type VII, k = 0.14 N/m).

Other examples for two MAC Type VII cantilevers are presented in Table 5.5 (cantilever **a** corresponds to the example shown in Figure 5.10), where all the cantilevers display an enhancement of the third mode oscillation amplitude.

	Efficiency A_3/A_1		Oscillation amplitude (nm)		
Cantilever	Before	After	Before	After	Oscillation increment (%)
a	0.09	0.75	8.22	15.04	83
b	0.08	0.83	10.17	15.30	50
c	0.09	0.88	9.97	13.65	37

Table 5.5: Third mode oscillation amplitudes (MAC Levers Type VII) in air before and after the etching.

Finally, in Figure 5.11 it is presented the oscillation amplitude enhancement for the fourth resonance mode (MAC Lever Type VII) lever in air. Two areas of the thin film were removed, as

shown in Figure 5.8c: the fist area from the clamping to the position 26.22 μm and the second area from the position 62.72 μm to 98 μm. As depicted in the figure, the oscillation amplitude is greatly increased, from 2 nm to 8 nm.

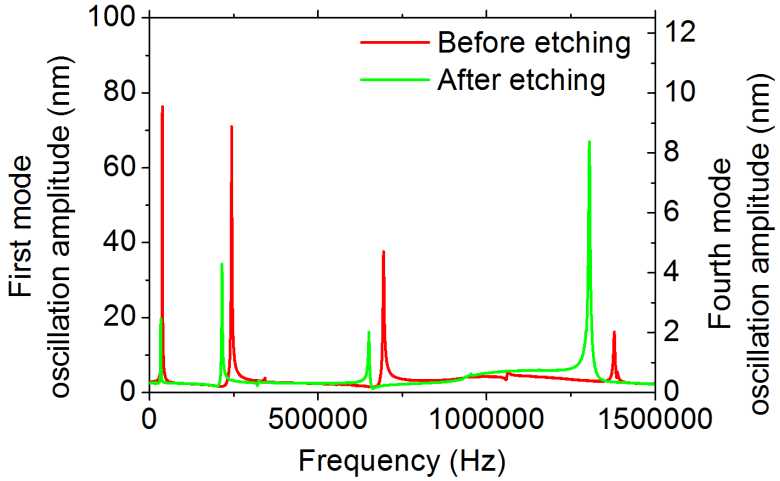

Figure 5.11: Experimental cantilever resonance spectra in air before and after etching the area to enhance the fourth mode oscillation amplitude (MAC Lever Type VII, k = 0.14 N/m).

In order to confirm in liquids the previous oscillation amplitude enhancements obtained in air, 3 resonance spectra from different MAC Type VII cantilevers before the etching were compared to 3 resonance spectra after the etching. We do not compare the same cantilever before and after the etching because it is difficult to etch properly the magnetostrictive film once the cantilever has been previously introduced in water. The resonance spectra for the second mode enhancement in water are shown in Figure 5.12, and the cantilever second mode oscillation amplitudes are summarized in Table 5.6.

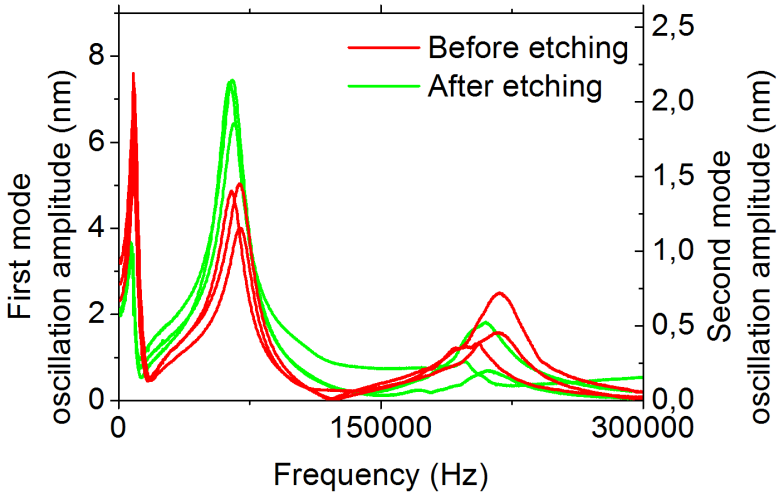

Figure 5.12: Different cantilever experimental resonance spectra in water before and after etching the area to enhance the second mode oscillation amplitude (MAC Lever Type VII, k = 0.14 N/m).

As shown in Table 5.6 and in Figure 5.12, the cantilever oscillation amplitude is always larger in the etched cantilever than in the completely covered ones (before etching). This demonstrate

that the etching induces an increase of the second resonance mode oscillation amplitude also in liquid environments.

	Before			After		
Cantilever	a	b	c	d	e	f
Oscillation amplitude (nm)	1.16	1.45	1.40	1.86	2.14	2.13

Table 5.6: Second mode oscillation amplitudes (MAC Levers Type VII) in liquid before and after the etching.

The former experiment was repeated for the third resonance enhancement in liquids. The resulting spectra are presented in Figure 5.13, and the oscillation amplitudes are summarized in Table 5.7.

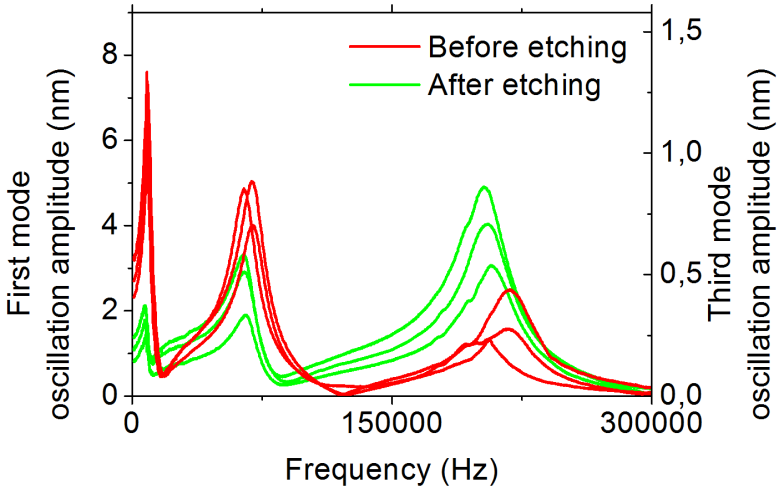

Figure 5.13: Different cantilever experimental resonance spectra in water before and after etching the area to enhance the third mode oscillation amplitude (MAC Lever Type VII, k = 0.14 N/m).

As in the second resonance enhancement case, the etched cantilevers present higher oscillation amplitude than the totally covered ones, confirming the enhancement of this particular resonance mode.

	Before			After		
Cantilever	a	b	c	d	e	f
Oscillation amplitude (nm)	0.44	0.28	0.24	0.86	0.71	0.54

Table 5.7: Third mode oscillation amplitudes (MAC Levers Type VII) in liquid before and after the etching.

Medium force constant cantilevers (commercially coated)

The study presented above was repeated for cantilevers with higher force constant. Specifically, MAC Levers Type II were used. An example for the second mode enhancement is presented in Figure 5.14, where the oscillation amplitude of the second mode rises up from 3.7 nm before the etching to 8.1 nm after the etching, duplicating the oscillation amplitude.

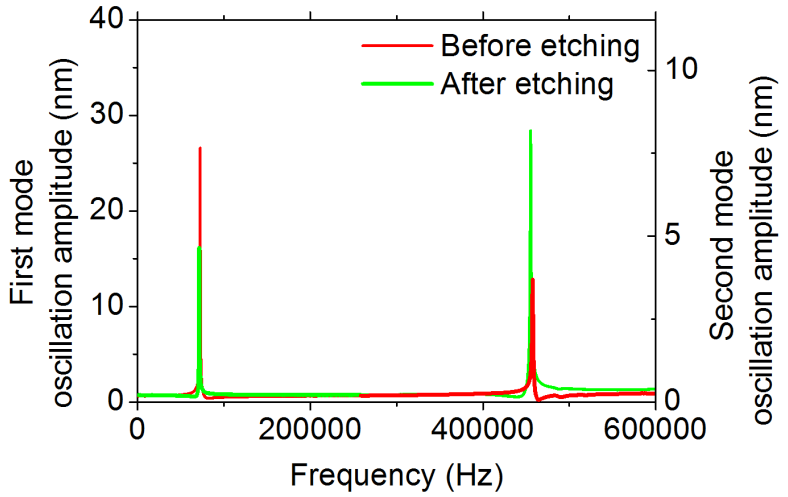

Figure 5.14: Experimental cantilever resonance spectra in air before and after etching the area to enhance the second mode oscillation amplitude (MAC Lever Type II, k = 2.8 N/m).

Another example is shown in Table 5.8, where a noticeable enhancement is also shown.

	Efficiency A_2/A_1		Oscillation amplitude (nm)		
Cantilever	Before	After	Before	After	Oscillation increment (%)
a	0.17	0.47	8.16	27.12	232
b	0.14	0.51	3.70	8.18	121

Table 5.8: Second mode oscillation amplitudes (MAC Levers Type II) in air before and after the etching.

Finally, several cantilever resonance spectra are displayed in Figure 5.15. As in the former case, completely coated cantilevers (before etching) were compared to the etched ones. The second resonance mode oscillation amplitude for each cantilever is summarized in Table 5.9. As shown, etched cantilevers present higher oscillation amplitude for the second resonance mode, confirming the oscillation amplitude enhancement.

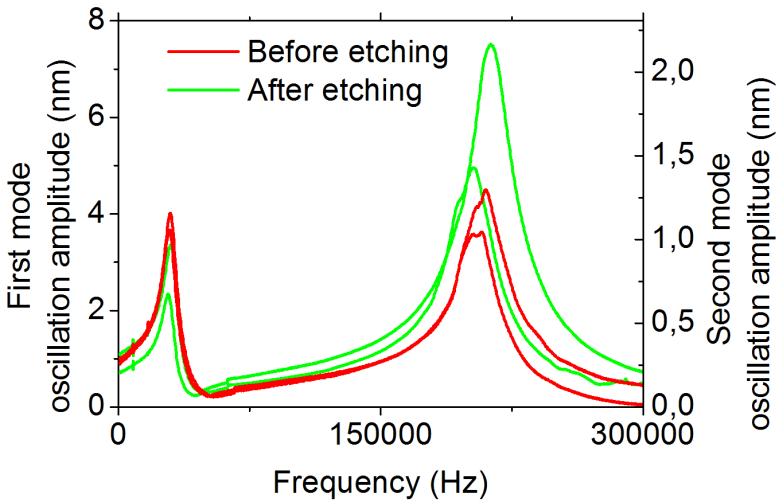

Figure 5.15: Different cantilever experimental resonance spectra in water before and after etching the area to enhance the second mode oscillation amplitude (MAC Lever Type II, k = 2.8 N/m).

	Before		After	
Cantilever	a	b	c	d
Oscillation amplitude (nm)	1.30	0.64	2.17	1.43

Table 5.9: Second mode oscillation amplitudes (MAC Levers Type II) in liquid before and after the etching.

Therefore, from the experiments presented for commercial MAC levers, it is demonstrated that it is possible to increase both efficiency and oscillation amplitude of high modes, removing a specific area of the magnetostrictive layer. However, further experiments are required in order to improve the control over the efficiency enhancement, tuning the FIB etching parameters and its reproducibility.

Low force constant cantilevers (coated with Fe-B-N)

High resonance modes enhancement was also performed for Fe-B-N coated cantilevers. As shown in Figure 5.16, the second resonance mode oscillation amplitude enhancement for CSC38/Al BS levers coated with 50 nm of Fe-B-N is achieved, raising the second mode oscillation amplitude from 11.7 nm to 40 nm. However, the oscillation amplitude of the first mode is slightly increased as well, from 14.5 nm to 22.7 nm. This increase could be due to the fact that the initial Fe-B-N coating magnetization was different in both experiments, before and after the etching. We have experimentally noticed that resonance spectra of the Fe-B-N coated cantilevers can deviate for different experiments, showing even lower oscillation efficiencies than expected for higher resonance modes. Therefore, further development of the Fe-B-N deposition conditions is needed, in order to increase the resonance spectra reproducibility for both, oscillation amplitude and efficiency.

AFM imaging when operating with higher modes

In order to demonstrate that the cantilevers are still functional after the etching, images performed in liquid environment are shown after the film removal to enhance the second resonance

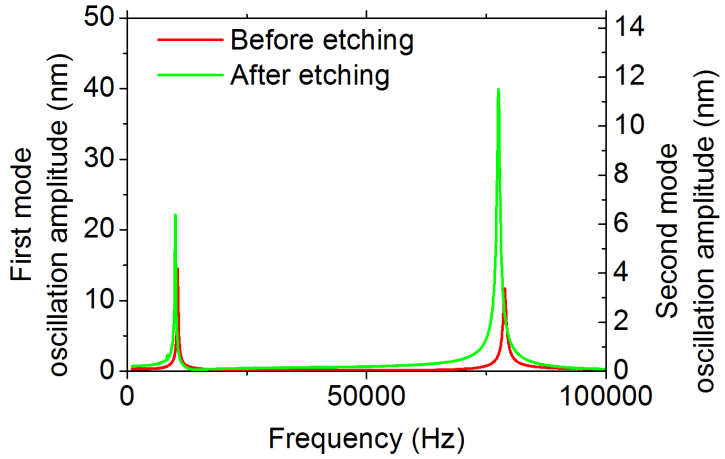

Figure 5.16: Experimental cantilever resonance spectra in air before and after etching the area to enhance the second mode oscillation amplitude (CSC38/Al BS lever coated with 50 nm of Fe-B-N, k= 0.03 N/m).

mode oscillation amplitude (Figures 5.17, 5.18, 5.19 and 5.20).

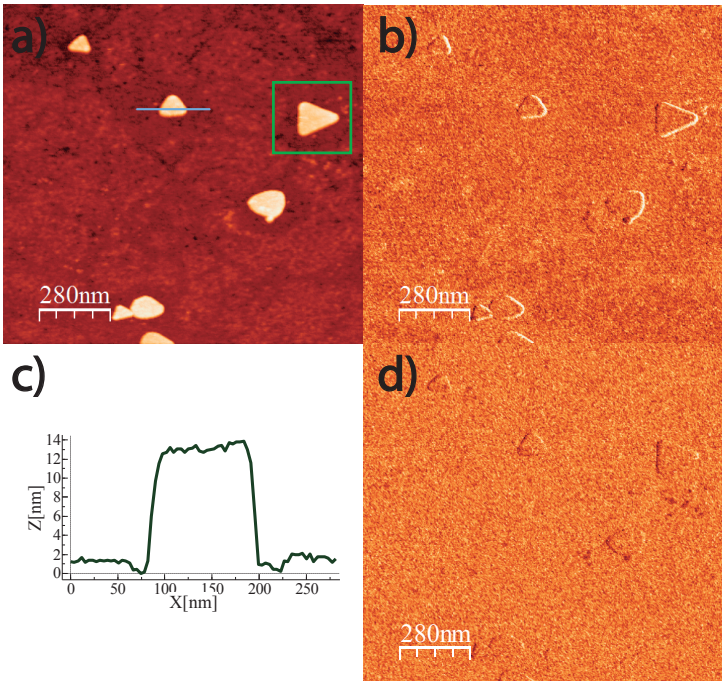

Figure 5.17: Gold nanoprisms topography image a) and profile c) deposited on silicon in water. X b) and Y d) components of the second eigenmode.

In Figure 5.17, AFM images of gold nanoprisms deposited on silicon and imaged in liquid are displayed [109][2]. The second resonance mode was excited simultaneously to the first. The gold nanoprisms present a height of about 12 nm and sizes of about 100 nm, as expected (Figure 5.17c). Also, the X and Y components of the cantilever second resonance mode are displayed,

[2]I gratefully acknowledge Dr. S. Mitchell, Dr. S. Hormeño and Dr. J. M. dela Fuente for the sample synthesis and preparation.

where the gold nanoprisms do not exhibit any contrast respect to the silicon surface.

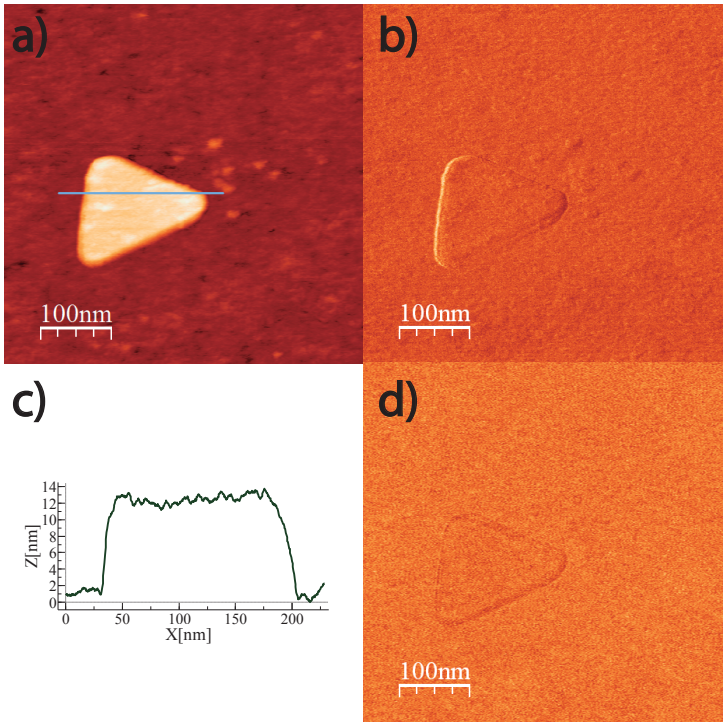

Figure 5.18: Zoom of the gold nanoprisms topography image corresponding to the prism contained inside the green square of Figure 5.17 a) and its profile c) in water. X b) and Y d) components of the second eigenmode.

A zoom out from previous image (green square in Figure 5.17a) is shown in Figure 5.18. As displayed in the profile, the high resolution is maintained, demonstrating that after the FIB etching, cantilevers are still functional and achieve high resolution.

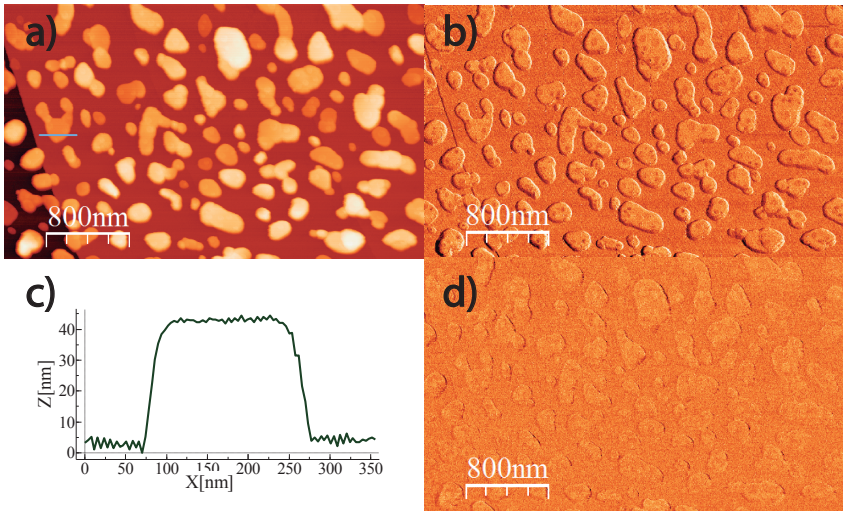

Figure 5.19: Gold nanoprisms topography image a) and profile c) deposited on Highly Ordered Pyrolytic Graphite (HOPG) in water. The prisms are coated with polyethylene glycol (PEG) polymer. X b) and Y d) components of the second eigenmode.

In Figures 5.19 and 5.20, functionalizated gold nanoprims are imaged. The former gold nanoprims are functionalizated with a 5000 Da polyethylene glycol (PEG) polymer and deposited on Highly Ordered Pyrolytic Graphite (HOPG). Due to the coating, the shape of the gold nanoprisms is rounder than in the previous images (nude prisms) and the lateral size is increased.

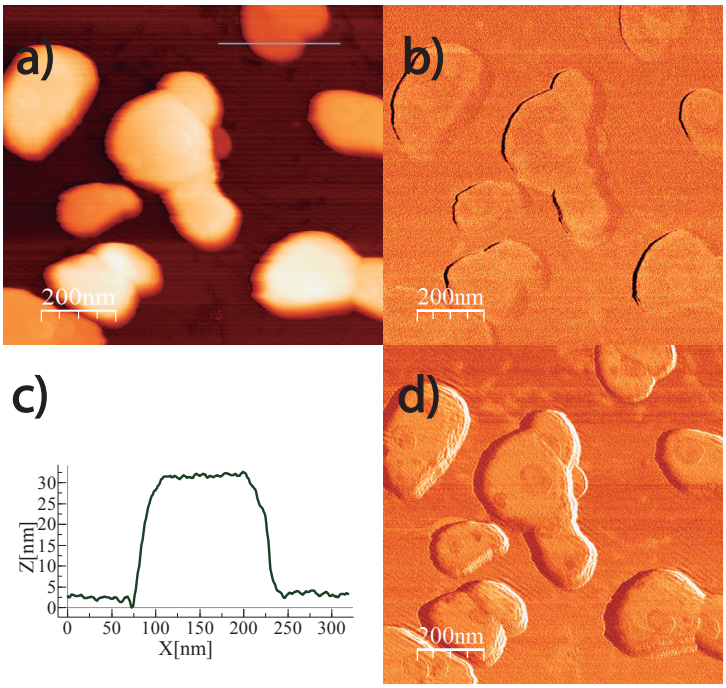

Figure 5.20: Gold nanoprisms topography image a) and profile c) deposited on Highly Ordered Pyrolytic Graphite (HOPG) in water. The prisms are coated with polyethylene glycol (PEG) polymer. X b) and Y d) components of the second eigenmode.

Also, as shown in Figures 5.19b, 5.19d, 5.20b and 5.20d, a contrast in the X and Y component of the second resonance mode appears in some areas of the nanoprisms surface. This contrast is due to impurities (probably counter ions accumulation on the PEG functionalized nanoprisms surface).

The AFM images presented above demonstrate that, after the magnetostrictive film etching, it is possible to use the cantilevers to perform high resolution imaging in liquid environment.

5.3 Implantation of Ga$^+$ ions by FIB to enhance a particular resonance mode

In the previous section, the oscillation amplitude increase of a specific resonance mode by means of magnetostrictive layer etching was demonstrated. An alternative method will be presented in this section: instead of etching certain areas of the magnetostrictive layer, its local magnetic properties are modified, in particular the low coercivity and high magnetostrictive coefficient of the pristine layer, by a low dose of FIB implanted Ga$^+$ ions according to [105, 110–112]. Thus, the cantilever structure is maintained and only the magnetic material properties are changed.

In this section we will discuss the Ga$^+$ ions implantation in the magnetostrictive thin film in order to enhance the second or the third resonance modes. The areas where the Ga$^+$ ions were implanted are the same ones selected before for *Configuration 2* and *Configuration 3*. The

study was performed on the same kind of cantilevers: Fe-B-N coated CSC38/Al BS cantilevers (25 nm in this case to facilitate the Ga^+ implantation) and MAC Lever Type VII.

5.3.1 Study of Ga^+ implantation

Monte Carlo simulations based on the Stopping and Range of Ions in Matter (SRIM) software [113–115] were performed in order to simulate the Ga^+ ion implantation before proceeding with the experiments. By these simulations we may estimate as well the maximum dose of ions that can be used without significantly etching the magnetostrictive film surface. As the implanted ions penetrate in the material, they change its internal structure, thus changing its magnetic properties. On the other hand, we need to study how the ions implant in the thin film, and which is the optimal density of Ga^+ ions to implant in the magnetic materials in order to avoid surface sputtering and consequently thinning of the film.

The SRIM software can be used for calculations of three dimensional ions distribution in the solid after its exposure to an ion beam. This software offers as output different parameters, such as penetration depth, its spread along the ion beam (called straggle) and all target atom cascades. Also, it is possible to study the vacancies concentration, sputtering rate, ionization and phonon production in the target material.

Ga^+ implantation in Fe-B-N films

The main input parameters used on the Fe-B-N film simulation were the following:

1. The stoichiometry of the magnetic material Fe-B-N was Fe = 74%, B = 19% and N = 7% [20].
2. The thickness of the film for the simulation was 200 nm.
3. The calculations were performed considering a number of 50000 ions. This number is large enough since increasing the number of ions did not affect the statistic results.
4. An accelerating voltage of 30 keV.

After the introduction of the previous parameters in the SRIM software, a Fe-B-N density of 8.605×10^{22} atoms/cm^3 = 6.339 g/cm^3 is obtained. Furthermore, the software provides us with the value of the Surface Binding Energy (E_{Surf}) for each material, and an estimation for the bulk Fe-B-N material. A surface atom has fewer electronic bonds which must break, and therefore E_{Surf} is lower. From the calculation we obtained an estimated E_{Surf} for Fe, B and N of 4.34 eV, 5.73 eV and 2 eV, respectively. The global Fe-B-N layer E_{Surf} equals 4 eV.

It is also interesting to find out whether the removal of near surface atoms occurs. When a collision cascade transfers to an atom an energy higher than the E_{Surf}, the atom may be sputtered. The sputtering of a surface can be quantified by the sputtering yield, defined as the mean number of sputtered target atoms per incident ion (in our case, Ga^+ ions). If the target is made of several elements, there is a separate sputtering yield for each element.

$$Sputtering\ Yield = (Number\ of\ Sputtered\ Atoms)/(Number\ of\ Incident\ Ions) \quad (5.4)$$

From the sputtering yield figures we can estimate the Fe-B-N surface etching. During an irradiation process E_{Surf} may change. This is because the sputtering of a target may make it rough or even damage it. The surface atoms of rough and/or harmed targets are bound with fewer electronic bonds. Therefore, the sputtering yield raises up and the E_{Surf} decreases.

Hence, for this case, the sputtering yield is only a rough estimation since this calculation does not include the surface roughening effects.

The calculated Ga$^+$ ions penetration depth in Fe-B-N is shown in Figure 5.21a. The plot ordinate units are (atoms/cm^3)/(atoms/cm^2). When the penetration depth value is multiplied by the ion dose in units of atoms/cm^2, the penetration depth is directly converted to the Ga$^+$ ions density atoms/cm^3 on the target. The penetration depth average range is 130 Å. Above 200 Å, the density of the implanted ions starts to decrease rapidly. According to this, we have chosen a thickness of 25 nm for the magnetostrictive layer. The lateral range is not too high, less than 60 Å(Figure 5.21b). Thus, they will not spread beyond the exposed area when implanting and, therefore, an excellent lateral resolution can be achieved. The ions penetration depth in the Fe-B-N film can be enhanced by increasing the energy of the Ga$^+$ ions. Unfortunately, the FIB system facility available in our laboratory does not allow this increase.

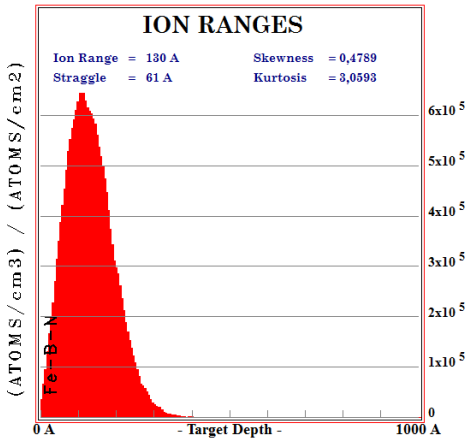

(a) Ion depth ranges

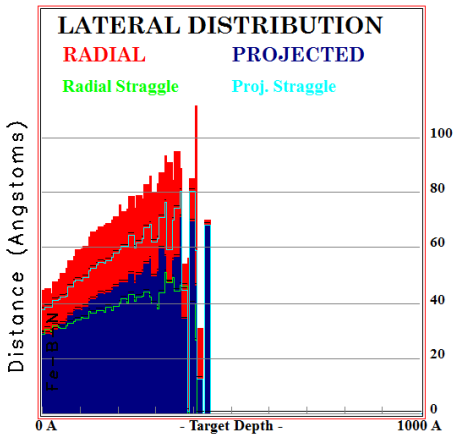

(b) Ion lateral ranges

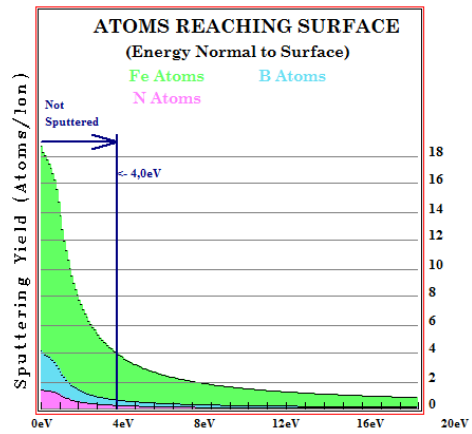

(c) Integral sputtering yield

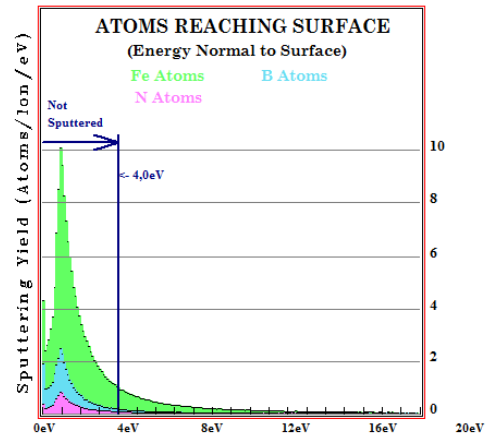

(d) Differential sputtering yield

Figure 5.21: Ion Ga$^+$ ranges and integral and differential sputtering yield for sputtered atoms on Fe-B-N films.

During the Ga$^+$ implantation on the cantilever coating, an undesired sputtering process may damage the exposed surface. For this reason, it is important to estimate the sputtering yield of the Ga$^+$ ions implantation. Figure 5.21c shows the integral sputtering yield of the process.

This magnitude describes the energy transfer between the impinging Ga^+ ions and the surface atoms. The vertical line at 4.0 eV is the average E_{Surf} estimated by the software for the Fe-B-N layer. Therefore, only the atoms that acquire an energy higher than E_{Surf} are sputtered from the target. The intersection between the vertical line and the integral sputtering yield curve corresponds to the number of sputtered atoms by each incident Ga^+ ion. The number of atoms sputtered for each incident Ga^+ ion that arrives to the Fe-B-N layer is 4. The differential sputtering yield plot (Figure 5.21d) shows the energy distribution of the atoms reaching the surface. The most common energy for the atoms reaching the surface is below 3 eV, not enough to be sputtered. The differential plot allows us to know whether slight variations in energy around E_{Surf} may produce large variations in the sputtering yield. Although the value of the E_{Surf} would vary in the [3-5] eV interval, this will not produce big variations in the sputtering yield, since the value of the differential plot at this energies is not high enough.

Different groups have reported that doses of $10^{15} - 10^{16}$ ions/cm^2 are enough to destroy the magnetic properties of magnetic films [105, 110–112]. Thus, we have performed a FIB implantation experimental test in order to find the maximum dose before starting to sputter the Fe-B-N layer. The profile in Figure 5.22 shows that for a dose of 10^{16} ions/cm^2, the surface is not sputtered. The conditions used in the FIB were a dose of $D = 2000$ μC/cm^2 (equivalent to 1.25×10^{16} ions/cm^2), a current of $I = 6$ pA and an aperture of $A = 20$ μm. Using the former calculations and applying this conditions, a coating removal of 3 nm was estimated. Nevertheless, in the experimental profile of Figure 5.22, we do not appreciate any depth in the implanted surface. The E_{Surf} estimated by the software used to calculate the sputtering yield was clearly underestimated.

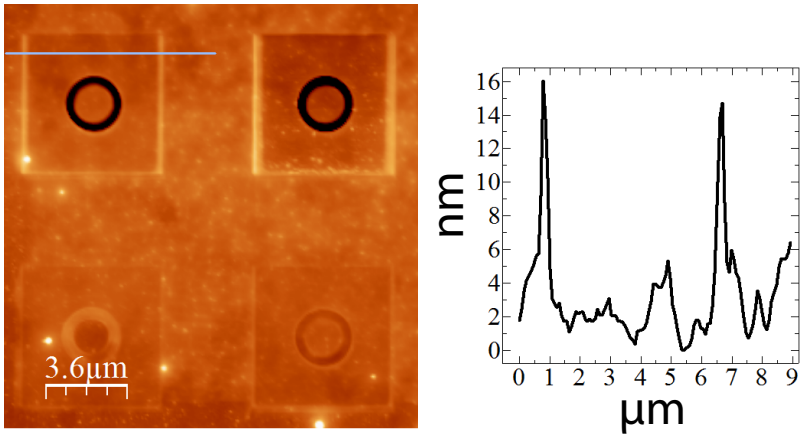

Figure 5.22: AFM images of an array of 5×5 μ square patterns for different FIB implanting conditions on Fe-B-N on the chip (left). Profile of a square with a dose of 10^{16} ions/cm^2 (right).

Ga^+ implantation in Co-Sn films

In the MAC Levers case, no data about the magnetostrictive layer composition was available, so the composition was analysed by X-ray fluorescence (XRF). The XRF technique is based on the emission of characteristic secondary (or fluorescent) X-rays from a material that has been excited with high-energy X-rays or gamma rays. Further analysis of the detected photons energy provides information of the sample stoichiometry. Figure 5.23 shows the main elements present in MAC levers: cobalt and tin, with trace amounts of platinum and selenium.

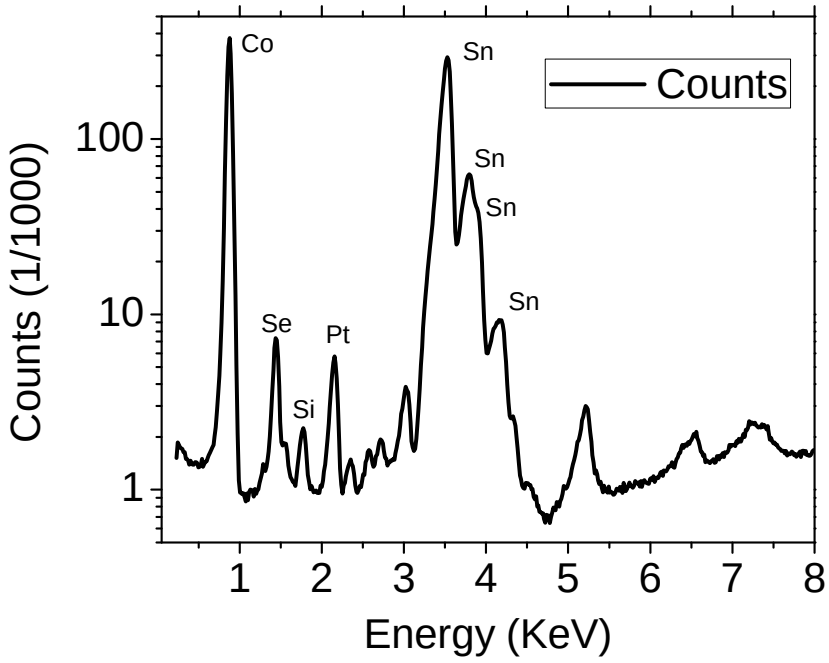

Figure 5.23: X-ray fluorescence measurement performed on the magnetostrictive coating of MAC levers.

The implantation modelling discussed in the former section was repeated considering now cobalt and tin. There are not much data in the literature about this kind of Sn-Co magnetostrictive films, but reference [116] reports on a high magnetostrictive coefficient for thin films of $Sn_{30}Co_{70}$. Therefore, assuming that this material had been selected to coat MAC cantilevers, this stoichiometry composition was introduced as input data for the SRIM simulations. The other input parameters are kept the same as before, just changing the atomic masses of the target material.

Figure 5.24a shows an average range of the Ga^+ ions in $Sn_{30}Co_{70}$ film of 120 Å, and a lateral range below 120 Å(Figure 5.24b). It is, therefore, more difficult to implant Ga^+ ions in this material than in Fe-B-N, because in Fe-B-N the Ga^+ ions reach deeper into the film. The sputtering yield is 6 atom/ion (Figure 5.24c), and the differential value around this energy is substantially low (Figure 5.24d). Thus, variations in E_{Surf} will not produce big differences in the sputtering yield, leading to a stable implantation process.

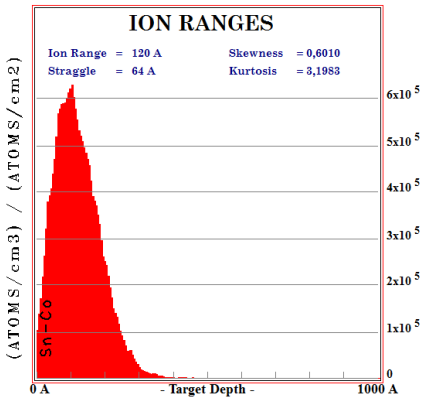

(a) Ion depth ranges

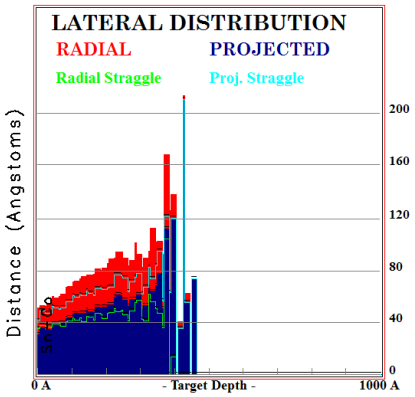

(b) Ion lateral ranges

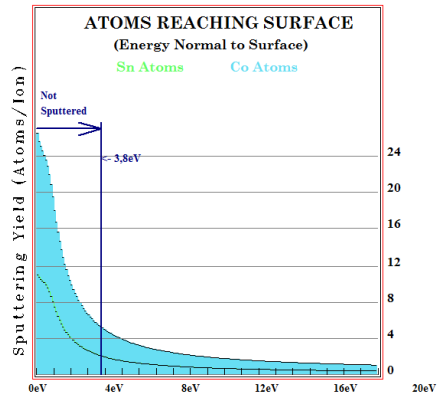

(c) Integral sputtering yield

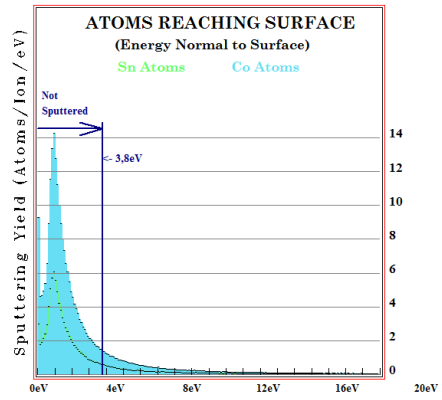

(d) Differential sputtering yield

Figure 5.24: Ion Ga^+ ranges and integral and differential sputtering yield for sputtered atoms on $Sn_{30}Co_{70}$ films.

The study of the conditions required to implant Ga^+ ions without producing sputtering in the surface was repeated for the MAC levers coating. Figure 5.25 shows an AFM image of an implanted area on a MAC Lever chip and the corresponding profile.

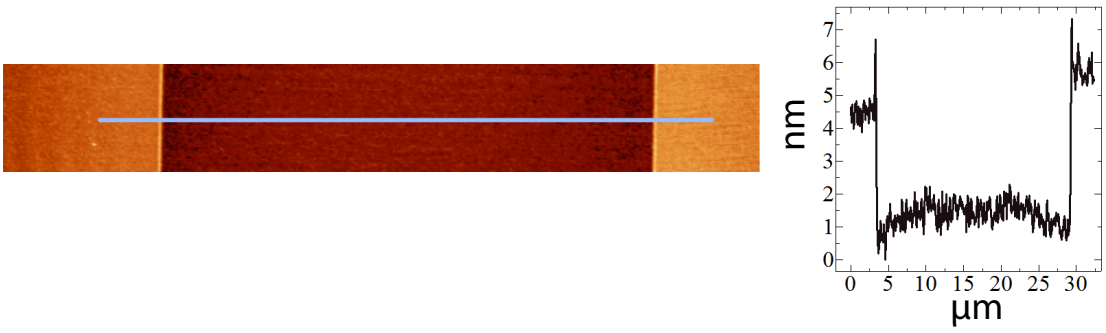

Figure 5.25: AFM image (left) and profile (right) of a square pattern on with a dose of 10^{16} ions/cm^2.

The conditions used in the implantation process were a dose of $D = 1600\ \mu C/cm^2$ (equivalent to 10^{16} ions/cm^2), a current of $I = 6$ pA and an aperture of $A = 20\ \mu m$. Although the AFM profile shows a 3 nm film etching, this undesired etched depth is much lower than the magnetostrictive film thickness (90-100 nm).

Figure 5.26 shows an example of cantilevers in *Configuration 2* (a) and *3* (b) after Ga$^+$ implantation. The slight contrast indicates the difference between the exposed area and the one not exposed.

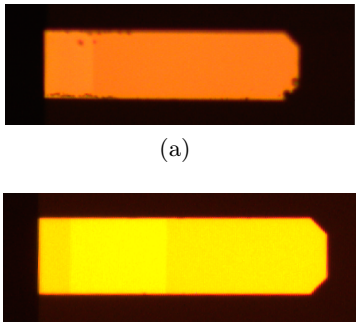

(a)

(b)

Figure 5.26: MAC Lever Type VII after Ga$^+$ implantation in order to enhance the second (a) and third (b) resonance mode.

5.3.2 Experimental results

The experiments were repeated for Fe-B-N coated CSC38/Al BS (25 nm in this case) levers and commercial MAC Levers. The cantilever resonance spectra were measured before and after Ga$^+$ implantation to enhance a specific high mode (*Configuration 2* and *Configuration 3*, Figure 5.3). An example of the second mode efficiency enhancement (*Configuration 2*) is shown in Figure 5.27 for a MAC Lever Type VII.

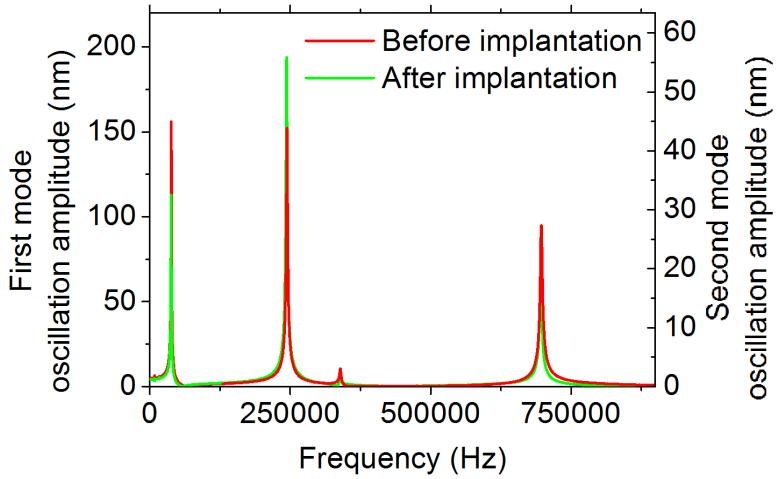

Figure 5.27: Experimental cantilever resonance spectra in air before and after Ga$^+$ implantation to enhance the second mode oscillation amplitude (MAC Lever Type VII, k = 0.14 N/m).

The oscillation amplitude of the second resonance mode increased from 43.86 nm before Ga$^+$ implantation to 55.87 nm after Ga$^+$ implantation, an increment of 27 %. It can be noticed

that the resonance frequencies are not shifted as in the previous section. In this case, there is not an etching but an implantation, leading to small variations in the cantilever mass.

The oscillation amplitude gain for the third resonance mode after Ga^+ implantation was also measured for CSC38/Al BS levers coated with Fe-B-N. The results are shown in Figure 5.28[3].

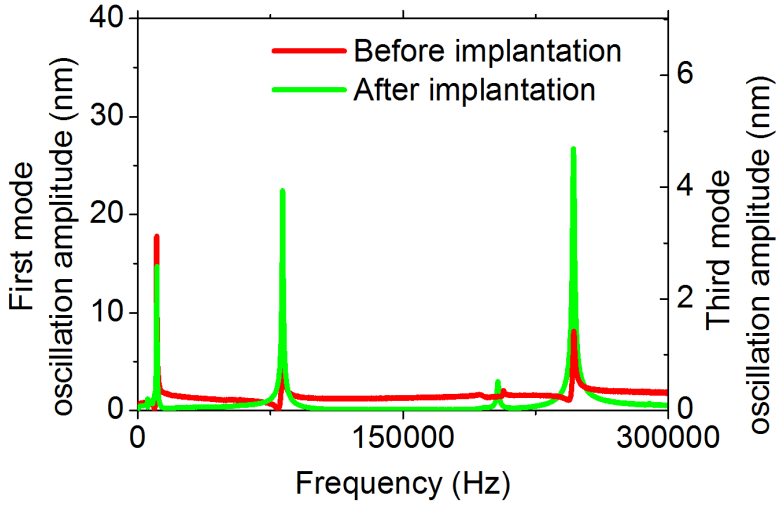

Figure 5.28: Experimental cantilever resonance spectra in air before and after Ga^+ implantation to enhance the third mode oscillation amplitude (CSC38/Al BS lever coated with 50 nm of Fe-B-N, k= 0.03 N/m).

Before the Ga^+ implantation, the cantilever oscillation amplitude was 1.5 nm. After the Ga^+ implantation, the oscillation amplitude increased to 4.8 nm, showing and increasing in the third mode oscillation amplitude.

Therefore, we have shown that it is also possible to increase the oscillation amplitude of a particular mode by means of Ga^+ implantation. Furthermore, a reduction on the cantilever damage was accomplished by replacing the etching process by Ga^+ ion implantation.

5.4 Torsional enhancement

As mentioned in section 1.4, torsional resonance modes can be used to perform quantitative mapping of material properties, such as Young modulus [64]. Also, they can be employed to quantify biological molecules [19] or in nanomedicine, for example, to reveal significant differences in the fractal dimensionality of cancerous cells with respect to normal cells [65]. Torsional modes in usual rectangular or triangular cantilevers used in AFM are difficult to excite. However, by means of tailoring the film coating in cantilevers magnetostrictively excited, it is possible to enhance torsional modes.

In this last section, it will be theoretically and experimentally demonstrated that it is also possible to enhance torsional modes by selective etching of the magnetostrictive coating. For this purpose, rectangular and triangular cantilevers with different coating areas were modelled with COMSOL Multiphysics.

The amplitude of the first torsional resonance between a rectangular cantilever totally (left in Figure 5.29) and a partially (right in Figure 5.29) coated with 50 nm of Fe-B-N was compared.

[3] A intensity of 250 mA_p through the coil was used.

The partially coated one has the magnetostrictive film in its diagonal. The silicon nitride cantilever dimensions are 200×40×0.6 μm.

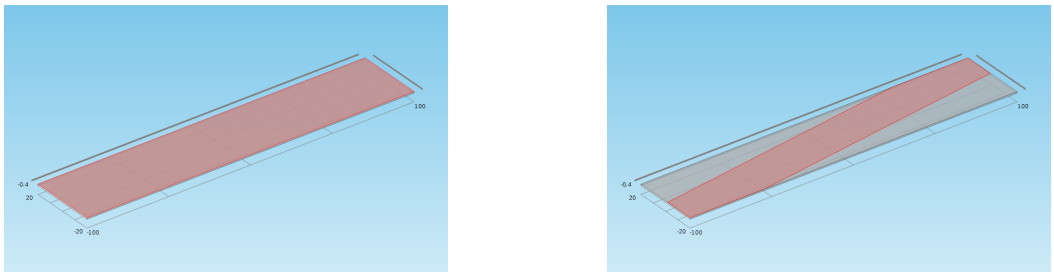

Figure 5.29: Sketch of a rectangular cantilever totally (left) and partially (right) coated with a magnetostrictive film (pink).

During the simulations, a harmonic strain is introduced in the film simulating the magnetostrictive effect induced by an applied magnetic field. The value of the strain amplitude in the magnetostrictive film for both the totally and partially coated cantilevers was 10^{-6}. We have chosen such a low strain value (30 times lower than the magnetostrictive coefficient of Fe-B-N $\lambda = 30 \cdot 10^{-6}$) as simulation input in order to reduce the computational burden. Higher strain values would increase the cantilever oscillation amplitude. Nevertheless, an increment on the strain value will not affect the ratio between the totally and partially coated cantilevers oscillation amplitude.

The torsional shape at resonance for the totally coated cantilever has a flexural component, as shown on the left image of the Figure 5.30. This is because the symmetry of the cantilever leads to very low torsional oscillations, producing a slight bending at the end of the cantilever. However, when the cantilever is diagonally coated, the symmetry is broken. Thus, the cantilever will achieve an enhancement of the torsional movement, as depicted on the right image of the Figure 5.30.

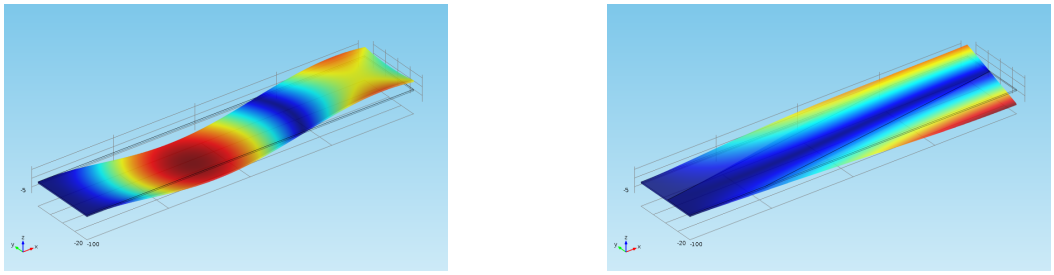

Figure 5.30: Shape of the torsional for a totally (left) and a partially (right) coated rectangular cantilever.

This result can be more clearly appreciated in Figure 5.31, where the torsional amplitude is amplified twenty-fold in the diagonally coated cantilever. Torsional amplitude is defined as the amplitude displacement of the cantilever corner at the free end in the **y** direction, which correspond to the short axis of the cantilever.

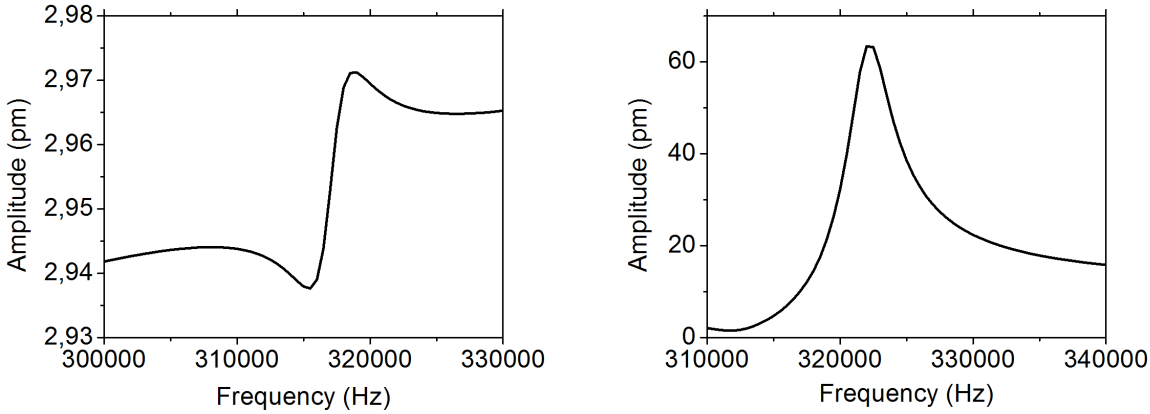

Figure 5.31: First torsional resonance for a totally (left) and a partially (right) coated rectangular cantilever.

The same study on a triangular cantilever coated with 100 nm of Fe-B-N was performed, with a 200 μm base, 100 μm height and a thickness of 1 μm. The cantilever is made of silicon nitride and the value of the strain induced in the magnetostrictive film is 10^{-6}. In order to enhance the torsional amplitude, only one arm of the triangle is coated, as shown in Figure 5.32.

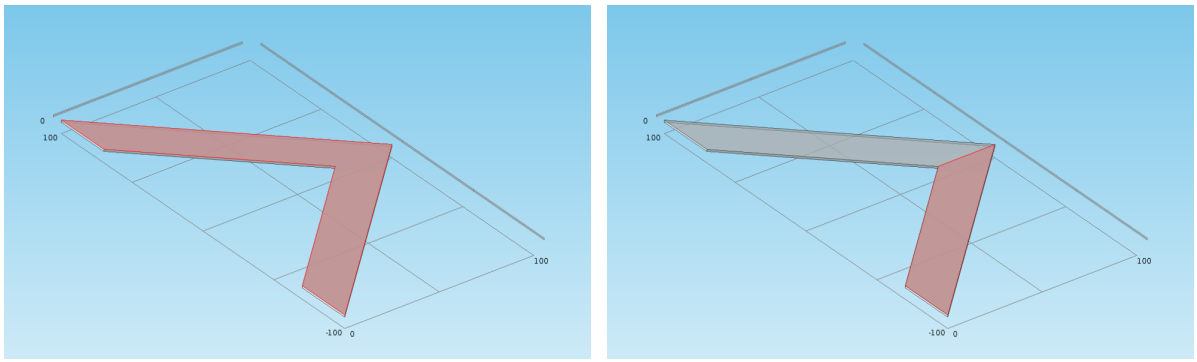

Figure 5.32: Triangular cantilever totally (left) and partially (right) coated with a magnetostrictive film (pink).

As in the previous rectangular case, the shape of the torsional mode when the cantilever is completely coated has a flexural component due to the symmetry of the coating. Nevertheless, if only one arm is coated, a true torsional shape emerges since the symmetry is broken, as presented in Figure 5.33.

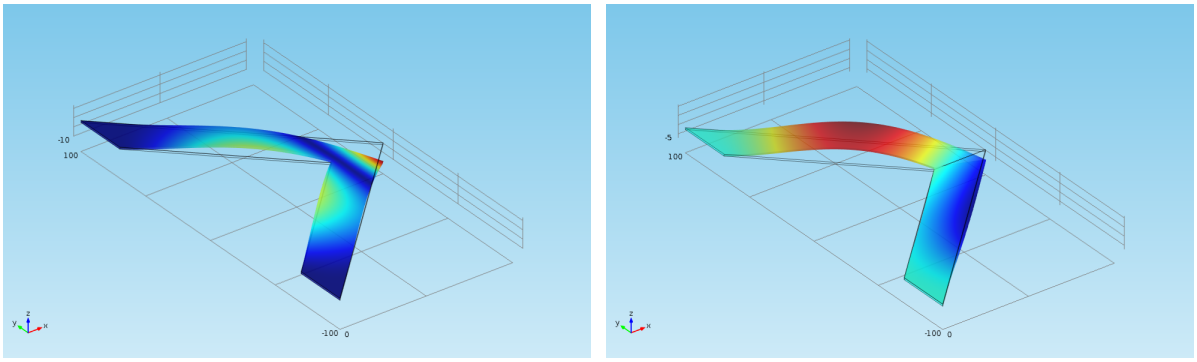

Figure 5.33: Shape of the torsional resonance for a totally (left) and a partially (right) coated triangular cantilever surface with magnetostrictive thin film.

The resonance spectra of the first torsional mode plotted in Figure 5.34 show almost a twenty-fold amplification of the torsional amplitude. Thus, by tailoring the design of the magnetostrictive film it is possible to increase the response of torsional resonances.

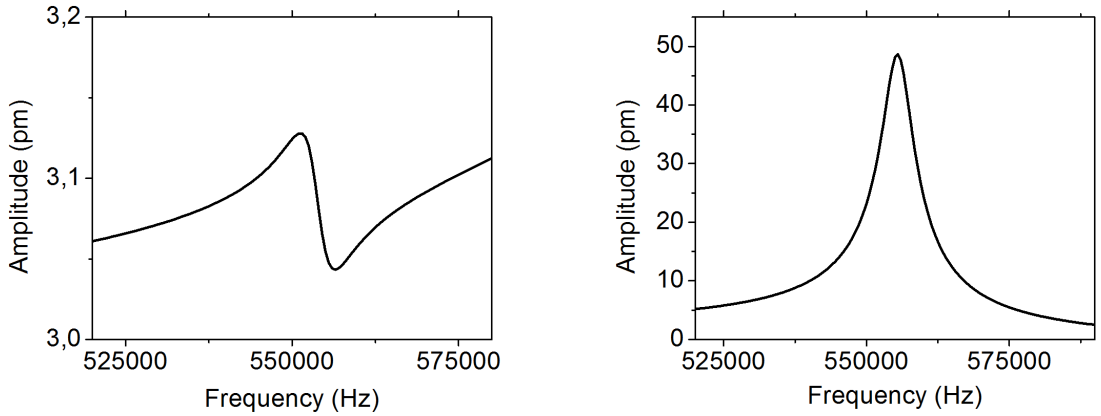

Figure 5.34: First torsional resonance for a totally (left) and a partially (right) coated triangular cantilever.

The torsional enhancement was experimentally tested. For that purpose, a MAC Lever Type VII was etched by means of FIB. An example is shown in Figure 5.35.

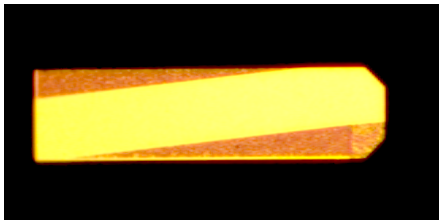

Figure 5.35: MAC Lever Type VII after FIB etching in order to enhance the oscillation amplitude of the first torsional resonance.

In Figure 5.36, an example of a cantilever resonance spectra before and after the etching is shown, where the torsional oscillation amplitude increases from 0.7 to 2.24, 3.2 times higher after the etching. Although more experiments are needed in order to improve the conditions and the area to etch, the oscillation amplitude of the cantilever torsional resonance can be enhanced by means of an adequately patterning the magnetostrictive coating.

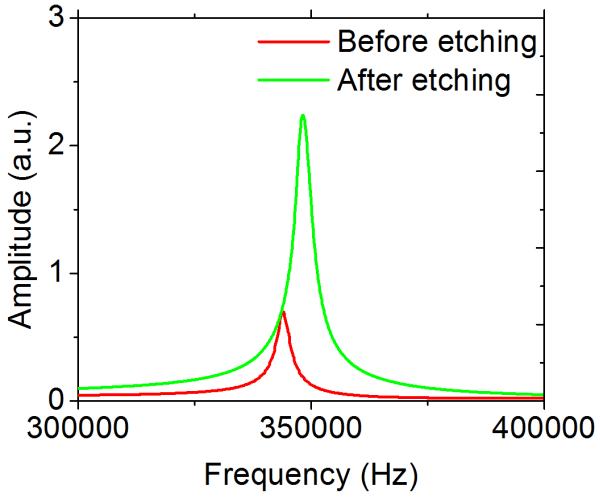

Figure 5.36: Experimental cantilever resonance spectra in air before and after etching the area to enhance the first torsional resonance (MAC Lever Type VII, k = 0.14 N/m).

5.5 Conclusions

In this chapter it is demonstrated that a selective patterning by ion beam etching of the magnetostrictive cantilever coating leads to an increment of both the efficiency and oscillation amplitude of high modes, paving the way for a solution to the complex problem of exciting high modes in liquids for Multifrequency AFM applications. Thus, depending on which resonance it is interesting to enhance, the coated area geometry should be specifically designed. This enhancement can be also applied to torsional resonances. For AFM in liquids, in particular, it opens the chances to sensitivity improvement: the higher the resonance mode, the higher the quality factor and sensitivity.

An alternative technique to the ion beam selective etching has also been explored. We have shown an increment in the higher modes efficiency by Ga^+ ions implantation in the magnetic material, without modification of the mechanical parameters of the original cantilever, thus allowing for a more accurate comparison with unpatterned cantilevers.

Growing the magnetostrictive film through shadow masks on the specific desired areas of the cantilever during the microfabrication process would simplify fabrication and reduce damage as well, but for this exploratory work, a FIB tool has been extremely useful and practical.

Chapter 6

Magnetic pulsed actuation method for AFM

6.1 Introduction

During the Fe-B-N magnetostrictive thin film deposition on cantilevers under the growth conditions discussed in chapter 2, an external magnetic field was intentionally applied to induce a well defined magnetic anisotropy direction with independence of the shape anisotropy of the elongated cantilever. Also, along our previously described experiments, we have observed that the coated cantilever magnetostrictive excitation performance, in terms of oscillation amplitude corresponding to a constant AC excitation current, may be improved by applying an external DC magnetic component helping to reach the maximum slope on the magnetic hysteresis curve. A consequence of this is, in general, a clear increase of the oscillation amplitude. Such effect is due to the well known magnetic rotational hysteresis, corresponding to the magnetization rotation between the direction of the effective remanence magnetization and the direction of the magnetization under an external DC applied field that, in general, will not need to coincide with the direction of the applied AC magnetic field.

Inspired by this observation, we have developed an original alternative method to excite the cantilever taking advantage of the different values and orientation of the magnetization remanence after successive applications of pulsed magnetic fields in two mutually perpendicular directions. The alternate application of magnetic pulses along the short and the long cantilever axis, will indeed lead to a periodic change of the magnetization state between a remanence in one direction and a different remanence in the perpendicular one as sketched on Figure 6.1.

On Figure 6.2, the corresponding magnetostriction induced dynamics of the cantilever (top curve) between two states, A and B, is represented in synchronism with the applied current pulses (red and blue) by two mutually perpendicular small coils. During each semi cycle, the magnetostrictive film on the cantilever will expand along its long or short axis, depending on which direction of the film is magnetized. As the magnetostrictive film volume is maintained, a film expansion in a particular axis (for example, x direction) lead to a film shrinkage in the perpendicular direction (y direction). This leads to the bending of the cantilever sketched in the A (upwards) and B (downwards) states in Figure 6.1 and 6.2. Therefore, the cantilever tip position is switched up and down by changes in the magnetization along the two perpendicular axis induced by perpendicular magnetic field pulses. The use of narrow current pulses (about 10^{-6} s width) allows to reach peak intensities much larger than the maximum current amplitude of the sinusoidal AC current as in the previous standard magnetic actuators configuration. Therefore, large oscillation amplitudes can be reached at high frequencies without facing thermal

issues due to Joule heating of coils or hysteresis energy losses at electromagnets.

As previously explained, in order to induce a cantilever bending actuation, two magnetic pulses must be applied in perpendicular directions. Thus, coil A (red line in Figure 6.2) and coil B (blue in Figure and 6.2) will generate magnetic fields perpendicular to each other, coil A parallel to the short axis, and coil B parallel to the long axis of the cantilever. Each pulse will leave the remanent magnetization parallel to the direction of the magnetic field (black line in Figure 6.2) until the next pulse is applied.

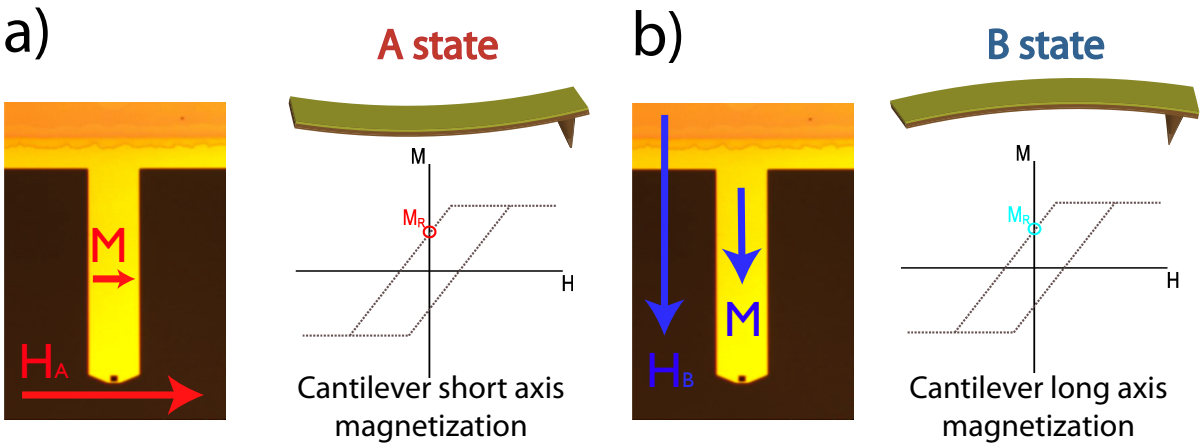

Figure 6.1: Scheme of the magnetic fields directions created by coils A (H_A) and B (H_B) and their effect on the cantilever bending state.

The relation between the narrow magnetic pulses (typically less than 1% of the duty cycle) and the resulting square magnetostriction signal is depicted on Figure 6.2. Due to rotational hysteresis, alternate remanences are oriented in two perpendicular directions and, therefore, magnetostriction dynamic effects are equivalent to that induced by a square or a sinusoidal field actuation.

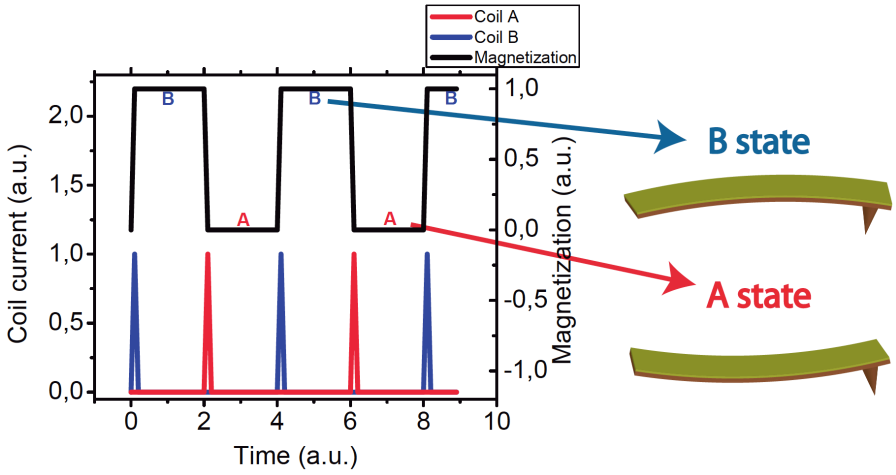

Figure 6.2: Magnetostriction induced cantilever dynamics under magnetic pulsed excitation. Notice that red pulses are perpendicular to blue pulses.

Moreover, in the frequency domain, considering a Fourier analysis, the square magnetization signal is equivalent to an infinite sum of sinusoidal excitations

$$f(t) = \frac{V_0 a}{a+b} + \frac{V_0}{\pi} \sum_{n=1}^{\infty} \left[\left(\frac{1}{n} (\sin(n\omega a) \cos(n\omega t) \right) + \left(\frac{1}{n} (1 - \cos(n\omega a) \sin(n\omega t) \right) \right] \quad (6.1)$$

where $f(t)$ is the actuation signal (**magnetization**) expressed as an infinitive addition of pure tones (a sinusoidal waveform), a and b are the amount of time in A and B state respectively (the pulse period is $T = a + b$), $\omega = 2\pi/T$ is the pulse radian frequency of the magnetization signal ($\omega = 2\pi f$) and V_0 is a constant related to the $f(t)$ amplitude. The delay between magnetic pulses, a or b, can be tuned. This has an application in modulating the oscillation amplitude of the fundamental frequency and higher harmonics, as we will discuss later. As a magnetic pulse is applied at each semi cycle, the cantilever is positively bended during part of the cycle, and negatively during the rest (drawn on the right of the Figure 6.2). As the resulting signal is a square wave, it is easily ascertainable that when $a = b$, the amplitude of the fundamental frequency (ω) is maximum. Hence, if the delay between the pulses of the coils A and B is reduced (decreasing the value of a or b in the pulse train, which is equivalent), the amplitude of the fundamental harmonic in equation 6.1 is reduced as well, decreasing the oscillation amplitude of the cantilever at the fundamental frequency. Otherwise, the amplitude of higher harmonics will increase.

Therefore, by tuning the delay between the pulses generated by coils A and B, the relative cantilever oscillation amplitude of various harmonics can be controlled.

6.2 Liquid cell set-up

In order to experimentally test the pulse excitation method, we have modified the liquid cell AFM prototype design presented in chapter 3. We have used two rectangular coils of an enamelled copper wire (diameter of 100 μm) with a ferrite flat core (with a relative permeability $\mu_r = 400$), dimensions of $3.5 \times 4 \times 2$ mm and 20 turns, in the proximity of the cantilever chip. One coil, the one that creates the H_A magnetic field (short axis direction), is used as a base for the cantilever (Figure 6.3). The other coil creates the H_B magnetic field (long axis direction) and it is placed besides the first one. In order to create and synchronize the current pulses, the following sequence is performed:

- First, two synchronized but mutually delayed voltage pulses are provided by two Agilent 33120A pulse generators connected in master/slave mode.

- Second, a current amplifier is used with the aim of convert the voltage pulses into current pulses.

The voltage sources and the oscilloscope are controlled via GPIB protocol by LabView software. A lock-in amplifier (Recovery Signal) is used to read the oscillation amplitude of the cantilever, which is also controlled by LabView.

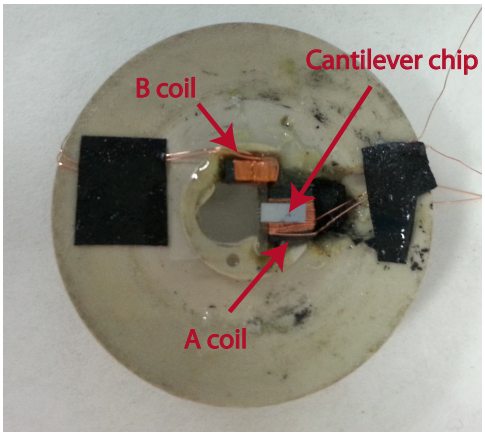

Figure 6.3: Sketch of the liquid cell actuated by perpendicular magnetic pulses.

The magnetic field distribution and its strength was simulated by means of a finite elements method (FEM) calculation performed with the COMSOL Multiphysics tool [76]. In the simulations, a current of 200 mA is applied to the coil. Thus, with the ferrite implemented into the prototype ($\mu_r = 400$), it is possible to reach 7 G and 11 G in the cantilever short and long axis direction, respectively. Considering that the simulations were carried out with 200 mA as input, and the fact that the current amplifier can deliver peak currents up to 10 A, substantially larger magnetic fields should be reached. Therefore, from the analysis of these simulations, it may be stated that coils can create a magnetic field high enough to saturate the magnetization in both the long and short cantilever axis.

Experimental resonance spectra were obtained in air (MAC Mode Type I cantilevers from Agilent [106], $110 \times 35 \times 1$ μm, silicon with a constant force of $k = 0.95$ N/m) and liquid (silicon nitride cantilever from Olympus with Fe-B-N, $100 \times 40 \times 0.8$ μm, $k = 0.76$ N/m), as shown in Figure 6.4. Resonance spectra were performed applying 0.6 A_p (duty cycle = 0.1 %) to produce a square magnetization signal with the MAC Lever and 5 A_p (duty cycle = 1 %) with the Olympus lever (Fe-B-N films show higher coercivity).

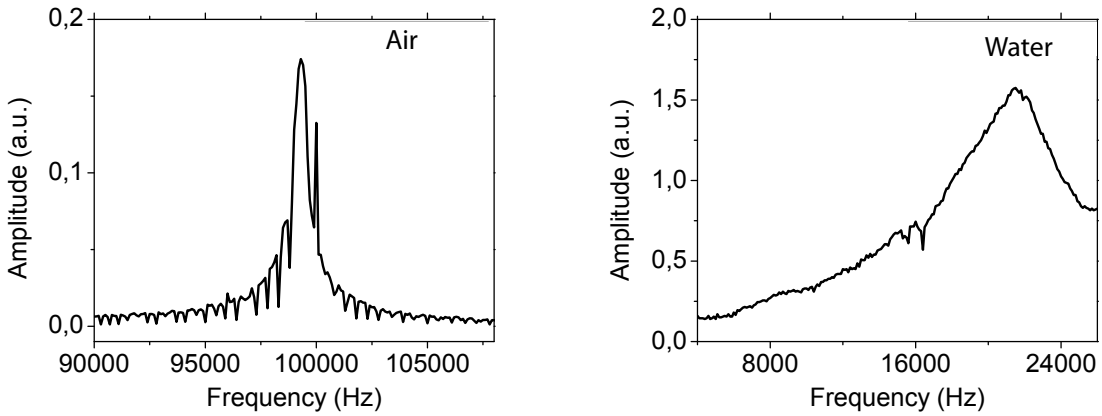

Figure 6.4: Experimental resonance spectra of a MAC Mode Type I in air (left) and Fe-B-N coated Olympus cantilever in water (right).

On Figure 6.4, it can be noticed that the resonance spectrum produced by the magnetic pulse excitation method on the Fe-B-N coated cantilevers in water is clean. Little ripples in the cantilever resonance spectrum on MAC Mode Levers in air are due to the excitation of the driving magnetic field harmonics. In water environment, however, they are masked by the high damping and a much cleaner spectrum is obtained.

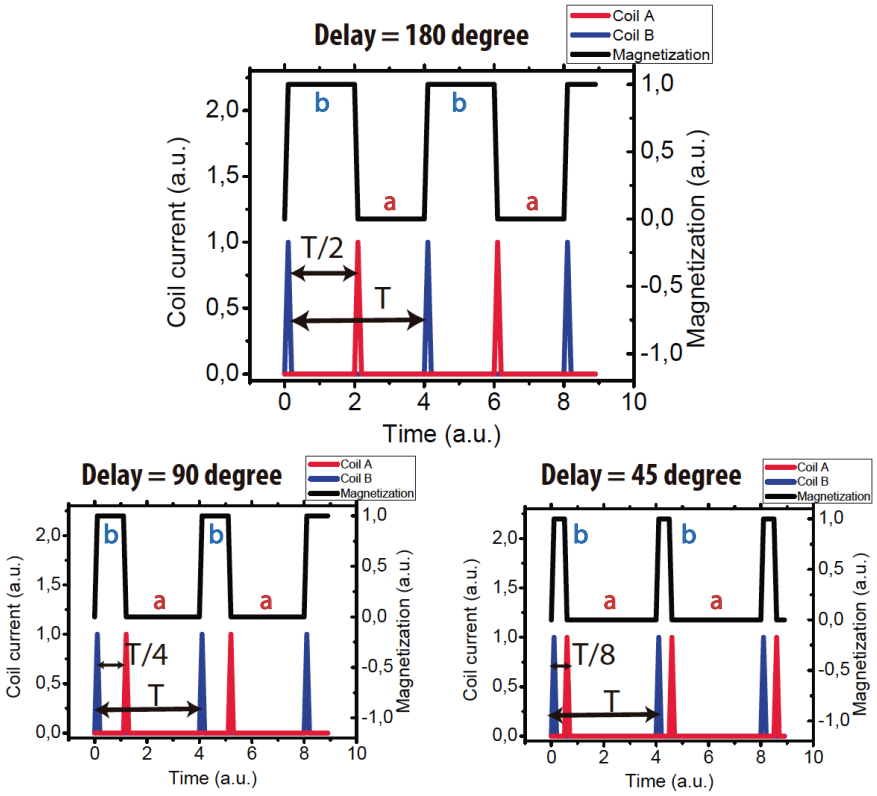

Figure 6.5: Scheme of the amplitude modulation under magnetic pulsed excitation obtained by means of varying the delay between current pulses in coils.

As previously stated, it is possible to modulate the oscillation amplitude by tuning the delay between the current pulses. The delay can be defined as the elapsed time between the current pulse in coil B and coil A. A delay of 0° is then equivalent to apply the pulses at the same time. A delay of 180° is equivalent to half of the period $T/2$, 90° is the quarter of the period $T/4$, and so on (Figure 6.5). Therefore, for a square wave magnetization in the magnetostrictive film, a delay of 180° has to be applied. From equation 6.1 and considering that T is the period of the magnetization signal, if b is reduced, the amplitude of the fundamental harmonic (at the frequency of $f = 1/T$) will be also reduced. Hence, if the frequency $f_0 = 1/T$ is the fundamental frequency of the pulses in coils, the equivalent of the excitation function in a Fourier series will be:

$$f(t) = C + a_1 \sin(2\pi f_0 t) + b_1 \cos(2\pi f_0 t) + a_2 \sin(2\pi 2 f_0 t) + b_2 \cos(2\pi 2 f_0 t) + ... \qquad (6.2)$$

where the coefficients a_1 and b_1 correspond to the sinusoidal amplitude of the excitation function at this frequency. If the delay between pulses is reduced, a_1 and b_1 will decrease and higher harmonics coefficients ($i > 1$) a_i and b_i will increase. As a consequence, the oscillation amplitude of the cantilever will be smaller at the fundamental frequency, and higher at higher harmonics.

Figure 6.6 shows how the amplitude is modulated, by changing the elapsed time between magnetic pulses. Narrowing the elapsed time between magnetic pulses leads to a lowering in the total contribution to the fundamental harmonic $(1/T)$. Little ripples are also due to the excitation of harmonics of the resonance frequency.

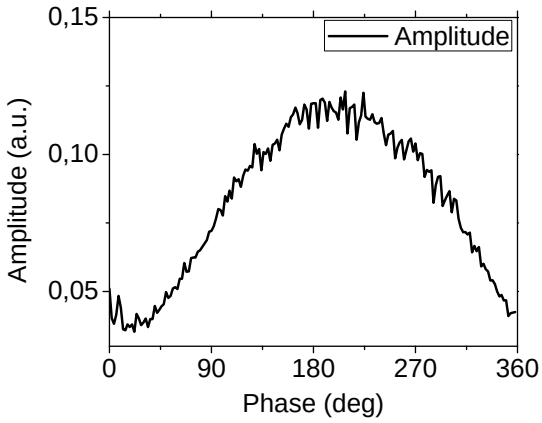

Figure 6.6: Experimental oscillation amplitude of the cantilever as a function of the delay between pulses from coils A and B for a MAC Lever type I in air.

An AFM image of a gold surface in air and an horizontal profile measured with a cantilever MAC Lever type I is shown in Figure 6.7. A current of 0.6 A_p was used, with a duty cycle of 0.1% and a delay of 180°. It is then demonstrated that it is possible to use this technique to measure surfaces by AFM.

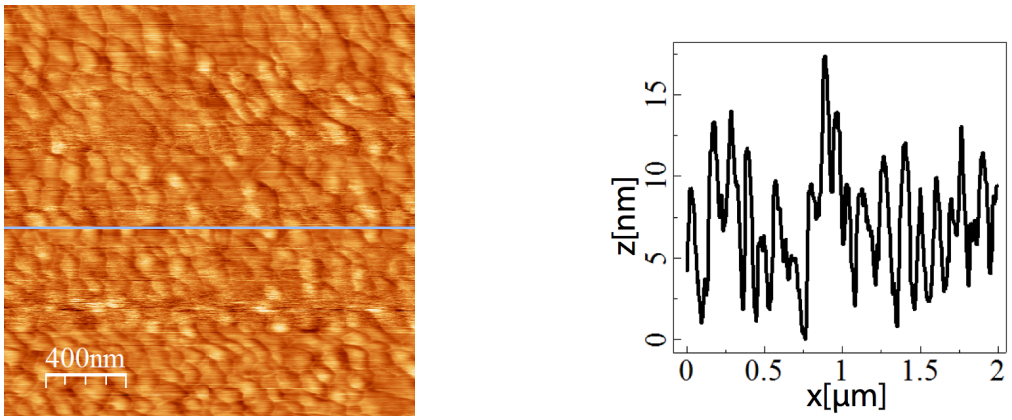

Figure 6.7: Image of a gold surface using the magnetic pulsed excitation method in air and an horizontal line profile.

6.3 Conclusions

Magnetic pulsed actuation method for AFM takes advantage of the rotational anisotropy effect in magnetostrictive materials and the corresponding two different remanent magnetizations in perpendicular directions. The application of ultra short magnetic pulses along those directions

-long and short axis of the cantilevers- leads to a magnetization switch between these two directions and to a magnetostrictive related periodic bending of the cantilever and, consequently, to a large oscillation amplitude. Torsional modes can be excited also, in principle, on specifically designed cantilevers.

We have demonstrated, by simple preliminary experiments, the promising characteristics of this novel AFM mode, particularly useful at minimizing thermal dissipation effects, and its capability to provide clean and controllable cantilever resonance spectra in liquids. It might be further developed into a very versatile Multifrequency AFM, as this technique is able to excite infinite harmonics of the fundamental frequency [11, 12]. It can be also combined with the previously developed patterning of the magnetostrictive film into appropriate areas on the cantilever to tailor and select specific high resonance modes. It will need, however, much more engineering work (outside the reach of this thesis) in order to develop the appropriate electronics to be able to use those harmonics as new information channels for AFM.

Chapter 7

Solvent resistant ultra flat metal surfaces

Current interest in ultra flat surfaces is being boosted by their increasing demand as substrates for Scanning Probe Microscopy. Easy preparation and common use flat surfaces such as silicon [117], highly oriented pyrolytic graphite [78] or mica [118] led way to other materials (gold [119], platinum [120], silver [121], aluminum [121], copper [122]) where a specific surface conductivity or chemistry are required. Some of these surfaces must be used in liquid environments, and they must be resistant without being degraded.

In this chapter, we will present the fabrication process of ultra flat metal surfaces such as gold, platinum, aluminium or copper by a template stripped method. Clean large areas are fabricated with roughness as low as 1.5 Å root-mean-square in 25 μm^2 measured areas. Due to the lack of any adhesives during the fabrication process, the final structure is fully compatible with UHV environment, resistant to organic solvents, as well as very stable to heating (below 180 ^{o}C) and mechanical loads.

7.1 Introduction

Low roughness materials are essential in biological applications from protein and DNA adsorption [16], self-assembled monolayers (SAMs) on gold [123], supported or tethered lipid bilayers [124] to single molecule studies [125]. However, for many applications it is not enough to rely on small regions from a sample as it is important to have large ultra flat regions and a totally template-free surface.

Several techniques have been used to create flat surface metals. Low deposition rates and high temperatures have shown to increase the flatness [126]. Subsequently, it is possible to obtain atomically flat surfaces by means of annealing [127]. However, this method creates only small flat domains (terraces) of just several nanometres in width and makes difficult to keep the surface absolutely clean before the experiments. In order to achieve very low roughness on large regions template-stripping methods are required [128]. Firstly, a metal layer is deposited on top of an atomically flat and recently cleaved mica crystal or on a crystalline silicon substrate by thermal evaporation. Secondly, the surface of the metal layer is bonded to a silicon or other substrate holder by means of epoxies. Later on, the metallic layer can be released from the original silicon substrate or any other ultraflat template by cryogenic cleavage [129] or chemical stripping employing tetrahydofuran (THF), N,N-di-methylformamide (DMF) or dimethylsulfoxide (DMSO) [128]. Unfortunately the use of epoxies is usually not compatible with the presence of organic solvents, neither with the afterwards sample used in UHV environments.

Moreover, we have observed that, in the presence of solvents, or after a long time of immersion in water, most epoxies swell and generate film roughness, as shown in Figure 7.1. In order to avoid these problems, epoxies can be replaced by cold welding at high pressure [130, 131]. In this method, two flat pieces (mica, silicon, etc.) coated with the desired metal are placed in a press, with the metal films facing each other and touching. Then, 500 psi of pressure is applied normal to the interface between the two pieces for a few minutes. Once removed from the press, one of the flat pieces is mechanically stripped by placing sharp tweezers between one corner of the two silicon pieces and gently applying leverage. However, mechanical stress may cause damages in the flat metallic surface and substrate residues are not totally removed.

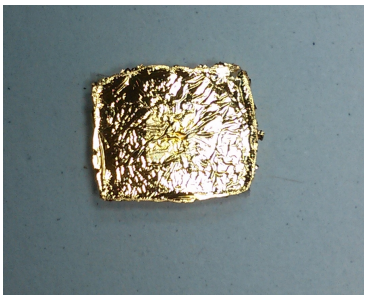

Figure 7.1: Picture of gold film supported by epoxy resin after some hours of immersion in water.

In this chapter, we present a technique to create ultra flat large area surfaces without the use of any adhesive. The resulting structures are fully compatible with all organic solvents and with UHV environment. Furthermore, as we do not use any chemical product or high pressure, the integrity of the surface is preserved.

7.2 Ultra flat surface preparation

The deposition process of the metallic structures is carried out in two steps, each of them in a different HV chamber: first, the evaporation of the two first metallic layers, and second, the sputtering of the rest of the materials.

A piece of freshly cleaved mica or silicon $\langle 111 \rangle$ prime wafer is loaded into a vacuum deposition chamber. Previously, the organic residuals of the silicon are removed by piranha solution (a 1:3 by volume mixture of 30% hydrogen peroxide and concentrated sulphuric acid) for 10 minutes to remove organic contamination and then rinsed with de-ionized water, and dried with nitrogen.

Firstly, 1000 Å of the desired metal (Au, Al, Pt or Cu) is grown onto the mica or silicon substrate. Secondly, 100 Å of titanium (or chromium) is evaporated to form an adhesive layer (Figure 7.2a). This last layer serves also as a diffusion barrier between the evaporated metal and the next layers to be sputtered. Deposition is carried out at a pressure of less than $1.0 \cdot 10^{-6}$ mbar. The evaporation rate, which is typically 0.5 Å/s, and film thickness were monitored by a quartz crystal thickness controller and checked with a profilometer.

In the next step, the sample is transferred to a UHV sputtering system, where a copper protective layer followed by a titanium mask layer are deposited. In both cases, the target potential and the argon pressure is chosen to be -1.0 kV and $6.0 \cdot 10^{-3}$ Torr, respectively. The thickness of the copper layer is 1 μm, while the titanium layer is 0.04 μm. The titanium layer is deposited through a shadow mask in order to form a lateral barrier for the tin-lead alloy (Figure 7.2b) that will be added in the next step: the stripping process. The sample structure is shown in the left image of Figure 7.3.

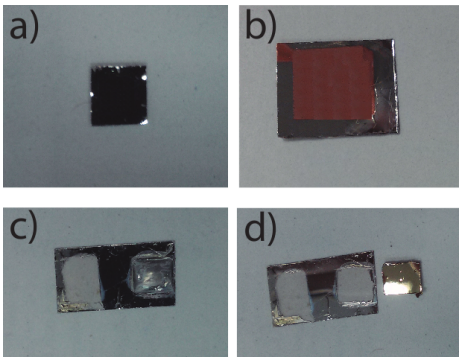

Figure 7.2: Successive steps in the fabrication process.

Once the deposition of metals is finished, we can proceed with the stripping process, which is performed in air. A piece of solid tin-lead alloy is placed on top of the copper surface, onto the titanium free area. Afterwards, the sample is transferred to a hot plate at 250 ^{o}C. Once the piece of solid tin-lead alloy is melted and wets the copper surface as shown in Figure 7.2c, the sample is removed from the hot plate. In this process, when the sample is heated in the hot plate the mica or silicon/metallic structure (right image of Figure 7.3) is separated due to the difference in the thermal expansion coefficient between them. This is driven by thermally induced stress at the interface, as in the liquid-nitrogen release technique performed by Mazurkievwicz et al [129].

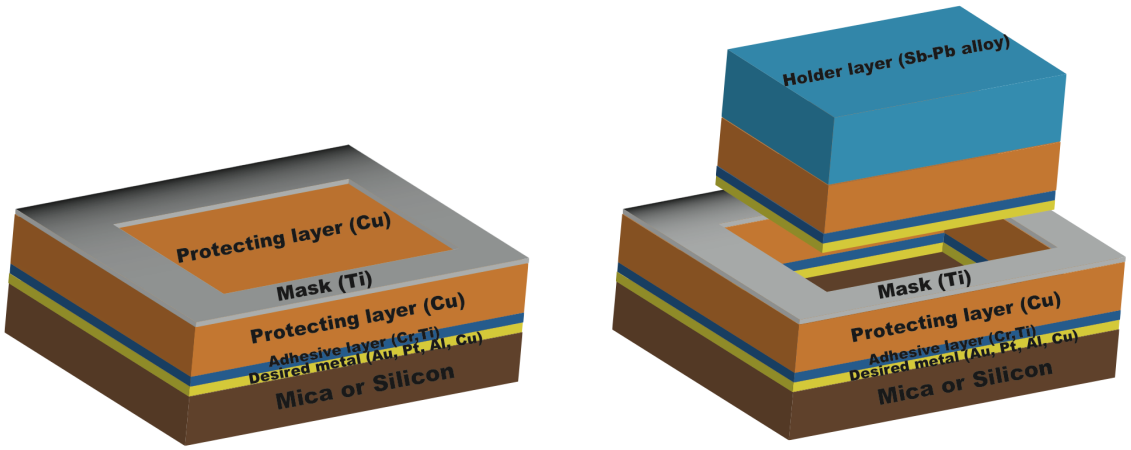

Figure 7.3: Sample structure, before (left) and after (right) detaching, with the desired metal layer on mica or silicon. Above, the adhesive layer and the protecting layer (for example, titanium and copper). Finally, the titanium mask and the tin-lead alloy as a support.

Finally, we use a diamond tip and metal tweezers to strip an ultra flat metallic structure from the mica substrate (Figure 7.2d). The diamond tip is used to scribe the contour of the solidified tin-lead alloy. This procedure is needed in order to separate the titanium mask from the tin-lead alloy. After this, a light lateral upper push with the tweezers tip on the tin-lead alloy is enough to pry the sample up. The large area ultra flat metallic surface is easily stripped off without need of using any chemicals and therefore avoiding contamination of the fresh surface.

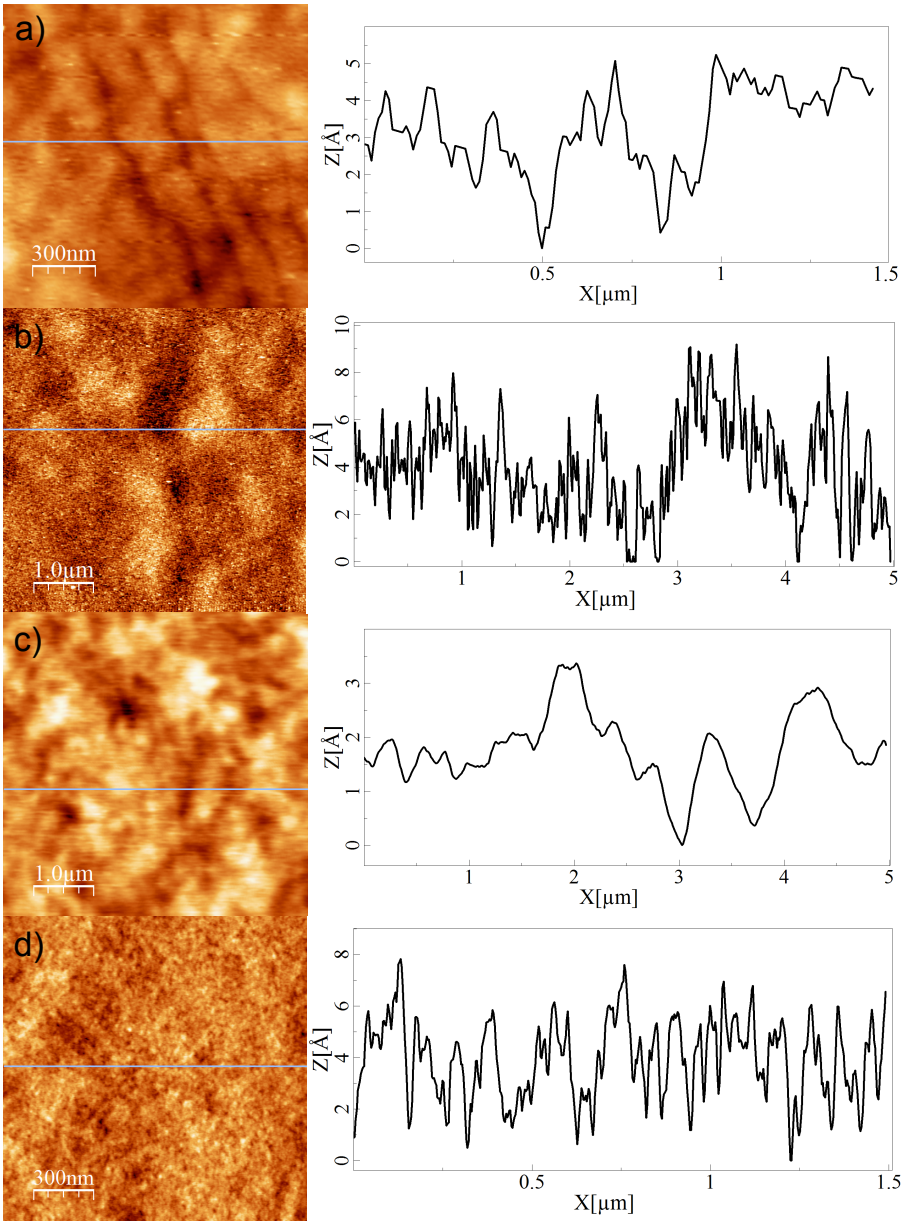

Figure 7.4: Dynamic atomic force microscopy 5×5 μm topographic images of gold (a), platinum(b), aluminium (c) and copper (d). A profile is shown on the right side of each image.

With the purpose of analysing the roughness of the surfaces, we have used the Atomic Force Microscopy (AFM). Studies were performed using an AFM from Nanotec Electrónica [73]. Topographic surface images were processed using the WSxM program [132]. For the operation in dynamic non-contact mode, the nominal force constants of the cantilevers [75] were 2.7 N/m. Figure 7.4 shows gold, platinum, aluminum and copper surfaces images, measured after the stripping procedure. These images show large scale flatness and defect free surfaces, like pits or ridges.

The obtained roughness data for the different samples is presented in Table 7.1. The low peak to valley value for large scanning sizes should be noticed, demonstrating that flatness extends over a long range. The results of the roughness are similar to those in stripping methods [128, 129], but overcoming the swelling problem in liquid environments. We also carry out measurements of the surface roughness after introducing the samples in organic solvents and

Material	Image size (μm×μm)	Mean (Å)	RMS (Å)	PV (nm)
Gold	5×5	1.55	1.98	3.30
Gold	1.5×1.5	1.14	1.45	1.10
Platinum	5×5	1.54	1.97	4.05
Platinum	1.5×1.5	1.32	1.67	1.61
Aluminum	5×5	1.10	1.48	3.45
Aluminum	1.5×1.5	0.80	1.24	3.08
Copper	5×5	1.76	2.50	5.48
Copper	1.5×1.5	1.53	1.92	1.73

Table 7.1: Average, root mean square and peak to valley roughness from AFM images.

storing the surfaces immersed in water for several weeks. No changes in roughness were observed in any of the two cases.

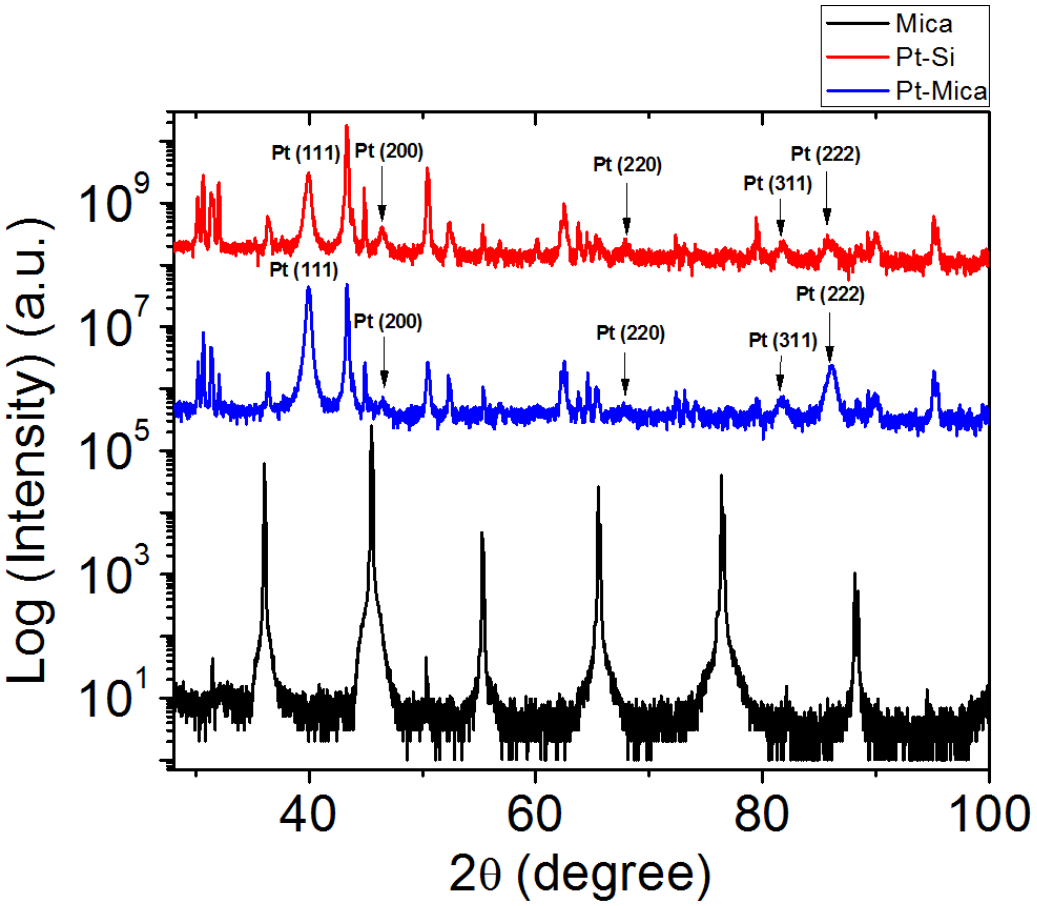

Figure 7.5: X-ray diffraction curves of platinum detached from mica (blue) and silicon (red) and the X-ray diffraction curve of the used mica (black).

For monolayer formation and molecular applications, it is crucial both, crystal orientation and surface grain size. The cristallinity of the fabricated metallic structures was characterized by X-ray diffraction (XRD) using a Bragg-Brentano configuration and $1/4^o$ slits. XRD measurements were performed using Cu Kα radiation ($\lambda = 1.5418$ Å). XRD scans of the structures

are shown in Figures 7.5 and 7.6. It is observed that ⟨111⟩ diffraction peaks are predominant. Moreover, in Figure 7.5 we can see the ⟨200⟩, ⟨220⟩ and the ⟨311⟩ diffraction peaks. The relative intensity values, as compared with those at ⟨111⟩ orientation are 1.68%, 1.36% and 1.68% respectively, when platinum is grown on mica substrates. For silicon substrates, the relative intensity values are 13.83%, 8.69% and 7.74%. Thus, it is possible to confirm the dominance of the ⟨111⟩ crystalline texture, as compared with their expected intensities for randomly oriented polycrystalline platinum (47.55%, 27.67% and 30.79%) [133]. None of the mica peaks (black) appear on the blue scan. The other peaks shown in Figure 7.5 are due to chromium, copper and tin-lead alloy, which are present in the spectrum due to the extremely thin layer of platinum, which is reached by the X-rays.

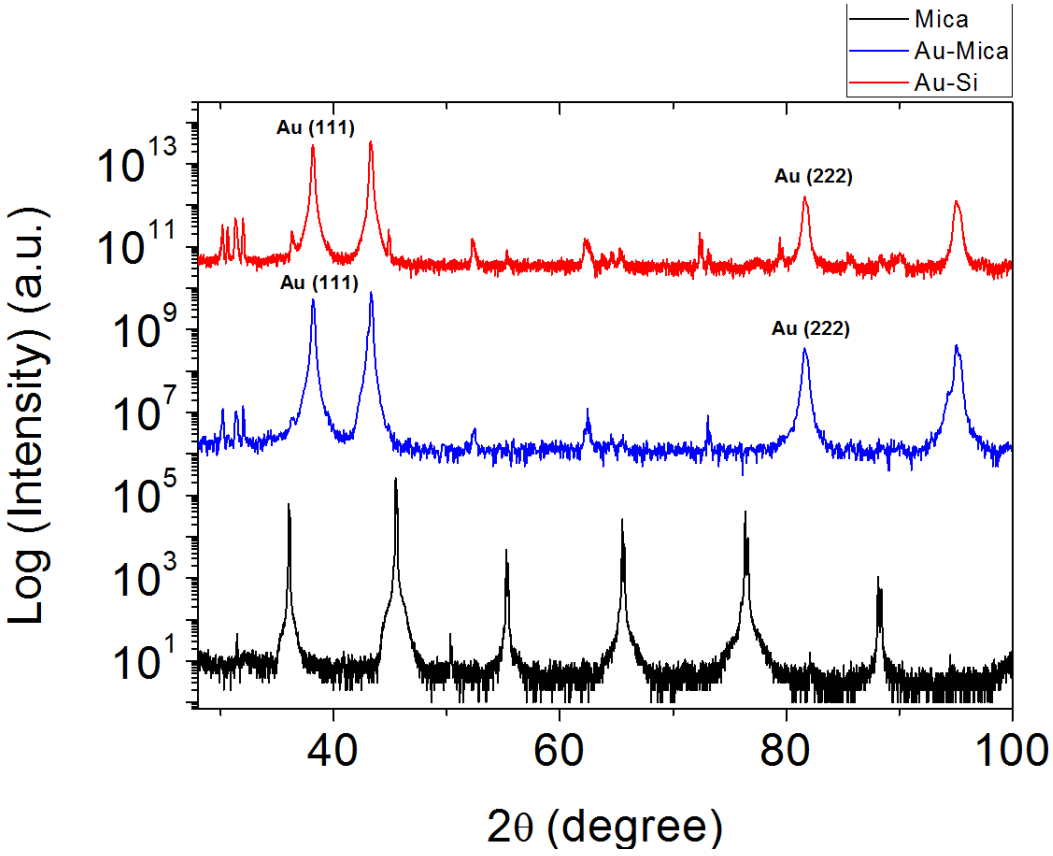

Figure 7.6: X-ray diffraction curves of gold detached from mica (blue) and silicon (red) and the X-ray diffraction curve of the used mica (black).

As well as for platinum, it is shown in Figure 7.6 that the ⟨111⟩ diffraction peak is the one that dominates in the gold diffractogram. Since we do not observe the presence of ⟨200⟩, ⟨220⟩ and ⟨311⟩ diffraction peaks, neither for mica or silicon substrates, we can confirm a primarily ⟨111⟩ crystalline texture. As in the case of platinum, there are no mica diffraction peaks (black) in the gold diffractogram curve (blue). The other peaks in Figure 7.6 come from copper and tin-lead alloy.

7.3 Conclusions

In this chapter, we have demonstrated than solvent resistant ultraflat metal surfaces can be prepared by means of template-stripping methods, with no need of a clean room environment

or expensive and difficult processes. Remarkably, it is a highly reproducible method. These surfaces have $\langle 111 \rangle$ preferential orientation and a long range flatness, up to length scales of 25×25 μm^2. Furthermore, the use of tin-lead alloy instead of epoxies gives the samples robustness and stability over time, as well as ultra-high vacuum, water and organic solvent resistance. This technique is also helpful for UHV measurements since no volatile elements are used during fabrication.

Conclusions and perspectives

Conclusions

- The main objective of this thesis was the application of the magnetostrictive effect to the actuation of the cantilevers used in Atomic Force Microscopy. For that purpose, cantilevers coated with a magnetostrictive film were used in a specially designed liquid cell and tested by means of acquiring different organic molecules images. Despite the scientific studies performed in this thesis, the application of the already well known magnetostrictive concepts to obtained real cantilever actuator has required an engineer work.

  We have developed this novel cantilever excitation technique with the aim of overcoming the different drawbacks of the current methods. Magnetostrictive actuation provides clean cantilever resonance spectra in liquid environment, which is fundamental for AFM quantitative imaging.

- Analytical theoretical models and computational simulations based on finite element methods were applied with the purpose of comparing the efficiency and the oscillation amplitude of the different actuation techniques, which were also experientially tested. Both, theory and experiments, have shown that magnetostrictive excitation presents higher efficiency and strength in exciting high resonance modes as compared to the other magnetic actuation methods. This is relevant in Multifrequency AFM, as some of the techniques enclosed in that AFM sub-field use the cantilever high resonance modes for imaging.

- In order to perform AFM imaging by means of the magnetostrictive actuation, a liquid cell was designed. This liquid cell is compatible with a Nanotec Electrónica AFM microscope. This work was performed in collaboration with the company Nanotec Electrónica, under a knowledge transfer to industry project (TRA2009_0206).

  The successive steps in the cell design were presented, overcoming the main problems that appeared during the design process. Since in magnetostrictive actuation the magnet is not placed underneath the sample, but above the cantilever, an inverted optical microscope can be placed under the sample. This configuration is becoming highly demanded by bio-AFM researchers. In the final design, the electromagnet was placed close to the cantilever to increase the magnetic field generated at low currents, a key feature to prevent thermal issues related to the Joule dissipation in the coil. The position and shape of the electromagnet allow the application of a magnetic field parallel to the cantilever surface, which is a fundamental arrangement for a proper magnetostrictive actuation. In addition, in the new design, the electromagnet vibration produces low mechanical noise in the liquid cell. Furthermore, the magnetostrictive material used in the cantilever coating presents a high corrosion resistance when immersed in water environments and, as it is deposited on the cantilever side which is opposite to the tip side, the radius is maintained. Some images in liquid environment were shown as a preliminar test: thiol islands on gold

terraces, carbohydrate monolayers on graphite or fatty acids on mica.

A patent (Corrosion-resistant magnetostrictive micro-mechanical element for microactuators and dynamic mode atomic force microscopy and operation compatible with corrosive media. M. Penedo, I. Fernández-Martínez, J. L. Costa-Krämer, M. Luna and F. Briones. WIPO Patent WO/2010/043746A1, April 2010) has been registered based on part of this thesis research results. Although a similar idea has already been registered in another patent [134], it is not until this thesis work when, for the first time, magnetostriction has been successfully implemented as a reliable (feasible) cantilever excitation method.

- We have also approached the magnetostrictive cantilever actuation in a original way: instead of a sinusoidal excitation whose amplitude must be low in order to avoid thermal issues in the liquid cell, short magnetic pulses at high amplitude are applied to the cantilever by means of two mutually perpendicular electromagnets, taking advantage of the magnetic rotational hysteresis in the thin magnetostrictive coating film. This actuation method is particularly useful because it minimizes thermal dissipation effects, providing at the same time clean and controllable resonances spectra in liquids. Another important feature of this technique is that it is able to excite the harmonics of the fundamental frequency, increasing its oscillation amplitude and becoming an interesting tool for Multifrequency AFM.

- In the search for further increase of the high resonance modes efficiency and oscillation amplitude, an original method was developed with the purpose of enhancing the oscillation amplitude of individual eigenmodes. Our previous theoretical study had shown that it is possible to enhance a particular resonance mode by adequately patterning the magnetostrictive coating layer on cantilever specific areas. To etch the magnetostrictive film a Focused Ion Beam system was used. This enhancement was experimentally confirmed, paving the way to the use of high resonance modes which are otherwise unreachable due to the low efficiency of other magnetic actuation methods and also due to the small magnetic field generated by the electromagnets at high frequencies. The same Focused Ion Beam system was used, as well, to locally change the magnetic properties of the magnetostrictive material, by means of Ga^+ ions implantation. This procedure presents the advantage of reducing the damages on the microcantilever.

- In the context of Scanning Probe Microscopy in liquid environments, a novel technique to fabricate solvent resistant ultraflat surfaces of different metals (gold, aluminum, platinum or copper) was developed by means of template-stripping. The technique is based on the multilayer deposition of different metals on mica or silicon. It allows low temperature tin welding to copper, which leads to a water resistant support. This technique overcomes the problems that present the traditional methods based on epoxies which, after being immersed in water for a long time, swell and generate film roughness. This original development can lead to an industrial product and consequently, the results were not published.

Summarizing, in this thesis we have developed a novel magnetostrictive actuation technique for the cantilevers used in AFM that overcomes the different drawbacks of the current methods: the generation of spurious resonances, the inefficiency in exciting high resonance modes, or the heating of the liquid media. This new method not only provides clean spectra and high efficiency and strength in the excitation of high resonance modes but also, by means of etching cantilever specific areas of the magnetostrictive coating, it is possible to further increase the oscillation amplitude and efficiency of the cantilever high resonance modes. Moreover, the same effect can

be achieved by Ga^+ implantation, by locally changing the magnetic properties of the material and reducing, as well, the damage on the cantilever. We have also designed and built a liquid cell for the magnetostrictive actuation, specially designed to be used in a Nanotec Electrónica AFM. Finally, we have developed a different and original approach to the magnetostrictive actuation, by applying short magnetic pulses, reducing the thermal effect due to the small current pulses and increasing the oscillation amplitudes of the harmonics, ideal for Multifrequency AFM.

Perspectives

Good perspectives for better performance and reproducibility of magnetostrictive actuation are expected by growing the magnetostrictive film through shadow masks on cantilever specific surface areas during the microfabrication process. In this way, the evaporation of the materials on the specific areas would be simpler and would reduce the damage to the cantilever. The aim of this exploratory work was to show how a smart patterning of the cantilever can enhance the oscillation amplitude of high resonance modes.

The high efficiency of the magnetostrictive cantilever actuation can also be advantageous for resonant cantilever bio/chemical sensors. This is due to high efficiency of high resonance modes excitation in air and in liquids, which maximizes the sensitivity of these devices.

This novel magnetostrictive actuation method will certainly improve AFM imaging in liquid environments, both for qualitative and quantitative measurements. For AFM in liquids, in particular, it opens the chances to sensitivity improvement: the higher the resonance mode, the higher the quality factor and sensitivity. Magnetostrictive actuation will improve the current Mutifrequency techniques and opens the the possibility to create new methods which require higher modes high oscillation amplitudes produced efficiently and with low noise.

Conclusiones y perspectivas

Conclusiones

- El objetivo principal de esta tesis ha sido la aplicación del efecto magnetostrictivo en la actuación de las micropalancas usadas en el Microscopio de Fuerzas Atómicas (AFM). Con esta finalidad, se han utilizado micropalancas con recubrimiento magnetostrictivo en celdas líquidas especialmente diseñadas para medir diferentes materiales biológicos y demostrar así el potencial de este método innovador de actuación magnetostrictiva. Este trabajo de ingeniería ha buscado la aplicación de conceptos magnetostrictivos bien establecidos en actuadores para la excitación de micropalancas.

  Hemos desarrollado esta innovadora técnica de excitación de micropalancas con el propósito de superar los problemas que presentan las técnicas actuales. La actuación magnetostrictiva proporciona espectros de resonancia de micropalancas limpios en entornos líquidos. Esto es fundamental para el análisis cuantitativo de las medidas AFM.

- Se han desarrollado modelos teóricos analíticos y computacionales basados en elementos finitos para comparar la eficiencia y la amplitud de oscilación de varias técnicas de actuación, siendo experimentalmente contrastados. Teoría y experimentos han mostrado que la excitación magnetostrictiva presenta una mayor eficiencia y fuerza en la excitación de los modos altos de resonancia en comparación con otras técnicas de actuación magnética. Estos resultados tienen una gran implicación en el AFM Multifrecuencia, ya que algunas de las técnicas encuadradas dentro de este sub-campo de AFM utilizan modos altos de resonancia de las micropalancas para la medición.

- Con la intención de realizar medidas AFM utilizando la actuación magnetostrictiva se diseñó una celda líquida. Esta celda líquida es compatible con el AFM comercial de Nanotec Electrónica. Este trabajo ha sido realizado en colaboración con la empresa Nanotec Electrónica, bajo un proyecto de transferencia de conocimiento a la industria (TRA2009_0206).

  Se han presentado las sucesivas etapas en el diseño de la celda, superando los problemas principales que han aparecido durante todo el proceso de desarrollo. Debido a que el electroimán no está situado bajo la muestra sino dentro de la celda líquida sobre la micropalanca, se posibilita un diseño de AFM donde un microscopio óptico invertido puede ser situado bajo la muestra. Esta configuración está siendo altamente demandada por investigadores bio-AFM. Además, el electroimán ha sido situado cerca de la micropalanca para incrementar el campo magnético generado a corrientes bajas, una característica clave para prevenir problemas de calentamiento relacionadas con disipación Joule en los hilos de cobre del electroimán. La posición y forma del electroimán permite la aplicación de un campo magnético paralelo a la superficie de la micropalanca, aspecto imprescindible para una actuación magnetostrictiva correcta. Además, la vibración del electroimán produce

un ruido mecánico bajo en la celda líquida. El material magnetostrictivo usado en el recubrimiento de la micropalanca presenta una alta resistencia a la corrosión en entornos líquidos y, como es depositado sobre la superficie de la micropalanca opuesta a la punta, el radio efectivo de ésta no se ve afectado. Como prueba de funcionamiento se han realizado medidas de islas de tioles sobre oro, monocapas de carbohidratos sobre grafito o ácidos grasos sobre mica.

Se ha registrado una patente (Corrosion-resistant magnetostrictive micro-mechanical element for microactuators and dynamic mode atomic force microscopy and operation compatible with corrosive media. M. Penedo, I. Fernández-Martínez, J. L. Costa-Krämer, M. Luna and F. Briones. WIPO Patent WO/2010/043746A1, April 2010) a lo largo de la investigación realizada en esta tesis. Aunque una idea similar había sido ya previamente registrada [134], no es hasta este trabajo de tesis cuando, por primera vez, la actuación magnetostrictiva ha sido implementada de forma fiable.

- Nos hemos aproximado de una manera original a la actuación magnetostrictiva de micropalancas: en lugar de una excitación sinusoidal, cuya amplitud debe ser baja para evitar problemas térmicos en la celda líquida, aplicamos pulsos magnéticos cortos de alta amplitud a la micropalanca en dos direcciones mutuamente perpendiculares mediante dos electroimanes, aprovechando la histéresis magnética rotacional de la capa magnetostrictiva de la micropalanca. Este método de actuación es particularmente útil, ya que minimiza efectos de disipación térmica, proporcionando simultáneamente espectros de resonancia limpios y controlables en líquidos. Otra característica importante de la técnica es la capacidad de excitación de armónicos de la frecuencia fundamental, aumentando su amplitud de oscilación, transformando esta técnica en una herramienta útil para AFM Multifrecuencia.

- En la búsqueda de un mayor aumento de la eficiencia y de la oscilación de los modos altos de resonancia de la micropalanca, se ha desarrollado un método original de incremento selectivo de la amplitud de un modo de resonancia en particular. Un estudio teórico previo ha mostrado que es posible aumentar la amplitud de oscilación de una resonancia particular a través de un patrón adecuado de la capa magnetostrictiva en determinadas áreas de la micropalanca. Con este objetivo, se ha eliminado el recubrimiento en áreas específicas de las micropalancas mediante la técnica por Haz de Iones Focalizados (FIB). Este aumento en la eficiencia y la oscilación ha sido experimentalmente confirmado, permitiendo el uso de modos altos de resonancia imposibles de conseguir con la eficiencia típica de los modos de actuación magnética y los bajos campos magnéticos generados por los electroimanes a altas frecuencias. Además, el mismo efecto fue generado con la implantación de iones de Ga^+ con el FIB, que inducen un cambio local en las propiedades magnéticas del material magnetostrictivo y reduce el daño en las micropalancas.

- En el contexto de la microscopía de sonda de barrido en entornos líquidos, se ha desarrollado una técnica novedosa para fabricar superficies ultra planas de diferentes metales (oro, aluminio, platino o cobre), resistentes a líquidos según el método de "template stripping". La técnica está basada en el depósito de multicapas de diferentes metales sobre mica o silicio, soldando finalmente la estructura a estaño, transformándose en un soporte resistente a medios acuosos. Esta técnica supera los problemas que presentan los métodos tradicionales basados en resinas que, después de inmersiones largas en líquidos, absorben agua y generan rugosidad en la superficie. Este desarrollo original podría ser utilizado industrialmente, por lo que los resultados no han sido publicados.

En resumen, en esta tesis se ha desarrollado una técnica original de actuación magnetostrictiva para las micropalanca usadas en AFM que supera los diferentes problemas existentes en las

técnicas de excitación actuales: generación de resonancias espurias, ineficiencia en la excitación de los modos altos de resonancia, o calentamiento del medio liquido. Este nuevo método no solo proporciona espectros de resonancia limpios con alta eficiencia y fuerza en la excitación de estos modos de resonancia, sino que, mediante patrones específicos de la capa magnetostrictiva sobre de la micropalanca, es posible un mayor aumento en la oscilación y eficiencia de los modos altos de resonancia de la micropalanca. De igual modo, se puede conseguir el mismo efecto con la implantación de iones de Ga^{+}, con un cambio local de las propiedades magnéticas del material, reduciendo también el daño en las micropalancas. También hemos diseñado y construido una celda líquida para la actuación magnetostrictiva, especialmente diseñada para ser usada en un microscopio AFM de la empresa Nanotec Electrónica. Finalmente, hemos desarrollado un método de excitación de micropalancas original, mediante la aplicación de pulsos magnéticos cortos, reduciendo los efectos térmicos y aumentando las amplitudes de oscilación de los armónicos de la frecuencia fundamental, algo deseable en AFM Multifrecuencia.

Perspectivas

Se espera una mejor reproducibilidad en el aumento de la eficiencia y oscilación con la deposición de la capa magnetostrictiva a través de máscaras de sombra en áreas específicas de la micropalanca durante el proceso de microfabricación, simplificando el proceso y asimismo reduciendo el daño en la palanca. Pero la intención de este trabajo exploratorio ha sido mostrar cómo un recubrimiento en áreas específicas de la micropalanca puede incrementar la amplitud de oscilación de los modos altos de resonancia.

La alta eficiencia de la actuación de la micropalanca puede ser utilizada en sensores bio/químicos basados en micropalancas. Esto es debido a la alta eficiencia en la excitación de los modos altos de resonancia, maximizando así la sensibilidad en estos sensores mecánicos.

Este método de actuación magnetostrictiva puede mejorar el funcionamiento del AFM en entornos líquidos, tanto para medidas cualitativas como cuantitativas. Para el AFM en líquidos, en particular, abre la puerta a la mejora de la sensibilidad: el uso de modos más altos de resonancia con factores de calidad más altos hace que la sensibilidad aumente. La actuación magnetostrictiva mejorá las técnicas acutales de AFM Multifrecuencia, posibilitando la creación de nuevos métodos que requieran el uso de modos altos de resonancia con grandes amplitudes de oscilación producidas eficientemente y con bajo ruido.

Appendices

Appendix A

Mathematical functions

A.1 Hydrodynamic function

Equation 4.19 comes from the result of the Navier-Stokes equations for incompressible fluids assuming harmonic small velocities

$$\nabla \cdot \hat{u} = 0, \qquad \nabla \cdot \hat{P} + \eta \nabla^2 \cdot \hat{u} = -i\rho\omega\hat{u} \tag{A.1}$$

where $\hat{u}$ and $\hat{P}$ are, respectively, the Fourier transformed velocity and pressure field, ρ is the density of the fluid and η is its viscosity.

In order to calculate the hydrodynamic function, we use a numerical approximation of Maali [135], based on Sader calculations [88]

$$\Gamma_r = c_1 + c_2 \left(\frac{\delta}{b}\right) \tag{A.2}$$

$$\Gamma_i = d_1 \frac{\delta}{b} + d_2 \left(\frac{\delta}{b}\right)^2 \tag{A.3}$$

where Γ_r and Γ_i are the real and the imaginary part of $\Gamma(\omega)$. The parameters for an infinitely thin ($d \ll b, d \ll L$) rectangular beam are $c_1 = 1.0553$, $c_2 = 3.7997$, $d_1 = 3.8018$ and $d_2 = 2.7364$. δ is the length giving the thickness of the thin viscous layer surrounding the cantilever in which the velocity has dropped by a factor of $1/e$. It is defined by [136]

$$\delta = \sqrt{\frac{2\eta}{\rho_{fluid}\omega}} \tag{A.4}$$

A.2 Green's function

To derive the Green's function $G(x, x', \omega)$, we notice that the governing equation for $G(x, x', \omega)$ is

$$\frac{\partial^4 G(x, x', \omega)}{\partial x^4} - B^4 G(x, x', \omega) = \delta(x - x') \tag{A.5}$$

where $\delta(x - x')$ is the Dirac delta function. The boundary conditions for $G(x, x', \omega)$ at the clamped and free ends of the cantilever are

$$\left[G(x,x',\omega) = \frac{\partial G(x,x',\omega)}{\partial x}\right]_{x=0} = 0 \tag{A.6}$$

$$\left[\frac{\partial^2 G(x,x',\omega)}{\partial x^2} = \frac{\partial^3 G(x,x',\omega)}{\partial x^3}\right]_{x=1} = 0 \tag{A.7}$$

And the $G(x,x',\omega)$ Green's function is

$$G(x,x',\omega) = \frac{1}{4B(\omega)^3\left[1+cosB(\omega)coshB(\omega)\right]} \times$$
$$\times \begin{cases} ([cosB(\omega)+coshB(\omega)][coshB(\omega)x - cosB(\omega)x] \\ +[sinB(\omega)-sinhB(\omega)][sinhB(\omega)x - sinB(\omega)x]) \\ \times(sin(B(\omega)[x'-1]) + sinh(B(\omega)[x'-1])) \\ +([cosB(\omega)+coshB(\omega)][sinB(\omega)x - sinhB(\omega)x] \\ -[sinB(\omega)+sinhB(\omega)][cosB(\omega)x - coshB(\omega)x] \\ \times[cos(B(\omega)[x'-1]) + cosh(B(\omega)[x'-1])]) : 0 \le x \le x' \le 1 \\ \\ ([cosB(\omega)+coshB(\omega)][coshB(\omega)x' - cosB(\omega)x'] \\ +[sinB(\omega)-sinhB(\omega)][sinhB(\omega)x' - sinB(\omega)x']) \\ \times(sin(B(\omega)[x-1]) + sinh(B(\omega)[x-1])) \\ +([cosB(\omega)+coshB(\omega)][sinB(\omega)x' - sinhB(\omega)x'] \\ -[sinB(\omega)+sinhB(\omega)][cosB(\omega)x' - coshB(\omega)x'] \\ \times[cos(B(\omega)[x-1]) + cosh(B(\omega)[x-1])]) : 0 \le x' \le x \le 1 \end{cases} \tag{A.8}$$

A.3 Bilayered cantilever constants

For a bilayered cantilever, the effective Young's modulus E_{eff} is [137]

$$E_{eff} = \frac{E_1^2 r_1^4 + E_2^2 r_2^4 + 2E_1E_2r_1r_2(2r_1^2+2r_2^2+3r_1r_2)}{E_1r_1+E_2r_2} \tag{A.9}$$

where E_1 and E_2 are the Young's modulus of each layer, and r_1 and r_2 are

$$r_1 = d_1/d \qquad r_2 = d_2/d \tag{A.10}$$

where $d = d_1 + d_2$ and d_1 and d_2 are the thickness of first and second layer respectively. The effective density ρ_{eff} is

$$\rho_{eff} = \rho_1 r_1 + \rho_2 r_2 \tag{A.11}$$

Or

$$\mu_{eff} = dbL\rho_{eff} \tag{A.12}$$

where d, b and L are the total thickness, the width and the length of the cantilever respectively.

The neutral axis z_0 is [138]

$$z_0 = \frac{1}{2}\frac{E_1d_1^2 - E_2d_2^2}{E_1d_1 - E_2d_2} \tag{A.13}$$

Appendix B

Green's functions solution

B.1 Ideal acoustic actuation

The cantilever response in the ideal acoustic excitation case is due to the periodic movement of cantilever base, as shown in Figure 4.5. The governing equation for the deflection of the cantilever can be written in the following form [93]

$$EI\frac{\partial^4 u(x,t)}{\partial x^4} + \mu\frac{\partial^2 u(x,t)}{\partial t^2} = f_h(x,t) \tag{B.1}$$

where $u(x,t)$ is the absolute cantilever motion and $f_h(x,t)$ is the hydrodynamic force per unit length to cantilever motion. Since $w(x,t) = u(x,t) - y(t)$

$$EI\frac{\partial^4 w(x,t)}{\partial x^4} + \mu\frac{\partial^2 w(x,t)}{\partial t^2} + \mu\frac{\partial^2 y(t)}{\partial t^2} = f_h(x,t) \tag{B.2}$$

Scaling the spatial variable x with the length of the beam L ($\zeta = \frac{x}{L}$) and taking the Fourier transform of Equation B.1

$$\frac{EI}{L^4}\frac{\partial^4 W(\zeta,\omega)}{\partial \zeta^4} - \mu\omega^2 W(\zeta,\omega) = F_h(\zeta,\omega) + \mu\omega^2 Y(\omega) \tag{B.3}$$

Rearranging as Equation 4.24

$$\frac{d^4 W(\zeta,\omega)}{d\zeta^4} - B^4(\omega)W(\zeta,\omega) = \frac{\mu\omega^2 L^4}{EI}Y(\omega) \tag{B.4}$$

Comparing Equation B.4 with Equation 4.24, we can note that

$$s_{acoustic}(\zeta,\omega) = \frac{\mu\omega^2 L^4}{EI}Y(\omega) \tag{B.5}$$

We can define the motion of the cantilever

$$W_{acoustic}(\zeta,\omega) = \int_0^1 G(\zeta,\zeta',\omega)\frac{\mu\omega^2 L^4}{EI}Y(\omega)d\zeta' \tag{B.6}$$

Since $Y(\omega)$ is ζ' independent

$$W_{acoustic}(\zeta,\omega) = \frac{\mu\omega^2 L^4}{EI}Y(\omega)\int_0^1 G(\zeta,\zeta',\omega)d\zeta' \tag{B.7}$$

B.2 Magnetic gradient and Brownian actuation

The cantilever movement is consequence of the magnetic gradient force between a non homogeneous magnetic field and the magnetic film growth on the cantilever. We suppose a magnetic film is directly evaporated onto the cantilever as we can see in Figure 4.6. The cantilever bends under the influence of magnetic force acting on the film, due to a magnetic gradient. A magnetic field on z direction magnetizes the magnetic film on the cantilever, creating a constant magnetic moment $\mathbf{m}$. The magnetic force acting on a magnetic moment $\mathbf{m}$ can be written as the derivative of the magnetic energy [94]

$$d\mathbf{F}_{grd} = \nabla(d\mathbf{m} \cdot \mathbf{B}) = \nabla(\mathbf{M}_{film} dV \cdot \mathbf{B}) \tag{B.8}$$

From equation 4.45, the net force per unit length is

$$F_{gradient} = M_{film,z}\, b\, d_2 \cos(\varphi) \frac{\partial B_z}{\partial z} \tag{B.9}$$

Then, the normalized external driving force $s(\zeta, \omega)$ per unit length is

$$s_{gradient}(\zeta, \omega) = \frac{M_{film,z}\, b\, d_2 \cos(\varphi) L^4}{EI} \frac{\partial B_z}{\partial z} \tag{B.10}$$

And the motion of the cantilever

$$\begin{aligned} W_{gradient}(\zeta, \omega) &= \int_0^1 G(\zeta, \zeta', \omega) \frac{M_{film,z}\, b\, d_2 \cos(\varphi) L^4}{EI} \frac{\partial B_z}{\partial z} d\zeta' \\ W_{gradient}(\zeta, \omega) &= \frac{M_{film,z}\, b\, d_2 \cos(\varphi) L^4}{EI} \frac{\partial B_z}{\partial z} \int_0^1 G(\zeta, \zeta', \omega) d\zeta' \end{aligned} \tag{B.11}$$

We also can consider as homogeneously distributed force the Brownian motion. The only difference with the case above is that the magnetic gradient force is frequency independent, but the Brownian motion is frequency dependent [93]

$$F_{Brownian}(\omega) = 4K_B T \left(\frac{\pi}{4} \rho b^2\right) \omega\ img\left\{\Gamma(\omega)\right\} \tag{B.12}$$

where K_B is Boltzmanns constant, T is the absolute temperature, ρ is the density of the fluid and $img\left\{\Gamma(\omega)\right\}$ indicates the imaginary part of the hydrodynamic function $\Gamma(\omega)$. As before, the normalized external driving force $s(\zeta, \omega)$ per unit length is

$$s_{Brownian}(\zeta, \omega) = \frac{F_{Brownian}(\omega) L^4}{EI} \tag{B.13}$$

And the motion of the cantilever

$$W_{Brownian}(\zeta, \omega) = \frac{F_{Brownian}(\omega) L^4}{EI} \int_0^1 G(\zeta, \zeta', \omega) d\zeta' \tag{B.14}$$

B.3 Magnetic torque actuation

In this method, the magnetic film is magnetized on x direction (Figure 4.7), and a oscillatory magnetic field $\mathbf{B}$ is uniformly distributed on z direction, led to a distributed applied moment on the microcantilever. From equation 4.51, the force per unit length is

$$F_T(x) = M_x B_z \sin(\varphi) d_2 b(\delta(x) - \delta(x - L)) \tag{B.15}$$

Scaling $\zeta = \frac{x}{L}$, the force per unit length is

$$F_{torque}(\zeta) = M_x B_z \sin(\varphi) d_2 b(\delta(\zeta) - \delta(\zeta - 1)) \tag{B.16}$$

Then, the normalized external driving force $s(\zeta, \omega)$ is

$$s_{torque}(\zeta, \omega) = \frac{M_x B_z \sin(\varphi) d_2 b\, L^4}{EI}(\delta(\zeta) - \delta(\zeta - 1)) \tag{B.17}$$

And the motion of the cantilever is

$$\begin{aligned} W_{torque}(\zeta, \omega) &= \int_0^1 G(\zeta, \zeta', \omega) \frac{M_x B_z \sin(\varphi) d_2 b\, L^4}{EI}((\delta(\zeta') - \delta(\zeta' - 1)))d\zeta' \\ W_{torque}(\zeta, \omega) &= \frac{M_x B_z \sin(\varphi) d_2 b\, L^4}{EI} \int_0^1 G(\zeta, \zeta', \omega)(\delta(\zeta') - \delta(\zeta' - 1))d\zeta' \\ W_{torque}(\zeta, \omega) &= \frac{M_x B_z \sin(\varphi) d_2 b\, L^4}{EI}(G(\zeta, 0, \omega) - G(\zeta, 1, \omega)) \end{aligned} \tag{B.18}$$

B.4 Magnetostrictive actuation

This excitation can be induced by different phenomena: photothermal [97], piezoelectricity [98] or magnetostriction [62]. However, the excitation basis is the same: a thin film on the cantilever expands and bends the cantilever, periodically in time.

According to Guerrero and Wetherhold in [99], the strains on the x and y axis produced in the magnetostrictive film due to a magnetic field parallel to the surface are

$$\begin{aligned} \epsilon_{xx} &= \frac{3}{2}\lambda_x(\alpha_x^2 - \frac{1}{3}) \\ \epsilon_{yy} &= \frac{3}{2}\lambda_y(\alpha_y^2 - \frac{1}{3}) \end{aligned} \tag{B.19}$$

where λ_x and λ_y are the magnetostriction coefficient of the film in the x and y axis and α_x^2 and α_y^2 are the x and y magnetization directions

$$\begin{aligned} \alpha_x &= \frac{M_x}{M_s} \\ \alpha_y &= \frac{M_y}{M_s} \end{aligned} \tag{B.20}$$

where M_x is the x component of the magnetization and M_s is the saturation magnetization. The normal stress $\sigma_{x,i}$ along the longitudinal direction of a bilayered beam with different expansional strains is

$$\sigma_{x,i} = \frac{E_i}{1 - \nu_i^2}(\epsilon_x - \epsilon_{x,i}^e), \qquad i = f, s \tag{B.21}$$

where $\epsilon_{x,i}^e$ is the expansional strain of the i-layer along the x axis, ϵ_x is the external strain, E_i and ν_i are the Young's modulus and Poisson's ratio of the i-layer.

In agreement with van de Riet [100], for a free cantilever

$$u(x,y,z) = \alpha_x x + \frac{xz}{R_x}$$
$$v(x,y,z) = \alpha_y y + \frac{yz}{R_y}$$
$$w(x,y,z) = \alpha_z z - \frac{x^2}{2R_x} - \frac{y^2}{2R_y} - \frac{\nu z^2}{2(1-\nu)}\left(\frac{1}{R_x} + \frac{1}{R_y}\right) \tag{B.22}$$

where (u,v,w) is the corresponding point on the deformed cantilever, and α_x and R_x are

$$\alpha_x = \frac{E_f d_2}{E_s d_1}\left[\left(1-\nu_f\nu_s\right)\epsilon_{xx} + \left(\nu_f - \nu_s\right)\epsilon_{yy}\right]$$
$$\frac{1}{R_x} = \frac{6}{d_1}\alpha_x \tag{B.23}$$

and similarly for α_y and R_y. The resulting internal bending moment is uniform along x axis

$$M_{int} = -EI\frac{d^2w}{dx^2} = -E_{eff}I(-\frac{1}{R_x}) = \frac{E_{eff}I}{R_x} = K \tag{B.24}$$

If we scale $\zeta = \frac{x}{L}$, and considering that we just have internal bending moment in the interval $[0,1]$ on the cantilever

$$M_{magnetostriction}(\zeta) = K\int_0^1 \delta(\zeta - \zeta_0)d\zeta_0 \tag{B.25}$$

where E_{eff} is defined in A.1. The shear force is [96]

$$Q_{magnetostriction}(\zeta) = \frac{\partial M_{magnetostriction}(\zeta)}{\partial\zeta} = K\int_0^1 \delta'(\zeta - \zeta_0)d\zeta_0 \tag{B.26}$$

And the force per unit length is

$$F_{magnetostriction}(\zeta) = -\frac{\partial Q_{magnetostriction}(\zeta)}{\partial\zeta} = -K\int_0^1 \delta''(\zeta - \zeta_0)d\zeta_0 \tag{B.27}$$

Therefore, the normalized external driving force $s(\zeta,\omega)$ is

$$s_{magnetostriction}(\zeta,\omega) = \frac{-KL^4}{EI}\int_0^1 \delta''(\zeta - \zeta_0)d\zeta_0 \tag{B.28}$$

Finally, due to the delta Dirac function properties, the motion of the cantilever is

$$W_{magnetostriction}(\zeta,\omega) = \int_0^1 G(\zeta,\zeta',\omega)\frac{-KL^4}{EI}\int_0^1 \delta''(\zeta_0 - \zeta)d\zeta_0 d\zeta'$$
$$= \int_0^1 \frac{-KL^4}{EI}\int_0^1 G(\zeta,\zeta',\omega)\delta''(\zeta_0 - \zeta)d\zeta_0 d\zeta' = \int_0^1 \frac{-KL^4}{EI}\int_0^1 G''(\zeta,\zeta',\omega)\delta(\zeta_0 - \zeta)d\zeta_0 d\zeta'$$
$$= \int_0^1 \frac{-KL^4}{EI}G''(\zeta,\zeta',\omega)d\zeta' = \frac{-KL^4}{EI}(G'(\zeta,1,\omega) - G'(\zeta,0,\omega)) \tag{B.29}$$

Appendix C

Lorentz force on cantilevers

C.1 Rectangular cantilevers

The Lorentz force is

$$\mathbf{F} = l(\mathbf{I} \times \mathbf{B}) \tag{C.1}$$

where l is the length of the conductor, $\mathbf{B}$ the magnetic field and $\mathbf{I}$ the current through the conductor.

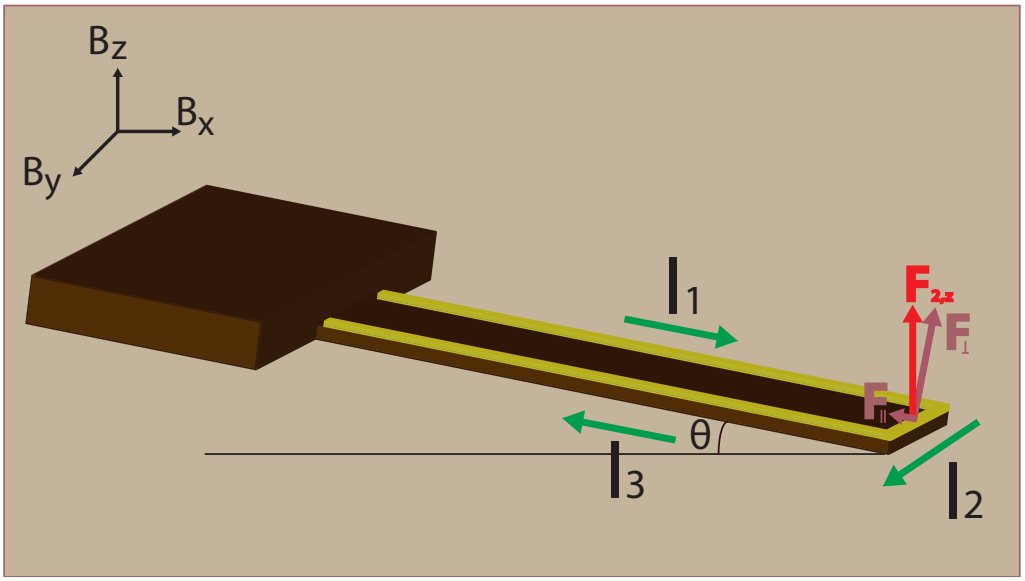

Figure C.1: Scheme of a rectangular cantilever with a gold rectangular wiring path.

We rewrite the components of I_1, I_2 and I_3 through the different paths on the surface of the cantilever

$$\begin{aligned} \mathbf{I}_1 &= I_1 \cos(\theta)\hat{\mathbf{x}} - I_1 \sin(\theta)\hat{\mathbf{z}} \\ \mathbf{I}_2 &= I_2\hat{\mathbf{y}} \\ \mathbf{I}_3 &= -I_3 \cos(\theta)\hat{\mathbf{x}} + I_3 \sin(\theta)\hat{\mathbf{z}} \end{aligned} \tag{C.2}$$

where θ is the angle between the $\hat{\mathbf{x}}$ vector and the long axis of the cantilever. For $\mathbf{I}_1$

$$\mathbf{F}_1 = l_1(\mathbf{I}_1 \times \mathbf{B}) = l_1 I_1 \cos(\theta) B_z \hat{\mathbf{y}} - l_1 I_1 \cos(\theta) B_y \hat{\mathbf{z}} - l_1 I_1 \sin(\theta) B_y \hat{\mathbf{x}} + l_1 I_1 \sin(\theta) B_x \hat{\mathbf{y}} \quad \text{(C.3)}$$

For $\mathbf{I}_2$

$$\mathbf{F}_2 = l_2(\mathbf{I}_2 \times \mathbf{B}) = -l_2 I_2 B_z \hat{\mathbf{x}} + l_2 I_2 B_x \hat{\mathbf{z}} \quad \text{(C.4)}$$

For $\mathbf{I}_3$

$$\mathbf{F}_3 = l_3(\mathbf{I}_3 \times \mathbf{B}) = -l_3 I_3 \cos(\theta) B_z \hat{\mathbf{y}} + l_3 I_3 \cos(\theta) B_y \hat{\mathbf{z}} + l_3 I_3 \sin(\theta) B_y \hat{\mathbf{x}} - l_3 I_3 \sin(\theta) B_x \hat{\mathbf{y}} \quad \text{(C.5)}$$

Taking into account only the $\hat{\mathbf{z}}$ component

$$\begin{aligned} \mathbf{F}_{1,z} &= -l_1 I_1 \cos(\theta) B_y \hat{\mathbf{z}} \\ \mathbf{F}_{2,z} &= l_2 I_2 B_x \hat{\mathbf{z}} \\ \mathbf{F}_{3,z} &= l_3 I_3 \cos(\theta) B_y \hat{\mathbf{z}} \end{aligned} \quad \text{(C.6)}$$

$\mathbf{F}_{1,z}$ and $\mathbf{F}_{3,z}$ creates a pure moment, with forces equal in magnitude ($l_1 = l_3$ and $I_1 = I_3$), oppositely directed, and displaced by perpendicular distance. They have importance in torsional excitation, but in flexural excitation the most important force is $\mathbf{F}_{2,z}$. Now, it is calculated the module of the components normal and parallel to the long axis of the cantilever

$$\begin{aligned} |F_\perp| &= |\mathbf{F}_{2,z}| \cos(\theta) \\ |F_\parallel| &= |\mathbf{F}_{2,z}| \sin(\theta) \end{aligned} \quad \text{(C.7)}$$

Therefore, this is equivalent to a point force at the end of the cantilever, as magnetic torque excitation.

C.2 Triangular cantilevers

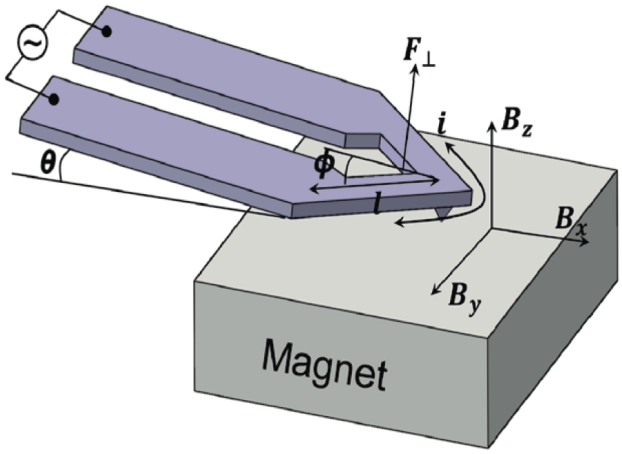

Figure C.2: Scheme of a triangular cantilever. Adapted from [51].

Here, the intensity I can be written as

$$\mathbf{I} = i_x\hat{\mathbf{x}} + i_y\hat{\mathbf{y}} + i_z\hat{\mathbf{z}} \tag{C.8}$$

i_z appears since the cantilever is tilted θ with respect to the main frame. Thus, the Lorentz force is

$$\mathbf{F} = k(i_yB_z - i_zB_y)\hat{\mathbf{x}} + k(i_zB_x - i_xB_z)\hat{\mathbf{y}} + k(i_xB_y - i_yB_x)\hat{\mathbf{z}} \tag{C.9}$$

where k is a constant related to the path of the current I. The component $\hat{\mathbf{y}}$ is not important for the flexural excitation of the cantilever. It is possible to calculate from $\hat{\mathbf{x}}$ and $\hat{\mathbf{z}}$ the module of the normal and parallel components to the long axis of the cantilever of the excitation force

$$\begin{aligned} |F_\perp| &= k(i_yB_z - i_zB_y)\sin(\theta) + k(i_xB_y - i_yB_x)\cos(\theta) \\ |F_\parallel| &= k(i_yB_z - i_zB_y)\cos(\theta) + k(i_xB_y - i_yB_x)\sin(\theta) \end{aligned} \tag{C.10}$$

A simulation of a triangular cantilever OMCL-TR from Olympus ($100\,\mu m$ long, $106\,\mu m$ width and $0.8\,\mu m$ thickness) with a gold coating film (100 nm) was performed in the FEM software COMSOL Multiphysics. A I current of $100\,mA$ is introduced on the gold coating film, and the cantilever is tilted $\theta = 11°$. In Figure C.3 is shown the $\hat{\mathbf{x}}$, $\hat{\mathbf{y}}$ and $\hat{\mathbf{z}}$ components of the current density on gold film.

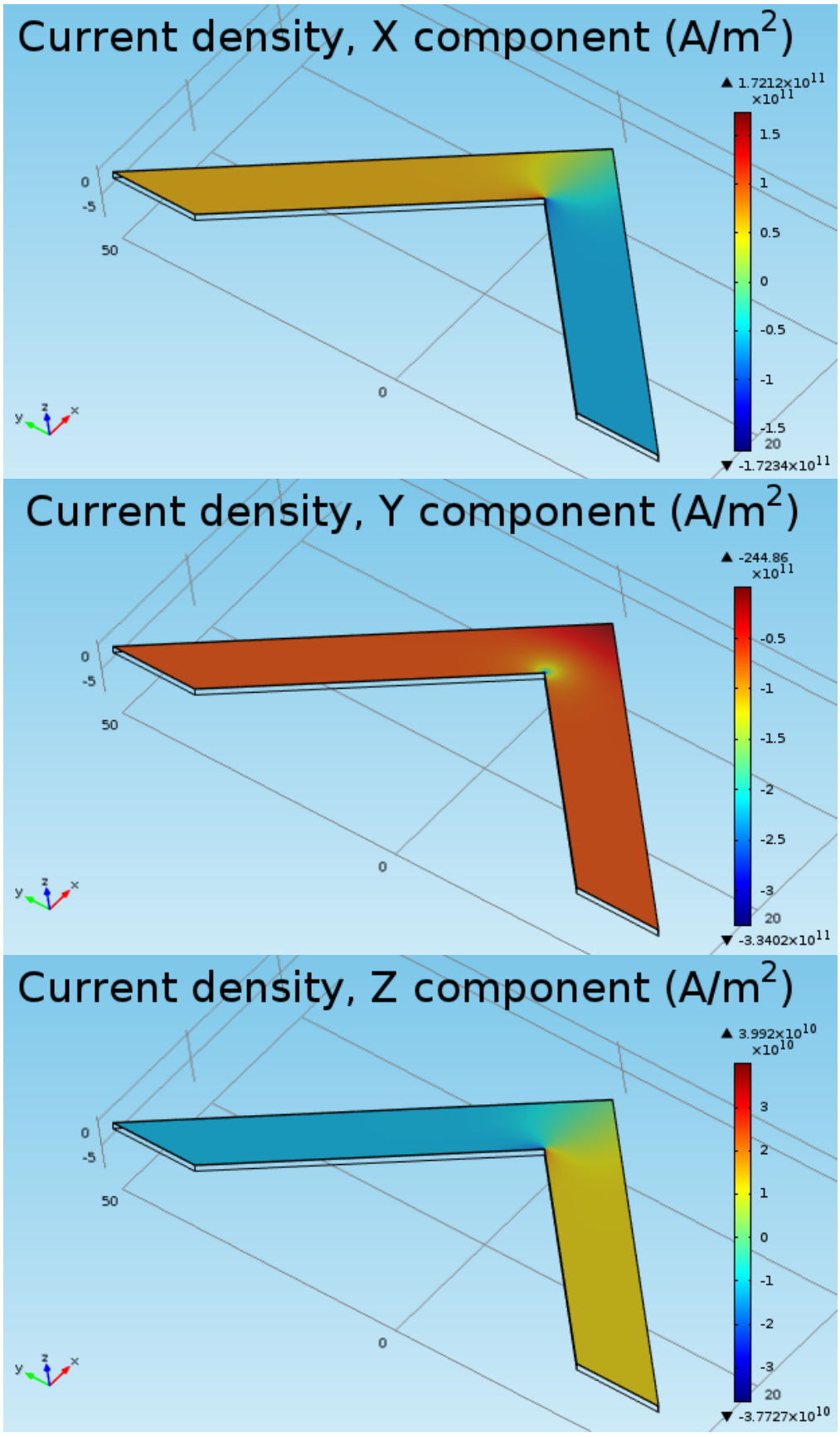

Figure C.3: Images showing the $\hat{\mathbf{x}}$, $\hat{\mathbf{y}}$ and $\hat{\mathbf{z}}$ components of the current density on the gold film coating of a triangular cantilever.

Finally, in Figure C.4 the total pressure on the top of the cantilever surface is shown. There is a point concentration of the pressure around the vertex of the internal triangle of the cantilever. Therefore, it can be approximated as a point force actuation method.

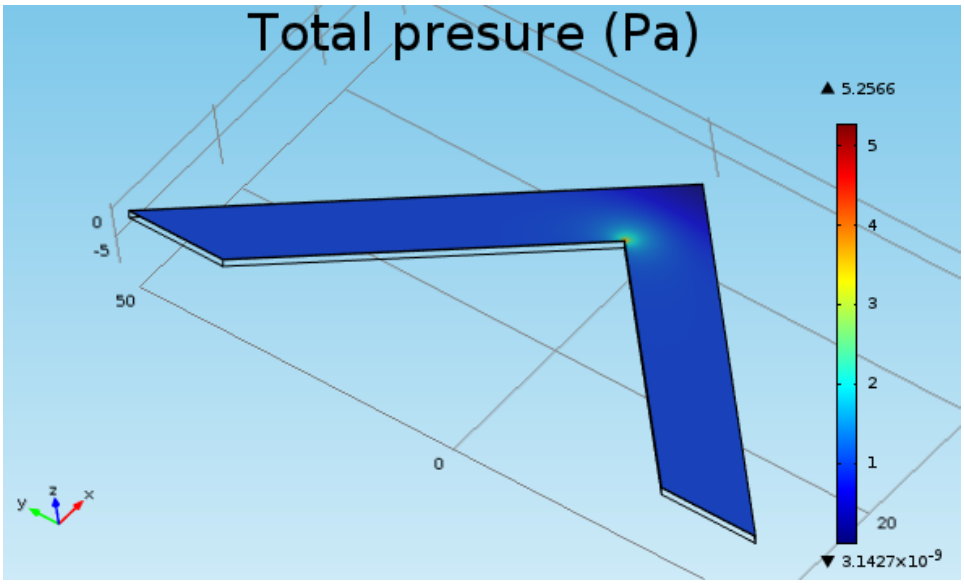

Figure C.4: Total pressure on the top face of the triangular cantilever, perpendicular to the top surface.

Bibliography

[1] B. Bhushan. *Springer Handbook of Nanotechnology* (Springer, 2010)

[2] Y. Martin and H. K. Wickramasinghe. Magnetic imaging by force microscopy with 1000 Å resolution. *Applied Physics Letters* **50**(20), 1455–1457 (1987)

[3] C. V. Manzano, O. Caballero-Calero, S. Hormeño, M. Penedo, M. Luna, and M. Martín-González. ZnO morphology control by pulsed electrodeposition. *The Journal of Physical Chemistry C* **117**(3), 1502–1508 (2013)

[4] L. Fumagalli, G. Gramse, D. Esteban-Ferrer, M. A. Edwards, and G. Gomila. Quantifying the dielectric constant of thick insulators using electrostatic force microscopy. *Applied Physics Letters* **96**(18), 183107 (2010)

[5] D. Martinez-Martin, E. T. Herruzo, J. Dietz, C .and Gomez-Herrero, and R. Garcia. Noninvasive protein structural flexibility mapping by bimodal dynamic force microscopy. *Physical Review Letters* **106**(19), 198101 (2011)

[6] R. D. Piner, J. Zhu, F. Xu, S. Hong, and C. A. Mirkin. "Dip-pen" nanolithography. *Science* **283**(5402), 661–663 (1999)

[7] R. Garcia, M. Calleja, and F. Perez-Murano. Local oxidation of silicon surfaces by dynamic force microscopy: Nanofabrication and water bridge formation. *Applied Physics Letters* **72**(18), 2295–2297 (1998)

[8] D. J. Muller. AFM: A nanotool in membrane biology. *Biochemistry* **47**(31), 7986–7998 (2008)

[9] L. W. Francis, P. D. Lewis, C. J. Wright, and R. S. Conlan. Atomic force microscopy comes of age. *Biology of the Cell* **102**(2), 133–143 (2010)

[10] A. San Paulo and R. Garcia. High-resolution imaging of antibodies by tapping-mode atomic force microscopy: attractive and repulsive tip-sample interaction regimes. *Biophysical Journal* **78**(3), 1599–1605 (2000)

[11] E. T. Herruzo and R. Garcia. The emergence of multifrequency force microscopy. *Nature Nanotechnology* **7**(4), 217–226 (2012)

[12] X. Xu, J. Melcher, S. Basak, R. Reifenberger, and A. Raman. Compositional contrast of biological materials in liquids using the momentary excitation of higher eigenmodes in dynamic atomic force microscopy. *Physical Review Letters* **102**, 060801 (2009)

[13] A. Raman, S. Trigueros, A. Cartagena, A. P. Z. Stevenson, M. Susilo, E. Nauman, and S. A. Contera. Mapping nanomechanical properties of live cells using multi-harmonic atomic force microscopy. *Nature Nanotechnology* **6**(12), 809–814 (2011)

[14] A. Cartagena, M. Hernando-Perez, J. L. Carrascosa, P. J. de Pablo, and A. Raman. Mapping in vitro local material properties of intact and disrupted virions at high resolution using multi-harmonic atomic force microscopy. *Nanoscale* **5**(11), 4729–4736 (2013)

[15] D. Kiracofe, A. Raman, and D. Yablon. Multiple regimes of operation in bimodal AFM: understanding the energy of cantilever eigenmodes. *Beilstein Journal of Nanotechnology* **4**(1), 385–393 (2013)

[16] N. F. Martinez, J. R. Lozano, E. T. Herruzo, F. Garcia, C. Richter, T. Sulzbach, and R. Garcia. Bimodal atomic force microscopy imaging of isolated antibodies in air and liquids. *Nanotechnology* **19**(38), 384011 (2008)

[17] Y. Jun Li, K. Takahashi, N. Kobayashi, Y. Naitoh, M. Kageshima, and Y. Sugawara. Multifrequency high-speed phase-modulation atomic force microscopy in liquids. *Ultramicroscopy* **110**(6), 582–585 (2010)

[18] N. Balke, S. Jesse, A. Morozovska, E. Eliseev, D. Chung, Y. Kim, L. Adamczyk, R. Garcia, N. Dudney, and S. Kalinin. Nanoscale mapping of ion diffusion in a lithium-ion battery cathode. *Nature Nanotechnology* **5**(10), 749–754 (2010)

[19] S. Husale, H. H. Persson, and O. Sahin. DNA nanomechanics allows direct digital detection of complementary DNA and microRNA targets. *Nature* **462**(7276), 1075–1078 (2009)

[20] I. Fernandez Martinez. *Stress and nanostructure control for the development of magnetoelectro-mechanical micro-devices*. PhD Thesis, Universidad Autonoma de Madrid, http://digital.csic.es/handle/10261/12578 (2008), URL `http://digital.csic.es/handle/10261/12578`

[21] G. Binnig, C. F. Quate, and C. Gerber. Atomic force microscope. *Physical Review Letters* **56**, 930–933 (1986)

[22] G. Binnig, H. Rohrer, C. Gerber, and E. Weibel. Tunneling through a controllable vacuum gap. *Applied Physics Letters* **40**(2), 178–180 (1982)

[23] URL `http://www.spmtips.com/`

[24] W. H. Roos and G. J. Wuite. Nanoindentation studies reveal material properties of viruses. *Advanced Materials* **21**(10-11), 1187–1192 (2009)

[25] G. Meyer and N. M. Amer. Novel optical approach to atomic force microscopy. *Applied Physics Letters* **53**(12), 1045 –1047 (1988)

[26] T. Fukuma, M. Kimura, K. Kobayashi, K. Matsushige, and H. Yamada. Development of low noise cantilever deflection sensor for multienvironment frequency-modulation atomic force microscopy. *Review of Scientific Instruments* **76**(5), 053704 –053704–8 (2005)

[27] R. Garcia and R. Perez. Dynamic atomic force microscopy methods. *Surface Science Reports* **47**(6), 197–301 (2002)

[28] B. Anczykowski, D. Krüger, and H. Fuchs. Cantilever dynamics in quasinoncontact force microscopy: Spectroscopic aspects. *Physical Review B* **53**(23), 15485 (1996)

[29] R. Garcia and A. San Paulo. Attractive and repulsive tip-sample interaction regimes in tapping-mode atomic force microscopy. *Physical Review B* **60**(7), 4961 (1999)

[30] J. Cleveland, B. Anczykowski, A. Schmid, and V. Elings. Energy dissipation in tapping-mode atomic force microscopy. *Applied Physics Letters* **72**(20), 2613–2615 (1998)

[31] M. Köber, E. Sahagún, M. Fuss, F. Briones, M. Luna, and J. J. Saenz. Adhesion hysteresis in dynamic atomic force microscopy. *Physica Status Solidi (RRL)* **2**(3), 138–140 (2008)

[32] B. Gotsmann, C. Seidel, B. Anczykowski, and H. Fuchs. Conservative and dissipative tip-sample interaction forces probed with dynamic AFM. *Physical Review Letters* **60**(15), 11051 (1999)

[33] H. Ueyama, Y. Sugawara, and S. Morita. Stable operation mode for dynamic noncontact atomic force microscopy. *Applied Physics A: Materials Science and Processing* **66**, S295–S297 (1998)

[34] T. Albrecht, P. Grütter, D. Horne, and D. Rugar. Frequency modulation detection using high-Q cantilevers for enhanced force microscope sensitivity. *Journal of Applied Physics* **69**, 668 (1991)

[35] T. Uchihashi, M. J. Higgins, S. Yasuda, S. P. Jarvis, S. Akita, Y. Nakayama, and J. E. Sader. Quantitative force measurements in liquid using frequency modulation atomic force microscopy. *Applied Physics Letters* **85**(16), 3575–3577 (2004)

[36] M. J. Higgins, C. K. Riener, T. Uchihashi, J. E. Sader, R. McKendry, and S. P. Jarvis. Frequency modulation atomic force microscopy: a dynamic measurement technique for biological systems. *Nanotechnology* **16**(3), S85 (2005)

[37] B. W. Hoogenboom, H. J. Hug, Y. Pellmont, S. Martin, P. L. T. M. Frederix, D. Fotiadis, and A. Engel. Quantitative dynamic-mode scanning force microscopy in liquid. *Applied Physics Letters* **88**(19), 193109 –193109–3 (2006)

[38] S. Scheuring, P. Ringler, M. Borgnia, H. Stahlberg, D. J. Müller, P. Agre, and A. Engel. High resolution AFM topographs of the Escherichia coli water channel aquaporin Z. *The EMBO journal* **18**(18), 4981–4987 (1999)

[39] C. Carrasco, A. Luque, M. Hernando-Perez, R. Miranda, J. Carrascosa, P. Serena, M. de Ridder, A. Raman, J. Gomez-Herrero, I. Schaap, D. Reguera, and P. de Pablo. Built-in mechanical stress in viral shells. *Biophysical Journal* **100**(4), 1100–1108 (2011)

[40] S. Liu, A. Keong Ng, R. Xu, J. Wei, C. Ming Tan, Y. Yang, and Y. Chen. Antibacterial action of dispersed single-walled carbon nanotubes on Escherichia coli and Bacillus subtilis investigated by atomic force microscopy. *Nanoscale* **2**, 2744–2750 (2010)

[41] N. Kodera, D. Yamamoto, R. Ishikawa, and T. Ando. Video imaging of walking myosin V by high-speed atomic force microscopy. *Nature* **468**(7320), 72–76 (2010)

[42] D. Kiracofe and A. Raman. Quantitative force and dissipation measurements in liquids using piezo-excited atomic force microscopy: a unifying theory. *Nanotechnology* **22**(48), 485502 (2011)

[43] I. Revenko and R. Proksch. Magnetic and acoustic tapping mode microscopy of liquid phase phospholipid bilayers and dna molecules. *Journal of Applied Physics* **87**(1), 526–533 (2000)

[44] E.-L. Florin, M. Radmacher, B. Fleck, and H. E. Gaub. Atomic force microscope with magnetic force modulation. *Review of Scientific Instruments* **65**(3), 639–643 (1994)

[45] S. M. Lindsay, Y. L. Lyubchenko, N. J. Tao, Y. Q. Li, P. I. Oden, J. A. DeRose, and J. Pan. Scanning tunneling microscopy and atomic force microscopy studies of biomaterials at a liquid–solid interface. *Journal of Vacuum Science and Technology A: Vacuum, Surfaces, and Films* **11**(4), 808–815 (1993)

[46] J. P. Cleveland. *Measuring and understanding forces on atomic length scales with the atomic force microscope*. PhD Thesis, University of California, Santa Barbara (1995)

[47] W. Han, S. M. Lindsay, and T. Jing. A magnetically driven oscillating probe microscope for operation in liquids. *Applied Physics Letters* **69**(26), 4111–4113 (1996)

[48] URL `http://www.home.agilent.com/`

[49] URL `http://www.asylumresearch.com/Products/iDrive/iDrive.shtml`

[50] A. Buguin, O. Du Roure, and P. Silberzan. Active atomic force microscopy cantilevers for imaging in liquids. *Applied Physics Letters* **78**(19), 2982–2984 (2001)

[51] B. Lee, C. B. Prater, and W. P. King. Lorentz force actuation of a heated atomic force microscope cantilever. *Nanotechnology* **23**(5), 055709 (2011)

[52] O. Enders, F. Korte, and K. H.-A. Lorentz-force-induced excitation of cantilevers for oscillation-mode scanning probe microscopy. *Surface and Interface Analysis* **36**(2), 119–123 (2004)

[53] N. Umeda, S. Ishizaki, and H. Uwai. Scanning attractive force microscope using photothermal vibration. *Journal of Vacuum Science and Technology B* **9**(2), 1318–1322 (1991)

[54] H. Yamashita, N. Kodera, A. Miyagi, T. Uchihashi, D. Yamamoto, and T. Ando. Tip-sample distance control using photothermal actuation of a small cantilever for high-speed atomic force microscopy. *Review of Scientific Instruments* **78**(8), 083702–083702 (2007)

[55] D. Kiracofe, K. Kobayashi, A. Labuda, A. Raman, and H. Yamada. High efficiency laser photothermal excitation of microcantilever vibrations in air and liquids. *Review of Scientific Instruments* **82**(1), 013702–013702–7 (2011)

[56] Y. J. Li, N. Kobayashi, H. Nomura, Y. Naitoh, M. Kageshima, and Y. Sugawara. High-Speed Phase-Modulation Atomic Force Microscopy in Constant-Amplitude Mode Capable of Simultaneous Measurement of Topography and Energy Dissipation. *Japanese Journal of Applied Physics* **47**(7), 6121–6124 (2008)

[57] P. Paoletti, M. Basso, V. Pini, B. Tiribilli, and M. Vassalli. Self-driven soft imaging in liquid by means of photothermal excitation. *Journal of Applied Physics* **110**(11), 114315–114315 (2011)

[58] A. Labuda, K. Kobayashi, Y. Miyahara, and P. Grutter. Retrofitting an atomic force microscope with photothermal excitation for a clean cantilever response in low Q environments. *Review of Scientific Instruments* **83**(5), 053703–053703 (2012)

[59] T. Fukuma, K. Onishi, N. Kobayashi, A. Matsuki, and H. Asakawa. Atomic-resolution imaging in liquid by frequency modulation atomic force microscopy using small cantilevers with megahertz-order resonance frequencies. *Nanotechnology* **23**(13), 135706 (2012)

[60] I. Fernandez-Martinez, M. Martin-Gonzalez, R. Gonzalez-Arrabal, R. Alvarez-Sanchez, F. Briones, and J. L. Costa-Kramer. Nitrided FeB amorphous thin films for magneto mechanical systems. *Journal of Magnetism and Magnetic Materials* **320**(68-75) (2008)

[61] I. Fernandez-Martinez, J. L. Costa-Kramer, and F. Briones. Stress and magnetoelastic properties control of amorphous $Fe_{80}B_{20}$ thin films during sputtering deposition. *Journal of Applied Physics* **103**(11), 113902–113902–5 (2008)

[62] M. Penedo, I. Fernandez-Martinez, J. L. Costa-Kramer, M. Luna, and F. Briones. Magnetostriction-driven cantilevers for dynamic atomic force microscopy. *Applied Physics Letters* **95**(14), 143505–143505–3 (2009)

[63] B. Kumar, J. C. Bonvallet, and S. R. Crittenden. Dielectric constants by multifrequency non-contact atomic force microscopy. *Nanotechnology* **23**(2), 025707 (2012)

[64] M. Dong, S. Husale, and O. Sahin. Determination of protein structural flexibility by microsecond force spectroscopy. *Nature nanotechnology* **4**(8), 514–517 (2009)

[65] M. Dokukin, N. Guz, R. Gaikwad, C. Woodworth, and I. Sokolov. Cell surface as a fractal: Normal and cancerous cervical cells demonstrate different fractal behavior of surface adhesion maps at the nanoscale. *Physical Review Letters* **107**(2), 028101 (2011)

[66] S. Jesse, S. V. Kalinin, R. Proksch, A. Baddorf, and B. Rodriguez. The band excitation method in scanning probe microscopy for rapid mapping of energy dissipation on the nanoscale. *Nanotechnology* **18**(43), 435503 (2007)

[67] A. del Moral. *Handbook of Magnetostriction and Magnetostrictive Materials* (Del Moral Publisher SL, 2008)

[68] R. O'handley. *Modern magnetic materials: principles and applications* (Wiley New York, 2000)

[69] E. Du Tremolet de Lacheisserie. *Magnetostriction: theory and applications of magnetoelasticity* (Boca Raton Florida: CRC, 1993)

[70] J. L. Costa-Kramer, J. L. Menendez, A. Cebollada, F. Briones, D. Garcia, and A. Hernando. Magnetization reversal asymmetry in Fe/MgO(0 0 1) thin films. *Journal of Magnetism and Magnetic Materials* **210**, 341–348 (2000)

[71] J. L. Menendez, G. Armelles, A. Cebollada, F. Briones, F. Peiro, F. Guell, A. Cornet, M. Fernandez Gubieda, J. Gutierrez, and C. Meyer. Nitrogen incorporation effects in Fe (001) thin films. *Journal of Applied Physics* **89**(11), 6314–6319 (2001)

[72] G. F. Fitzgerald. On the rotation of the plane of polarization of light by reflection from the pole of a magnet. *Proceedings of the Royal Society of London* **25**, pp. 447–450 (1876)

[73] URL `www.nanotec.es`

[74] URL `http://probe.olympus-global.com/`

[75] URL `www.nanosensors.com`

[76] URL `http://www.comsol.es/`

[77] S. Xu, P. Laibinis, and G. Liu. Accelerating the kinetics of thiol self-assembly on gold - A spatial confinement effect. *Journal of the American Chemical Society* **120**(36), 9356–9361 (1998)

[78] M. Fuss, M. Luna, D. Alcantara, J. M. de la Fuente, P. M. Enriquez-Navas, J. Angulo, S. Penades, and F. Briones. Carbohydrate-carbohydrate interaction prominence in 3D supramolecular self-assembly. *The Journal of Physical Chemistry B* **112**(37), 11595–11600 (2008)

[79] A. Raman, J. Melcher, and R. Tung. Cantilever dynamics in atomic force microscopy. *Nano Today* **3**(1-2), 20 – 27 (2008)

[80] R. W. Stark. Bistability, higher harmonics, and chaos in AFM. *Materials Today* **13**(9), 24 – 32 (2010)

[81] M. K. Ghatkesar, T. Braun, V. Barwich, J.-P. Ramseyer, C. Gerber, M. Hegner, and H. P. Lang. Resonating modes of vibrating microcantilevers in liquid. *Applied Physics Letters* **92**(4), 043106 (pages 3) (2008)

[82] K. L. Ekinci, Y. T. Yang, and M. L. Roukes. Ultimate limits to inertial mass sensing based upon nanoelectromechanical systems. *Journal of Applied Physics* **95**(5), 2682–2689 (2004)

[83] S. Dohn, R. Sandberg, W. Svendsen, and A. Boisen. Enhanced functionality of cantilever based mass sensors using higher modes. *Applied Physics Letters* **86**(23), 233501–233501 (2005)

[84] C. A. Van Eysden and J. E. Sader. Frequency response of cantilever beams immersed in viscous fluids with applications to the atomic force microscope: Arbitrary mode order. *Journal of Applied Physics* **101**(4), 044908–044908 (2007)

[85] C. A. Van Eysden and J. E. Sader. Frequency response of cantilever beams immersed in compressible fluids with applications to the atomic force microscope. *Journal of Applied Physics* **106**(9), 094904–094904 (2009)

[86] E. T. Herruzo and R. Garcia. Frequency response of an atomic force microscope in liquids and air: Magnetic versus acoustic excitation. *Applied Physics Letters* **91**(14), 143113–143113–3 (2007)

[87] L. Landau and E. Lifshitz. *Theory of Elasticity* (Pergamon, Oxford, 1970)

[88] J. E. Sader. Frequency response of cantilever beams immersed in viscous fluids with applications to the atomic force microscope. *Journal of Applied Physics* **84**(1), 64–76 (1998)

[89] S. Rast, C. Wattinger, U. Gysin, and E. Meyer. Dynamics of damped cantilevers. *Review of Scientific Instruments* **71**(7), 2772 –2775 (2000)

[90] R. D. Blevins. *Formulas for natural frequency and mode shape* (Van Nostrand Reinhold Co., New York :, 1979)

[91] F. Rubio-Sierra, R. Vázquez, and R. Stark. Transfer function analysis of the micro cantilever used in atomic force microscopy. *EEE Transactions on Nanotechnology* **5**(6), 692–700 (2006)

[92] A. Gannepalli, A. Sebastian, J. Cleveland, and M. Salapaka. Thermally driven non-contact atomic force microscopy. *Applied Physics Letters* **87**(11), 111901–111901 (2005)

[93] X. Xu and A. Raman. Comparative dynamics of magnetically, acoustically, and brownian motion driven microcantilevers in liquids. *Journal of Applied Physics* **102**(3), 034303 (2007)

[94] T. H. Boyer. The force on a magnetic dipole. *American Journal of Physics* **56**(8), 688–692 (1988)

[95] M. R. Paul and M. C. Cross. Stochastic dynamics of nanoscale mechanical oscillators immersed in a viscous fluid. *Physical Review Letters* **92**(23), 235501 (2004)

[96] M. Gere and S. P. Timoshenko. *Mechanics of Materials*. 4th Ed. (Pws Pub Co, 1997)

[97] D. Ramos, J. Tamayo, J. Mertens, and M. Calleja. Photothermal excitation of microcantilevers in liquids. *Journal of Applied Physics* **99**(12), 124904 (pages 8) (2006)

[98] D. Crawley and J. de Luis. Use of piezoelectric actuators as elements of intelligent structures. *The American Institute of Aeronautics and Astronautics* **25**, 1373– 1385 (1987)

[99] V. H. Guerrero and R. C. Wetherhold. Strain and stress calculation in bulk magnetostrictive materials and thin films. *Journal of Magnetism and Magnetic Materials* **271**(2-3), 190 – 206 (2004)

[100] E. van de Riet. Deflection of a substrate induced by an anisotropic thin film stress. *Journal of Applied Physics* **76**(1), 584–586 (1994)

[101] M. Lantz, Y. Liu, X. Cui, H. Tokumoto, and S. Lindsay. Dynamic force microscopy in fluid. *Surface and interface analysis* **27**(56), 354–360 (1999)

[102] H. J. Butt and M. Jaschke. Calculation of thermal noise in atomic force microscopy. *Nanotechnology* **6**(1), 1 (1995)

[103] E. T. Herruzo. *Desarrollo de la microscopia de fuerzas bimodal para la cuantificacion de propiedades nanomecanicas*. PhD Thesis, Universidad Autonoma de Madrid (2011)

[104] M. Kageshima, T. Chikamoto, T. Ogawa, Y. Hirata, T. Inoue, Y. Naitoh, Y. J. Li, and Y. Sugawara. Development of atomic force microscope with wide-band magnetic excitation for study of soft matter dynamics. *Review of Scientific Instruments* **80**(2), 023705 (2009)

[105] M. Martin-González, F. Briones, J. García-Martín, J. Montserrat, L. Vila, G. Faini, A. Testa, D. Fiorani, and H. Rohrmann. Nano-patterning of perpendicular magnetic recording media by low-energy implantation of chemically reactive ions. *Journal of Magnetism and Magnetic Materials* **322**(18), 2762–2768 (2010)

[106] URL `http://www.home.agilent.com/en/pc-1678650/mac-levers`

[107] D. Ramos, J. Tamayo, J. Mertens, M. Calleja, and A. Zaballos. Origin of the response of nanomechanical resonators to bacteria adsorption. *Journal of Applied Physics* **100**(10), 106105–106105 (2006)

[108] J. Tamayo, D. Ramos, J. Mertens, and M. Calleja. Effect of the adsorbate stiffness on the resonance response of microcantilever sensors. *Applied Physics Letters* **89**(22), 224104–224104 (2006)

[109] B. Pelaz, V. Grazu, A. Ibarra, C. Magen, P. del Pino, and J. M. de la Fuente. Tailoring the synthesis and heating ability of gold nanoprisms for bioapplications. *Langmuir* **28**(24), 8965–8970 (2012)

[110] J. Jamet, T. Aign, P. Meyer, S. Lemerle, J. Ferré, J. Gierak, C. Vieu, H. Bernas, T. Devolder, and V. Mathet. Irradiation effects and magnetization reversal in nanostructures with perpendicular anisotropy. Effect of the dipolar coupling. *Journal of the Magnetics Society of Japan* **23**(SUPP/1), 71–76 (1999)

[111] R. Hyndman, P. Warin, J. Gierak, J. Chapman, J. Ferré, J. Jamet, V. Mathet, and C. Chappert. Structural and magnetic properties of FIB-irradiated microstructures on a Pt/Co multilayer. *Journal of Magnetism and Magnetic Materials* **240**(1), 50–52 (2002)

[112] J. Fassbender, D. Ravelosona, and Y. Samson. Tailoring magnetism by light-ion irradiation. *Journal of Physics D: Applied Physics* **37**(16), R179 (2004)

[113] URL `http://www.srim.org/`

[114] J. P. Biersack and L. G. Haggmark. A Monte Carlo computer program for the transport of energetic ions in amorphous targets. *Nuclear Instruments and Methods* **174**(1), 257–269 (1980)

[115] J. Ziegler, M. D. Ziegler, and J. P. Biersack. SRIM - The stopping and range of ions in matter (2010). *Nuclear Instruments and Methods in Physics Research Section B: Beam Interactions with Materials and Atoms* **268**(11), 1818–1823 (2010)

[116] T. McGuire, J. Aboaf, and E. Klokholm. Co-Sn thin films: Magnetic and transport properties. *Journal of Applied Physics* **53**(11), 8219–8221 (1982)

[117] H. Xu, X. Zhao, C. Grant, J. R. Lu, D. E. Williams, and J. Penfold. Orientation of a monoclonal antibody adsorbed at the solid/solution interface: A combined study using atomic force microscopy and neutron reflectivity. *Langmuir* **22**(14), 6313–6320 (2006)

[118] M. S. Wang, A. Zameer, S. Emadi, and M. R. Sierks. Characterizing antibody specificity to different protein morphologies by AFM. *Langmuir* **25**(2), 912–918 (2009)

[119] B. Pattier, J.-F. Bardeau, M. Edely, A. Gibaud, and N. Delorme. Cheap and robust ultraflat gold surfaces suitable for high-resolution surface modification. *Langmuir* **24**(3), 821–825 (2008)

[120] J. J. Blackstock, Z. Li, M. R. Freeman, and D. R. Stewart. Ultra-flat platinum surfaces from template-stripping of sputter deposited films. *Surface Science* **546**(2-3), 87 – 96 (2003)

[121] H. Hirayama. Growth of atomically flat ultra-thin Ag films on Si surfaces. *Surface Science* **603**(10-12), 1492 – 1497 (2009)

[122] M. Furukawa, H. Tanaka, and T. Kawai. Scanning tunneling microscopy observation of two-dimensional self-assembly formation of adenine molecules on Cu(111) surfaces. *Surface Science* **392**(1-3), L33 – L39 (1997)

[123] P. Gupta, K. Loos, A. Korniakov, C. Spagnoli, M. Cowman, and A. Ulman. Facile route to ultraflat SAM-protected gold surfaces by amphiphile splitting. *Angewandte Chemie International Edition* **43**(4), 520 – 523 (2004)

[124] R. Naumann, S. M. Schiller, F. Giess, B. Grohe, K. B. Hartman, I. Krcher, I. Kper, J. Lbben, K. Vasilev, and W. Knoll. Tethered lipid bilayers on ultraflat gold surfaces. *Langmuir* **19**(13), 5435–5443 (2003)

[125] V. K. Yadavalli, J. G. Forbes, and K. Wang. Functionalized self-assembled monolayers on ultraflat gold as platforms for single molecule force spectroscopy and imaging. *Langmuir* **22**(16), 6969–6976 (2006)

[126] J. A. Derose, T. Thundat, L. A. Nagahara, and S. M. Lindsay. Gold grown epitaxially on mica: conditions for large area flat faces. *Surface Science* **256**(1-2), 102 – 108 (1991)

[127] C. Nogues and M. Wanunu. A rapid approach to reproducible, atomically flat gold films on mica. *Surface Science* **573**(3), L383 – L389 (2004)

[128] M. Hegner, P. Wagner, and G. Semenza. Ultralarge atomically flat template-stripped Au surfaces for scanning probe microscopy. *Surface Science* **291**(1-2), 39 – 46 (1993)

[129] J. Mazurkiewicz, F. J. Mearns, D. Losic, L. Weeks, E. R. Waclawik, C. T. Rogers, J. G. Shapter, and J. J. Gooding. Cryogenic cleavage used in gold substrate production. *Journal of Vacuum Science Technology B: Microelectronics and Nanometer Structures* **20**(6), 2265 –2270 (2002)

[130] D. W. Mosley, B. Y. Chow, and J. M. Jacobson. Solid-state bonding technique for template-stripped ultraflat gold substrates. *Langmuir* **22**(6), 2437–2440 (2006)

[131] J. J. Blackstock, Z. Li, and J. Gun-Young. Template stripping using cold welding. *Journal of Vacuum Science and Technology A: Vacuum, Surfaces, and Films* **22**(3), 602–605 (2004)

[132] I. Horcas, R. Fernandez, J. M. Gomez-Rodriguez, J. Colchero, J. Gomez-Herrero, and A. M. Baro. WSxM: A software for scanning probe microscopy and a tool for nanotechnology. *Review of Scientific Instruments* **78**(1), 013705 (pages 8) (2007)

[133] R. W. G. Wyckoff. *Crystal Structures*, Volume 1. Second Ed. (Interscience Publishers, New York, 1963)

[134] S. M. Lindsay and T. Jing. Force sensing probe for scanning probe microscopy. Patent US6121611 A. (2000)

[135] A. Maali, C. Hurth, R. Boisgard, C. Jai, T. Cohen-Bouhacina, and J.-P. Aimé. Hydrodynamics of oscillating atomic force microscopy cantilevers in viscous fluids. *Journal of Applied Physics* **97**(7), 074907 (2005)

[136] L. Landau and E. Lifshitz. *Fluid Mechanics* (Cambridge University Press, 1971)

[137] J. W. Yi, W. Y. Shih, and W. H. Shih. Effect of length, width, and mode on the mass detection sensitivity of piezoelectric unimorph cantilevers. *Journal of Applied Physics* **91**(3), 1680–1686 (2002)

[138] R. Sandberg, W. Svendsen, K. Mølhave, and A. Boisen. Temperature and pressure dependence of resonance in multi-layer microcantilevers. *Journal of Micromechanics and Microengineering* **15**(8), 1454 (2005)

List of Publications

Publications related to this work

Selective enhancement of individual cantilever resonance modes for AFM operation in liquids and mechanical sensors by means of a Focused Ion Beam
by M. Penedo, A. Raman, P. Prieto, R. Alvaro, J.V. Anguita, M. Luna and F. Briones
in preparation

Magnetic pulsed actuation method for Atomic Force Microscopy
by M. Penedo, M. Luna and F. Briones
in preparation

Enhanced efficiency in the excitation of high modes by means of magnetostrictive actuation
by M. Penedo, A. Raman, I. Fernández-Martínez, M. Luna and F. Briones
in preparation

Solvent resistant ultra flat metal surfaces
by M. Penedo, I. Fernández-Martínez, M. Luna and F. Briones
in preparation

Magnetostriction-driven cantilevers for dynamic atomic force microscopy
by M. Penedo, I. Fernández-Martínez, J. L. Costa-Krämer, M. Luna and F. Briones
in Applied Physics Letters **95** 143505 (2009)

Further publications

Gold nanoparticle coated silicon tips for Kelvin probe force microscopy in air
by S. Hormeño, M. Penedo, C. V. Manzano and M. Luna
in Nanotechnology **24** 395701 (2013)

ZnO morphology control by pulsed electrodeposition
by V. Manzano, O. Caballero-Calero, S. Hormeño, M. Penedo, M. Luna and M. S. Martín-González
in Journal of Physical Chemistry C **117** 1502 (2013)

Ammonia induces aquaporin-4 rearrangement in the plasma membrane of cultured astrocytes
G. Bodega, I. Suárez, L. A. López-Fernández, M. I. García, M. Köber, M. Penedo, M. Luna, S. Juárez, S. Ciordia, M. Oria, J. Córdoba and B. Fernández

in Neurochemistry International **61** 1314 (2012)

Patents

Corrosion-resistant magnetostrictive micro-mechanical element for microactuators and dynamic-mode atomic force microscopy and operation compatible with corrosive media
M. Penedo, I. Fernández-Martínez, J. L. Costa-Krämer, M. Luna and F. Briones
WIPO Patent WO/2010/043746A1, April 2010